

LOW PRESSURE METAL-ORGANIC VAPOR PHASE EPITAXY (MOVPE)
OF $Zn_{1-x}Cd_xS/GaAs$: GROWTH, CHARACTERIZATION, AND DEVICE
APPLICATION

By

JOE S. CHO

A DISSERTATION PRESENTED TO THE GRADUATE SCHOOL
OF THE UNIVERSITY OF FLORIDA IN PARTIAL FULFILLMENT
OF THE REQUIREMENTS FOR THE DEGREE OF
DOCTOR OF PHILOSOPHY

UNIVERSITY OF FLORIDA

1995

to

my wife, Zeva

and

my family

ACKNOWLEDGMENTS

The author wishes to thank the many individuals that have made this work possible. First, many thanks go to Dr. Tim Anderson for his guidance and support. This work could not have been possible without the advice of all the committee members: Dr. Chang-Won Park, Dr. Mark Orazem, Dr. Spiros Svoronos, and Dr. Kevin Jones.

Steven Schein has kept the Surge area running smoothly throughout my stay, and experimental work would have been unbearable without him. Eric Bretschneider has been a great partner in keeping the II-VI MOVPE system running. The author thanks Shirley, Nancy, and Debbie for their cheerful personalities and many laughs.

The author owes much gratitude to the Materials Science, Electrical Engineering, and Physics departments for the use of many characterization techniques. The author thanks Dr. Lew Johns for the great football and softball games. He has taught the author more than he could have ever imagined.

TABLE OF CONTENTS

	<u>page</u>
ACKNOWLEDGMENTS	iii
ABSTRACT.....	vi
 CHAPTERS	
1 INTRODUCTION	1
2 GROWTH OF $Zn_{1-x}Cd_xS$ EPILAYERS ON GaAs.....	19
2.1 Growth Facilities	21
2.2 Experiment.....	24
2.3 Film Quality Optimization Study.....	27
2.3.1 Taguchi Method / Design of Experiments.....	27
2.3.2 Factorial Design of Experiments Results	35
2.3.3 Influence of Other Process Parameters	45
2.3.3.1 Buffer layer.....	45
2.3.3.2 Growth rate.....	49
2.3.3.3 Etchant.....	49
2.4 Growth Characteristics	53
2.4.1 Flow Mechanics.....	53
2.4.2 Thickness Uniformity	59
2.4.3 Growth Kinetics.....	65
2.4.4 Crystal Structure.....	69
2.4.5 Surface Morphology	74
2.4.6 Defects	77
2.4.7 Solid Phase Composition.....	85
2.4.8 Optical Purity.....	87
2.5 Summary.....	90
3 PROPERTIES OF $Zn_{1-x}Cd_xS$ EPILAYERS ON GaAs.....	93
3.1 Sample Preparation.....	94
3.2 Bandgap Energy	95
3.2.1 Experiment	95
3.2.2 Results.....	96

3.3	Complex Refractive Index	102
3.3.1	Experiment	102
3.3.2	Results.....	105
3.4	Thermal Expansion Coefficient	114
3.4.1	Experiment	120
3.4.2	Results.....	121
3.5	Doping.....	126
3.5.1	Experiment	133
3.5.2	Dopant p-type.....	133
3.5.3	Dopants n-type	136
3.5.4	Point Defect Equilibrium Analysis	141
3.5.4.1	Low sulfur partial pressure	143
3.5.4.2	High sulfur partial pressure.....	145
3.6	Summary.....	146
4	MODEL OF SOLID VAPOR DISTRIBUTION	148
4.1	Model Development and Results	150
4.2	Summary.....	169
5	WAVEGUIDE FABRICATION AND THEORETICAL CALCULATIONS	171
5.1	Sample Preparation	173
5.2	Experiment and Results	174
5.3	Theoretical Calculations	176
5.3.1	Optical Confinement	176
5.3.2	Carrier Confinement	197
5.3.3	Physical Aspects of Laser Fabrication	203
5.4	Summary.....	205
6	CONCLUSIONS AND FUTURE WORK	206
	REFERENCES	213
	BIOGRAPHICAL SKETCH	225

Abstract of Dissertation Presented to the Graduate School
of the University of Florida in Partial Fulfillment of the
Requirements for the Degree of Doctor of Philosophy

LOW PRESSURE METAL-ORGANIC VAPOR PHASE EPITAXY (MOVPE)
OF ZnCdS/GaAs: GROWTH, CHARACTERIZATION, AND DEVICE
APPLICATIONS

By

Joe S. Cho

August 1995

Chairman: Dr. Timothy J. Anderson
Major Department: Chemical Engineering

A comprehensive investigation of ZnCdS grown on GaAs by the low pressure metal-organic vapor phase epitaxy (MOVPE) technique has been conducted. Optimization, growth characteristics, film properties, solid-vapor equilibrium and device applications are key issues that have been addressed.

The Taguchi method or design of experiments (DOE) approach is taken to determine the effects of process parameters on the crystalline quality of epilayers. Its main advantage over the standard methodology of changing one-factor-at-a-time is the reduction of experimental runs needed to obtain the same precision of information. In addition, DOE can statistically evaluate significance of multi-parameter interactions.

Thin ZnCdS films have been grown on (100) and (111) oriented GaAs substrates using diethyl zinc (DEZn), dimethyl cadmium (DMCd) and H₂S. The lowest reported full width at half maximum of peaks obtained from X-ray diffraction spectra has been obtained using this chemistry. Critical process parameters and their setpoints have also been identified that influence the desirable 2-dimensional and undesirable 3-dimensional growth. A nucleation/growth mechanism is presented to explain the preferential initiation of one growth mode over the other. Other growth characteristics including flow mechanics, film thickness uniformity, defect density, crystal structure, solid phase composition and optical purity have been studied as a function of growth parameters.

The general growth characteristics highly influence the optical, physical and electrical properties of ZnCdS. The bandgap energy and complex refractive index have been measured by reflectometry and ellipsometry, respectively. Thermal expansion coefficients have been calculated from lattice constant changes at various temperatures. In-situ doping studies have also been performed to determine the maximum electron and hole concentrations.

A simple model based on the regular solution approach was developed to explain the solid-vapor equilibrium distribution. For the first time, the interaction parameters for binary II-VI compounds were calculated from Stringfellow's delta lattice parameter model based solely on material properties of II-VI compounds. The results show a good fit to experimental data across a wide range of temperature values.

The measured properties of ZnCdS have been used in theoretical calculations of double heterostructure lasers. The complex refractive indices are needed to evaluate the

optical confinement of a symmetric three-layer slab waveguide: ZnCdS/ZnSe/ZnCdS. The relationship between the active layer thickness and optical confinement have also been investigated. Bandgap energies along with electron affinities have been used to determine the carrier confinement. Calculations based on photothreshold values confirm these results.

CHAPTER 1

INTRODUCTION

A new era for the electronics industry began in 1947 with the invention of the bipolar transistor by Bardeen, Brattain, and Shockley. This new electronic device, like so many other diodes and transistors of that time period, was manufactured from germanium. Due to its unfavorable material properties, however, germanium soon proved to be incompatible with certain applications. In particular, germanium devices tended to exhibit high injection leakage currents because of its narrow bandgap energy of 0.66 eV. As a result, germanium devices could only operate to a maximum temperature of 100 °C. Furthermore, with the advent of planar processing technology, the ability to form a stable passivation layer on the semiconductor became an absolute requirement. Germanium oxide is unsuitable in this role since it readily dissolves in water and decomposes at 800 °C, which is well below the temperatures required in subsequent processing. These qualities made germanium an unattractive choice as the major semiconductor for future development in device fabrication.

In the 1960s, silicon quickly replaced germanium as the major semiconductor material for device application. With silicon's larger bandgap energy of 1.1 eV, Si-based devices exhibited smaller junction leakage currents and therefore could operate at higher temperatures, a maximum of 150 °C. Unlike germanium oxide, silicon dioxide is easy to produce and highly stable. Besides the enhanced performance and ease of fabrication that

silicon offers over germanium, electronic-grade silicon is about ten times less expensive than germanium for the same purity.

To date, 95% of the semiconductor electronic devices sold worldwide are silicon-based. Integrated circuit (IC) sales in the United States are expected to grow by 16% annually from \$11 billion in 1986 to \$90 billion by the year 2000 [1]. This phenomenal growth is driven by extensive applications in previously untapped markets such as the automobile industry. To satisfy the need for reliable, high speed, and high frequency devices with low power requirements, miniaturization must continue at a rapid pace. The device speed has increased four orders of magnitude since 1960 while the critical dimension (CD) of devices has decreased from approximately 10.0 to 1.0 μm [2]. An important side benefit to enhanced performance with miniaturization is that not only does the individual device size shrink but so does the cost to make it. With an opportunity to increase the device density per wafer, the cost of a random-access memory chip is reduced by 50% every two years for each successive generation [3]. Although miniaturization is the present solution to achieving ever increasing demands for high speed devices, progress into this and other applications will eventually be limited by the material properties of silicon as it once was for germanium.

Although silicon will undoubtedly continue to dominate solid state electronics well into the near future, a growing need for high speed switching devices and development of solid state optoelectronics in the visible spectrum have placed the major focus of research and development on compound semiconductors, specifically the III-V and II-VI alloys. The two main groups are differentiated by the chemical nature of the constituent elements.

The III-V and II-VI materials are solid solutions comprised of elements from the III (Al, In, Ga) and V (N, P, As, Sb); and the II (Zn, Cd, Hg) and VI (S, Se, Te) columns of the periodic table, respectively. One factor for such growing interest lies in their inherent nature to form a large expanse of ternary and higher order solid solutions, often of continuous composition with broadly varying physical properties. The ability of ternary and higher order alloys to exactly lattice match commercially available substrates by use of compositional degrees of freedom, reduces strain induced misfit dislocations. Interfacial defects are the main sources of non-radiative recombination centers which hinder electromagnetic emission in photonic devices and must therefore be minimized to improve their reliability. Figure 1-1 correlates the bandgap energy and the lattice constants at room temperature for many II-VI compounds [4]. Similar information for III-V and IV materials is available elsewhere [5]. Many II-VI compounds are direct bandgap semiconductors with bandgap energies and lattice constants spanning from 3.68 eV and 5.41 Å for ZnS to 1.56 eV and 6.48 Å for CdTe. This wide range of bandgap energies makes II-VI materials the most versatile of all the families of compound semiconductors for optoelectronic applications.

The popularity of alloys formed from these elements is partially due to their desirable characteristics which include superior carrier transport properties. These and other material properties of selected semiconductors including silicon and germanium are listed in Table 1-1. With high electron mobilities, III-V compounds show great potential in fabrication of high speed devices such as field effect transistors (FETs), high electron

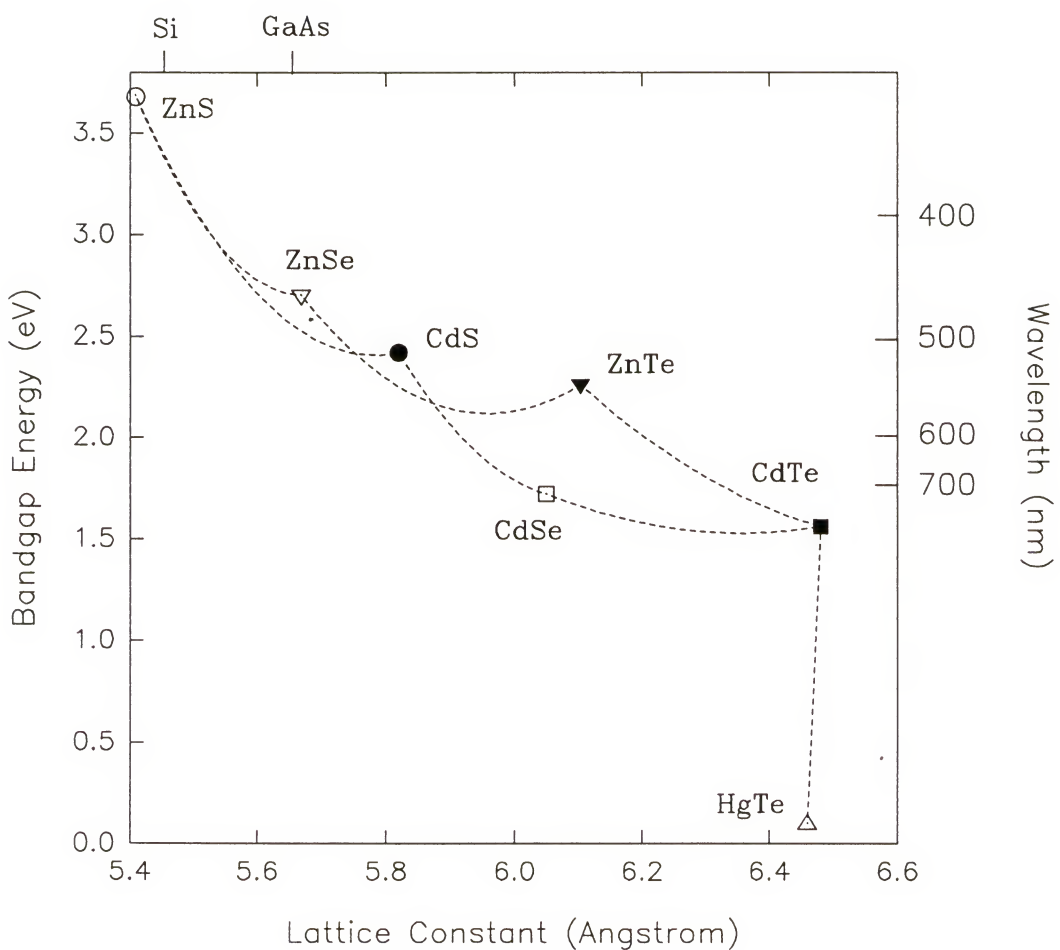


Figure 1-1. Correlation of bandgap energy and lattice constant at room temperature for II-VI compounds.

mobility transistors (HEMTs), and bipolar transistors. In addition, many III-V alloys are direct bandgap semiconductors and can radiatively recombine electrons and holes to emit light when electrically or optically excited. This is the fundamental principle for the production of light emitting diodes (LEDs) and diode lasers.

Table 1-1 Various Properties of Selected Semiconductors at T = 300 K [6].

Semi-conductor	Bandgap Energy (eV)	Electron Mobility (cm ² /V·s)	Hole Mobility (cm ² /V·s)	Dielectric Constant	Lattice Constant (Å)	Density (g/cm ³)	Melting Point (K)
Si	1.12	1,400	470	11.7	5.431	2.328	1685
Ge	0.67	3,900	1,900	16	5.646	5.327	1231
GaAs	1.42	8,000	340	13.2	5.653	5.32	1510
GaN	3.36	380	---	12.2	---	6.10	1500
GaP	2.26	110	75	11.1	5.451	4.13	1750
GaSb	0.72	5,000	1,000	15	6.096	5.619	980
InAs	0.36	33,000	460	14.6	6.058	5.66	1215
InP	1.35	4,600	150	12.4	5.869	4.787	1330
InSb	0.17	77,000	1,000	17	6.479	5.775	798
AlAs	2.16	1,200	400	---	5.662	3.81	1870
AlSb	1.6	200	420	14.4	6.136	4.218	1330
AlP	3.0	---	---	11.6	5.451	2.85	1770
CdS	2.5	300	50	11.6	5.832	4.82	1750
CdTe	1.5	1,000	100	11	6.482	5.86	1365
PbS	0.41	600	700	17	5.936	7.61	1390
PbSe	0.26	1,000	900	---	6.124	8.15	1340
PbTe	0.32	1,800	900	30	6.462	8.16	1180
ZnO	3.35	200	180	8.5	4.580	5.66	--
ZnS	3.7	165	5	5.2	5.420	4.079	2100
ZnSe	2.58	540	30	8.4	5.668	5.42	1790
ZnTe	2.26	340	100	9	6.101	5.72	1568

Commercial applications include extensive use of GaAs/AlGaAs lasers for compact disk players and for red light emitting alphanumeric displays. The GaAs/AlGaAs system is one of the more important III-V systems for red-light emitting lasers. It was fortunate

that Al and Ga can be interchanged with minimal lattice mismatch problems since the sizes of the atoms are nearly equal. This allowed relatively easy fabrication of heterostructures with minimal misfit dislocations and hinted at the potential of optoelectronics. The ability to integrate optics with solid state electronics opens up new applications such as optical computers whereby photons act as carriers instead of holes and electrons. The obvious advantage is the potential for high speed processing at light speed without electromigration problems often associated with present, conventional high speed devices. Although GaAs is well studied and thoroughly investigated, it has not been fully implemented because of its inability to form a stable oxide. One element oxidizes more readily than the other, leaving a metallic phase at the interphase. This difficulty in finding a feasible passivation layer is not only confined to GaAs but extends to other III-V materials as well. Nevertheless, compound semiconductors will still play a significant role in meeting future demands of increased processing speed and integration of optics with solid state electronics.

Investigations of II-VI materials ensued during the later development stages of III-V compounds. Most of the II-VI compounds are characterized by direct bandgap energies with the exception of the mercury chalcogenides (HgSe and HgTe) which behave more as semi-metals rather than semiconductors. Both CdS and CdSe are highly photoconductive and have been the focus of research in solar cells. Properly doped ZnS is highly luminescent and is one of the key materials for electroluminescent (EL) devices. Although research on these materials is ongoing, little is known about the chalcogenides of magnesium and beryllium along with the oxides of cadmium and mercury. The II-VI

compounds generally form in either the wurtzite or the zinc blende structures. BeO, ZnO, ZnS, CdS, ZnSe, CdSe, and MgTe have all been known to take the wurtzite structure while the sulfides, selenides, and tellurides of beryllium, zinc, cadmium, and mercury have been known to take the zinc blende structure [7]. Some of the compounds that normally form in the wurtzite and zinc blende structures have been observed to transform into the sodium chloride (NaCl) structure under high pressure. CdO, MgO, MgS, and MgSe are the only compounds that normally take the NaCl structure at room temperature and atmospheric pressure.

Many of the physical properties of II-VI compounds can be attributed to the types of bonds formed in crystalline structures. The tetrahedral lattice sites characterized by the wurtzite and zinc blende crystal structures indicate that the bonding mechanism is homopolar. The homopolar bond is better understood in terms of the tetravalent atom which requires four bonds. The bonding is a sp^3 hybridized bond directed toward the corners of a tetrahedron. The electronic wave function for the sp^3 hybridization is a mixture of s^2p^2 state rearranged to form the sp^3 state. Unlike the pure homopolar bonds seen in the C^{4+} ions for a purely symmetrical diamond structure, II-VI compounds have an inherent electrical polarity with associated electronegativities due to the ionization state of the II and VI column atoms. The disparity of the ionization state is less for the III-V materials, and as a result, III-V materials tend to have bonds that are more covalent than ionic.

The general order of pure covalent to more ionic bonding is the following: IV, III-V, II-VI, and NaCl. In covalent bonding, the electron spin pairing is shared equally, while for

the II-VI materials, there is more exchanging of electrons. As a result, this forms an ionic electrostatic attraction which is characteristic of the ionic bond. The ionic character increases as the atomic weight decreases (e.g., from HgTe to ZnS). The ionic bond has the effect of strengthening the lattice, raising the melting temperature and increasing the bandgap energy.

The wide interest in the growth and study of the II-VI compounds is fostered by the great promise of blue light emitting optoelectronics. Commercially, this is a desirable characteristic. As of today, there are various materials, primarily III-V materials, that can be used to make lasers or laser diodes that emit in the yellow and red regions of the visible spectrum. With two of the three primary colors determined, the only one remaining is the blue. With access to all the primary colors, there is now capability to form any color for applications in high definition televisions and flat panel displays. Candidates for this application include the II-VI materials, GaN, and SiC. With the advent of the fiberoptic, blue light would also allow more pieces of information to be transmitted for a given time frame since the wavelength of the blue light is smaller than that used in current technology. This results in a more economically favorable position for the telecommunications industry. To date, blue light has not been achieved with complete success, although the 3M Corporation and others have achieved good results using ZnSe for production of blue light emission [8-9].

Thin films of ZnS, CdS, and its alloy have been grown by many epitaxial growth techniques. The most common techniques are liquid phase epitaxy (LPE), molecular beam epitaxy (MBE), vapor phase epitaxy (VPE), metal-organic molecular beam epitaxy

(MOMBE), chemical spray deposition, and metal-organic vapor phase epitaxy (MOVPE).

There are of course advantages and limitations to each technique as discussed in general reviews [10-11].

LPE is a growth technique that allows the deposition of thin epitaxial films of material from saturated or supersaturated liquid solutions. The apparatus needed for LPE technique is very simple and the grown material is of extremely high quality. High purity of the grown material is partially due to the availability of high purity starting materials and the inherent purification process as the grown material undergoes a transition from the liquid to the solid state. Some of the disadvantages are the inability to create abrupt interfaces, difficulty in compositional control due to melt back effects, and poor thickness uniformity.

The interest in LPE growth of II-VI materials is heightened by its successful application to III-V materials. Although reports have not been found concerning LPE growth of ZnCdS or its binaries, attempts have been made to grow ZnSe on ZnSSe substrates by LPE [12]. Smooth mirror-like layers were grown on (100) and (111)A surfaces, but only at low cool rates. The resulting layers were all n-type with moderate doping and low mobility. Ion microprobe analysis showed contamination of Na, Al, and Si. Photoluminescence (PL) measured at 77 K showed a strong blue emission, although deep-level emission dominated the spectrum. Although the potential exists for producing optoelectronic quality materials with LPE, it is extremely difficult to control the optical and electrical properties due to contamination and the interface quality is expected to be poor. This is evident by the lack of activity with this technique in the last five or six years.

MBE allows the growth of sharp interfaces and as a result, also of high quality superlattices. First attempts at MBE growth were applied to the growth of III-V materials such as GaAs, GaP, and AlN [13-16]. The concept of the MBE process is relatively simple. The constituent elements are derived from Knudsen-style effusion sources containing solid-element material. They are heated and sublimed onto a heated substrate in a controlled ultra high vacuum (UHV) environment. In addition, it can be equipped with in situ monitoring tools such as reflection high-energy electron diffraction (RHEED) to monitor real time growth mechanisms, crystallization, and even defect formation. These characteristics make the MBE technique ideally suitable for research conditions, but because of the low throughput, it has limited commercial value. Another problem is that some elements form condensed polymorphs (e.g., phosphorous) or gaseous polymers (e.g., Se) which increases the difficulty of growth.

Considerable attention has recently been devoted to the growth of ZnSe on GaAs with no mention of ZnCdS, ZnS, or CdS MBE growth in literature. Yoneda et al. [17] determined the principal donor impurity incorporated in unintentionally undoped ZnSe came from the Se source. They were able to demonstrate that the free carrier concentration can be dramatically reduced from a typical level of 10^{17} cm^{-3} to where the material was highly resistive (resistivity $> 10^4 \Omega\text{-cm}$) by purifying the Se source. Purity of the reactants had long been associated with the electrical properties of ZnSe and other II-VI semiconductor materials. Elemental sources were often used which had improved purity of crystalline or powder sources. In addition, the use of elemental sources also provided better control of the material stoichiometry. This is important to minimize

dopant compensation by native defects. Unfortunately, the growth temperature was still high and contamination with impurities was not reduced.

The VPE technique has also been used to grow single crystal thin films of II-VI materials [18]. In this technique, the halides or hydrides of the constituent elements are passed over a heated substrate to react and deposit a thin film. This technique has been used to form ZnS, CdS, and ZnO. Studer et al. [19] used this technique to grow polycrystalline thin films of ZnS on glass substrates using H₂S and ZnCl₂ at growth rates of 0.5 to 1.0 $\mu\text{m}/\text{min}$. A hydrogen sulfide partial pressure of 0.5 Torr and a growth temperature of 500 to 650 °C provided the best conditions for ZnS growth. This method was extended to the growth of a ZnS-CdS solid solution and, as such, was the first reported study of the pseudobinary growth.

MOMBE has also been recognized as a promising low temperature growth technique. It combines the advantages of growth in a clean environment used for MBE and the versatility of molecular sources used in MOVPE. In a clean environment (UHV), it is now possible to keep the surface of the substrate extremely clean, resulting in growth of high purity and high quality epilayers. The separation of the individual reactant beams minimizes premature gas phase reactions between the sources in the reactor and operation at low Knudsen values simplifies the transport. As in MBE, there is a possibility of *in situ* process monitoring such as RHEED and quadrupole mass spectrometry (QMS). The low growth rate and temperature permits thickness control at the atomic layer level which is important for fabricating novel devices such as SLSs. Unlike traditional MBE, the use of molecular sources allows flexibility in dopant precursors, the possibility of selective area

growth, and lower growth temperature due to the higher surface mobility of the chemical species.

Another distinct advantage of MOMBE in comparison to MBE is the ease in controlling reactant delivery rates. In MBE, the elemental evaporation rate is controlled by the source temperature. The high vapor pressure and polymer property formation characteristic of sulfur make this element difficult to reproducibly deliver in traditional MBE. MOMBE allows use of alkyl or hydride chalcogens as alternative sources to elemental sulfur to achieve a stable and reproducible reactant delivery rate. Since these sources are chemically stable and will not easily pyrolyze at typical substrate temperatures, they are often pre-cracked in a high temperature cracker to obtain a reasonable growth rate. Temperatures far in excess of the elemental sublimation temperature can be used to produce lower molecular weight sulfur polymers. To eliminate gas phase pre-reactions, the MOMBE technique uses impingement of reactants directly onto the substrate and the low pressure minimizes collisions between the gaseous reactants. The reactor pressure is typically below 10^{-4} Torr to ensure the mean free path of the source gases is longer than the distance between the gas inlet and the substrate. Therefore, even when the highly reactive hydride gases are to be used as source materials, the unwanted premature reactions can be minimized in MOMBE. In addition, with the high temperature cracker for source gases, the epitaxial growth temperature can be lowered to about 250 °C when the alkyl chalcogens are used as source materials. Lowering the growth temperature is important for conductivity control of the wide bandgap II-VI epilayers. As expected,

most of the MOMBE work has been on the growth of III-V materials with unfound citings on ZnCdS and CdS, but with limited reports on ZnS [20-21].

Deposition by the chemical spray process is unique to the growth of II-VI compounds and was mainly developed for the growth of CdS thin films as a fast and inexpensive method for the photovoltaic industry [22]. The constituents are contained in an aqueous solution of a metallic salt and organic compounds of VI elements. The elemental species are atomized by high pressure through a nozzle. The spray is directed onto a heated substrate which is maintained at 400 °C while growth occurs. Cadmium chloride and thiourea have been shown to produce high quality CdS thin films for photovoltaic cell applications. Growth rates of 3.0 to 4.5 $\mu\text{m}/\text{hr}$ have been obtained with carrier concentrations of 10^{15} to 10^{16} cm^{-3} and mobilities as high as $90 \text{ cm}^2/\text{V}\cdot\text{s}$ [23]. This technique has also been used successfully to grow ZnS and ZnCdS solid solutions.

The previously mentioned growth techniques have their unique disadvantages that make them undesirable options for growth studies of ZnCdS. The MBE and MOMBE have low throughput and would not be a commercially viable process. LPE and the chemical spray deposition process are difficult to control electrical and optical properties due to contamination. VPE has not been demonstrated to produce abrupt interfaces necessary for laser fabrication.

The MOVPE technique is the most flexible of the epitaxial techniques although the chemistry and the growth process are more complicated. This technique has been shown to produce abrupt interfaces and material quality that is comparable to those grown by the other techniques. One of the major problems is that the starting reactant materials are

expensive and there are many operating parameters that need to be controlled precisely to achieve high quality materials. MOVPE is based on the pyrolysis of group II organometallic species in the presence of group VI hydride gases in a open tube system, normally at reduced pressure. This technique requires only heating of the substrate in a cold wall reactor. The growth process is generally operated in the mass transport limited mode where the rate controlling step is the mass transfer of reactants from the bulk gas phase to the growth surface. The disadvantages of this technique include the unintentional incorporation of carbon as a deep level defect into the films, significant deposits on cold walls due to parasitic reactions, and toxicity and flammability of many precursors. Some of the early work on growth of II-VI compounds by this technique [24-26] and more recent reviews [27-28] can be found in the literature.

In MOVPE growth, three generic designs of reactors are used: horizontal, barrel, and vertical (Figure 1-2). The main distinction among the three types is the direction of the reactant gases in reference to the substrate. For the horizontal and barrel designs, the gas flow is tangential to the substrate, while in the vertical design, the gas flow is perpendicular. The main advantage of the barrel reactor is its high wafer capacity, typically accommodating fifteen to twenty wafers. These high throughput barrel reactors are often the choice for industrial applications. In contrast, the vertical reactor usually accommodates only one wafer at a time and is limited to research activities. One major disadvantage with the vertical reactor is that, with the perpendicular impingement of the reacting gases, the turbulence that surrounds the substrate makes it extremely difficult to produce uniform films. The horizontal reactor is essentially a single “slot” of the barrel

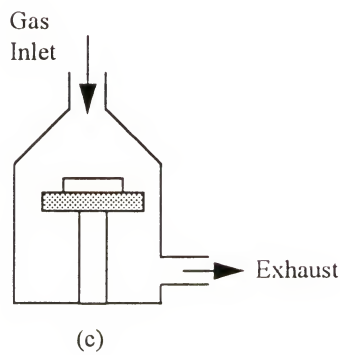
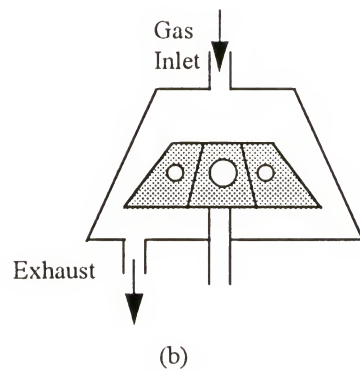
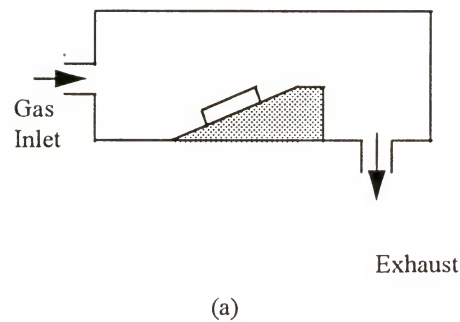


Figure 1-2. Schematic diagrams of the reactor designs for MOVPE growth systems: (a) horizontal, (b) barrel, and (c) vertical reactors.

reactor. It does have the capacity to process multi-wafers, yet its design is simple enough to lend itself easily to research activities. For these reasons, the horizontal reactor is commonly used for the growth studies.

In this dissertation, a thorough investigation of the growth and characterization of ZnCdS grown by low pressure MOVPE is presented along with an evaluation of potential applications to the fabrication of double heterostructure (DH) lasers for blue light emission.

Chapter 2 discusses the optimization and general characteristics of ZnCdS grown by MOVPE using DEZn, DMCd, and H₂S. The Taguchi or design of experiments method has been adopted to determine the effects of important growth parameters and possible multi-parameter convolution effects on the crystallinity of the epilayer. Detailed investigations were conducted to evaluate the effectiveness of possible solutions for improving crystallinity: etchants, ZnSe buffer layer, and growth rate. The general behavior of ZnCdS growth was also studied: flow mechanics, kinetics, film thickness uniformity, crystal structure, surface morphology, solid phase composition, extended defects, and optical purity. A 3-dimensional growth mode was correlated to process parameters and results explained with a nucleation and growth mechanism. The growth studies suggested improved crystalline growth of ZnCdS on (111) oriented GaAs substrates compared to (100) substrates. This was explained with energy minimization and charge balance arguments. The crystalline quality of the films was compared by measurement of the full width half maximum (FWHM) values of rocking curves from high resolution X-ray diffraction (HRXRD) measurements. ZnCdS films were further

characterized by photoluminescence (PL), transmission electron microscopy (TEM), scanning electron microscopy (SEM), Nomarski microscopy, electron probe microanalysis (EPMA), and low energy electron diffraction (LEED).

Chapter 3 describes the optical, physical, and electrical properties of lattice matched and nearly lattice matched ZnCdS grown on GaAs. The bandgap energy and complex refractive index are the two optical properties measured by reflectometry and ellipsometry, respectively. The former is needed to evaluate carrier confinement and the latter for optical confinement. The thermal expansion coefficients (TECs) were measured for a wide range of temperature and composition. TECs were calculated from lattice constant changes produced by temperature variation. The lattice constants were measured using HRXRD. A special sample heating stage was mounted on the goniometer that allowed temperature to be raised and controlled to within ± 2.0 °C. The in-situ doping studies were conducted to investigate the potential of ZnCdS as cladding layers for carrier injection luminescence. Triethyl gallium (TEGa) and triethyl aluminum (TEAl) were investigated as possible n-type dopants while bis-trimethylsilyl amido zinc (TMSAZ) was used as a novel p-type dopant. The dependence of doping level on growth temperature and dopant concentration in the gas phase was studied. Several authors have reported n-type behavior of unintentionally doped ZnCdS films and this was explained by solid state diffusion of Ga into the epilayer from the GaAs substrate. A simple defect equilibrium analysis showed the n-type behavior is not caused by non-stoichiometric point defects due to either low or high sulfur partial pressures.

Chapter 4 presents a model of the solid-vapor equilibrium based on the regular solution approach. For the first time the interaction parameter between binary constituent II-VI compounds was calculated from Stringfellow's delta lattice parameter (DLP) model based specifically on material properties of II-VI compounds. This was used to develop a relationship between the composition of the solid and vapor phase for the growth of ZnCdS. The one variable model is fitted to experimental data at a given temperature and then tested for predictive ability at other growth temperatures. The results are quite promising considering the model is a one parameter fit.

Chapter 5 discusses photopumping studies of a DH structure with a thin pseudomorphic layer of ZnSe as the active layer and ZnCdS as the cladding layers to demonstrate optical confinement. Results showed no lasing phenomena. Theoretical calculations were performed to predict feasible DH structures with ZnCdS as either the active or cladding layers. The ZnCdS/ZnSe/ZnCdS DH structure was shown to be a staggered configuration with the possibility of electron confinement but not of hole confinement based on bandgap energies and electron affinities. Calculations based on photothreshold values confirm these results. Solutions to the magnetic and electric field equations were used to evaluate the extent of optical confinement for a symmetric three-layer slab waveguide. The dependence of modes and cutoff on active layer thickness were also determined. Finally, conclusions and future work are presented in Chapter 6.

CHAPTER 2

GROWTH OF $Zn_{1-x}Cd_xS$ EPILAYERS ON GaAs

The II-VI compounds, especially ZnSe, have been the focus of research as potential semiconductors for fabrication of visible-light emitting, optoelectronic devices due to their direct and wide bandgaps (1.65 to 3.66 eV). The performance and reliability of these heterojunction devices are highly dependent on the degree of lattice matching between the epilayer and the substrate. Although successful growth of crystalline ZnSe by both MBE [17, 29-31] and MOVPE [32-35] techniques has been extensively documented, concerns still exist over possible interfacial misfit dislocations presumably caused by an inherent 0.27% lattice mismatch when grown on GaAs. These undesirable defects act as non-radiative recombination centers that diminish the efficiency and reliability of devices. One solution is to utilize pseudobinary or higher ordered alloys to achieve a closer lattice match to the substrate.

A viable alternative to ZnSe is $Zn_{1-x}Cd_xS$: important as a promising new material in its own right and also as a predecessor to wider bandgap pseudoternaries such as $Zn_xCd_yMg_{1-x-y}S$. Not only can $Zn_{1-x}Cd_xS$ be exactly lattice matched to GaAs at room temperature, but its bandgap energy is estimated to be 2.9 eV (blue to purple luminescence) at lattice matched conditions, assuming Vegard's Law. Thin films of $Zn_{1-x}Cd_xS$ have been grown by MOVPE [36-43], an evaporation growth technique [44], and a solution-growth technique [45]. Of these growth techniques, only MOVPE has been

used for growth on GaAs and its increased popularity is due to its versatility and ease of control. Even strained-layer superlattice structures of ZnCdS/ZnS have been grown with this technique [46].

Another pseudobinary system that may prove to be an alternative to ZnSe is ZnS_ySe_{1-y} . The advantages of one pseudobinary alloy compared to the other are similar as both can be lattice matched to GaAs with bandgap energies at lattice conditions of 2.9 eV (ZnCdS) and 2.8 eV (ZnSeS). One of the main differences, however, pertains to their mechanical properties. ZnCdS has a smaller thermal expansion coefficient than that of GaAs and therefore, will be under compressive strain, while ZnSeS will be under tensile strain. Of the two, compressive strain in the epilayer is more desirable because it minimizes defect generation [42].

Another difference lies in ease of compositional control. For both systems, the VI/II ratio is typically set high (greater than 50) to produce high quality films [47-48] and the growth processes are often operated in a mass transfer limited regime. As a result, the column II elements are the rate limiting reagents. For $Zn_{1-x}Cd_xS$, the compositional degree of freedom is on the column II sublattice (Cd and Zn) and, since these are mass transfer limited species, the solid solution composition should be nearly proportional to their inlet values. On the other hand, the compositional degree of freedom lies on the group VI sublattice in $ZnSe_yS_{1-y}$ and the solid solution composition will be determined by either thermodynamic or kinetic limitations. This latter situation can give large distribution coefficients.

Optimization of $Zn_{1-x}Cd_xS$ epilayers grown on GaAs was performed with the Taguchi method (design of experiments) and the standard method of varying one parameter while others were fixed. The full width at half maximum (FWHM) values of high resolution X-ray diffraction (HRXRD) peaks indicated that higher crystalline material was grown on (111) oriented substrates as compared to (100) substrates. Buffer layers, etchants, and growth rates were studied for their effectiveness in improving crystalline quality. Only the latter two factors were found to have a positive impact. In addition, the growth process was thoroughly characterized by analysis of the fluid mechanics, film thickness uniformity, reaction kinetics, crystal structure, surface morphology, extended defects, solid phase composition, and optical purity.

2.1 Growth Facilities

A schematic diagram of the MOVPE system used in the growth study is shown in Figure 2-1. The gas delivery and exhaust systems (Model SPI-MOCVD 450) were manufactured by the Spire Corporation, while the horizontal reactor design was custom. The growth system is composed of five major elements: (1) reactor, (2) load lock/substrate loading apparatus, (3) gas handling system, (4) metalorganic (MO) bubblers, and (5) exhaust/burn box unit. The 28 inch long, 4 inch inner diameter quartz reactor holds an 18° sloped SiC coated graphite susceptor mounted on a wedge-shaped quartz baffle to ensure laminar flow. The entrance of the reactor is also smoothly tapered in order to minimize large entrance effects that can produce turbulence and recirculation flows near the growth zone. Wet cleaned GaAs substrates are placed on a quartz tray

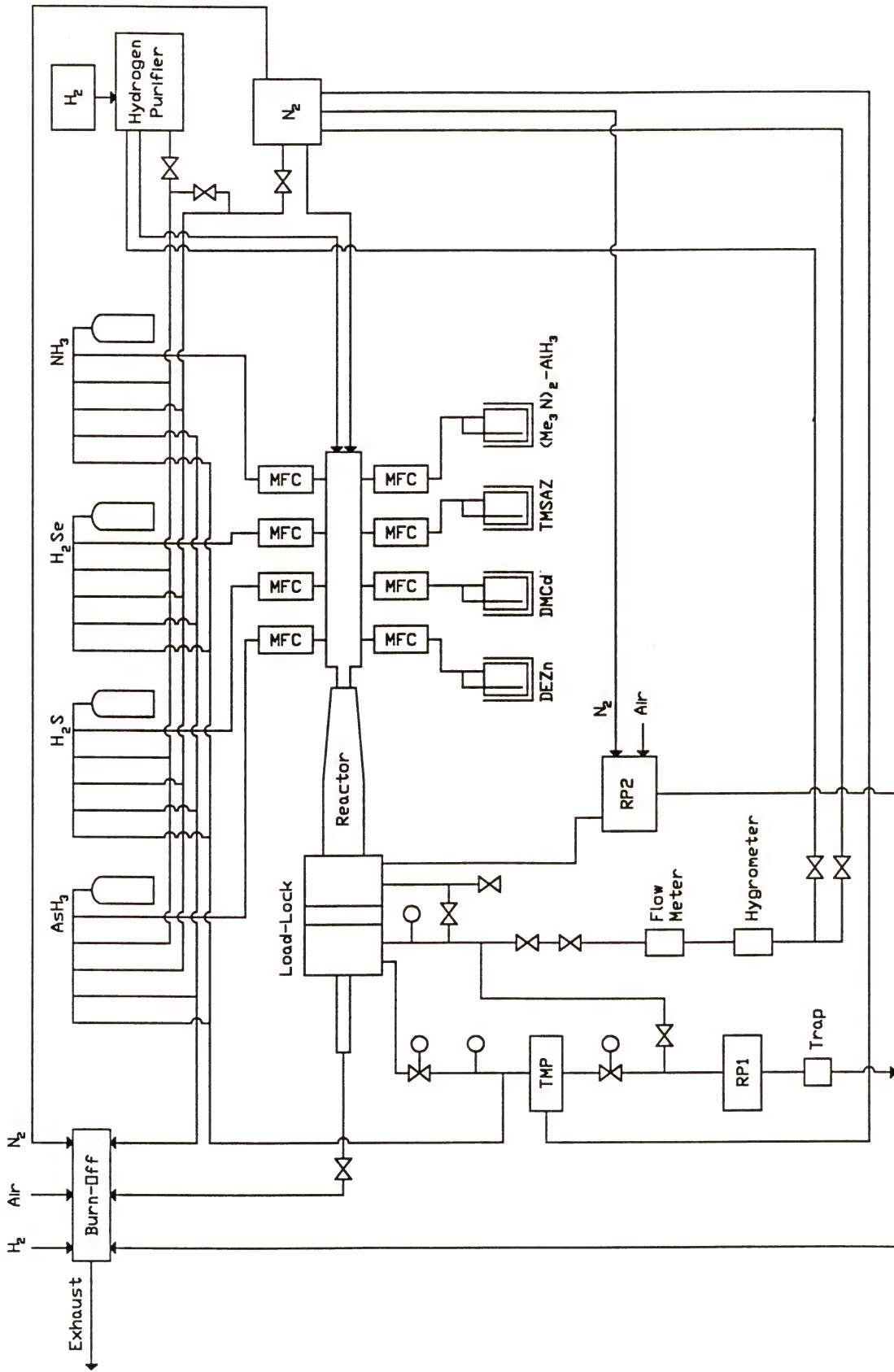


Figure 2-1. Schematic diagram of the MOVPE growth system where MFC=mass flow controller, TMP=turbo molecular pump, and RP1 and RP2=roughing pumps.

which transports the substrate from the load lock chamber through a gate valve and positions it on the susceptor using a three-axis motion fork. Elevated growth temperatures are generated by rf induction heating (20 kW), measured with an rf-shielded K-type thermocouple, and controlled by an Accufiber Incorporated (Model 10) high temperature measurement system.

Pure hydrogen sulfide (H_2S) and hydrogen selenide (H_2Se) are stored in high pressure cylinders, and the outlet pressure (typically 200 psi) is controlled by regulator valves. Diethylzinc (DEZn) and dimethylcadmium (DMCd) are contained in 200 ml stainless steel bubblers and high purity Pd filtered H_2 is used as a carrier gas to transport saturated vapor reactants to the reactor. Bubbler temperature is controlled by a Neslab constant temperature bath and bubbler pressure by a MKS throttling valve-Baratron pressure gauge feedback loop system.

Hazards associated with the MOVPE technique, especially the high toxicity of reactant materials, necessitate safety precautions. The effluent from the growth process is first pyrolyzed into inert by-products through thermal treatment in a burn box prior to further decontamination in the building's scrubber system. The entire building that houses the growth system is constantly monitored for toxic gas leaks by the MDA detector and for leaks in general in the ppm scale with a H_2 detector. If any of these sensors are activated, an audible/visual alarm will notify the occupants to immediately evacuate the building and all pneumatic valves on the growth system will automatically shut-off to minimize further gas leaks. In addition, the entire room is set at negative pressure relative to the outside so that in case of leaks, the gases will be confined to the building.

2.2 Experiment

DEZn and DMCd metalorganic group II sources were purchased from Air Products, both of high purity adduct grade (99.999%). Diethyl-ligand compounds are generally preferred over their dimethyl-ligand counterparts because of reduced carbon contamination in the films. Although DECd was available, its properties were not well characterized and its chemical stability was questionable. H₂Se and H₂S, the hydride gas VI sources, were purchased from Solkatronic with purity of 99.999% and 99.99%, respectively. They were selected for their wide availability and high purity. The substrates were LEC grown semi-insulating (100) GaAs sliced 0°, 2°, or 5° toward the <110> direction with an error of ± 0.5°; and semi-insulating (111)A and (111)B GaAs with an error of ± 0.5°. All the GaAs substrates were purchased from Sumitomo Electric Company for their low etch pit density (5x10⁴/cm²).

Unlike silicon, germanium, and some III-V compounds, high quality bulk II-VI crystals are not readily available and thus, most of the cited epitaxial growth is on III-V semiconductors. Although both high quality GaP and GaAs are available, GaAs wafers were chosen because the composition at lattice-matched conditions corresponds to the correct bandgap energy for blue light emission in ZnCdS.

The typical growth parameter settings are listed in Table 2-1. The metalorganic (MO) and gas inlet hydrogen flow rates can be controlled independently to dilute the respective reactant sources prior to entering the reactor.

Table 2-1. Growth Parameter Settings.

Parameters	Settings
Growth temperature	450 to 550 °C
Growth pressure	70 Torr
Overall DMCd mole fraction	0.6 to 1.14×10^{-4}
Overall DEZn mole fraction	0.7 to 1.69×10^{-4}
Overall H ₂ S mole fraction	80.4 to 141.4×10^{-4}
MO inlet hydrogen flow rate	0.5 to 1.0 slm
Gas inlet hydrogen flow rate	3.0 to 4.0 slm
Zn/Cd inlet molar ratio	0 to 1
VI/II inlet molar ratio	30 to 225

The wafers were sliced up into pieces approximately 2.0 x 2.0 cm squares. Prior to loading the substrate into the reactor, the following wet cleaning procedure was performed:

1. Blow dry with filtered N₂.
2. Rinse in warm trichloroethane for 5 minutes.
3. Rinse in warm acetone for 5 minutes.
4. Rinse in methanol for 1 minute.
5. Rinse in DI H₂O for 1 minute.
6. Etch in [7:20:100::H₂O₂:NH₄OH:DI H₂O] for 5 minutes.
7. Rinse in DI H₂O for 1 minute.
8. Blow dry with filtered N₂.

After the substrate was placed in the reactor, it was annealed in a reducing environment of H₂ at 550 °C for 10 minutes to desorb volatile materials remaining on the substrate. The thermal cleaning treatment was necessary to produce a highly specular finish with good morphology. Without it, the epilayer surface often showed a hazy, milky

appearance. Both concentration and flow stability were achieved prior to deposition by first flowing metalorganics over the substrate for six minutes. Bare GaAs was never exposed to pure H₂S due to potential formation of etch pits where 3-dimensional (3-D) growth can initiate.

The carrier gas was H₂ due to its high purity, extensive availability, and flow stabilizing qualities. Other common alternative carrier gases include N₂, Ar, and He. Reports have shown that H₂ and He tend to produce stable laminar flows while Ar and N₂ are more susceptible to turbulence, convection, and entrance effects [49].

Due to severe problems with parasitic gas phase reactions even, at room temperature, the metalorganics and the hydride gases were introduced into the reactor through two separate inlet lines: (1) metalorganics via a single 1/4 inch inner diameter quartz tube concentrically situated in the center of the entrance reactor face and (2) hydride gases through four radially symmetric equidistant 1/8 inch inner diameter ports located on the entrance metal flange. These preventative measures, however, were not entirely effective. The severity of this phenomenon was estimated by the quantity of deposits on the reactor walls and the quartz tube upstream of the deposition zone. The deposits were extremely thick and eventually a cone developed at the tip of the MO inlet tube. Particles can then dislodge and settle on the growth surface to act as nucleation sites and produce polycrystalline growth.

The lattice constant perpendicular to the growth surface was calculated from HRXRD measurements based on the (004) reflection of GaAs and the measure of crystalline quality was based on the FWHM of these rocking curves. The HRXRD system

was a four germanium crystal system using a Cu K α_1 radiation source. The solid phase composition was determined by electron probe micro-analysis (EPMA) and film thickness by cross sectional views of cleaved samples using scanning electron microscopy (SEM). The surface morphology was characterized by Nomarski interference contrast microscopy. Extended defects analysis were identified by cross sectional transmission electron microscopy (TEM) and corresponding low energy electron diffraction (LEED) patterns. Photoluminescence (PL) measurements were performed using a He-Cd laser ($\lambda = 3250 \text{ \AA}$) as the radiation source. The laser power was 2 mW with a beam spot size less than or equal to 1 mm and operated with a slit width of 300 μm . A filter was used to reduce background noise. The scan ranged from 25,850 to 13,700 cm^{-1} and counted every 10 cm^{-1} .

2.3 Film Quality Optimization Study

2.3.1 Taguchi Method / Design of Experiments

In optimizing the growth process to produce the best quality ZnCdS films grown on GaAs, a design of experiments (DOE) approach was taken. Although traditionally, the method of changing one parameter while keeping others constant is the standard methodology, a more efficient and enlightening method is the one employing the Taguchi method or more generally known as DOE. Although academia has been slow to incorporate this method, industry has broadly adopted the technique [50].

The DOE is more efficient than the traditional technique. The same information can be extracted from the DOE with fewer experiments than with the traditional technique. As an example, to gain the same precision for the effects of three main parameters, the one-factor-at-a-time method would need to use a total of twenty-four runs. For each parameter, eight runs are required: four at each level with all the observations conducted at some arbitrarily fixed levels of the other two factors. In comparison to the 2^3 factorial design, the traditional methodology requires a threefold increase of experimental runs to gain the same level of precision. In general, for z variables, a z -fold increase would be required.

Only the DOE method can provide information about possible convolution effects due to multi-parameter interactions. The traditional technique does not account for interaction effects and only provides an estimate of the effect of a single parameter at selected fixed environments. This requires the strict assumption that the effect would be the same at other settings of the other variables. In other words, the variables would act on the response additively which is not necessarily true. If the variables do act additively, the DOE method is more precise and, if the variables do not act additively, the DOE method can detect and estimate the interactions that measure the nonadditivity.

Six independent input process parameters with two initial conditions determine the growth environment of ZnCdS. Table 2-2 lists the input growth parameters and their potential effect on the measurable outputs of the growth process. The required quality of the epilayer is dependent on the particular device application, but the crystallinity, growth

rate, solid phase composition, and film thickness uniformity are four measurable output variables of importance to most devices.

Table 2-2. Growth Parameters for ZnCdS.

Parameters	Growth Characteristics Affected
(1) Growth temperature	a, b, c, d
(2) VI/II inlet molar ratio	a, c
(3) Substrate orientation	a
(4) Growth pressure	a, b, d
(5) Cd/II inlet molar ratio	c
(6) Ratio of flow rate in inlet gas to MO lines	b, d
(7) Anneal prior to growth	a
(8) Flow II or VI prior to growth	a

NOTE: a = crystallinity, b = growth rate, c = solid phase composition, and d = thickness uniformity

The growth temperature is expected to have a tremendous effect on the film quality. With a high growth temperature, better crystalline materials should be produced since the chemisorbed reactant atoms have more energy to migrate along the surface to find the correct lattice site. The production of misfit dislocations due to thermal expansion differences between the substrate and film, however, should increase with increasing temperature. A nonuniform film thickness can be produced by recirculation and turbulence in the gas flow patterns due to increased buoyancy driven flows at higher temperature. Furthermore, achieving a uniform temperature is more difficult at higher temperatures and can result in increased film thickness variation. Temperature also affects the growth rate; exponentially in the kinetically limited regime and through a power law relationship (T^n) in the mass transfer limited regime. The solid phase composition can also

be affected by the deposition temperature through its influence on processes such as reactant diffusion, desorption rates, and solid-gas phase equilibrium.

The VI/II inlet molar ratio is an often cited process variable in the MOVPE literature and represents the gas phase stoichiometry. In terms of the four selected output parameters, this variable can affect the crystallinity through its influence on the stoichiometry of the film. Compared to III-V compounds, both CdS and ZnS have wide homogeneity ranges. The dominant point defects in these compounds are believed to be anti-structure. These defects are stable equilibrium species, but high concentrations can lead to the formation of non-equilibrium extended defects (e.g., condensation of vacancies to form dislocations). If the stoichiometry of the gas phase becomes too extreme, two phase depositions may also occur (e.g., liquid Zn and ZnS). The VI/II ratio in most MOVPE experiments is greater than unity and, thus, its effects on the growth rate is expected to be negligible in the mass transfer limited regime. If the VI/II ratio is changed by varying the VI inlet flow rate at fixed II flow rates, then this parameter can affect the growth rate if H₂S or one of its byproducts participate in the limiting reaction when operating in the kinetically limited regime (e.g., desorption of sulfur at elevated temperatures). The VI/II inlet molar ratio can also influence the solid phase composition through its preferential participation in parasitic reactions with Cd and Zn precursors, and through its influence on equilibrium at the surface in the mass transfer limited regime. Its influence can possibly be large in the kinetically limited regime through its influence on limiting reaction rates. Finally, the influence on thickness uniformity is expected to be small, other than decreasing H₂S reactant depletion effects as the VI/II ratio increases.

The substrate orientation is also extremely important since the surface acts as the template for growth and quality of the first monolayer and, ultimately, the entire thin film itself. Since ZnCdS is more ionic than the more covalent bond type semiconductor GaAs, a large charge build up occurs at intimate contact. In order to alleviate the charge imbalance, the II cationic reactants Zn and Cd will have a tendency to bond with As and the VI atom S will bond with Ga.

The reactor pressure is set reasonably low to minimize deleterious gas phase reactions and to control the partial pressures of the reactants for growth rate modulation. The Cd/II inlet molar ratio is the main controlling factor for composition. The ratio of the flow rates in the main gas and the main MO lines affects the thickness uniformity of the epilayer while increased flow rate in the main MO line also increases the growth rate due to enhanced diffusion of reactants based on boundary layer theory. Parameters (7) and (8) in Table 2-2 condition the surface of the substrate to enhance high crystallinity of the grown epilayer. Annealing the substrate volatilizes any impurities left over from the wet cleaning procedure and vaporizes any native gallium and arsenic oxides that cause a rough appearance on the epilayer. Metalorganic II materials are first exposed to the substrate rather than VI hydride gases because H_2S is suspected of etching pits into the GaAs surface and increasing the dislocation density.

The relationship between the input process parameters and the resulting film characteristics is complex. It is not possible to fully simulate MOVPE processes, primarily because of unknown kinetic mechanisms and rate constants, complex 3-dimensional flows, uncertainty in boundary conditions, and the lack of appropriate theories to link

macroscopic phenomena (e.g., flow dynamics) to microscopic phenomena (e.g., stacking fault formation). As a result, researchers have relied on parametric studies (e.g., DOE) to characterize a growth system/chemistry.

Based on the discussion presented above, three of the process variables (temperature, VI/II ratio, and substrate orientation) were expected to have a dominant effect on the film quality. As a first attempt to characterize this growth chemistry, a two-level, three variable experiment design was performed, requiring eight growth runs. Table 2-3 shows the low and high values for the parameters to be investigated in the two-level, three variable factorial design.

Table 2-3. Parameter Values for Two-Level Factorial Design.

Parameter	Low	High
A = growth temperature	300 °C	550 °C
B = VI/II ratio	30	120
C = substrate orientation	(100) 2° toward <110>	(111)B

Figure 2-2 shows the elemental Cd yield as a function of temperature for DMCd. These data were taken by Cockayne and Wright as described in [51] by injecting DMCd/H₂ into a heated tube at constant temperature and measuring the decomposition byproducts through mass spectrometry. The temperature range that spans from minimum to maximum Cd yield is 300 to 420 °C. DMCd begins to pyrolyze in a H₂ atmosphere at 230 °C with complete decomposition at approximately 375 °C [52]. It is noted that such measurements do not fully represent what occurs in a MOVPE system, but the trends should translate well. Therefore, to ensure significant pyrolyzation, the lower temperature limit is set to 300 °C. The thermodynamic limit of ZnCdS growth is determined to be

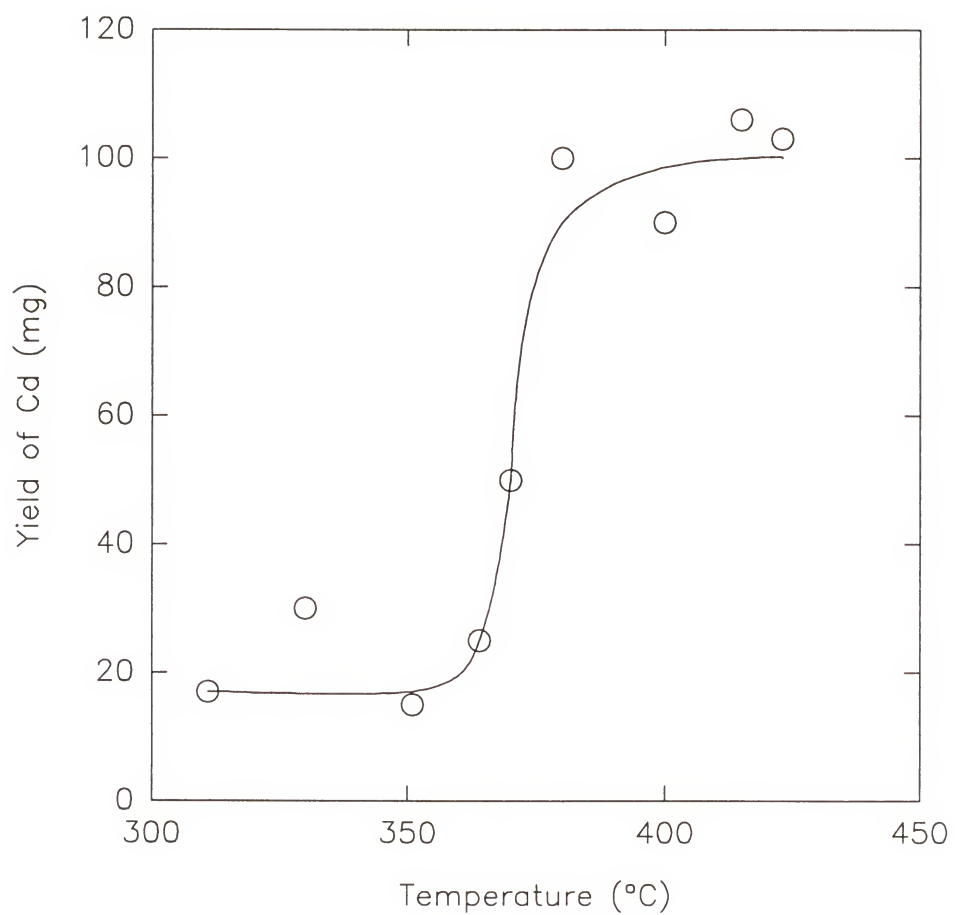


Figure 2-2. Pyrolysis of dimethylcadmium in H_2 [51].

between 550 and 600 °C; thus, the upper limit is set at 550 °C where growth is assured to occur. At a growth temperature of 600 °C, measurable growth does not occur even with higher concentration of reactants. These results are also consistent with other II-VI materials; the growth rate of CdS begins to drop between 400 and 450 °C and above 550 °C, no appreciable growth occurs [36]. Although direct temperature dependent data does not exist on the pyrolysis of DEZn, the average activation energy for pyrolysis is 33 and 35 kcal/mole for DMCd and DEZn, respectively [51]. With such similar activation energies, the yield of elemental Zn as a function of pyrolytic temperature of DEZn is presumed to be on the same order of magnitude to that for DMCd assuming the pre-exponential factors are similar.

The high and low values for the VI/II molar inlet ratio are chosen by spanning a sufficient range to cause a noticeable effect on the crystallinity of the epilayer, but still within the reasonable value of 50. The high and low values of substrate orientation are just two different families of index planes: (100) and (111)B. The specifically chosen index cuts from each family are based on best results from preliminary experiments.

In addition to the three variable settings specific to the DOE, the other growth parameter settings are selected for enhanced crystalline quality. A pressure of 70 Torr is the minimum value that can be used without striking an undesirable plasma in the reactor chamber. The plasma etches the GaAs substrate, leaving pits and surface defects that act as nucleation sites for unwanted polycrystalline ZnCdS growth. The inlet Cd/II was set at 0.52 and 0.45 for growth temperatures of 550 and 300 °C, respectively to achieve similar solid phase compositions. The ratio of hydrogen flow rates between the gas and MO inlet

lines was held constant at 4.0. The substrate was annealed and II materials flowed prior to growth.

2.3.2 Factorial Design of Experiments Results

Table 2-4 below outlines the three factorial full design which consists of eight experiments involving (A) growth temperature, (B) VI/II ratio, and (C) substrate orientation. The negative (-) and positive (+) signs indicate low and high values, respectively. The distribution of the high and low value designations for the two and three-factor convolution columns are calculated by multiplying the respective columns of the constituents. As an example, the first run (+) designation for AB is calculated by multiplying the first run designations of A and B: $(-) \times (-) = (+)$. The second row (-) designation of AB proceeds the same way: $(+) \times (-) = (-)$.

Table 2-4. Outline of three factorial design of experiment.

Run	A	B	C	AB	AC	BC	ABC	FWHM (arc-secs)
1	-	-	-	+	+	+	-	3807.0
2	+	-	-	-	-	+	+	2060.3
3	-	+	-	-	+	-	+	5389.0
4	+	+	-	+	-	-	-	545.5
5	-	-	+	+	-	-	+	3766.7
6	+	-	+	-	+	-	-	720.0
7	-	+	+	-	-	+	-	2524.0
8	+	+	+	+	+	+	+	753.3

The eight experiments designated in Table 2-4 were performed, and the sample crystallinity as determined by the FWHM of the (400) reflection peak taken from HRXRD

spectra, was measured. The effects of the three parameters and their convolutions on the FWHM from X-ray diffraction peaks are listed in Table 2-5.

The average effects from Table 2-5 are calculated by multiplying the FWHM values in the last column of Table 2-4 by the respective high and low designation of the desired interaction and then summing the eight products. Since no replicates are made, an estimate of the standard error can be made with some assumptions. The three factor (ABC) interaction is considered negligible and can be considered a measure of experimental error. Its high value is primarily due to the measurement of the rocking curves for the thin films grown on (100) GaAs. Since the films are of fairly poor quality, the measurement of the FWHM gets difficult and inaccurate. However, the opposite is true for the films grown on (111) substrates. The ABC convolution effect of 843.2 arc-seconds implies that only growth temperature (A) and substrate orientation (C) are statistically significant since the remaining effects have calculated values smaller than the estimated error. The results also suggest that the effects of two parameter interactions on the crystallinity is negligible.

Table 2-5. Effects of parameters and their convolutions.

Interaction	Average Effects
mean	2570.7
A	-2601.9
B	-35.5
C	-1259.5
AB	-205.2
AC	193.2
BC	-569.2
ABC	843.2

The data are interpreted as the effect on the FWHM when changing parameters from low to high values. For instance, by changing the substrate orientation from (100) 2° toward <110> to (111)B, the FWHM will decrease by 1259.5 arc-seconds. The statistics from the DOE indicate that changing the substrate orientation improves the crystallinity, and that more than double the improvement is obtained when increasing the growth temperature from 300 to 550 °C, decreasing the FWHM by 2601.9 arc-secs. As expected, the significance of the substrate orientation and growth temperature suggests that a heterogeneous process is central to the crystalline quality.

Although low growth temperature is desirable for minimizing point defects, crystal perfection might be expected to improve at high temperature since adsorbed reactants have greater surface mobility to locate the correct lattice sites. Furthermore, adsorbed species at high energy sites can more readily desorb at higher temperatures. The advantages of high growth temperature is witnessed by its effect on the FWHM of the epilayer grown on the five following substrate orientations: (111)B, (111)A, (100) 5° toward <110>, (100) 2° toward <110>, and (100) 0° toward the <110>. Each of the epilayers is the same composition and is grown with the same growth conditions except for the growth temperature and Zn/Cd gas phase composition which is controlled by varying the Zn inlet gas phase concentration. The column II materials' gas phase composition is adjusted for each of the various growth temperatures to reflect a solid composition corresponding to lattice matched conditions with the GaAs substrate ($x = 0.58$ atomic fraction of Cd). The VI/II ratio is also set to 60. Figure 2-3 shows a clear downward trend of the FWHM by increasing growth temperature from 250 to 550 °C.

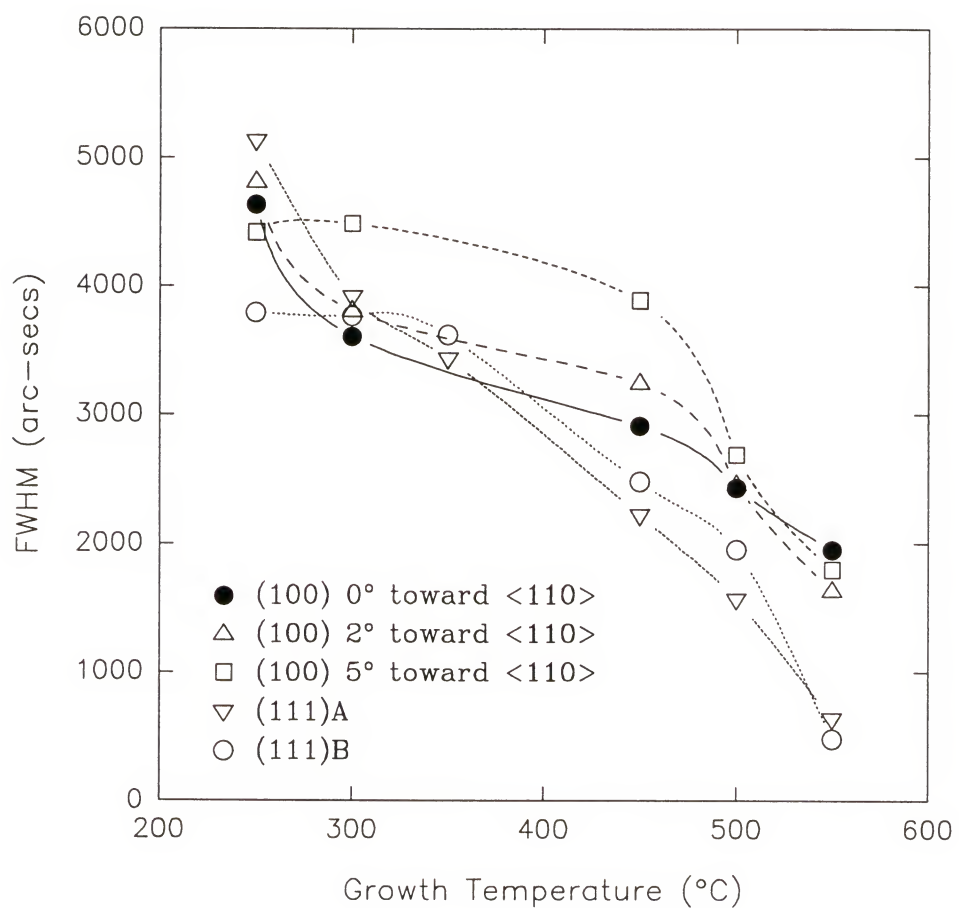


Figure 2-3. Correlation between FWHM and growth temperature for various GaAs substrate orientations.

This indicates that 550 °C is the optimum growth temperature for the highest degree of ZnCdS epilayer crystallinity. Furthermore, in the temperature range from 350 to 550 °C, the FWHM of the (111) family of planes is the same or less than that of the (100) family of planes. Both results are consistent with conclusions drawn from the DOE.

Although crystalline quality improves for all orientations, the change is substantial for the (111) family of planes compared to the (100) set. Energy minimization and charge dynamic arguments are used to explain this result.

The energy required to cut the crystal at some plane can be expected to be proportional to the number of bonds cut. The bond density across the (111) surface planes is $\sqrt{3} / 4d^2$ where d is the nearest planar distance. This is smaller than the density of any other planes including the (100) surface with a density of $3/(4d^2)$ and the (110) surface with a density of $3\sqrt{2} / 8d^2$. It is expected that the surface with the lowest energy and therefore the natural growth surface to be the (111) surface.

With a homogeneous surface of either all Ga or all As, the probability for crystalline growth on (111) planes is enhanced since the charge on the growth surface will naturally select for the correct and opposite charged adsorbed atoms for the lattice sites: type II atoms (Zn and Cd) if (111)B and type VI atoms (S and Se) if (111)A. Growth on (111) planes acts inherently like atomic layer epitaxy (ALE) because of the attraction and repulsion of cations and anions for a particularly charged growth surface. Once islands of oppositely charged reactant atoms form, a higher probability exists for nucleation to initiate at the step-kink formed by the substrate and islands rather than on top of the

islands themselves. This tendency promotes 2-dimensional (2-D) growth and produces highly crystalline ZnCdS epilayers.

The 2-D and 3-D growth types describe the nucleation and growth mechanisms of thin MOVPE films. Prior to nucleation, reactant atoms diffuse from the bulk gas phase across the boundary layer and adsorb on the surface where surface migration then occurs. Small islands of stable nuclei clusters coagulate on preferential sites on the substrate. The most likely nucleation sites are those positions of lowest free energy such as kinks and steps where eventually crystallites form. Growth continues with addition of atoms from adsorption and surface diffusion until the high surface density of crystallites begin to merge and coalesce into a thin film. After the initial monolayer is formed, each successive layer is grown on top of the previous layer. This type of growth mechanism is labeled 2-D growth [53]. With minimal surface imperfections and supersaturation of reactants in the gas phase, epitaxial films are highly probable. If the film grows both laterally and vertically without complete coalescence of the layers, this mechanism is described as 3-D growth.

Surprisingly, the insignificance of the VI/II inlet molar ratio indicates that the gas phase stoichiometry is unimportant to crystallinity. This is shown to be misleading. Growth layers of high perfection with smooth surfaces develop only with sufficiently high substrate temperature and specific supersaturation. Figure 2-4 plots the relationship between the FWHM and the VI/II ratio. As in previous experiments, all the epilayers are of same lattice matched composition with the same growth conditions except for the VI/II ratio. The growth temperature is 550 °C since this growth temperature produces the

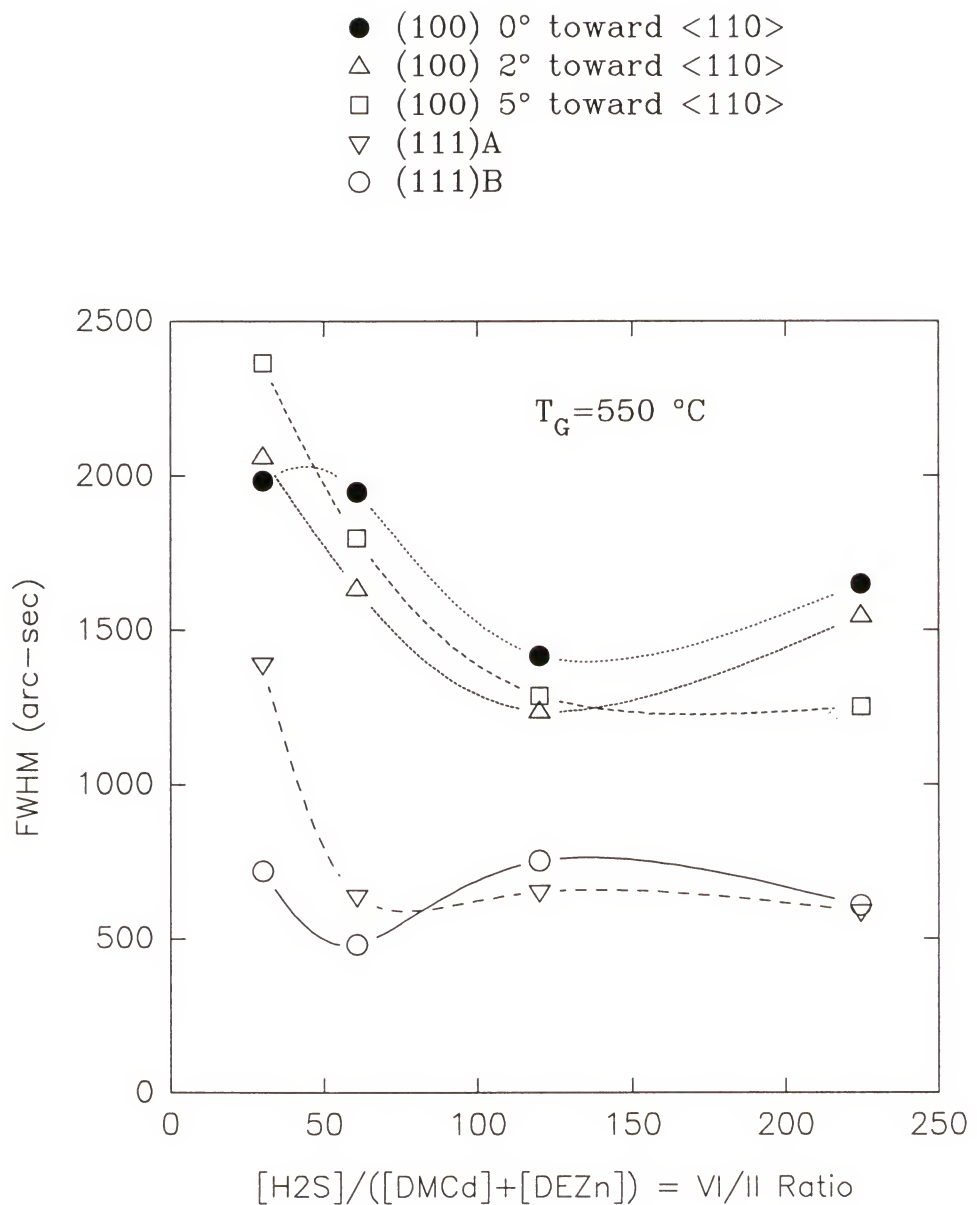


Figure 2-4. Correlation between FWHM and VI/II ratio.

highest film quality. The results show that for (111) and (100) substrates, VI/II values of 60 and 120, respectively, are needed to achieve high quality ZnCdS. This implies stoichiometric growth initiates at those critical VI/II ratios. Epilayers grown with VI/II values lower than the critical values, will be nonstoichiometric with higher point defect densities that may ultimately provide nucleation sites for even larger dislocation densities which contributes to the high FWHM. At VI/II values greater than the critical ones, the excess VI sources desorb from the surface to continue stoichiometric growth. For both families of substrate orientations, the FWHM clearly increases at VI/II values lower than the optimum, but the results are unclear for those values greater than the optimum. The FWHM rises a little and then plateaus. The difference in the optimum VI/II values can be explained by the difference in binding energy of the two sets of growth surfaces.

The lower binding energy of the (111) plane compared to the (100) plane allows a higher probability for the sulfur atoms to stick once adsorbed, thereby requiring an overall less number for stoichiometric growth. Again, the results show a distinct separation into two groups by their respective substrate orientations. The (100) substrates show consistently poorer crystal quality than the (111) substrates confirming the importance of a heterogeneous process on determining the crystallinity of the epilayer. Typical HRXRD peaks for ZnCdS growth on (100) and (111) orientation GaAs substrates are shown in Figures 2-5 and 2-6, respectively.

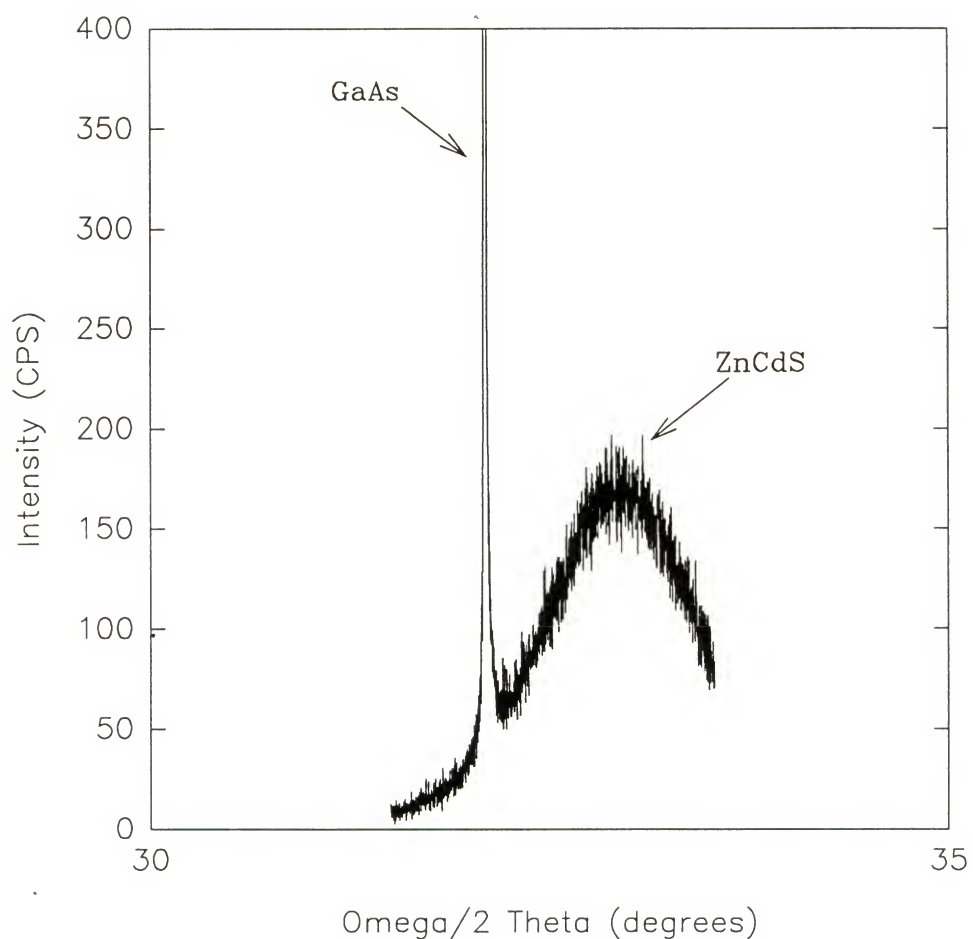


Figure 2-5. HRXRD rocking curves of ZnCdS grown on (100) 2° GaAs substrates.

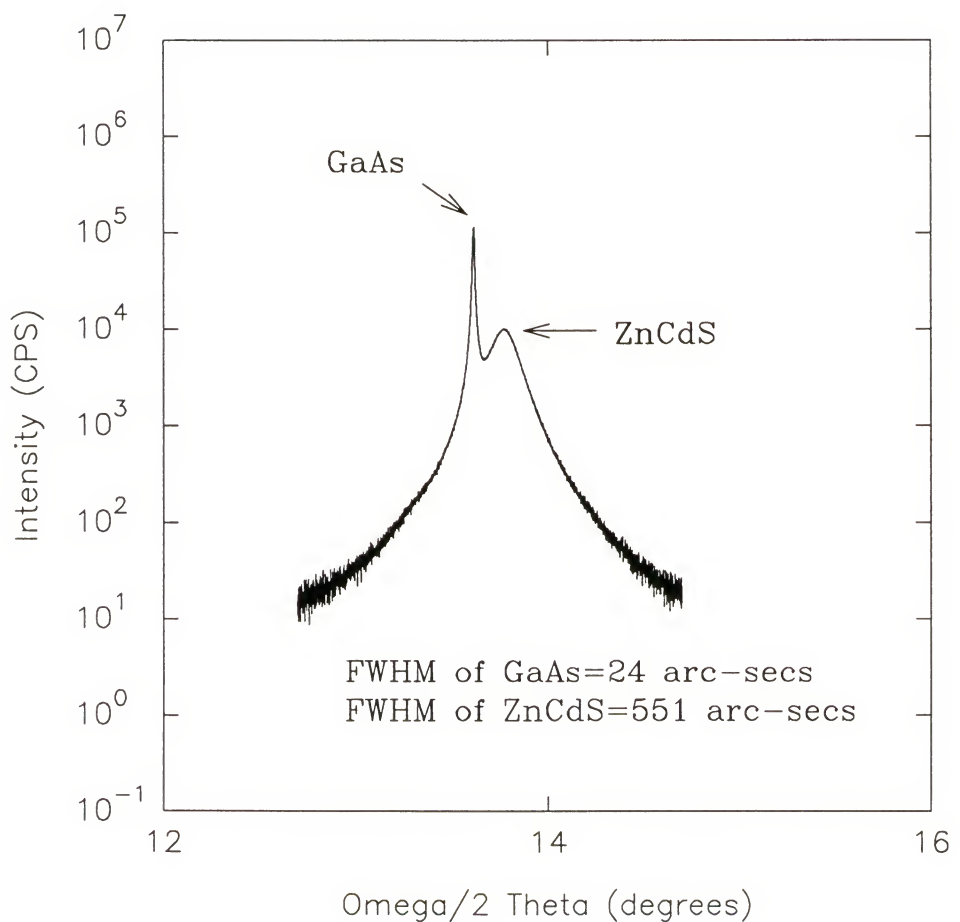


Figure 2-6. HRXRD rocking curves of ZnCdS grown on (111)A GaAs substrates.

2.3.3 Influence of Other Process Parameters

Although the design of experiments provides valuable data, more detailed investigations have been made to further improve the crystallinity of ZnCdS by understanding its relationship with selected process parameters: buffer layers, growth rate, and etchants.

2.3.3.1 Buffer layer

One way to improve the crystallinity of ZnCdS is to grow a buffer layer prior to the growth of ZnCdS. This is shown to be effective for many binary and pseudobinary III-V systems [54-55]. The use of a buffer layer was originally intended as a intermediary layer for composition grading to minimize interfacial dislocations between materials with significantly different lattice constants. Later it was discovered that a buffer layer also enhanced crystallinity by simply providing a clean surface for growth. Ideally, a buffer layer of GaAs should be grown, but without the capability of GaAs growth in the II-VI growth system, other alternative buffer layers are investigated.

A buffer layer of ZnSe is grown prior to the growth of ZnCdS and the HRXRD results are shown in Figure 2-7. The main reason for choosing ZnSe was its ability to grow a highly crystalline film on GaAs and it was thought to be relatively compatible with ZnCdS. The growth temperature of ZnCdS is held constant at 550 °C while the ZnSe buffer layer is grown at 350 and 550 °C. The ZnCdS epilayers are grown at lattice matched compositions with a VI/II ratio of 120. The optimum VI/II value is chosen for the (100) substrates since that value would also provide near optimum quality epilayers for

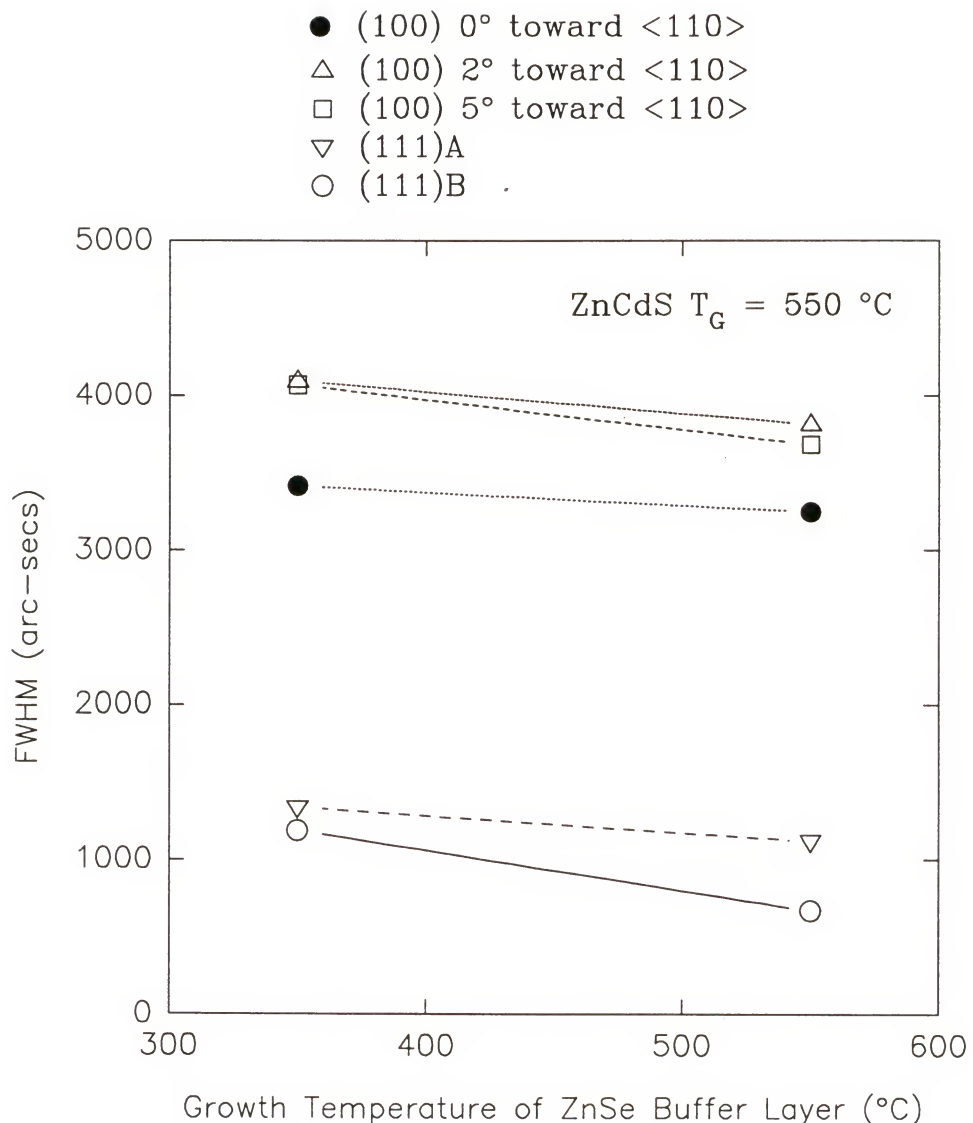


Figure 2-7. Effect of ZnSe buffer layer on ZnCdS crystallinity.

the (111) set. The ZnSe is grown with a VI/II ratio of 120 with a Zn mole fraction of 8.0×10^{-4} . The buffer layer is grown to about 0.1 to 0.15 μm .

The results are again clearly dominated by the substrate orientation. For the (111) substrates, the addition of a buffer layer does not produce a significant improvement. For the (100) substrates, the buffer layer degrades the crystallinity tremendously. With a ZnSe buffer layer grown at 350 °C, the FWHM of the epilayer increases by 523 and 2573 arc-seconds for (111) and (100) substrates, respectively. Although the ZnSe buffer layer grown at 550 °C shows slightly better quality ZnCdS epilayers, the difference is not substantial. It is concluded that ZnSe acting as a buffer layer does not significantly improve the crystallinity of ZnCdS.

Another postulated benefit of a buffer layer is that it provides an extremely clean surface for growth and annealing the buffer layer at a high temperature should accentuate the cleanliness. To test this hypothesis, a ZnSe buffer layer is grown at a low temperature and then subsequently ramped to a higher temperatures while still maintaining a Se overpressure (VI/II ratio = 250) to eliminate sublimation of the grown material and thus minimize formation of surface defects. The buffer layer initially grown at 550 °C, is ramped to 650 °C and held for ten minutes before the temperature is lowered to 550 °C for ZnCdS growth. The result of this procedure is worse than simply growing the buffer layer at the cited two temperatures (FWHM > 6000 arc-seconds). In general, the quality of a film can be no better than that of the substrate; in the study a GaAs wafer (high quality) or the ZnSe buffer layer (poor quality). Figure 2-8 plots the FWHM of the

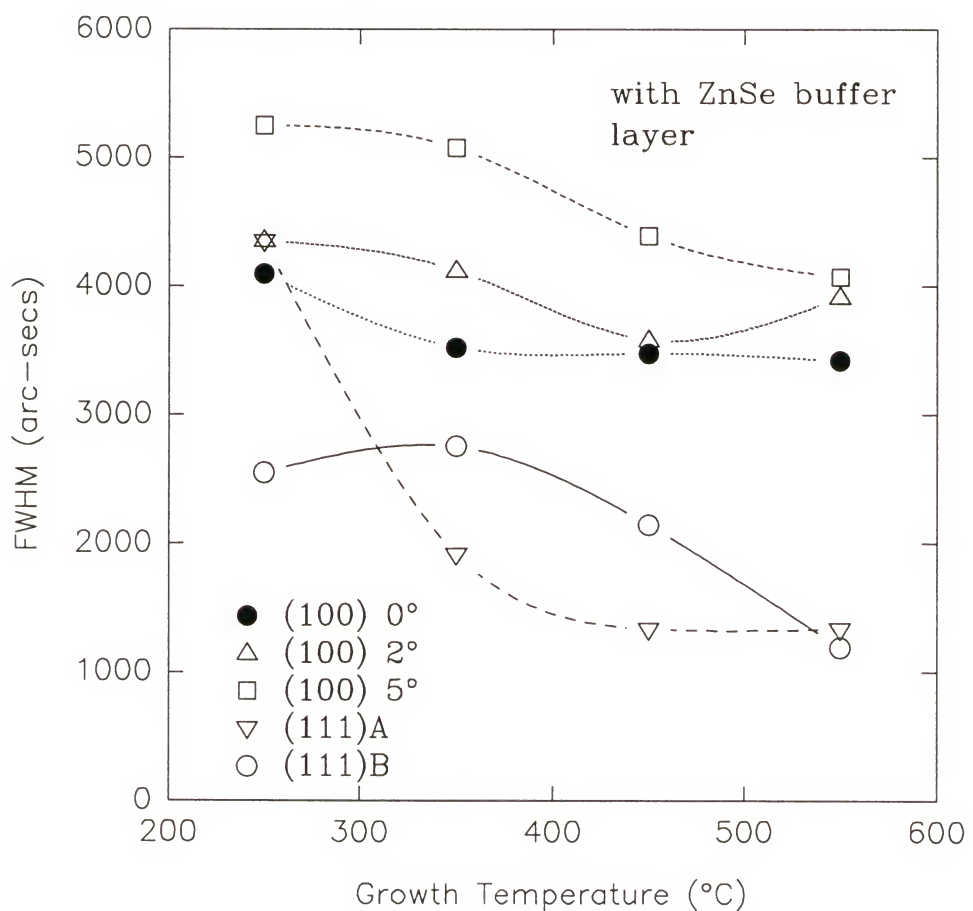


Figure 2-8. Correlation of ZnCdS growth temperature with ZnSe buffer layer and crystallinity.

epilayer as a function of the ZnCdS growth temperature grown with a ZnSe buffer layer. No advantage is gained with the buffer layer at any of the growth temperatures.

2.3.3.2 Growth rate

Besides buffer layers, slow growth rate can also improve crystallinity by allowing the adsorbed reactants a longer residence time to locate the correct lattice sites. With too fast a growth rate, the probability is higher to induce polycrystalline growth.

Slower growth rate decreases the FWHM of the epilayer, but the effect is more pronounced for (100) oriented substrates as compared to the (111) substrates as shown in Figure 2-9. For the (100) substrates, a drop of 0.5 $\mu\text{m}/\text{hr}$ in growth rate, from 1.6 to 1.1 $\mu\text{m}/\text{hr}$, can decrease the FWHM as much as a factor of two from 4104 to 2241 arc-seconds, while for (111) substrates the effect is minor. Extrapolation of the plots suggests that a growth rate of 0.7 $\mu\text{m}/\text{hr}$ would produce near crystalline perfect ZnCdS epilayers when grown on (100) substrates and for (111) substrates, the optimum growth rate is 0.8 $\mu\text{m}/\text{hr}$.

2.3.3.3 Etchant

Another important factor for improved crystallinity is the need to grow on a clean and smooth surface. The substrate cleaning and etching procedure can play a significant role in this matter. The ideal etchant should uniformly etch the substrate leaving the surface concentration unchanged. Figure 2-10 shows the results of measured FWHMs of films grown on GaAs using three different etchants in the normal cleaning process prior to growth. These three etchants are (1) 1% Br_2 in methanol, (2) [5:1:1:: H_2SO_4 : H_2O_2 : H_2O], and (3) [20:7:100:: NH_4OH : H_2O_2 : H_2O].

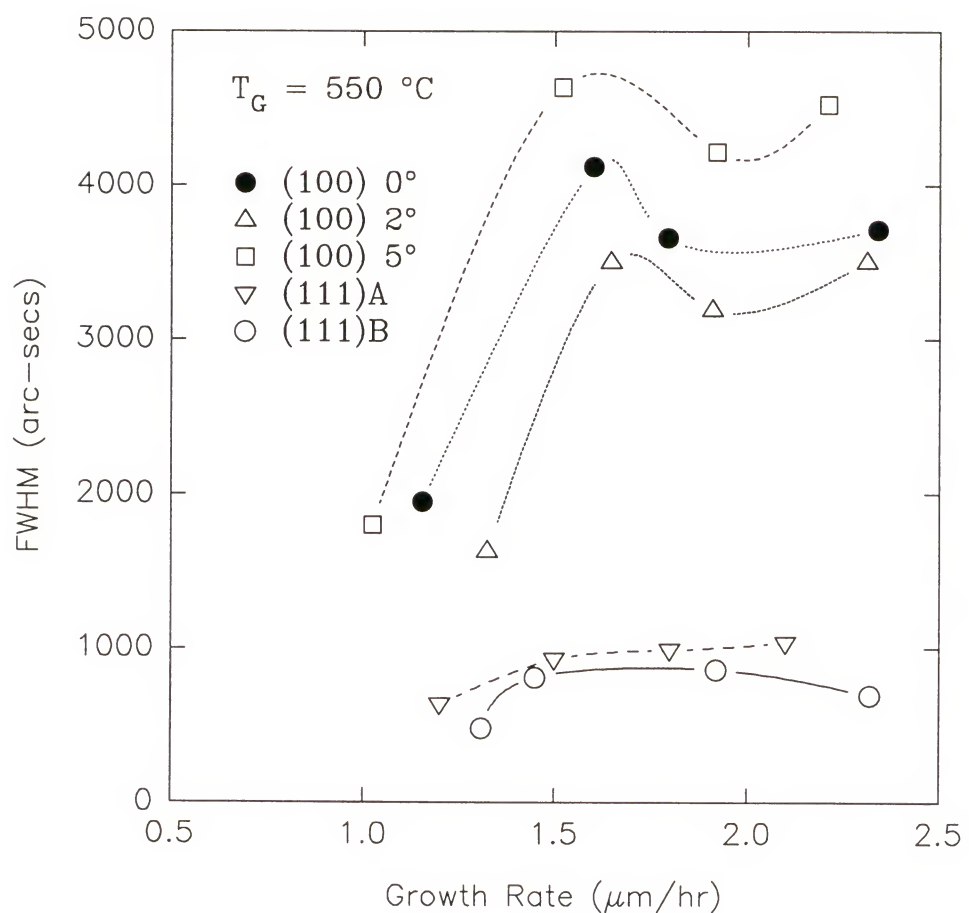


Figure 2-9. Correlation between FWHM and growth rate for five orientations all grown with thickness of 1.0 μm .

- 1) 1% Br_2 in MeOH for 20 seconds.
- 2) [5:1:1:: H_2SO_4 : H_2O_2 : H_2O] for 2 minutes.
- 3) [20:7:100:: NH_4OH : H_2O_2 : H_2O] for 5 minutes.

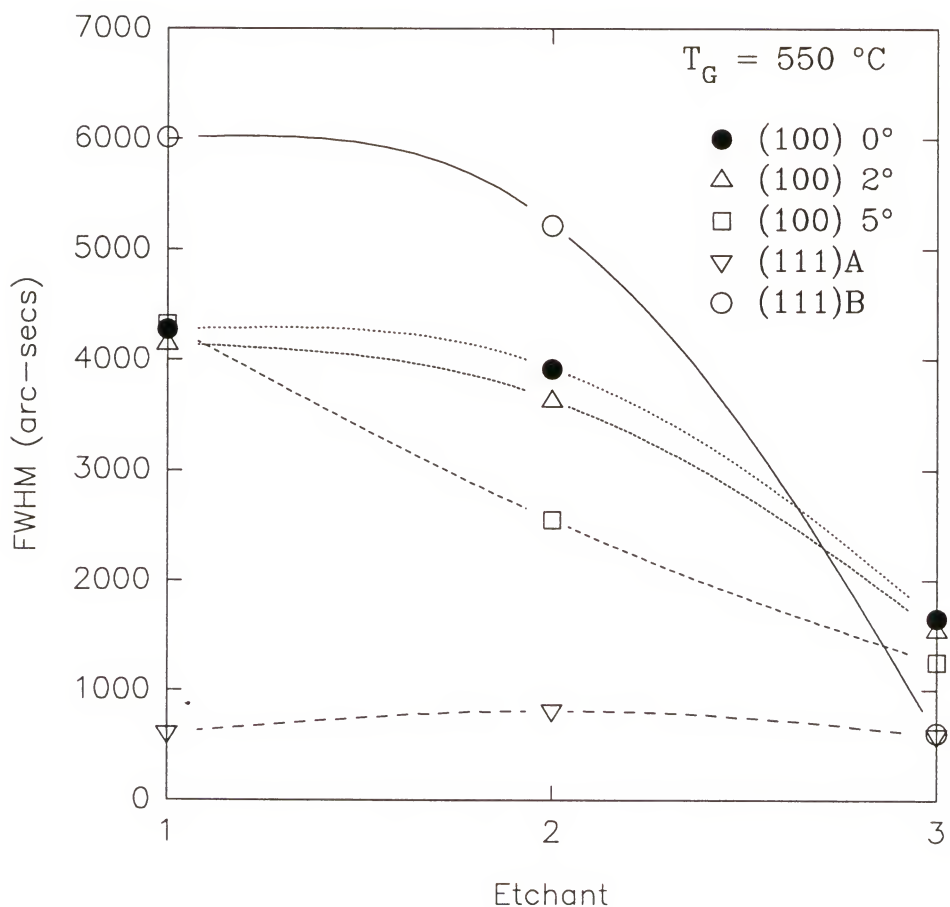


Figure 2-10. Correlation between FWHM and etchants used to prepare the GaAs substrates for growth of ZnCdS films.

The growth temperature is maintained at 550 °C with the reactor pressure at 70 torr. The Cd/II ratio is set at 0.52 and a VI/II ratio of 120 for optimum crystallinity. The results show that etchant (3) produces the smallest FWHM in the epilayer and this is true independent of the substrate orientation. Unlike the effects of growth rate on crystallinity, the results are not clearly differentiated by substrate orientation. The effect of all three etchants on the FWHM is similar for the (100) oriented substrates. The crystal quality is highest with use of etchant (3) and then decreases gradually with use of etchants (2) and (1). For the (111) oriented substrates, the plane ending in Ga is not affected as much as the plane ending in As. For the (111)B surface, etchants (1) and (2) dramatically increase the FWHM and is the most affected of all the orientations. In general, the order of least to worst affected is the following: (111)A < all (100) < (111)B. This is explained by differences in reactivity to the etchants.

Etching is generally an electrochemical reaction with anodic and cathodic reactions. Non-uniform dissolution can occur if the surfaces behave predominantly as anodes or cathodes. The (111)A Ga terminated face is the least reactive and the slowest etching plane while the (111)B As terminated face is the fastest etching plane [56]. The triply-bonded B (As) atoms have an electron configuration that results in one unshared pair of electrons since it has a total of five valence electrons to share in bonding. The triply-bonded A (Ga) atoms have no unshared electrons and thus the B atoms have a greater tendency to donate electrons (react with oxidizing agents) than the A atoms. With greater reactivity, there is greater chance for nonuniform etching and creating pits which can act as nucleation sites for 3-D growth of the epilayer. The greater reactivity can also enhance

the etch rate along dislocation lines existing in the substrate, providing even more nucleation sites for 3-D epilayer growth.

This is consistent with experimental results. The (111)A substrates show the best crystalline quality and the (111)B show the worst quality for both etchants (1) and (2). The (100) substrates with a mixture of both As and Ga ending plane, show crystalline quality in between. This suggests that etchants (1) and (2) either etch too fast and/or non-uniformly which are both highly undesirable. However, etchant (3) produces the highest quality epilayers and will be subsequently used as part of the cleaning procedure. The etchants can be ordered from best to worst: (3) > (2) > (1).

For direct comparison, SEM micrographs in Figure 2-11 show epilayers grown on (100) substrates cut 2° toward the nearest <110> orientation for each of the three different etchants. All surfaces exhibit a high degree of surface roughness, although the epilayer grown with the third etchant showed the smoothest surface morphology. On average, the pore size are 0.2, 0.3, and 0.5 μm diameter for etchants (3), (1) and (2), respectively. The micrographs show that the FWHM or crystallinity is not directly correlated to the surface roughness of the epilayer film. Although in general, a smooth epilayer surface (smaller pore size) corresponds to smaller FWHM.

2.4 Growth Characteristics

2.4.1 Flow Mechanics

The growth of good quality epilayers is highly dependent on the fluid mechanics of the system as well as the growth conditions. One important feature is the degree of

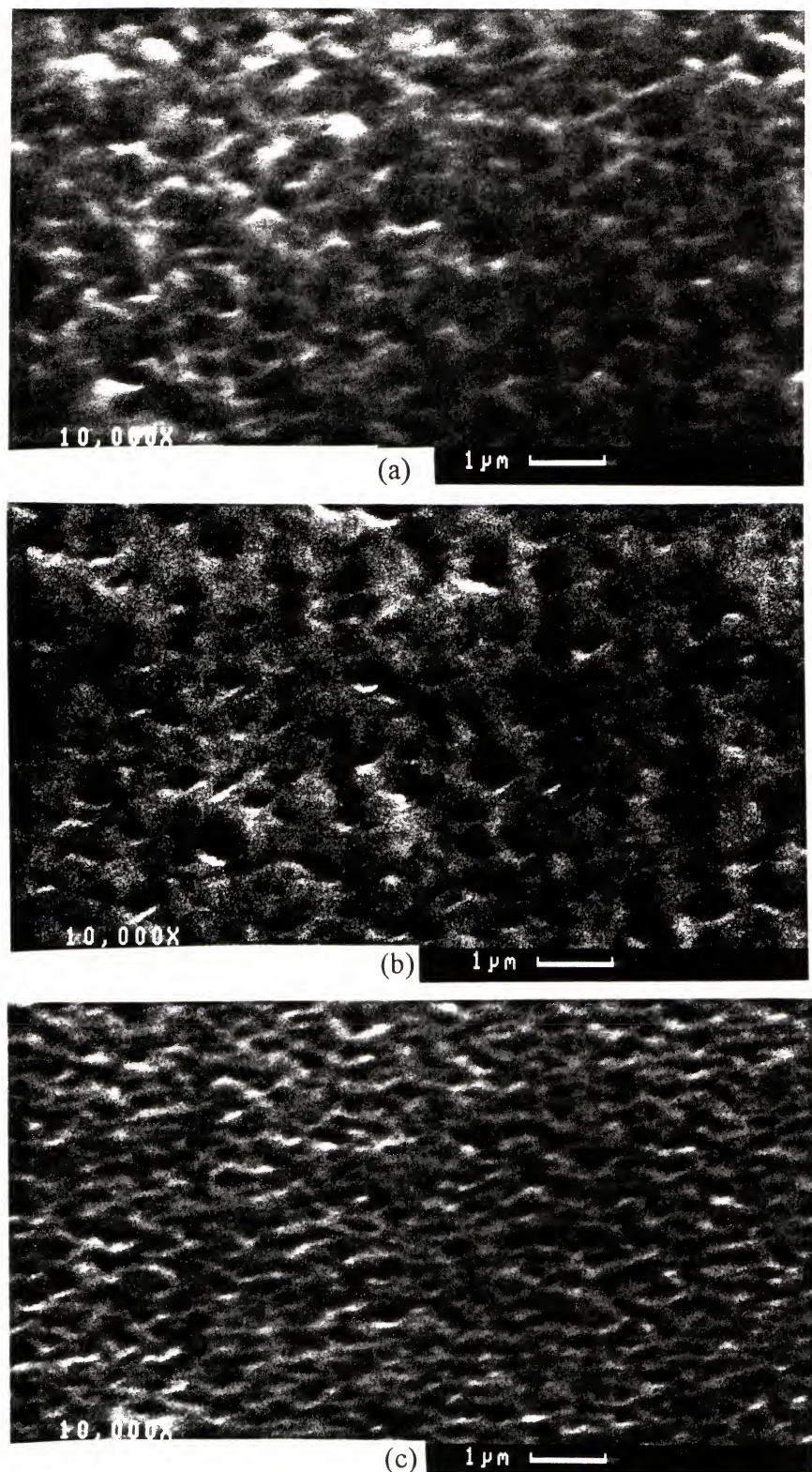


Figure 2-11. SEM micrographs of ZnCdS films prepared with (a) 1% Br_2 in methanol, (b) [5:1:1:: H_2SO_4] \cdot H_2O_2 \cdot H_2O], and (c) [20:7:100:: NH_4OH] \cdot H_2O_2 \cdot H_2O].

supersaturation: too high leads to rough surface morphologies and too low causes low growth rates. The concentration of reactant species in the gas phase near the growth surface is important to understanding the growth mechanism. In MOVPE, it is generally desirable to operate the reactor under laminar flow conditions. Simple laminar flow can be disturbed by a barrier in the flow path or a dramatic change in the diameter of the reactor tube. Vortices can also develop due to sudden changes in momentum. If the gas velocities are set too high, the flow characteristic can change from laminar to turbulent. When the average or mean velocity becomes larger, so does the velocity gradients between the layers. The friction between the layers can get so high that the local velocity components normal to the flow direction are no longer smoothed out but progressively develop until the flow is chaotic.

Equally important is the effect of temperature gradients that can cause free or natural convection normal to the flow direction driven by buoyancy forces under the influence of the gravity field. Another effect that may influence fluid flow is entrance effects. The gas that enters the reactor has to adjust itself to the new tube diameter and temperature conditions.

The dynamic behavior of a gas flowing through a tube at constant temperature can be characterized by the dimensionless Reynolds number (Re):

$$Re = \frac{vd\rho}{\eta} \quad (2-1)$$

where v is the mean linear velocity of the gas, d is the height of the tube, ρ is the density of the gas, and η is the dynamic viscosity of the gas. Laminar flow is characterized by low

Re with minimal friction between layers and any minor disturbances are damped out. At high Re, the friction between the layers is so strong that mixing and vortices develop at a critical velocity. For gases, the transition from laminar to turbulent flow occurs at a $Re = 2300$ for flow in a tube. Results for H_2 flow in the reactor used in this study are in Table 2-6 for an average height of 4.6 cm (mean of 5.8 and 3.4 for the front and back parts of the susceptor) and a flow velocity of 55.0 cm/sec at temperatures of 250 and 550 °C. Since most of the gas in the reactor is H_2 (approximately 98%), the assumption that all of the gas is H_2 is valid for characterizing the material properties of the gas. Under these typical growth conditions, all the flows will be laminar and are significantly smaller than the transition Re. The results show that increased temperature stabilizes the flow.

Table 2-6. Flow properties for horizontal reactor.

Properties	$T = 250\text{ }^{\circ}\text{C}$	$T = 550\text{ }^{\circ}\text{C}$
Reynolds number (Re)	10.0	4.7
Rayleigh number (Ra)	35.0	11.7
Velocity entrance lengths (x_v) (cm)	1.9	0.9
Temperature entrance lengths (x_T) (cm)	13.0	6.1

When forced convective flows are small or absent with existing temperature gradients, free or natural convective flows can occur due to density differences in the gas phase. When the temperature gradient is parallel to the gravity field with the hot zone above the cold zone, the system is said to be stable. However, when there exists a component of the temperature gradient perpendicular to the gravity field, the system is unstable. If the gradient is parallel to the gravity field with the cold zone above the hot zone, the situation is metastable. As long as the thermal diffusivity is large and the

temperature difference is small, the exchange of momentum on a microscopic level is so fast that a gas volume of lower density does not form inside a volume with higher density. As a result, buoyancy is not observed. The third situation is typical of the horizontal cold wall reactor and this is characterized by a dimensionless number, the Rayleigh number (Ra):

$$\text{Ra} = \frac{\alpha g c_p \rho^2 h^3 \Delta T}{\eta x} \quad (2-2)$$

where α is the coefficient of thermal expansion ($1/T$), g is the gravitational constant, c_p is the specific heat, ρ is the density, h is the free height above the susceptor, ΔT is the $T_{\text{bottom}} - T_{\text{top}}$, η is the dynamic viscosity, and x is the thermal conductivity. The results for temperatures of 250 and 550 °C are listed in Table 2-6. When the $\text{Ra} < 1707$, the gas flow is stable without free or natural convection and for $\text{Ra} > 1707$, there is always free convection. For H_2 , free convection does not exist and again increased temperature stabilizes gas flow from undesirable free convection.

A gas that enters a reactor must adapt its velocity profile to the new dimensions and when it approaches the hot susceptor, it must again adjust to both the velocity and temperature profiles. As an approximation, the lengths in which full adjustments are made are described by the following entrance length equations for velocity and temperature profiles, respectively [57]:

$$x_v = 0.04h\text{Re} \quad (2-3)$$

$$x_T = 0.28h\text{Re} \quad (2-4)$$

Due to the thermal expansion of the gas, x_V and x_T are coupled for the region above the susceptor, so for all practical cases it is best to just consider x_T . Uncoupled values of x_V and x_T are listed in Table 2-6 at temperatures of 250 and 550 °C. The long thermal entrance length of 13.0 cm for a temperature of 250 °C is typical and such undeveloped profiles transform into boundary layers. In practice the boundary layer dimensions are subject to large disturbances such as inclined susceptors. Therefore, the entrance regions are controllable factors in the MOVPE process and the reactors should be designed to eliminate their effects. Again increased temperature minimizes the entrance lengths for fully developed temperature and velocity profiles.

The critical Re number discussed above is for fully developed flow in a pipe, while the Ra number cited above is for a fluid confined between two semi-infinite parallel plates. The reactor design employed in this study, however, is more complex. First, the group II and VI flows are separated by concentric tubes that are 2.0 cm away from the susceptor. The susceptor itself is not of circular geometry, but a tilted flat plate that cuts across the bottom section of the tube. Furthermore, the only energy source is the heated susceptor. The possibility of both homogeneous and heterogeneous reactions further complicates the analysis of the reactor used in this study. Nevertheless, an examination of the analyzed results for simple situations can lead to some qualitative conclusions for the expected flow dynamics in the reactor.

Although the flow is laminar, in reality there are two regions with different characteristic flows: one near the susceptor and one above it [58-59]. Near the susceptor, the flow is laminar with relatively sharp concentration and temperature profiles. Above

the susceptor, these gradients are essentially flat. This indicates a mixed character of flows with significant amount of gas motion perpendicular to the direction of flow, leading to the observed flat profile of the concentration and temperature gradients. The mixed flow is also witnessed in our system with deposits on the reactor walls shaped in recirculating vortices downstream of the growth zone.

2.4.2 Thickness Uniformity

The gas velocity profile and temperature gradients formed near the susceptor plays an important role in the deposition process. Mass transport of the reactants from the bulk gas phase to the reacting surface occurs mainly by diffusion through a hydrodynamic boundary layer near the substrate. Although little modeling exists for vertical type reactors, many exist for horizontal type reactors. A detailed model of the flow dynamics, velocity, mass, and temperature profiles based on boundary layer theory have been developed [60]. Although the specific interest is the growth of Si from SiCl_4 , the results are applicable to other pyrolytic CVD processes based on the same type of geometry in horizontal reactors. Ban [61] measured thermal and concentration profiles and discovered two distinct zones above the susceptor. The region just above the susceptor shows sharp temperature and concentration gradients. Further above the susceptor, the gradients are nearly flat leading to mixed flow. With more pronounced gas motion perpendicular to the direction of flow, mixing occurs more efficiently leading to the observed flat profile of the gradients. For flat susceptors, the growth rate decreases with increasing distance down the susceptor because of reactant depletion. To counterbalance this effect, the susceptor

is often tilted to increase the fluid velocity and thus decrease the boundary layer thickness.

The critical angle for uniform deposition is calculated to be

$$\sin(\theta_c) = \left(\frac{2D_o}{b_o V_o} \right) \left(\frac{T_a}{T_o} \right)^{0.88} \quad (2-5)$$

where D_o is the diffusion coefficient of the precursor molecule at T_o , b_o is the distance from the front of the susceptor to the upper wall, V_o is the horizontal gas velocity at the front of the susceptor at T_o , and T_a is the average temperature of the gas. Figure 2-12 plots the critical angle of the susceptor for uniform deposition as a function of T_a . The results show that for most growth conditions the critical angle is less than 5° . D_o is taken as $5.15 \text{ cm}^2/\text{sec}$ (average D_o for DMCd and DEZn at 300 K), b_o is 5.8 cm , and V_o values range from 107.15 to 15.05 cm/sec for velocity in the MO line.

The angle of the susceptor is currently set at 18° which is quite steep and not within the normal range of 3° to 5° . By rearranging Equation 2-5, V_o is calculated to be 5.7 and 14.0 cm/sec for T_a values of 300 and 823 K , respectively, based upon similar constants used in Figure 2-12 with a critical angle of 18° . These values correspond to an upper limit of 250 sccm of gas flow through the middle MO line.

Since diffusion coefficients for DMCd and DEZn in H_2 are not easily found in literature, they were estimated from the Chapman-Enskog kinetic theory [62]:

$$D_{ab} = 0.001858 \frac{\sqrt{T^3 \left(\frac{1}{M_a} + \frac{1}{M_b} \right)}}{p \sigma_{ab}^2 \Omega} \quad (2-6)$$

where T is the temperature, and M_a and M_b are molecular weights, p is the pressure, σ_{ab} is a Lennard-Jones parameter, and Ω is a dimensionless function of the temperature and of the intermolecular potential field for one molecule of A and one of B. The σ_{ab} and Ω are values of hydrocarbons that best estimate DMCd (C_2H_6) and DEZn (C_4H_{10}). These values are tabulated in the back of reference [62]. The diffusion coefficient for DMCd is 5.85 and $33.17 \text{ cm}^2/\text{sec}$ for temperatures of 300 and 823 K, respectively. The diffusion coefficient for DEZN is 4.45 and $25.45 \text{ cm}^2/\text{sec}$ for temperatures of 300 and 823 K, respectively. This theory assumes low density which is true for this case at operating pressures of 70 Torr.

The flow rate of gas in the main MO line alone is not the only factor determining the thickness uniformity of $ZnCdS$ growth, but the ratio of the gas inlet and MO inlet flow rates. Figure 2-13 plots the relationship between the number of Moiré fringes and the ratio of the gas velocities. The Moiré fringes are caused by interference effects from thickness variation across the sample and are produced by the refraction of light due to the difference in refractive indices between the grown epilayer and the GaAs substrate. Although a crude estimation of uniformity, the number of fringes offer a convenient and accurate measure of thickness uniformity. With the assumption of zero absorption, the following relationship for film thickness is valid [63]:

$$d = \frac{1}{2n\Delta\nu} \quad (2-7)$$

where d is the film thickness, n is the refractive index of the epilayer, and ν is the frequency of radiation in wavenumbers (cm^{-1}). For an epilayer whose composition is

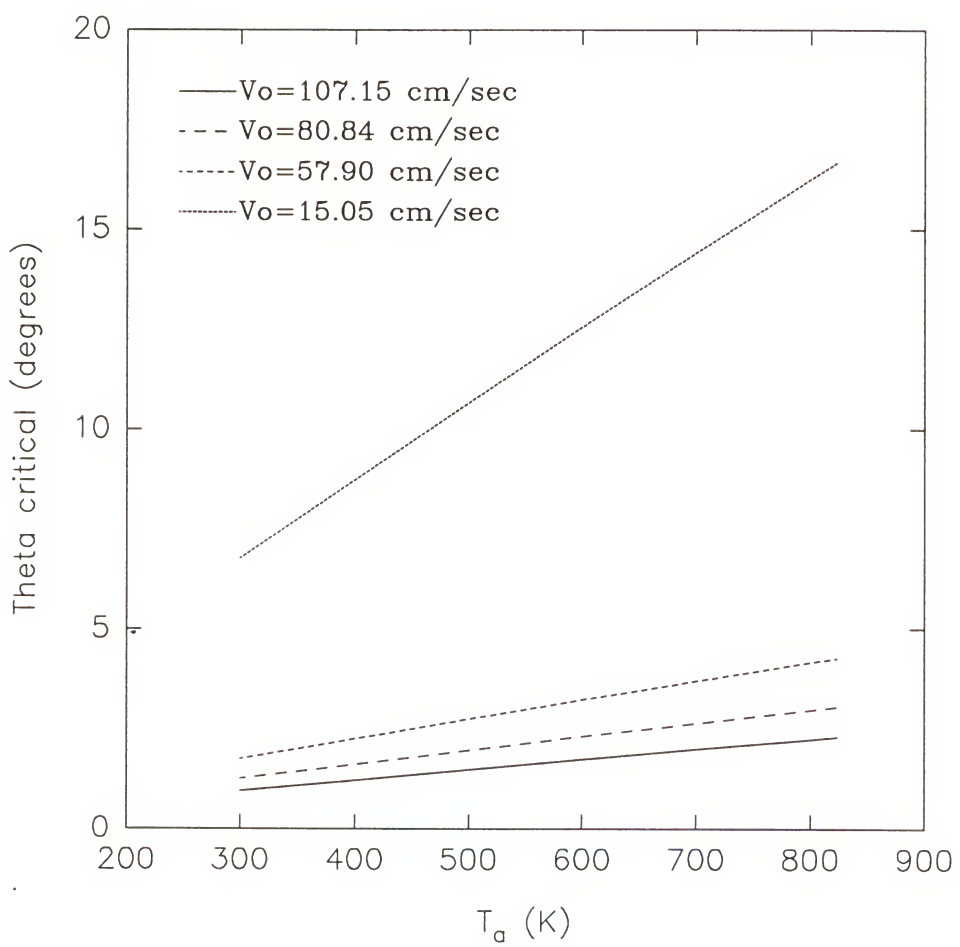


Figure 2-12. Critical angle of the susceptor for uniform deposition.

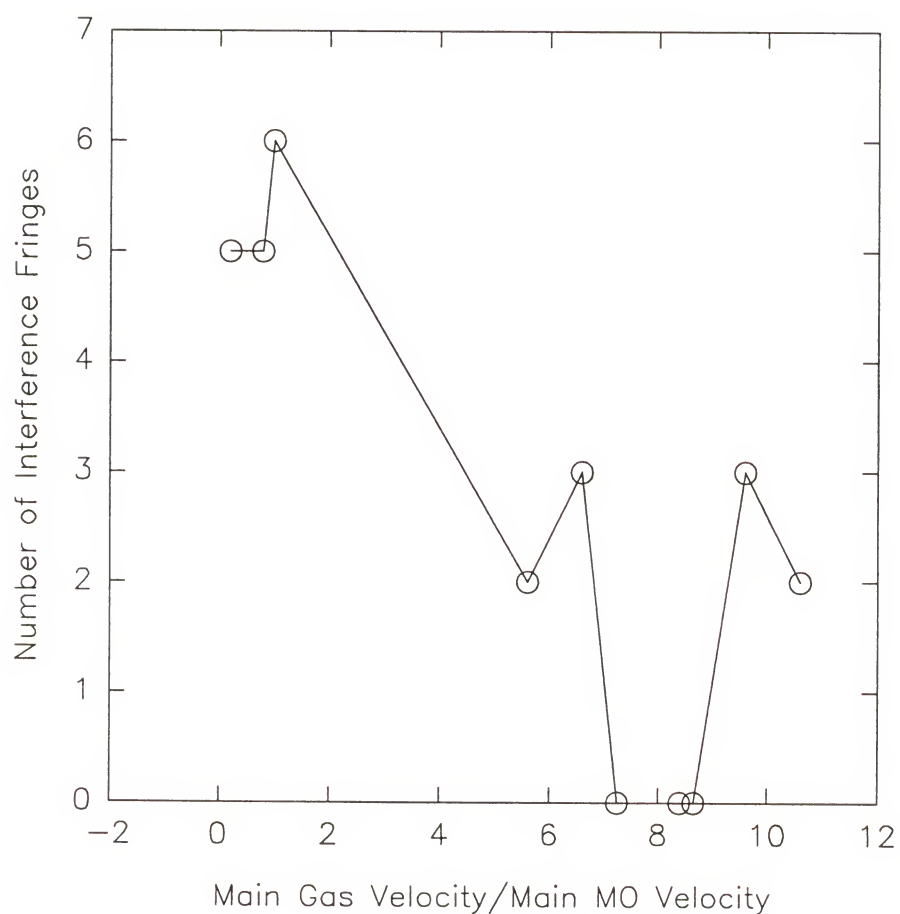


Figure 2-13. Correlation between the number of Moiré fringes and the ratio of gas velocities in the main gas and main MO inlet line.

$\text{Zn}_{0.45}\text{Cd}_{0.55}\text{S}$, the average calculated thickness variation is 0.7 μm from each transition in the visible color spectrum (red, orange, yellow and green). These calculations are based on the data in Table 2-7 where the refractive index data are extracted from Figure 3-8 in Chapter 3.

Table 2-7. Data for thickness calculations.

Color	Frequency (cm^{-1})	n of $\text{Zn}_{0.45}\text{Cd}_{0.55}\text{S}$
red	1.43×10^4	2.36
orange	1.61×10^4	2.37
yellow	1.72×10^4	2.39
green	1.89×10^4	2.46

Experimental data indicate that the film thickness is uniform (no observed fringes) with no observed fringes if the ratio of the main gas and main MO velocities is between 7.2 and 8.6. The MO enters the reactor through a 0.25 inch inner diameter quartz tube that is approximately 2.5 cm long. The hydride gases enter the reactor near the center of the metal flange from four equidistant orifices of 1/8 inch inner diameter. As a first order approximation, this would indicate the outer cylindrical curtain of gas needs to have a higher velocity than that of the MO in order to produce a uniformly thick deposition. This is in contrast to common sense which would suggest that if the velocities were the same in both inlet lines, the frictional drag between the two flows would be minimized and thereby minimize any turbulence or vortices. The maximum velocity for the main MO line is 1950 cm/min. If the velocity is any higher, one gets a jet effect on the epilayer and the growth becomes nonuniform.

The nonuniform film thickness can also result in concentration variation across the sample caused by preferential depletion of either Cd or Zn at the front of the substrate. Although difficult to prove due to large sample area and concomitant measurement error with current characterization techniques, this may be another source for the broadening of HRXRD peaks besides high defect concentrations.

2.4.3 Growth Kinetics

Figure 2-14 shows the variation of the growth rate with temperature. For both (100) 0° and 2° orientations, the growth is kinetically limited for temperatures between 25 and 300 °C and mass transfer limited between 300 and 450 °C. The former is indicated by the dependence of growth rate on temperature and conversely, the latter by its independence. Under the assumption that the crystal growth process is a lateral 2-D growth and that the overall activation energy of the surface reaction is nearly the same for both substrates, the higher index cut substrate with a higher number of nucleation sites would be expected to have a higher growth rate in the kinetically limited region. With more nucleation sites, more islands of activated complexes cover the surface and will eventually coalesce into a single coherent film faster than with fewer number of islands. If the energy barrier to form these islands of activated complexes are nearly the same for both substrates, then the number of islands is only limited by the number of nucleation sites available on the surface. As a result, with 2-D growth, the surface with more nucleation sites should be characterized by a higher growth rate. This is contrary to the

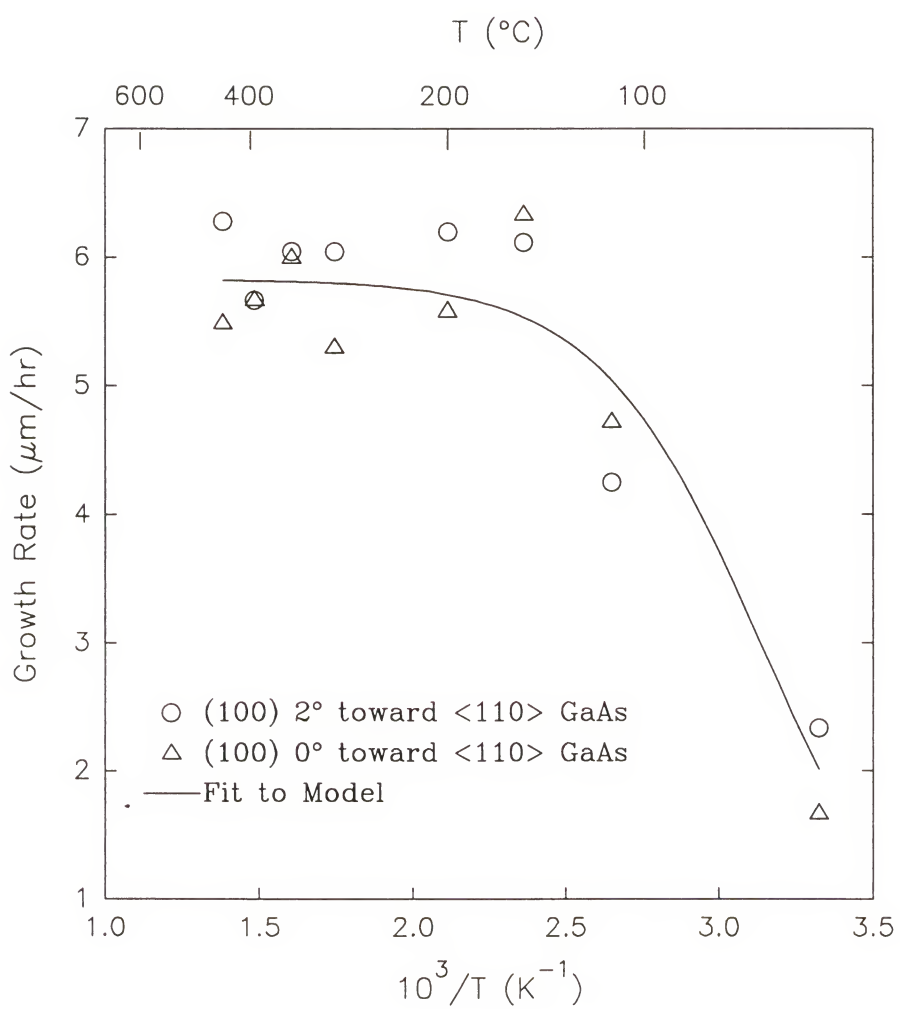


Figure 2-14. Dependency of growth rate on temperature.

experimental results. An index cut of 2° may not be significant enough to expose measurable differences in the density of nucleation sites.

In the mass transfer limited region, the growth rate for both substrates should be the same. Since the flux of the reactants to the surface is limiting growth, the number of active sites is irrelevant in determining the growth rate. Thus, both substrates should have the same number of activated complexes and therefore the same growth rates which is found to be true for ZnCdS growth.

As a first approximation to modeling the kinetics of film growth, the growth rate versus temperature data are fitted with a simple model proposed by Grove [64]. The model defines two fluxes: the first corresponds to the flux of the reactants from the bulk gas phase to the film growing surface and the second defines the flux of the reactants' consumption during the chemical reaction to form the film. The first flux can be approximated as a linear function of the concentration gradient between the bulk gas phase and the reacting surface:

$$F_1 = h_G(C_G - C_s) \quad (2-8)$$

where F_1 is the flux of reactants, h_G is the proportionality constant known as the gas phase mass transfer coefficient, and C_G and C_s are the concentrations of the reactants for the bulk gas phase and the reacting surface, respectively. The second flux is simply an assumed first order surface reaction with the concentration of the reactants at the reacting surface and is defined as

$$F_2 = k_s C_s \quad (2-9)$$

where k_s is the chemical surface reaction rate constant. Under steady state conditions where all the fluxes are equal, the growth rate is expressed by the following relationship:

$$V = \left(\frac{k_s \cdot h_G}{k_s + h_G} \right) \left(\frac{Y}{N_1} \right) C_t \quad (2-10)$$

where V is the growth rate, C_t is the total concentration of molecules in the gas, Y is the mole fraction of the reacting species, and N_1 is the number of reacting atoms in a unit volume for the solid. From the data in the Figure 2-14, the low temperature growth rate can be approximated with an exponential Arrhenius relationship.

In the kinetically limited growth regime, $k_s \gg h_G$ and temperature sensitive, and in the mass transfer limited growth regime, $h_G \gg k_s$ and temperature insensitive. Grove's simple model explains the temperature dependence of growth rate data shown in Figure 2-14. In this model, the fitting parameters are the pre-exponential factor for the rate constant (K_0), the activation energy for the reaction (E_a), and the gas-phase mass-transfer coefficient (h_G). The parameters for the best fit are 1.4×10^6 cm/sec for K_0 , 11.9 cm/sec for h_G , and 0.32 eV for E_a . These values are comparable to those for growth of silicon [65].

This is an extremely simplified model. There are basically four steps for film growth: (1) transport of reactants from bulk gas phase to reacting surface, (2) chemical reaction to form compound, (3) incorporation of compound into film, and (4) removal of by-products. This model does not take into account the flux of products from the reacting surface back out to the bulk gas phase. Since there exists a temperature gradient from the heated growth area to the cold wall, the gas properties will vary accordingly and this has not been taken into consideration. Nevertheless, even with these assumptions, this model provides

a good estimate to the kinetic properties of the ZnCdS growth process and describes the regions of growth: mass transfer limited and kinetically limited.

2.4.4 Crystal Structure

Two structural issues arise when evaluating the potential of the pseudobinary Zn_1-xCd_xS thin films grown on GaAs for optoelectronic devices applications. First, bulk ZnS exhibits the zinc blende structure at room temperature as does GaAs, but CdS is stable in the hexagonal wurtzite structure. The differences in the Gibbs free energies between these two structures for both compounds is small. Thus, the stable structure of solid solutions formed between these two compounds is difficult to predict given the added complexity of the cubic GaAs substrate. The second issue is related to the formation of misfit dislocations given the relatively low values of the elastic constants for the pure compounds. The misfit can arise in two ways: compositional and thermal. Presumably, the compositional component can be eliminated by film composition adjustment. The thermal component can not be eliminated but it can be minimized by growth at low temperature and proper selection of the film composition at growth temperature.

The critical thickness of ZnS grown on GaAs is on the order of 1.1 nm [66] and this hints at the critical thickness of ZnCdS if it is not perfectly lattice matched. The epilayer will grow with the same crystal structure of the substrate as long as the interfacial energy due to misfit is lower for this situation. Beyond the critical thickness, the bulk free energy will dominate over interfacial energy considerations and the epilayer will transform into its bulk equilibrium structure despite the higher interfacial energy cost due to interfacial misfit

[67-68]. The pseudomorphic to bulk phase is a nucleation-growth process and for the case of Cd rich ZnCdS, it is the transition from zinc blende to wurtzite structure.

Figure 2-15 depicts the correspondence between the measured lattice constant and the solid composition. The lattice constant is calculated from HRXRD spectra using the $\langle 004 \rangle$ reflection while the composition was measured by EPMA. Interpolation of this data gives the solid composition that lattice matches to GaAs as $x = 0.58$, the atomic percent of Cd in the solid epilayer. A discontinuity occurs at $x = 0.67$ where the slope of the plot suddenly increases. At this Cd composition, a transition occurs from the Zn rich cubic structure to a yet undetermined Cd rich crystal structure. Since ZnS normally crystallizes in the sphalerite structure and CdS in the wurtzite structure, there must be a composition at which a transition occurs between the two crystal structures. It is interesting to note that the slope of the linear relationship from $x = 0.0$ to $x = 0.67$ and therefore, the solid composition that lattice matches to GaAs are predicted by Vegard's law if the lattice constants of cubic ZnS (put in values) and cubic CdS (values) are taken as endpoints. It would seem plausible to suggest that in this solid composition range, the epilayer has a sphalerite structure, but between $x = 0.68$ to $x = 1.0$, the structure is shown to be a mixture of zinc blende and wurtzite.

Figure 2-16 displays the low energy electron diffraction (LEED) patterns measured on films with solid compositions of (a) $x = 0.82$ and (b) $x = 0.58$. Each sample is grown on (100) 2° orientation GaAs substrates. For $x = 0.82$, the crystal structure of the epilayer is unequivocally neither completely sphalerite nor completely wurtzite, but a superposition of both. This duality of crystalline structures may be one of the causes for the large

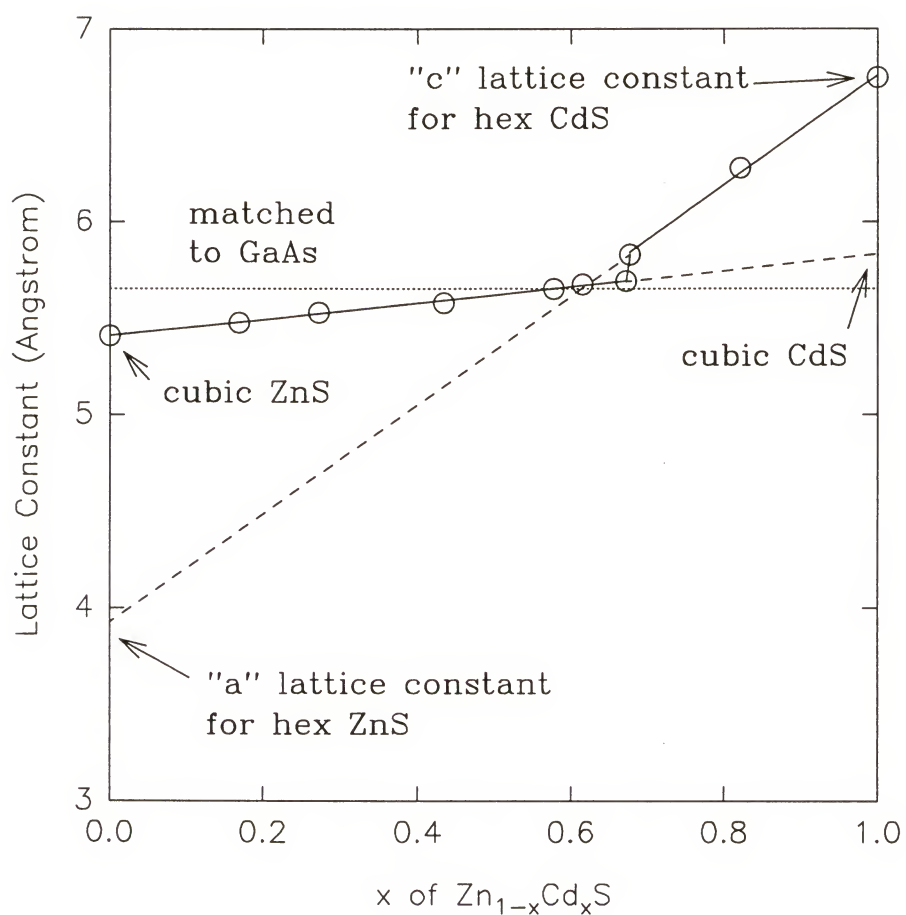
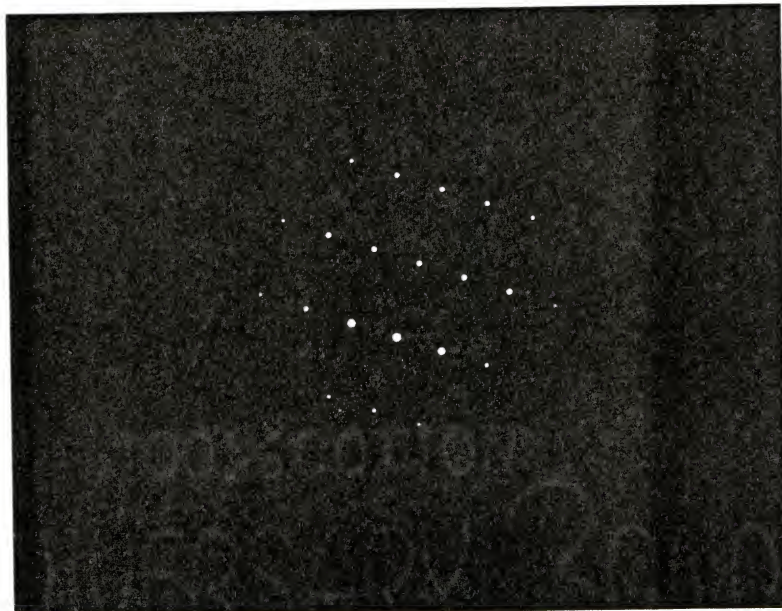
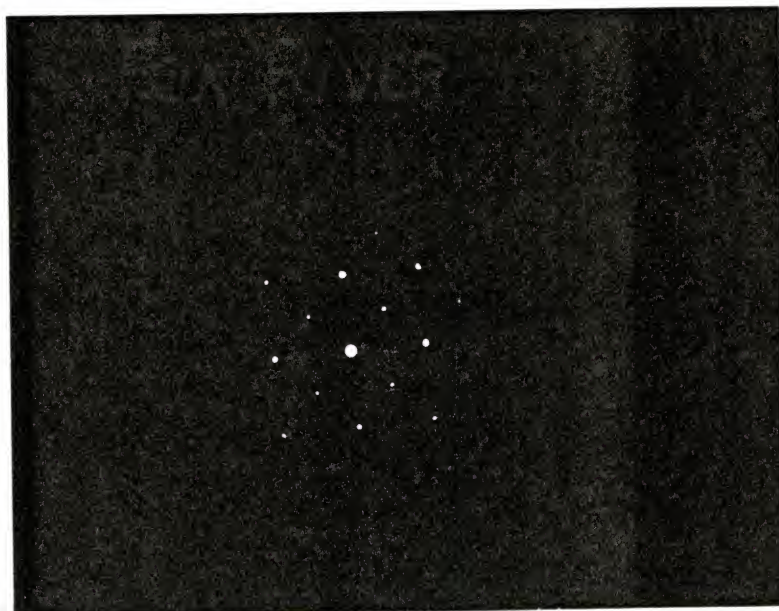


Figure 2-15. Correlation between the measured room temperature lattice constant and the solid composition.



(a)



(b)

Figure 2-16. LEED patterns of $Zn_{1-x}Cd_xS$ of (a) $x = 0.82$ and (b) $x = 0.58$.

FWHM of HRXRD peaks associated with Cd rich materials. For the nearly lattice matched sample with $x = 0.58$, the four fold symmetry of the LEED patterns indicates that it has the cubic structure. These results support the notion that in the composition range of $x = 0.0$ to $x = 0.67$, the crystal structure is sphalerite, and at $x = 0.67$ to $x = 1.0$, the crystal structure is a mixture of sphalerite and wurtzite. More studies need to be made to ascertain the exact crystal structure. Bulk $Zn_{1-x}Cd_xS$ normally crystallizes with the wurtzite structure for a composition range of $0.15 < x < 1$ [69]. Apparently growth on zinc blende GaAs stabilizes the zinc blende phase for $0 < x < 0.67$.

Since the direction of the HRXRD measurement is perpendicular to the growth surface, information about the orientation of growth can be extracted. The sudden rise in slope for Cd-rich compositions indicates that the longer axis of the mixed structure is perpendicular to the (100) plane. If the structure is tetragonal, the atomic bonding is stretched out in the $<100>$ direction with respect to the substrate and if the structure has some hexagonal characteristics, the epilayer is growing with the c-axis aligned along the $<100>$ direction. Reports have cited that the longer axis of the hexagonal structure, the c-axis, of the deposited ZnCdS line up perpendicular to the growth surface when grown on (111)B GaAs substrates [36]. These results indicate that this is also true when grown on (100) substrates.

Kaneko et al. [70] reported that with decreasing temperature and decreasing pressure, the only phases that exist are the pure cubic ZnS and a mixture of cubic ZnS plus hexagonal CdS. The alloy composition at which the pure cubic ZnS becomes the mixture shifts toward the Cd rich region. Apparently the lattice constant for cubic ZnS follows

that of Vegard's Law until the composition of Cd = 0.50 at 400 °C. These findings correspond at least qualitatively to our experimental transitional composition of Cd = 0.67 at a temperature of 350 °C and pressure of 70 Torr.

Figure 2-17 shows the FWHM of the HRXRD curves in the <004> direction versus the solid composition. The plot indicates that the minimum of the FWHM is at x = 0.58 (lattice matched conditions) with a value of about 2000 arc-seconds. The broad FWHM is most likely due to crystal defects throughout the sample. The growth temperature was set at 450 °C with the reactor pressure at 70 torr. The Cd/II ratio was varied from 0.4, 0.45, 0.52, to 0.62. Only (100) oriented GaAs substrates were used in this experiment.

2.4.5 Surface Morphology

Micro-porosity can form if the growth rate is controlled by mass transport while dense deposits are formed if controlled by surface reactions [71]. Gas phase reactant concentration and therefore growth rate is greatest at or near the tips of the crystallites under mass transfer limited conditions since the tips extend further into the boundary layer where a concentration gradient exists. The enhanced growth rates of the tips relative to the intercrystallite boundaries can cause porosity as the tips eventually coalesce and envelop voids. The result is surface roughness.

Figure 2-18 shows SEM micrographs of ZnCdS grown at three different temperatures with corresponding FWHMs. Growth temperatures of 450, 400, and 350 °C corresponds to sample (a) with 1160 FWHM, sample (b) with 2559 FWHM, and sample (c) with 4336 FWHM, respectively. Each sample is of the same composition as

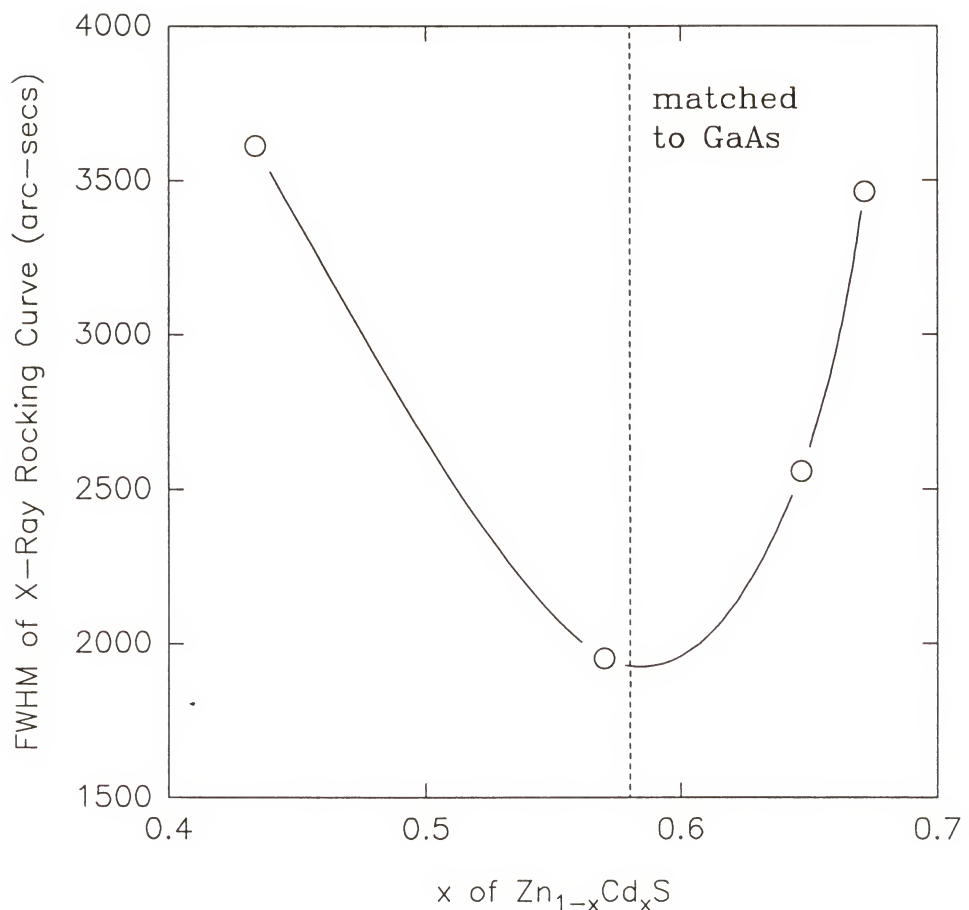


Figure 2-17. FWHM value for various solid composition.

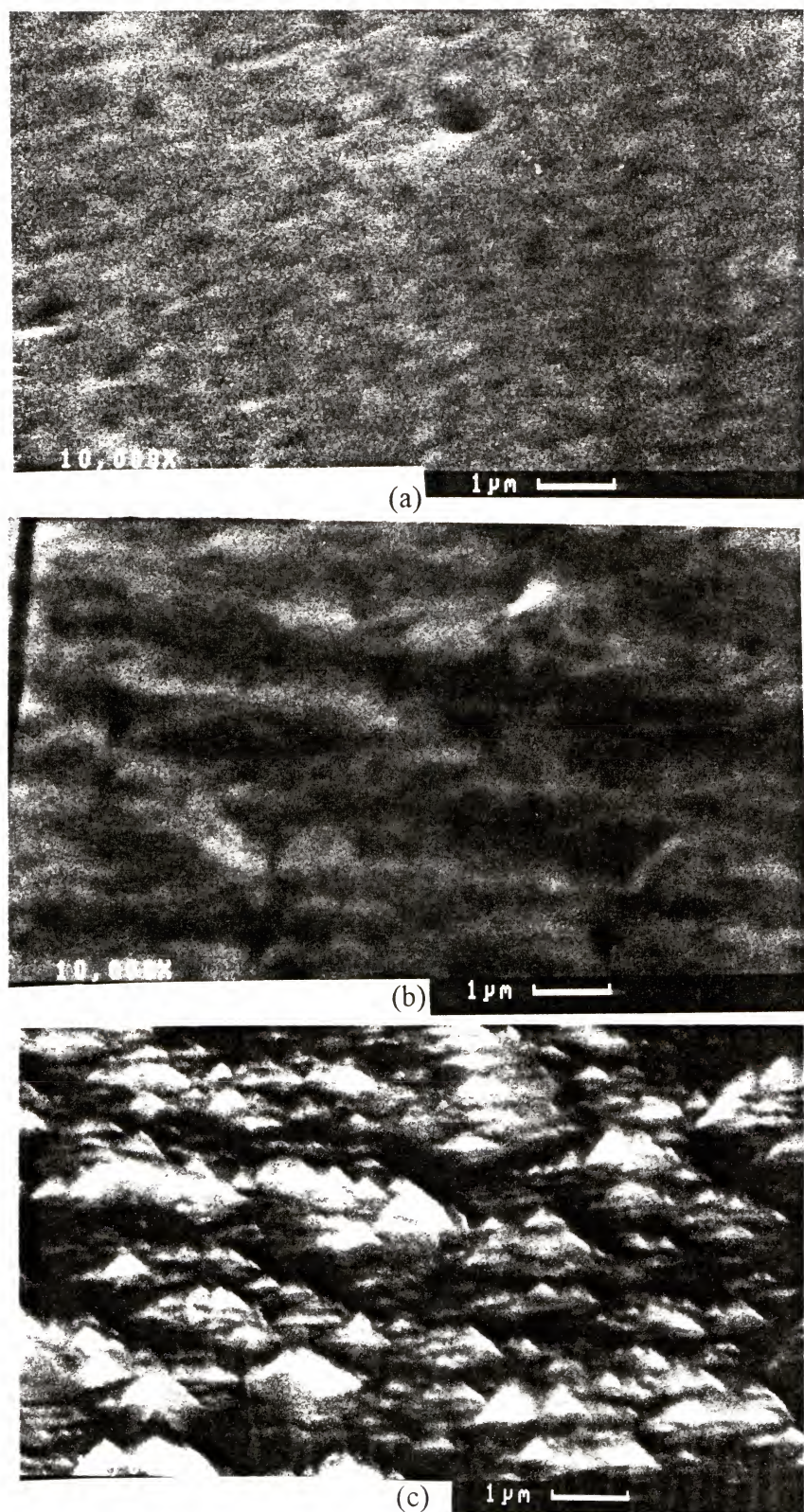


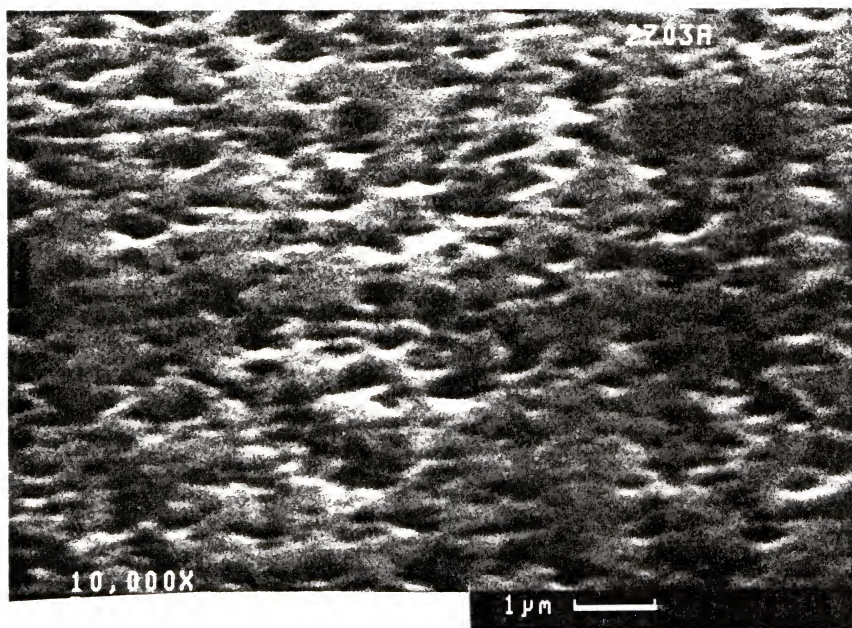
Figure 2-18. SEM micrographs of ZnCdS grown at (a) 450°C , (b) 400°C , and (c) 350°C .

determined by EPMA. Samples (a) and (c) show similar roughness with 1.0 μm diameter pore size but the surface in (c) is extremely rough with large isolated islands. At the lower temperature under kinetically limited regime, the surface morphology is indeed less rough, but the tradeoff is that 3-D growth occurs.

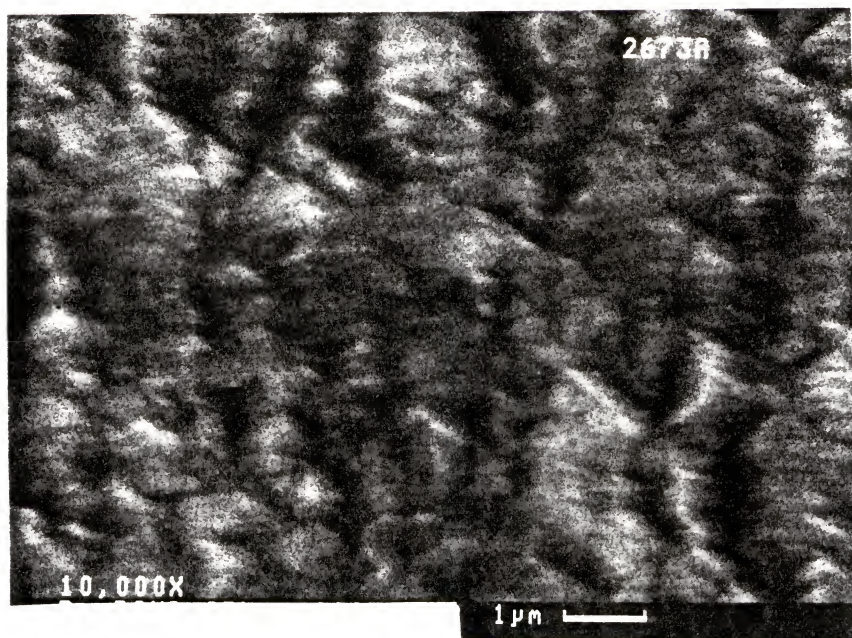
Figure 2-19 shows SEM micrographs of ZnCdS grown at two different VI/II ratios but otherwise the exact same growth conditions. Sample (a) with a VI/II ratio of 43.62, seems to have coalesced into a film and has proceeded in a 2-D growth as compared to sample (b) with a VI/II ratio of 10, is characterized by isolated islands that just started to merge in one dimension. This implies that 2-D growth begins for the (100) misaligned 2° toward the nearest <100> substrates with a VI/II ratio of around 50. This is consistent with previous results that show the best quality film grown on (100) substrates with a VI/II ratio of 120. At a VI/II ratio of 50, the quality slowly improves with increasing VI/II value. The poor quality of the growth layers with a high degree of surface roughness is the cause of the poor crystallinity reflected in the high FWHM of the HRXRD peaks.

2.4.6 Defects

Dislocations in the active device area that act as non-radiative recombination centers compromise the efficiency of optoelectronic device operation. These dislocations are also called dark line defects (DLDs) and are often caused by lattice mismatching as seen in Figure 2-20. The micrograph clearly shows the criss-crossing line defects on (100) 2°



(a)



(b)

Figure 2-19. SEM micrographs of ZnCdS at VI/II ratios of (a) 43.62 and (b) 10.

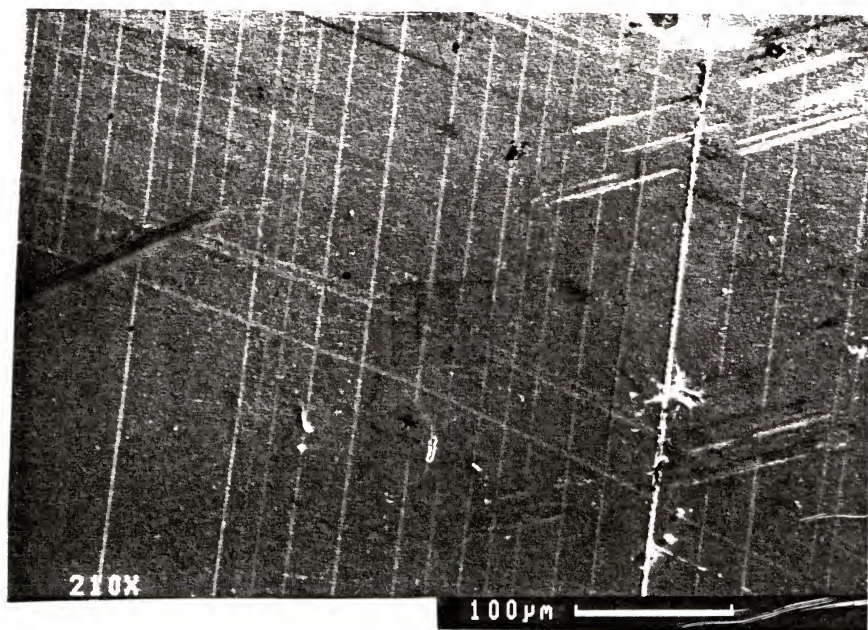


Figure 2-20. SEM micrograph of ZnCdS misfit dislocation defects grown on (100) GaAs from top view.

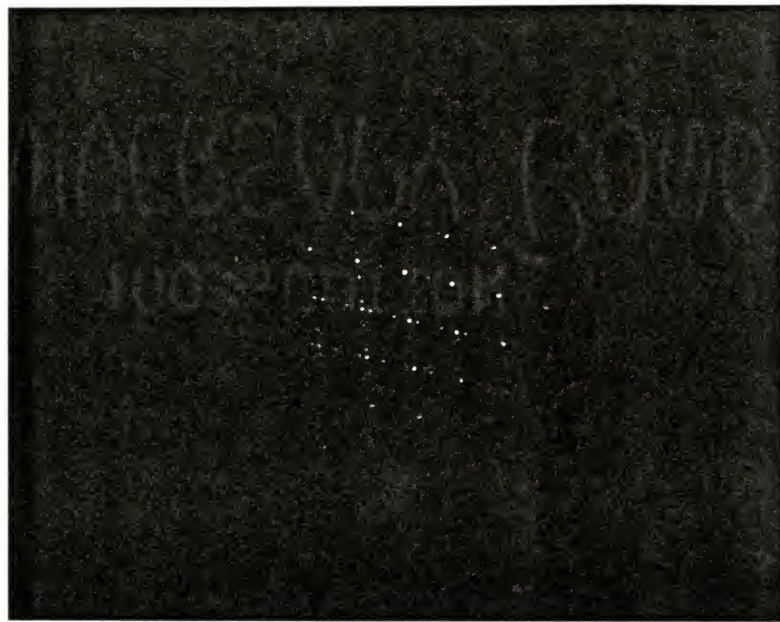
toward $<110>$ substrate. The solid phase composition is $x = 0.65$ (Cd atomic fraction) corresponding to 0.55% lattice mismatch to the GaAs substrate.

Even with lattice matching, stacking faults/microtwins pervade throughout the epilayer. Figure 2-21 is a cross sectional TEM micrograph of ZnCdS lattice matched to (100) orientation GaAs. This clearly illustrates the formation of 60° stacking faults along the (111) planes with an approximate density of about 10^{10} cm^{-2} . The relatively equal number of line defects propagating 60° and -60° from the growth surface, suggests no preferential stacking fault formation on either (111)A or (111)B planes. This is consistent with obtaining nearly the same quality ZnCdS epilayers whether grown on Ga or As ending (111) planes at various growth conditions with the exception of particular etchants as discovered in previous optimization experiments. The formation of stacking faults are also detected by LEED patterns.

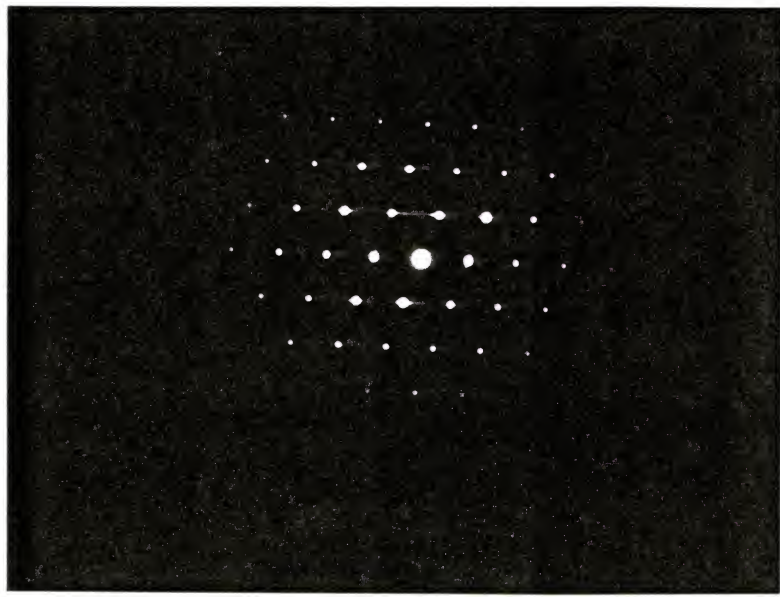
Figure 2-22(a) shows the LEED diffraction pattern for a sample whose Cd composition is $x = 0.82$ with characteristics of cubic and hexagonal structure. The beam direction is in the $<11\bar{2}0>$ direction and the streaking is indicative of defects which are likely to be stacking defaults/microtwins along the (0001) basal planes. Figure 2-22(b) displays the LEED pattern of a lattice matched ($x = 0.58$) epilayer to be cubic. The beam is in the $<110>$ direction and the streaking is indicative of defects along (111) planes. For the hexagonal structure, this basal plane is also the close packing plane just as the (111) planes are for the cubic structure. The only difference between the (111) planes of the cubic structure and the (0001) basal planes of the hexagonal structure is a change of



Figure 2-21. TEM cross section of ZnCdS grown on (100) GaAs with stacking faults.



(a)



(b)

Figure 2-22. LEED streaking patterns of $Zn_{1-x}Cd_xS$ of (a) $x = 0.82$ and (b) $x = 0.58$.

stacking sequence. These close packed planes are also the lowest energy planes where the probability of defect propagation is highest.

The density of dangling bonds is lower by as much as a factor of 2 at (111) heterojunction interfaces than for other planes [72]. In addition, the dislocation movement is easier on the (111) planes which are the slip planes in zinc blende lattices. Thus, stacking fault/microtwin formation along (111) planes provides the maximum relief stress. This same argument can be extended to the (0001) basal planes of wurtzite structures. Formation of stacking faults/microtwins can be explained by the nucleation and growth mechanism.

One possibility in exposure of (111) planes besides twinning that may serve as the initial growth surface for hexagonal growth is explained by the nucleation growth mechanism. Since the likelihood of all crystallites growing in a singular orientation is low, the initial crystallite formation is most likely faceted with several orientation planes including the (111) where hexagonal structured ZnCdS can initiate and grow in a matrix of zinc blende structure. The surface contamination is a source for step-kink formation that may serve as nucleation sites for initiation of misoriented crystallites different from the previous layer. The origin of hillocks of various shapes including tetrahedron and pyramids is normally attributed to such surface contamination. Besides two dimensional defects such as stacking faults/microtwins, three dimensional defects are visible on the growth surface.

Figure 2-23 shows a Nomarski contrast interference micrograph of a ZnCdS film grown on a (111)A substrate. Clearly, tetrahedral hillocks are visible on the surface of the

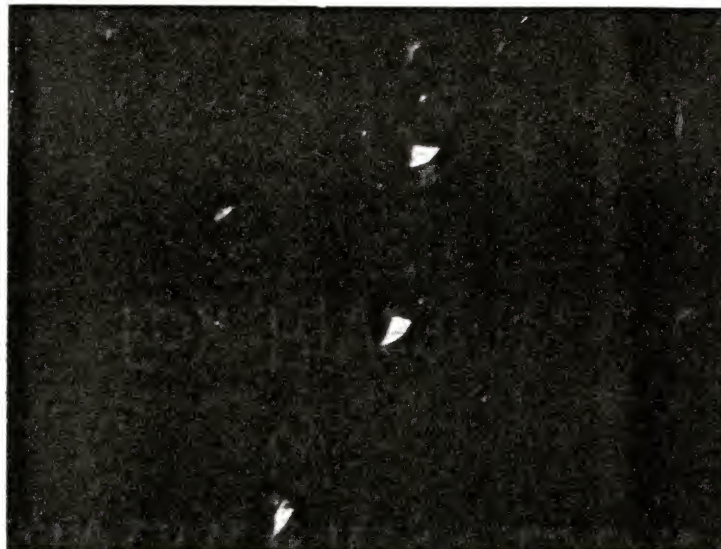


Figure 2-23. Nomarski micrograph of ZnCdS grown on (111) substrates.

epilayer. The growth rate of ZnCdS films grown on (111) oriented substrates is much slower than on (100) oriented substrates when the growth temperature is low. The (100) facet, angled 54.7° relative to the growth face will eventually dominate the shape of the hillock by overgrowing the slower growing (111) facet. Since the (111) face is surrounded by three (100) faces, the shape will be that of a normal tetrahedron. These hillocks are about 10-100 μm in lateral dimensions.

2.4.7 Solid Phase Composition

The dependence of the solid composition on growth temperature is illustrated in Figure 2-24. The solid composition of the thin films is determined by electron probe microanalysis (EPMA). In this study, the process parameters are fixed except the growth temperature. The flow rates of [DEZN] and [DMCd] are 28 and 43 $\mu\text{mole}/\text{min}$, respectively. The flow rate of H_2S is fixed to maintain a VI/II ratio of 117 and the gas phase molar ratio $[\text{DMCd}]/([\text{DMCd}]+[\text{DEZN}])$ is kept fixed at 0.6. The plots for both (100) 0° and 2° orientation substrates are nearly identical. As expected, with increased temperature, the solid composition approaches that of the inlet gas phase. At a high temperature, the growth process is limited by mass transfer and not kinetics. Thus the near surface gas phase composition should be close to equilibrium with the solid solution. At these relatively low temperatures, the Cd and Zn equilibrium composition in the gas phase is small and essentially all the Cd and Zn which arrives at the surface is incorporated. As discussed in Chapter 4, non-idealities in the solid solution give rise to a slightly Cd-enriched solid solution relative to the gas phase. In addition, the diffusivity of

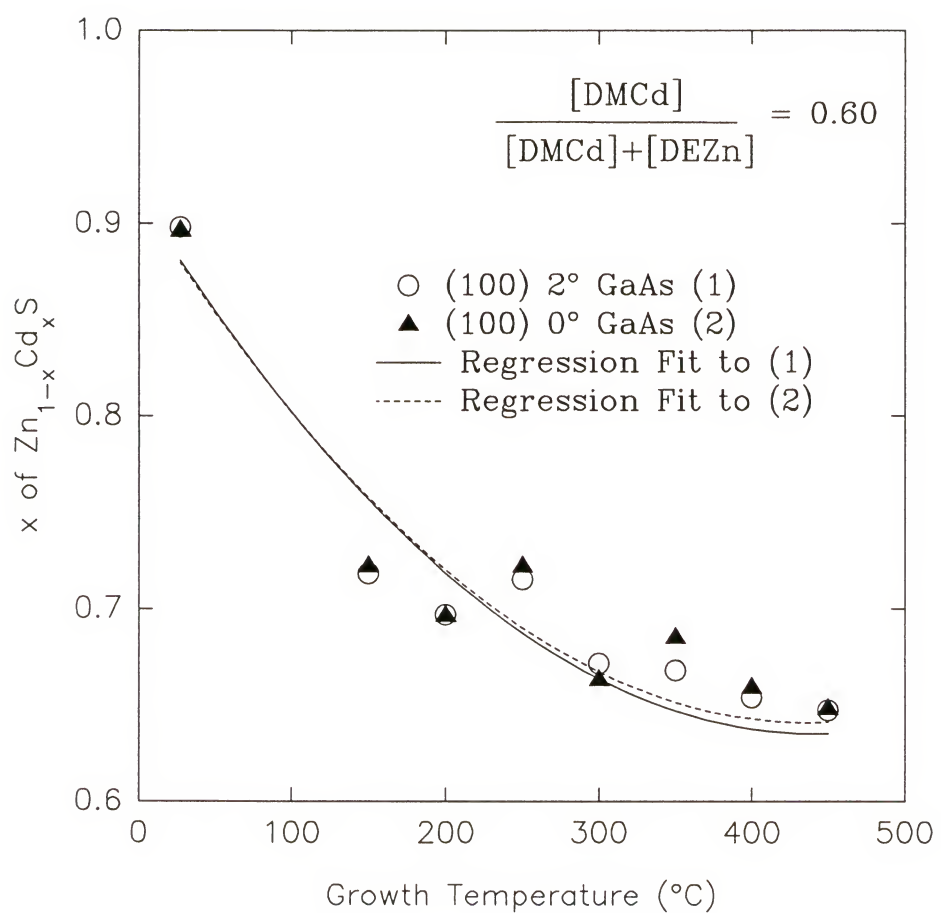


Figure 2-24. Second order regression correlation between solid composition and growth temperature.

DMCd is slightly larger than that of DEZn. The reasons for the solid composition deviating from the gas phase composition and producing Cd rich epilayers at lower temperatures are still unclear. One reason may be related to the observation that DMCd homogeneously decomposes more readily than DEZn, thus providing more reactive Cd than Zn to be incorporated into the solid phase matrix. The sticking coefficient for Cd may also be higher than that for Zn at low temperatures and relatively more Cd chemically adsorbs on the substrate than Zn [37].

Another explanation may have to do with thermodynamics. The solubility of ZnS in CdS increases with increasing temperature and the opposite is true of CdS in ZnS [73]. As a result, at low temperatures, the solid phase will be richer in Cd which is observed previously. These findings are also supported with physical arguments. As temperature increases, the Zn ion which has a smaller ionic radius (0.74 Å) should be more easily incorporated into the CdS lattice while Cd which has a larger ionic radius (0.97 Å) is not so easily incorporated into the ZnS lattice matrix.

2.4.8 Optical Purity

Figures 2-25 and 2-26 show low temperature photoluminescence (PL) measurements with Cd composition of $x = 0.58$ (lattice matched) and $x = 0.55$, respectively. At 40 K, there is a strong luminescence at 2.83 and 2.86 eV (blue and purple luminescence) for $x = 0.58$ and $x = 0.55$, respectively. The FWHM is 57 and 55 meV for each respective composition. With such broad peak widths, these are unlikely to be excitonic emissions. The source of these near bandgap energy emissions is still unclear,

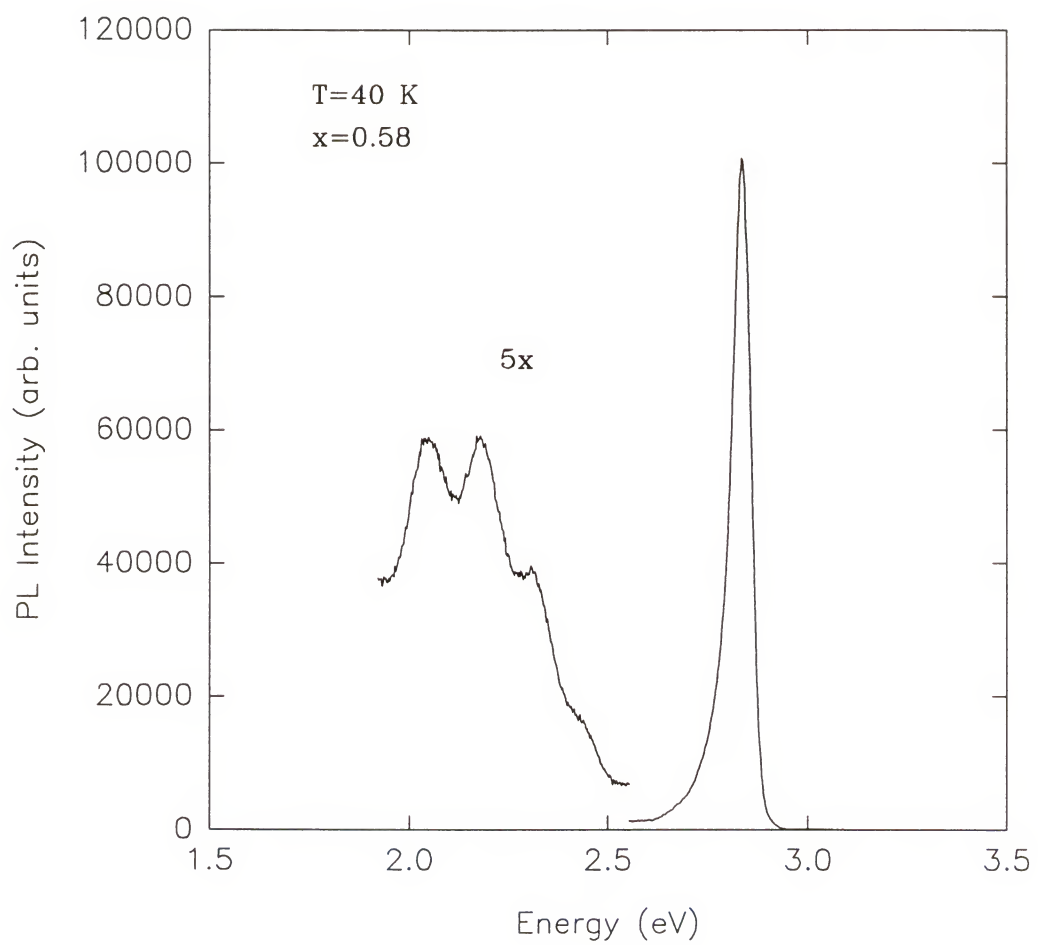


Figure 2-25. PL measurements of $Zn_{1-x}Cd_xS$ for solid composition of $x = 0.58$.

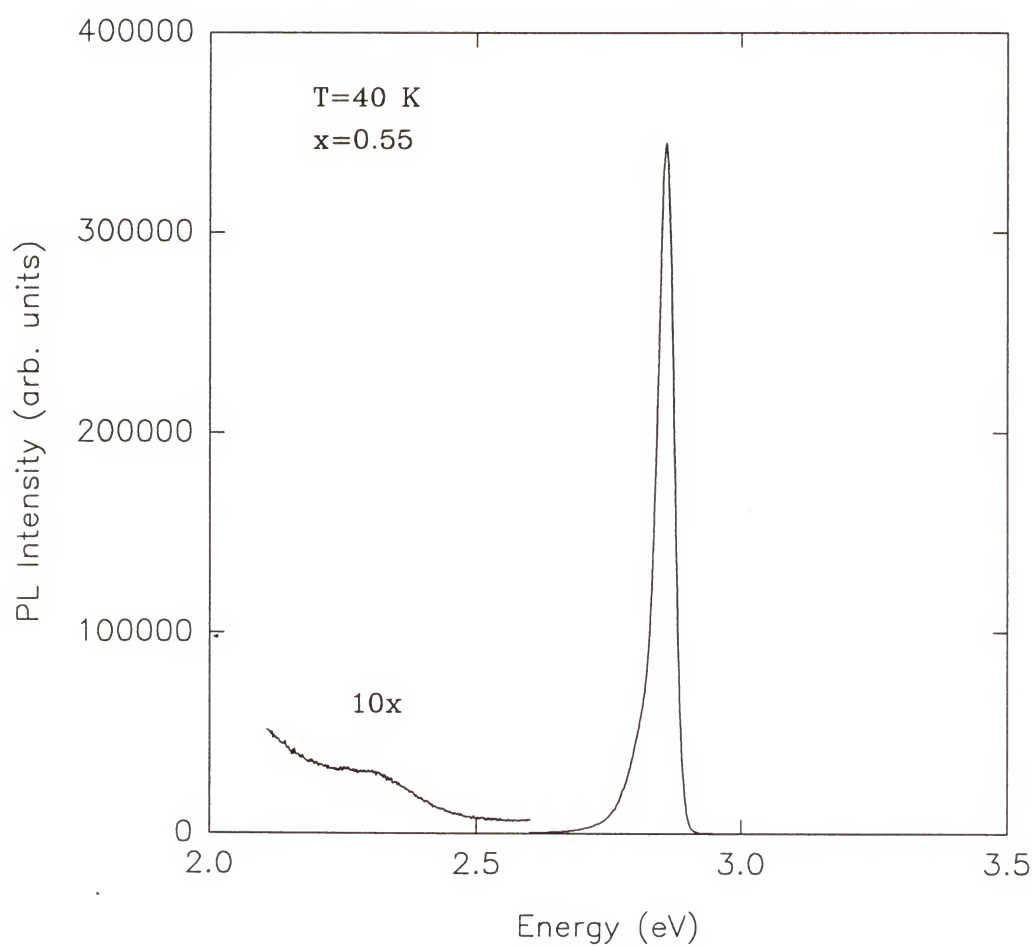


Figure 2-26. PL measurements of $Zn_{1-x}Cd_xS$ for solid composition $x = 0.55$.

although some have suggested free-to-acceptor (FA) [37] and donor-to-acceptor (DA) [38] transitions. There is also minimal deep level emissions at low temperature, an indication of relatively minor contamination. One report suggests that formation of deep luminescent centers arises mainly from incorporation of impurities or native defect-impurity complexes rather than through structural defects such as stacking faults, dislocations and twins [74]. One main reason for such broad optical peak widths is that the crystallinity of the epilayer is still poor as manifested by the large FWHM of the HRXRD peaks.

2.5 Summary

The optimization of ZnCdS growth on (100) and (111) orientation GaAs substrates is conducted by both the Taguchi and the standard method of varying one parameter while fixing the others. Upon investigation of growth temperature, VI/II ratio, and substrate orientation, statistical analysis indicates that only the growth temperature and substrate orientation made an impact on the crystalline quality of the epilayer. Changing the growth temperature from 300 to 550 °C decreases the FWHM of HRXRD peaks by 2601.9 arc-seconds and changing the substrate orientation from (100) 2° toward <110> to (111)A decreases the FWHM by 1259.5 arc-seconds. With further investigation, the ideal VI/II ratio is discovered to be convoluted with the growth temperature. ZnSe buffer layers, growth rate, and etchants are studied to estimate their impact on improving crystallinity. The use of a ZnSe buffer layer does not improve the crystallinity of the ZnCdS epilayers and, for (100) orientations, the crystallinity is significantly deteriorated. As expected,

lower growth rate improves crystalline perfection. Of the three etchants studied, only the ammonia hydroxide-based etchant consistently provides good quality ZnCdS epilayers regardless of the substrate orientation. Although ZnCdS growth on (111) substrates clearly surpasses that on (100) substrates, a summary of the ideal growth conditions are listed in Table 2-9 for both substrate orientations.

Table 2-9. Ideal Growth Conditions for (100) and (111) orientation GaAs substrates.

Growth Parameters	(100) Orientation GaAs Substrates	(111) Orientation GaAs Substrates
Temperature (° C)	550	550
VI/II	120	60
Pressure (Torr)	70	70
Growth Rate (μm/hr)	0.7	0.8
ZnSe buffer layer	no	no
Etchant	[20:7:100::NH ₄ OH:H ₂ O ₂ :H ₂ O]	[20:7:100::NH ₄ OH:H ₂ O ₂ :H ₂ O]
Ratio of gas inlet and MO inlet flow rates	7.2 to 8.6	7.2 to 8.6

The flow mechanics of the growth system is investigated by comparison with the results for simpler geometries. Although the Re and Ra numbers indicate laminar flow with no free convection, experimental data show vortices and recirculation exist as evident by the shape of the deposits downstream on the reactor walls. This is possibly produced by horizontal density variations and the 18° tilt of the susceptor/baffle assembly which forces gas flow upwards nearly perpendicular to the reactor wall. This flow instability is the main cause for non-uniform film thickness other than react depletion.

The general growth mechanisms have also been studied. The kinetics have been analyzed with a simple growth model proposed by Grove. The mass transfer limited

growth regime has been identified in the temperature range of 300 to 450 °C and the kinetically limited regime between 25 and 300 °C. The composition of $Zn_{1-x}C_xS$ at lattice matched conditions to GaAs is $x = 0.58$ with a zinc blende crystal structure. For compositions between $x = 0$ and $x = 0.67$, the $ZnCdS$ crystal structure is zinc blende, but from $x = 0.67$ to $x = 1.0$, the structure is a mixture of zinc blende and wurtzite. Typically the FWHM of HRXRD peaks of $ZnCdS$ grown on (111) substrates is 500 arc-seconds and that grown on (100) substrates is 2000 arc-seconds. This is mainly caused by the high degree of surface roughness in the epilayers. The composition of the solid phase tends to be Cd rich at low growth temperature. This may be caused by more efficient pyrolysis of the Cd precursor compared to the Zn precursor at low temperatures as well as higher sticking coefficients for Cd. The free energy to transform between zinc blende and wurtzite structures is small and stacking faults have been found on the (111) planes of zinc blende structures and (0001) planes of distorted wurtzite structures. These defects pervade throughout the epilayer even at lattice matched conditions to GaAs. From low temperature PL measurements, the $ZnCdS$ epilayers are free of deep level, optically active centers.

CHAPTER 3

PROPERTIES OF $Zn_{1-x}Cd_xS$ EPILAYERS ON GaAs

Optical, physical, and electrical properties of ZnCdS must be quantified to design and characterize optoelectronic devices. The two most vital optical properties are the bandgap energy and the complex refractive index (or equivalently the complex dielectric constant). Since the bandgap energy dictates the wavelength of the photoemission, its knowledge is essential for designing DH lasers and LEDs. The bandgap energy is also necessary for calculating valence and conduction band offsets. Both values will ultimately define the carrier confinement for injection luminescence.

The complex refractive index is critical for evaluating the degree of optical confinement and for computing many physical characteristics of the DH laser, including the active layer thickness and requirements for a suitable cladding layer. The absorption coefficient, the complex dielectric constant, and the complex refractive index are all interrelated through simple equations. Knowledge of either of the latter two constants completely describes the optical properties of a material.

One important physical property is the thermal expansion coefficient (TEC). Lattice and thermal mismatches are the two main sources of stress in heteroepitaxy. Lattice mismatch at a given temperature and composition is defined by the difference in interatomic spacing of the atoms between the epilayer and the substrate, and depends on the temperature and composition selected. The thermal mismatch is defined as the relative

change in the atomic spacing as the temperature varies for a fixed composition and depends upon the TEC of each respective material. Stress induced by these mismatches is often manifested in undesirable interfacial dislocations which are known to be nonradiative recombination centers [75]. The majority of stress can be avoided by adjusting the film composition to minimize the difference in lattice constants between the epilayer and the substrate. Unfortunately, thermal stress is usually present since the films are grown at a temperature different than room temperature.

The ability to change electrical properties through addition of intentional dopants is essential to fabrication of p-n junctions in carrier injection optoelectronic devices. The ideal dopant should be characterized by low diffusivity through the host material, low self-compensation, and high solubility. Many issues of low carrier concentration can be traced to inefficient dopant incorporation. This can be attributed to one or more factors. Low vapor pressure of some dopant precursors limits the partial pressure of the dopant in the reactor. The gas phase concentration of activated complexes can also be depleted by incomplete decomposition of dopant precursors or by parasitic gas phase reactions. At high growth temperature, surface migrating dopants can desorb due to low sticking coefficients and leave the growth surface dopant deficient.

3.1 Sample Preparation

ZnCdS is grown on (100) 2° toward the nearest <110> GaAs substrates by the low pressure MOVPE technique. The Zn and Cd mole fractions are 1.69×10^{-4} and 1.12×10^{-4} at lattice matched conditions, respectively. The composition is changed by fixing the mole

fraction of Cd and only varying the mole fraction of Zn. The H₂S mole fraction is adjusted to maintain a VI/II ratio of 120. The growth temperature is 550 °C to obtain the highest crystalline perfection. Prior to growth, the GaAs substrates are wet cleaned as specified in Section 2.2 of Chapter 2.

3.2 Bandgap Energy

3.2.1 Experiment

The bandgap energy of thin films grown on less absorbing materials are typically measured by absorption technique. With optical transmission measurements, incident radiation shines on the sample and the transmitted light is measured with varying wavelength. Almost all the light is transmitted through the sample at wavelengths with energies smaller than the bandgap energy, but is completely absorbed when the wavelength matches or exceeds that of the bandgap energy. This transitional wavelength (or equivalently energy) from transparency to absorption is a measure of the bandgap energy.

This technique, however, is unsuitable for epitaxial thin films grown on a more absorbing substrate as is the case for ZnCdS grown on GaAs. The incident light will be absorbed by the substrate before the transitional wavelength can be detected. In this situation, with a highly reflective substrate and transparent film, reflectivity measurements is more appropriate to determine bandgap energies and is commonly used to determine the film thickness of insulating materials on semiconductors and epitaxial layers.

Reflectivity measurements will produce interference oscillations at wavelengths with energies lower than the bandgap energy of the epilayer due to differences in refractive indices of the film and substrate. When the incident light energy matches or exceeds the bandgap energy of the epilayer, it will be absorbed and the oscillations will disappear. Similar to the absorption measurement, the transitional wavelength at which oscillations disappear is the measure of the epilayer bandgap energy.

The ZnCdS/GaAs sample is mounted on a holder so that it is standing freely. A monochromator acts as a tunable filter and is used to modulate the wavelength of the source radiation from a N₂ laser pumped tunable dye laser. The light enters the monochromator through a narrow entrance slit and the light rays are made parallel by a collimating lens. The desired range of wavelengths is selected by a grating before it is incident on the sample. The range of frequencies investigated is 15,000 to 45,000 cm⁻¹. A spectrophotometer is used to measure the reflected light from the sample at a 5° incidence angle normal to the surface.

3.2.2 Results

For the first time, room temperature bandgap energies have been measured by reflectivity measurements for the entire compositional range of ZnCdS as shown in Figure 3-1. The graph shows a smooth, quadratic polynomial fit based on error minimization with a correlation coefficient of 0.91 for the dependence of the bandgap energy with

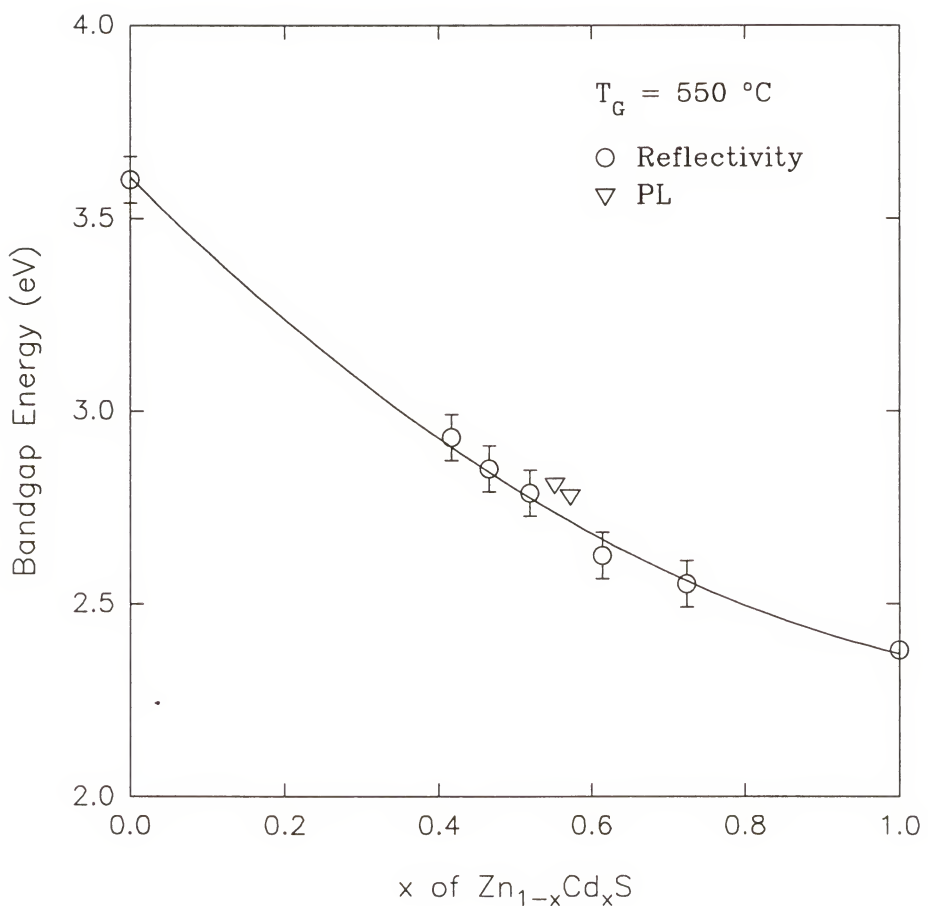


Figure 3-1. Variations of room temperature bandgap energy of $\text{Zn}_{1-x}\text{Cd}_x\text{S}$ with solid composition.

varying composition of $Zn_{1-x}Cd_xS$. This relationship is best described by the empirical expression:

$$E_g(x) = E_g(ZnS) - 2.00x + 0.76x^2 \quad (3-1)$$

where E_g is the bandgap energy for varying x composition. The bandgap energies are assumed to be 2.38 and 3.60 eV for CdS and ZnS, respectively [76]. There is a slight concave bowing typical of other II-VI systems with a bowing parameter of 0.76 and a value of 1.22 if plotted with the abscissa as $Zn_xCd_{1-x}S$. Hwok [77] indicate that for the solid composition, $Zn_xCd_{1-x}S$, the bowing parameter is 0.3, while Kaneco et al. [78] cite the bowing parameter to be 0.61. The reasons for such widely different values are unclear. One possible explanation is that the bandgap energy for the binary compounds, ZnS and CdS, are taken to be different for each of the literature citations. Hwok uses values of 2.4 and 3.6 eV for the bandgap energies of CdS and ZnS, respectively. Kaneco et al. use values of 2.42 and 3.66 eV, respectively. Although these differences would alter the bowing parameter slightly, they do not completely explain the large discrepancies.

Figure 3-2 shows a typical reflectivity measurement of a sample whose composition is $x = 0.55$ for Cd and whose thickness is 0.86 μm . The transitional wavelength is 454 ± 10 nm which corresponds to a bandgap energy of 2.73 ± 0.06 eV.

The maximum peak for the room temperature PL measurements of $x = 0.55$ and $x = 0.58$ compare quite well with the measured bandgap energies as shown in Figure 3-3 and Figure 3-4, respectively. For the nearly lattice matched sample with a Cd composition of $x = 0.58$, reflectivity measurements reveal the room temperature bandgap energy to be 2.71 eV while the peak energy from PL is 2.78 eV. For $x = 0.55$, the reflectivity

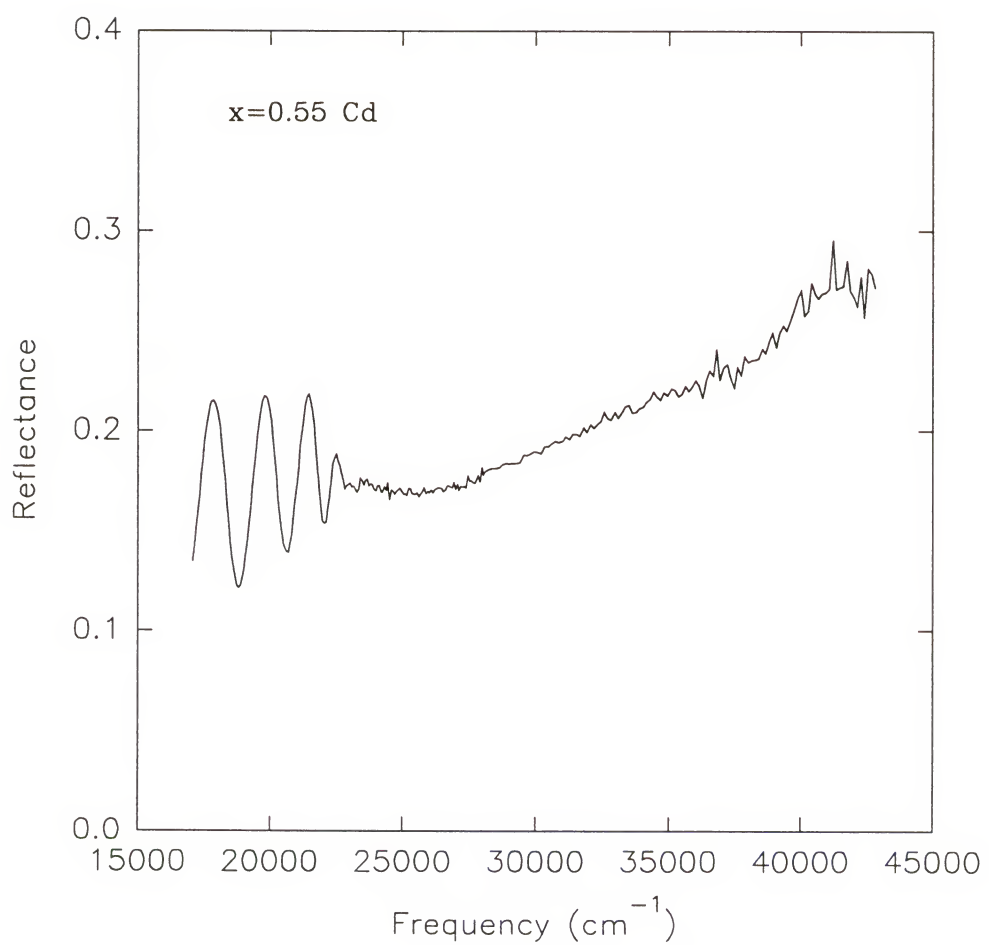


Figure 3-2. Reflectivity measurement of $x = 0.55$ Cd composition.

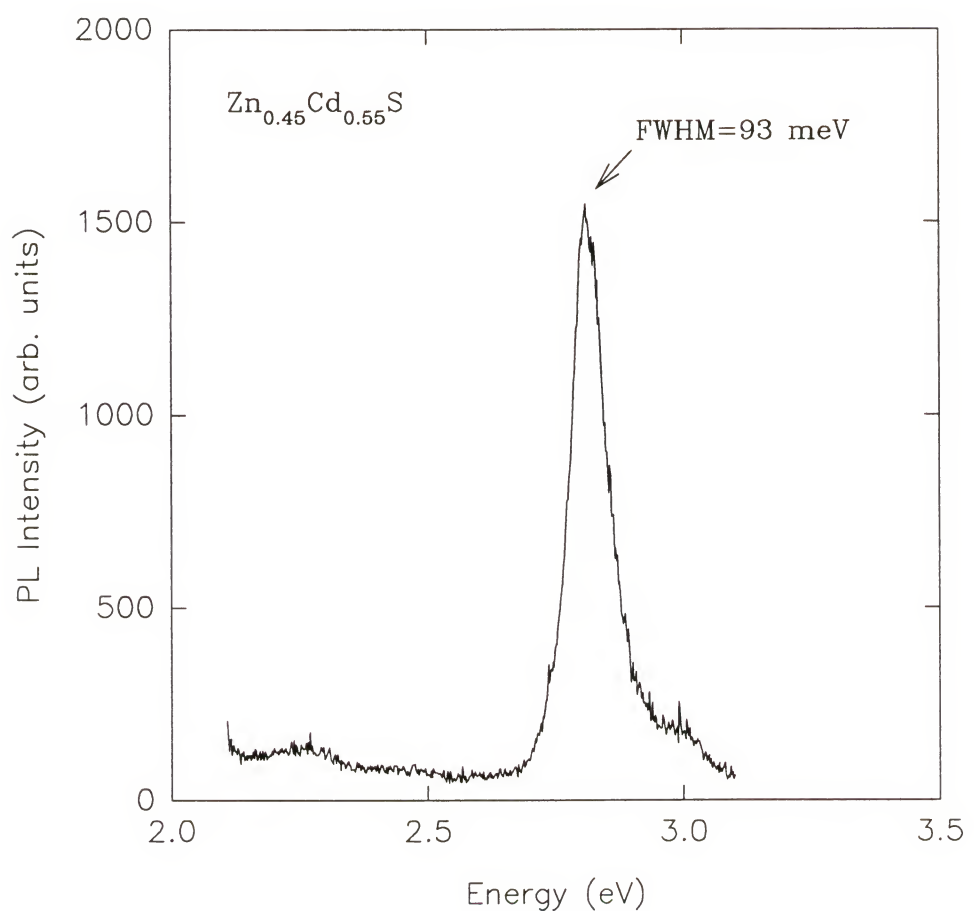


Figure 3-3. Room temperature PL measurement of $x = 0.55$.

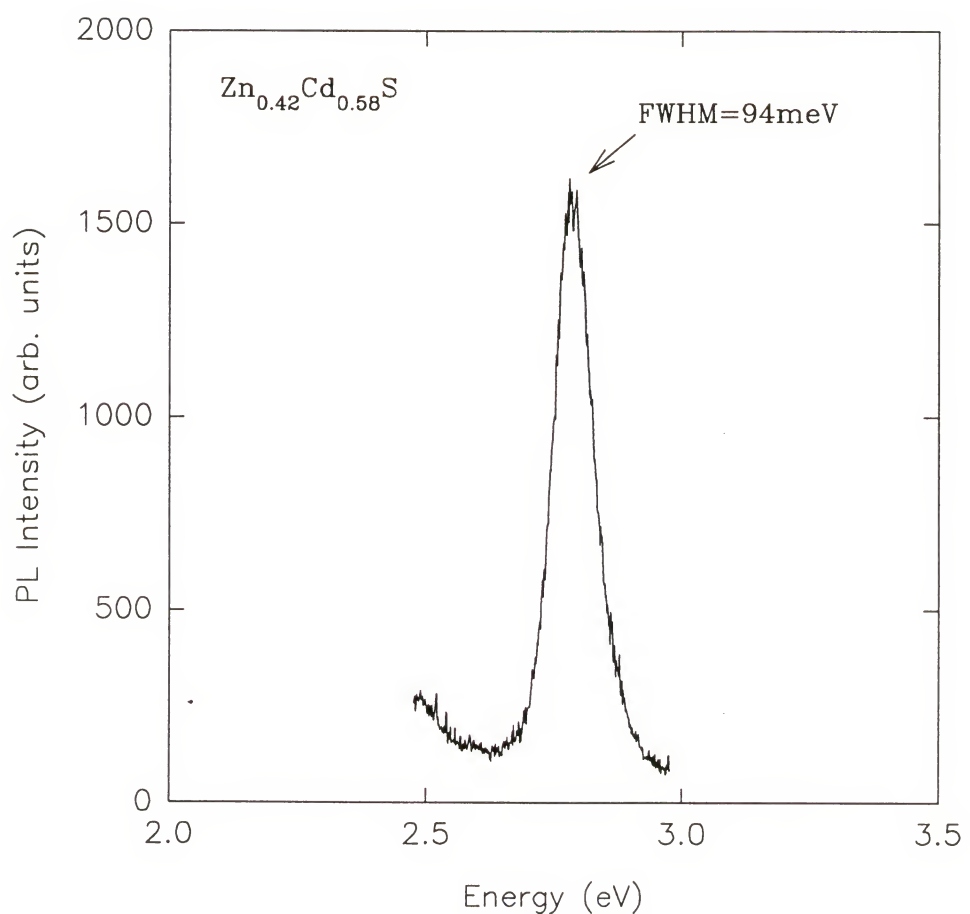


Figure 3-4. Room temperature PL measurement of $x = 0.58$.

measurements reveal the room temperature bandgap energy to be 2.73 while the maximum peak energy from the PL reveals the bandgap energy to be 2.81 eV. All the bandgap energies calculated from PL are just outside of measurement error of reflectivity results. The difference may be attributed to equating the maximum peak from PL to the bandgap energy which is not completely accurate. Under these circumstances, the results from PL and reflectivity may not be statistically different.

3.3 Complex Refractive Index

3.3.1 Experiment

The optical constants of a material must be known to adequately analyze and design discrete DH structures. Although some data do exist for various II-VI semiconductors, none exist for the pseudobinary solid solution, $Zn_{1-x}Cd_xS$. A traditional technique for measuring refractive index is the prism method whereby the angle of refraction is directly measured [79] and the method of minimum deviation was utilized [80]. This technique, however, has a distinct disadvantage. Bulk crystals are needed to make the prisms and this excludes the possibility of analyzing thin films grown on substrates. With development of new materials using advanced growth techniques, the analysis of thin films has become more important. Another significant drawback is that determination of the refractive index near or above the bandgap energy is impossible due to absorption. Since considerable interest in optical data lies near the bandgap energy, a different technique is needed.

Another common method is to measure reflectance/transmission spectra and apply the Kramers-Kronig (K-K) analysis to extract the optical data. This technique, however, is extremely surface sensitive and requires a clean and optically flat surface to obtain accurate results. Unfortunately, this condition can not always be satisfied. Also, in applying the K-K analysis to the data, accuracy of the computed optical properties depends on the bandwidth of the spectroscopic data, thus requiring measurements over the broadest wavelength range as reasonably allowed. This can also be impractical and extremely time consuming. The best technique is ellipsometry due to its higher speed and accuracy. Since ellipsometry is based on the state of polarization of polarized light, the error is minimized.

Ellipsometry was introduced in the 1800s, but was not extensively used since data acquisition and analysis were extremely tedious and slow [81]. With the introduction of high speed computers, however, this barrier was removed. Although ellipsometry can be used to determine the composition of multicomponent thin films, it is most often used to determine film thicknesses and the optical constants of bulk materials or thin films grown on substrates [82-84]. Most of the applications involve studying dielectric materials grown on silicon (e.g., oxide and nitride films).

In this technique, a highly collimated, monochromatic and polarized radiation source strikes the surface and the polarized state of the reflected light is analyzed with a second polarizer. To ensure accuracy and sensitivity, the angle of the light perpendicular to the surface (angle of incidence) is oblique, ranging from 69° to 75° . Ellipsometry is a powerful, simple, and nondestructive technique for measuring film thicknesses as

compared to other techniques such as SEM measurements of cleaved cross sections. It can also operate under atmospheric conditions while other techniques for measuring film composition require vacuum (e.g., Auger, SIMS, and EPMA).

Two samples with Cd composition of $x = 0.58$ and $x = 0.55$ were analyzed with the J. A. Woollam Co. variable angle of incidence spectroscopic ellipsometer (VASE). The samples exhibited several visible interference fringes indicative of thickness non-uniformity across the entire sample. This thickness variation will diminish the accuracy of the results. The calculation of the ZnCdS complex refractive indices is based on a double film model with ambient interaction. Subscripts 1, 2, and 3 refer to the ambient, ZnCdS epilayer, and the GaAs substrate, respectively. Superscripts p and s define orientations parallel and perpendicular to the plane of incidence. There are eight equations that describe the reflectance [85]:

$$\tan \Psi \exp(i\Delta) = \frac{R^p}{R^s} \quad (3-2)$$

$$R^p = \frac{r_{12}^p + r_{23}^p \exp(-i2\beta)}{1 + r_{12}^p r_{23}^p \exp(-i2\beta)} \quad (3-3)$$

$$R^s = \frac{r_{12}^s + r_{23}^s \exp(-i2\beta)}{1 + r_{12}^s r_{23}^s \exp(-i2\beta)} \quad (3-4)$$

$$r_{12}^p = \frac{N_2 \cos \phi_1 - N_1 \cos \phi_2}{N_2 \cos \phi_1 + N_1 \cos \phi_2} \quad (3-5)$$

$$r_{12}^s = \frac{N_1 \cos \phi_1 - N_2 \cos \phi_2}{N_1 \cos \phi_1 + N_2 \cos \phi_2} \quad (3-6)$$

$$r_{23}^p = \frac{N_3 \cos \phi_2 - N_2 \cos \phi_3}{N_3 \cos \phi_2 + N_2 \cos \phi_3} \quad (3-7)$$

$$r_{23}^s = \frac{N_2 \cos \phi_2 - N_3 \cos \phi_3}{N_2 \cos \phi_2 + N_3 \cos \phi_3} \quad (3-8)$$

$$\beta = 2\pi \left(\frac{d}{\lambda} \right) N_2 \cos \phi_2 \quad (3-9)$$

where Δ is the measured change in phase difference that occurs upon reflection, Ψ is defined as the angle whose tangent is the ratio of the magnitudes of the total reflection coefficients, R_i is the total reflection coefficient, d is the ZnCdS layer thickness, λ is the wavelength of incident light, N_i is the complex refractive index, r_{ij} is the Fresnel reflection coefficient of the ij interface, and ϕ_i is the angle of incidence. All the variables are known parameters from literature except for nine: ϕ_2 , ϕ_3 , Δ , Ψ , d , n_2 (real refractive index), k_2 (extinction coefficient), n_3 , and k_3 . The system of eight nonlinear equations is under specified with nine unknown variables. However, Δ and Ψ can be measured for two different ϕ_1 to completely specify the system.

3.3.2 Results

The measured Δ and Ψ values of a film with $x = 0.58$ Cd composition are illustrated in Figures 3-5 and 3-6, respectively. These same quantities are shown for a film with $x = 0.55$ Cd composition in Figures 3-7 and 3-8, respectively. The measured Δ and Ψ values are fitted for the film thickness and degree of thickness non-uniformity. They are then fixed and the optical constants, n and k , of the film are fitted based on least squares

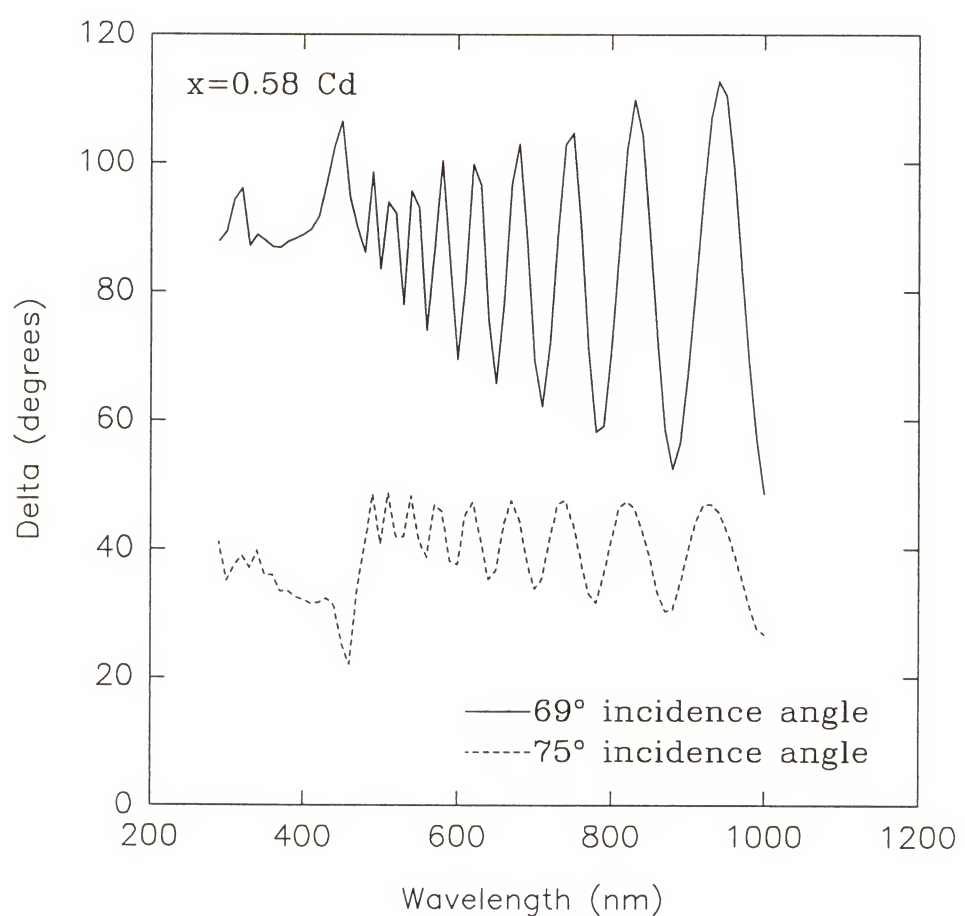


Figure 3-5. Δ values for a film with $x = 0.58$ Cd composition.

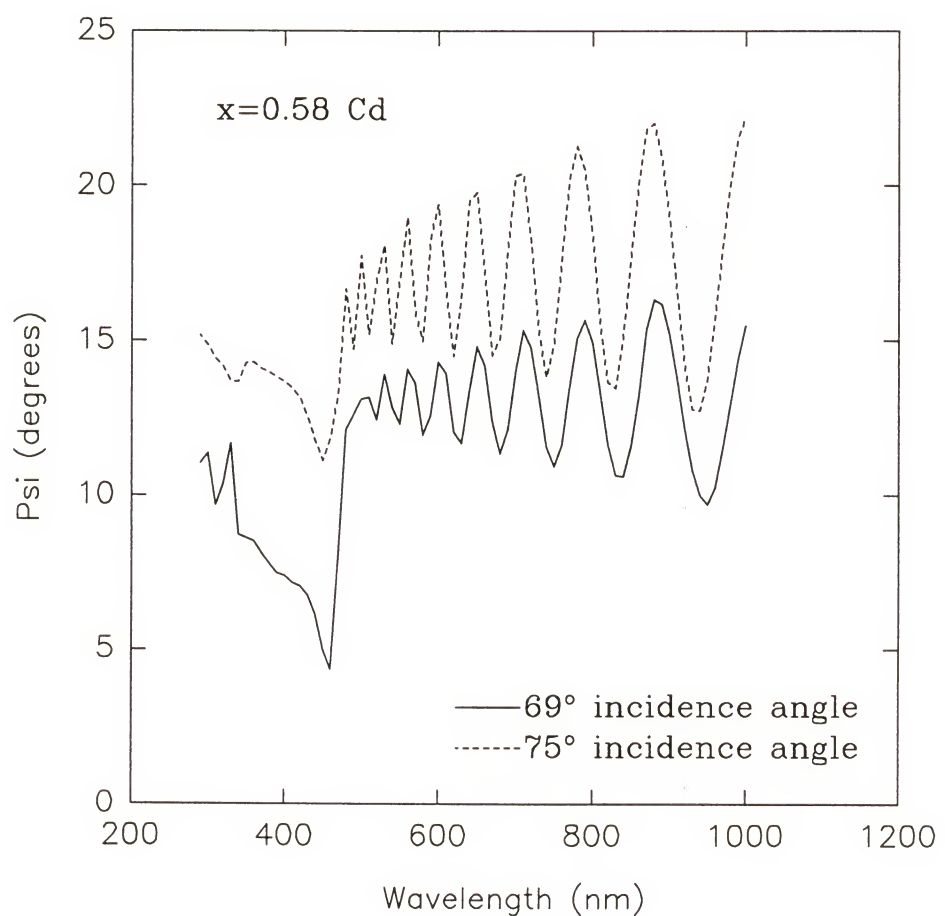


Figure 3-6. Ψ values for a film with $x = 0.58$ Cd composition.

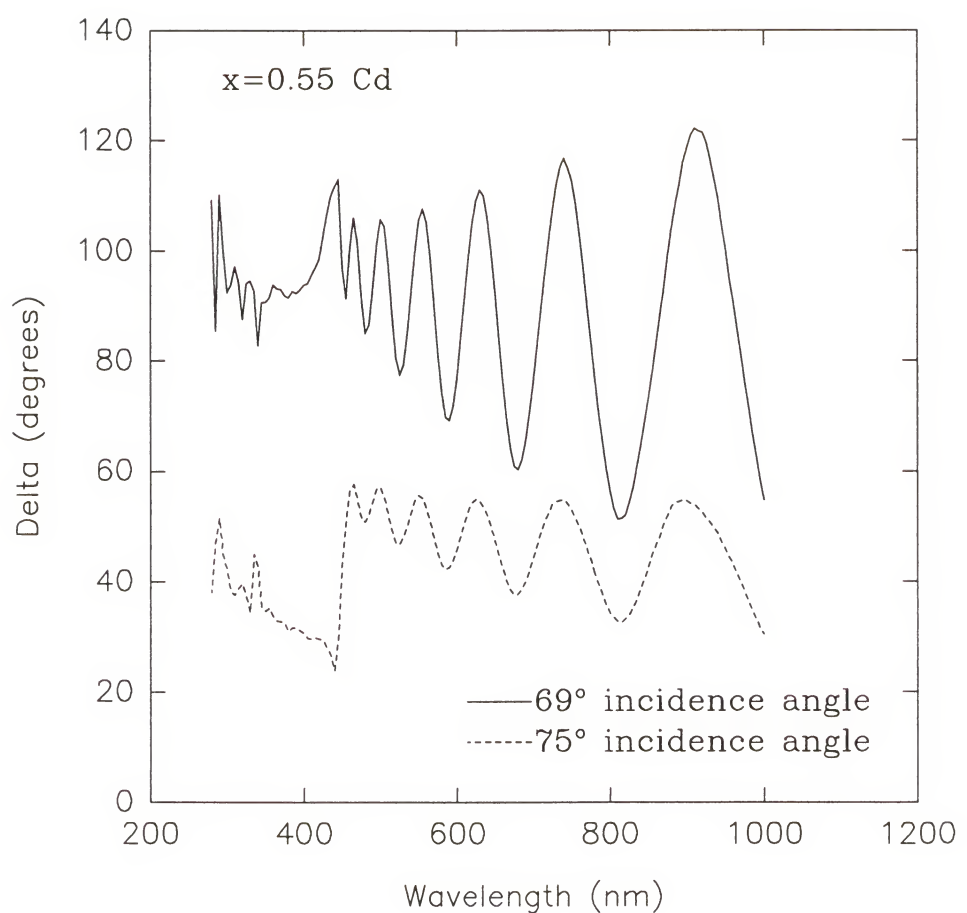


Figure 3-7. Δ values for a film with $x = 0.55$ Cd composition.

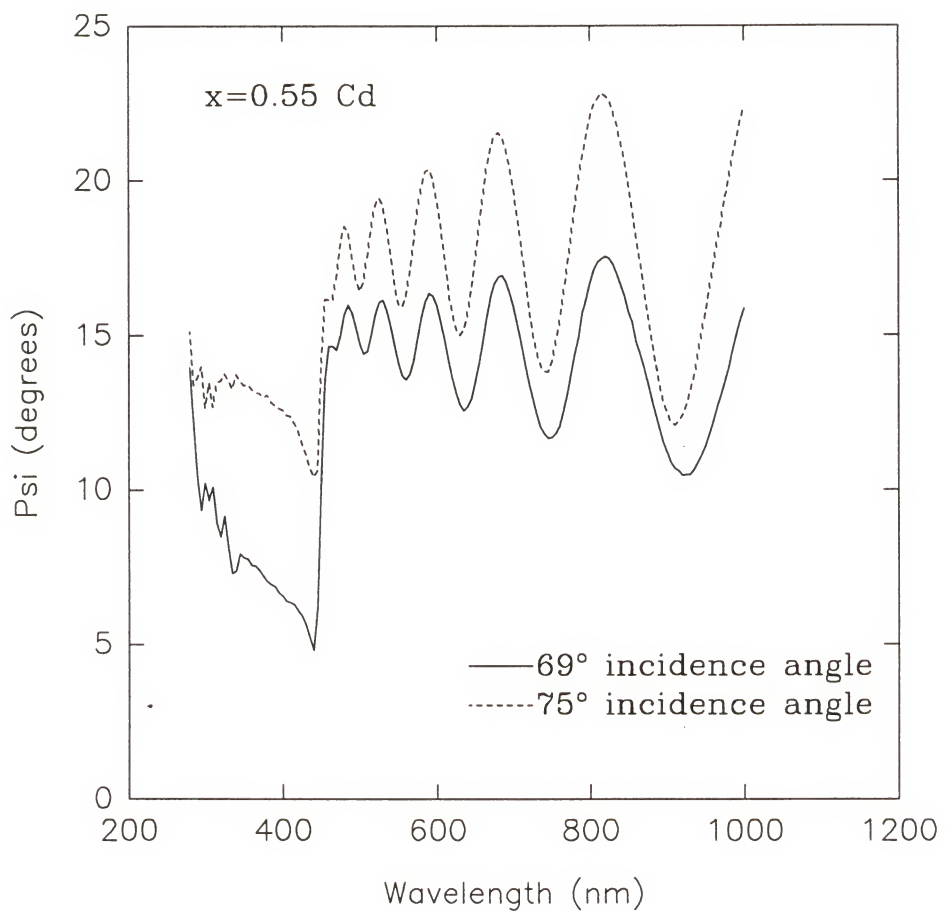


Figure 3-8. Ψ values for a film with $x = 0.55$ Cd composition.

method over the entire spectral range assuming the Cauchy dispersion relationships are valid:

$$n(\lambda) = A + \frac{B}{\lambda^2} + \frac{C}{\lambda^4} \quad (3-10)$$

$$k(\lambda) = D + \frac{E}{\lambda^2} + \frac{F}{\lambda^4} \quad (3-11)$$

where λ is the wavelength and A, B, C, D, E, and F are the fitting parameters.

The Cauchy parameters were fitted over the spectral range of 600 to 1000 nm. Using this model, the best fit to the data yielded film thicknesses for the $Zn_{0.45}Cd_{0.55}S$ and $Zn_{0.42}Cd_{0.58}S$ layers to be 858.9 and 1567.0 nm, respectively. The thickness variation for $x = 0.55$ and $x = 0.58$ are 9.96% and 5.98%, respectively. The thickness variation is determined from the best fit and describes the deviation from the value given in the model across the sampling area of the probing light beam which is about three mm in diameter. These film thickness calculations compare well to the results of the model presented in Section 2.4.2 in Chapter 2.

There is considerable uncertainty in the calculation of these optical constants due to the nonuniformity in the film thickness. In analyzing the data, any ray undergoing multiple reflections in the film is assumed to do so between interfaces that are parallel. This assumption works well for films with a small degree of nonuniformity (a few percent), but begins to fail when the thickness variation is large, particularly for thick (greater than 100 nm) films.

In manufacturing high quality DH lasers, the extent of optical confinement is critical for continuous wave operation. Confinement characteristics are related to the difference in refractive index between the guiding/cladding layers and the active layer. Although a minimum value for the difference can not be stated for effective confinement, it is instructive to look at other systems. In the AlGaAs/GaAs system for example, the refractive index of the active layer should be about 0.2 larger than that of the confining layers. The refractive index at 460 nm (blue light) of ZnSe, $Zn_{0.45}Cd_{0.55}dS$ and $Zn_{0.42}Cd_{0.58}S$ are 2.9, 2.78, and 2.79, respectively. For a potential ZnSe/ZnCdS DH system, ZnSe is the active layer while the ZnCdS serves as the confining layer material. The true refractive index can change with doping and the optical confinement layers are doped in DH structures. Again, using the GaAs system to determine a trend, it has been established that the refractive index of GaAs near the bandgap energy decreases with increasing dopant concentration for both p and n type material [86]. If this trend holds for the II-VI systems, the optical confinement would be enhanced for the ZnCdS/ZnSe/ZnCdS DH system. Although theoretical calculations can be performed, they are dependent on measured absorption coefficients and these are usually inaccurate [87-88] and, thus, direct measurements are usually required. It may be required to further decrease the index of refraction by the addition of another element (e.g., Mg) to the Zn-Cd-S system while adjusting the composition to maintain lattice matching conditions.

The values of n and k are plotted as a function of the wavelength in Figure 3-9 and 3-10 for samples with $x = 0.55$ and $x = 0.58$ Cd composition, respectively. Region I is characterized by strong absorption with possibility of reflectivity. The high values of n

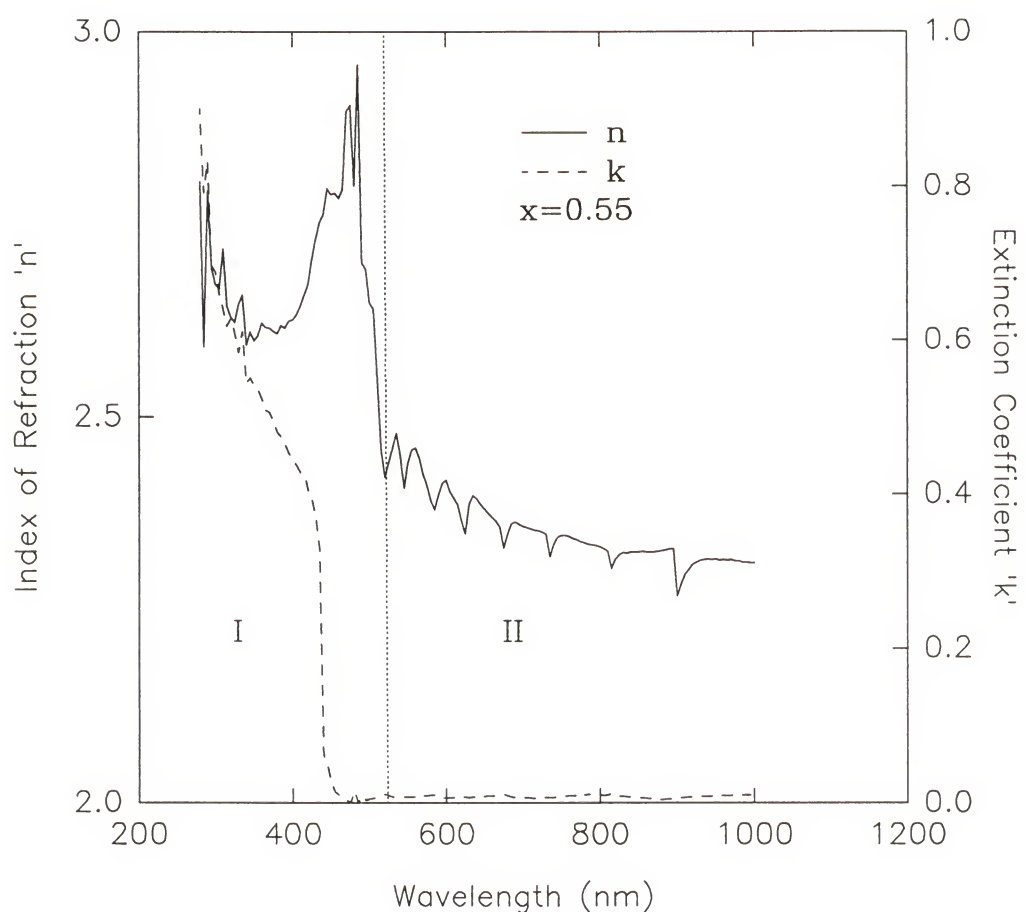


Figure 3-9. Refractive index values (n and k) for a film with $x = 0.55$ Cd composition.

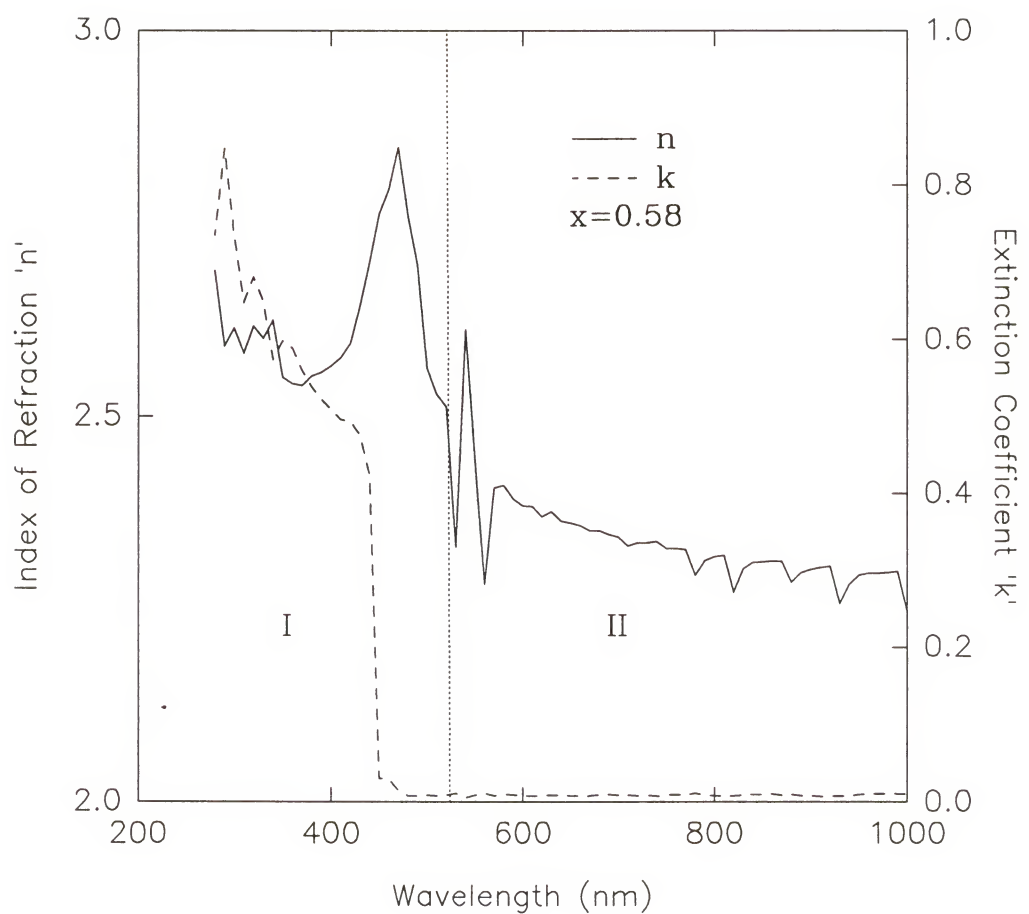


Figure 3-10. Refractive index values (n and k) for a film with $x = 0.58$ Cd composition.

and k indicate reflectivity, but the non-reflected portion of light is completely absorbed in the film. Region II is shown to have high transparency, no absorption and slight reflectivity. The reflectivity occurs from the induced polarization current corresponding to the outer valence electrons oscillating out of phase with the incident light. As the incident beam interferes with the reradiated light from the valence electrons, significant reflectivity occurs.

The real refractive index and the extinction coefficient are related to the real (ϵ_1) and imaginary (ϵ_2) components of the complex dielectric constant through the following two expressions:

$$\epsilon_1 = n^2 - k^2 \quad (3-12)$$

$$\epsilon_2 = 2nk \quad (3-13)$$

The absorption coefficient (α) is related to the extinction coefficient by the following simple expression:

$$\alpha = \frac{4\pi k}{\lambda} \quad (3-14)$$

where λ is the wavelength. For completeness, the complex dielectric constant and absorption coefficient are shown in Figures 3-11 through 3-14 for each composition.

3.4 Thermal Expansion Coefficient

Once a new material system has demonstrated potential for a particular device application, reliability issues become a concern. The lifetime and efficiency of

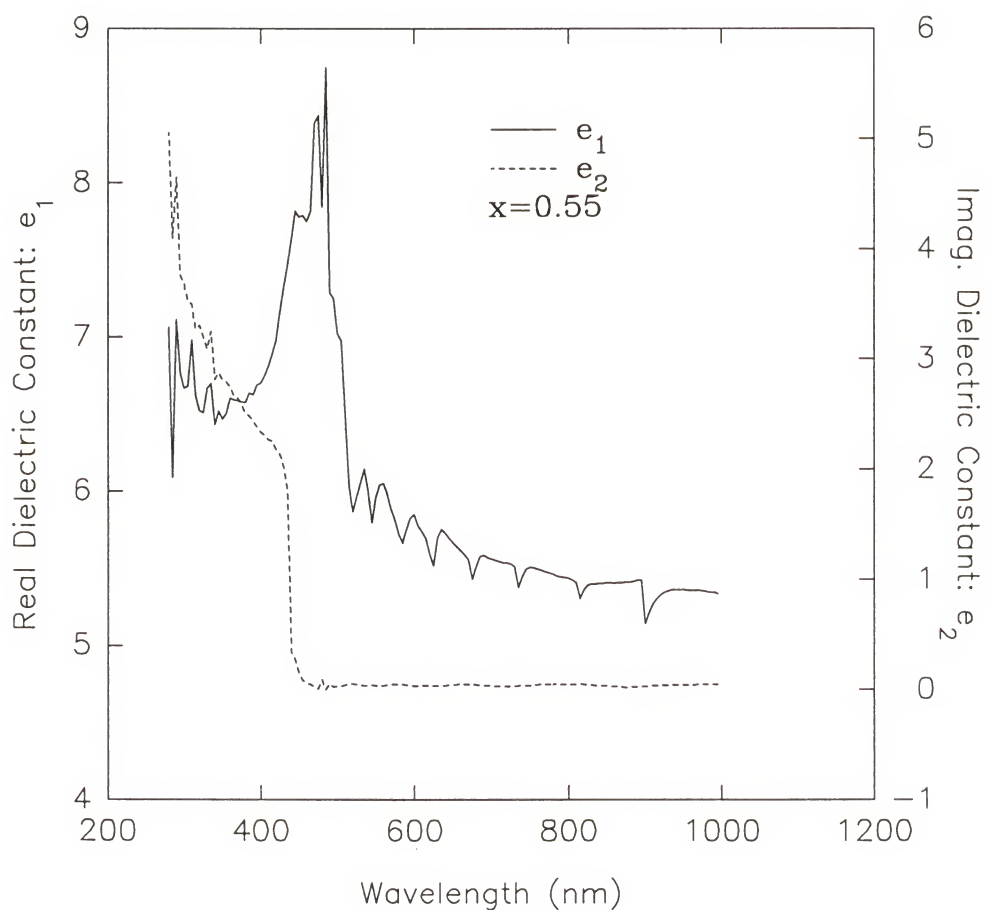


Figure 3-11. Dielectric constants (ϵ_1 and ϵ_2) for a film with $x = 0.55$ Cd composition.

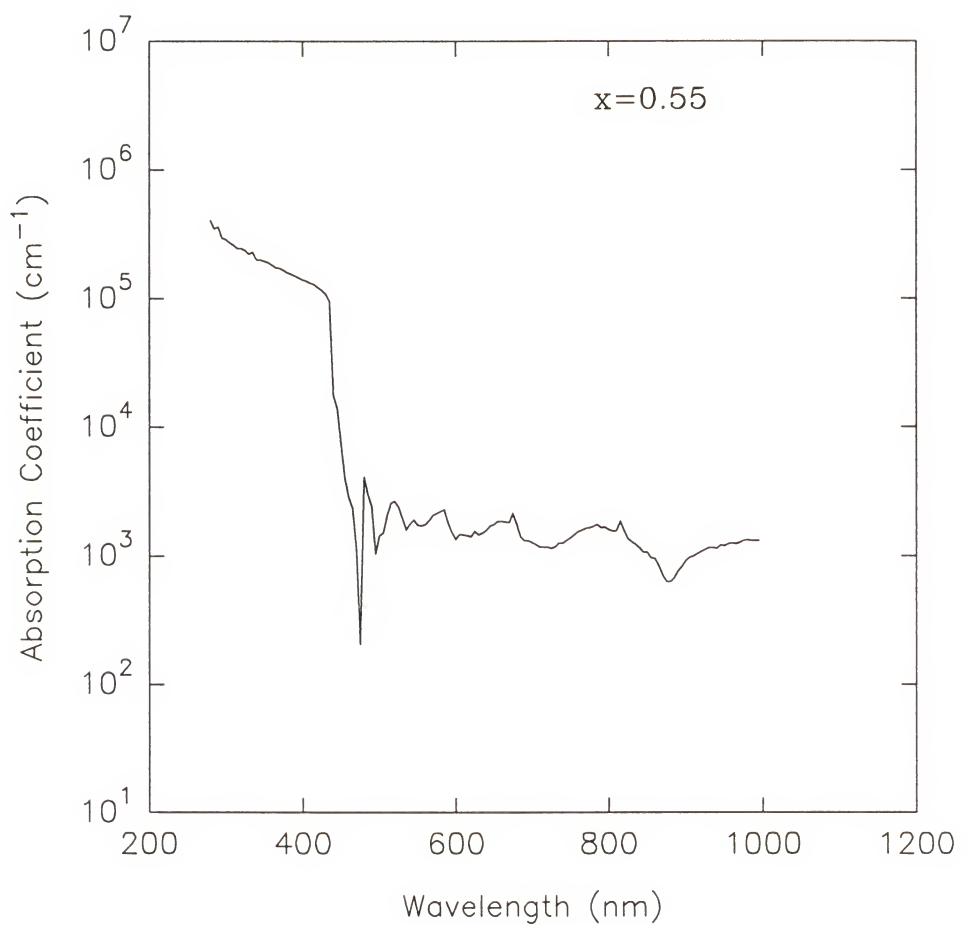


Figure 3-12. Absorption coefficient (α) for a film with $x = 0.55$ Cd composition.

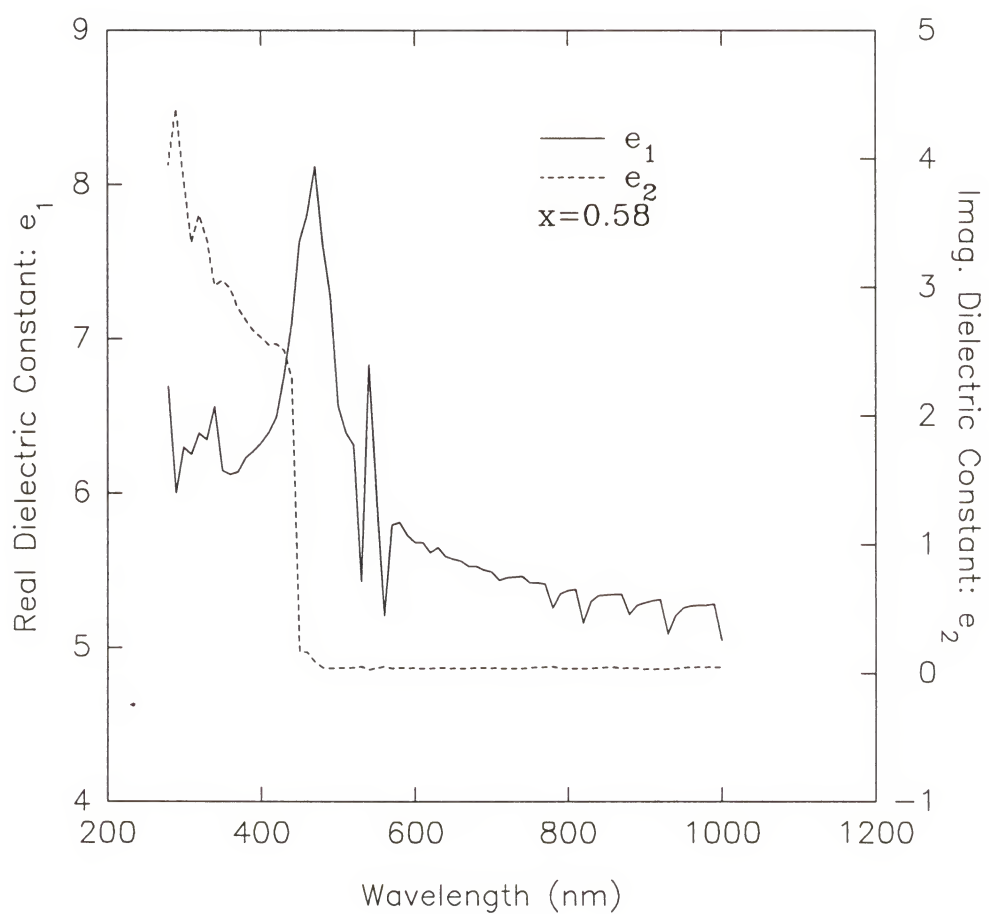


Figure 3-13. Dielectric constants (ϵ_1 and ϵ_2) for a film with $x = 0.58$ Cd composition.

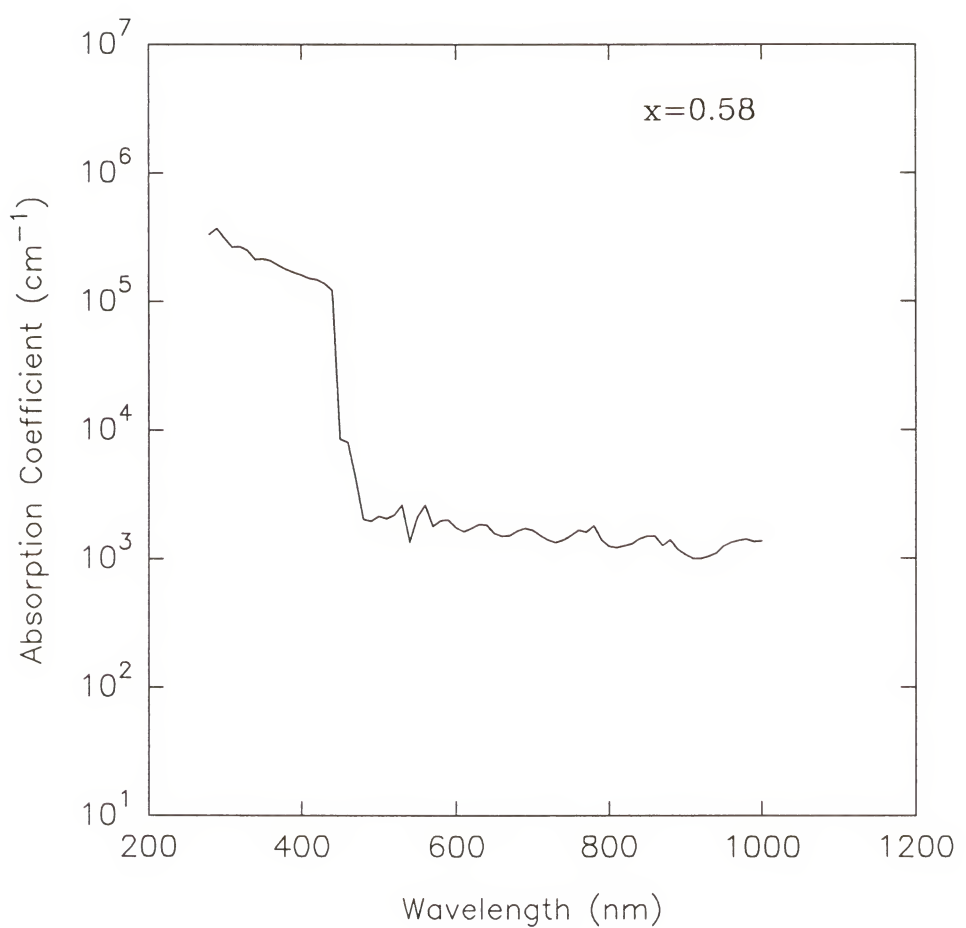


Figure 3-14. Absorption coefficient (α) for a film with $x = 0.58$ Cd composition.

optoelectronic devices depend strongly on the crystallinity of the epilayer, and hence, the substrate since extended defects can generate nonradiative recombination centers. In general, the growth of high quality, low extended defect density epitaxial films of electronic materials is affected by the quality of the growth surface, and is predicated upon its cleanliness and crystalline perfection. The density and mobility of extended defects during operation determine the capabilities and limitations of devices [89]. Although reliability studies on optoelectronic devices based specifically on ZnCdS have not yet been reported, it is expected to be a major concern for blue-light emitting devices, since II-VI materials have relatively low yield strengths and highly mobile dislocations easily form. As a result, reliability is an issue with II-VI materials and LEDs and laser diodes manufactured from these materials often are plagued with short life times. LEDs and laser devices based on ZnSe and ZnSSe are no exceptions [90-93].

One of the major sources of extended defects is interfacial strain between the epilayer and the substrate. In reference to room temperature, the source of the strain is traced to two factors: lattice mismatch between the substrate and film and thermal mismatch due to growth at elevated temperatures. Lattice mismatch occurs when the room temperature lattice constants of the epilayer and the substrate are not equal and the misaligned interfacial bonds are forced from their relaxed position, thereby, producing strain. The lattice mismatch with the GaAs substrate, however, can be accommodated by adjusting the composition in the pseudobinary solid solution $Zn_{1-x}Cd_xS$ on GaAs. Since the thermal expansion coefficients (TECs) of the film material and substrate are in all likelihood different, processing at an elevated temperature necessarily introduces strain.

The degree of compositional freedom coupled with TEC mismatches, poses the interesting problem of strain minimization with two different solutions. One approach suggests that the epilayer should be lattice-matched to the substrate at growth conditions where the thermal energy is greater and allow the thermal strain to be introduced during cooling. The other approach is to account for the thermal mismatch during cooling to yield lattice-matching at room temperature since the device operates at room temperature. Of course, the optimal solution may be a compromise between these two approaches. Strain caused by lattice mismatch can be anisotropic and calculations for III-V semiconductors have been reported [94-95]. Unfortunately, no study has been reported to determine these values for the ZnCdS system.

3.4.1 Experiment

There are two techniques for the absolute measurement of the linear TEC: optical [96-99] and capacitance [100]. Optical techniques have the advantage of requiring small samples and can be used for a large range of materials and temperature, while capacitance techniques have the advantage of high sensitivity. In this study, the TECs will be determined from lattice constants measured by HRXRD as a function of temperature.

The film compositions were determined by electron probe microanalysis (EPMA) using ZnS and CdS as the binary standards. A sample heating stage that was attached to the diffractometer was used to measure lattice parameters in the temperature range 25 °C to 250 °C in small increments. HRXRD was used to measure the lattice parameter perpendicular to the growth surface along the <004> direction. The temperature is

regulated by an Omega model W-CN76000 temperature controller whose accuracy is within ± 2.0 °C.

The lattice parameters were measured using Bond's method [101] to ensure high accuracy. Thus, every reflection is taken twice, once with the incident and reflected beams in one position and then another with the beams reversed by rotation of the stage by 180 degrees. The TEC of an epilayer is determined based upon the changes in the lattice parameter for given changes in temperature:

$$\text{TEC} = \frac{a_1 - a_2}{(0.5)(t_2 - t_1)(a_1 + a_2)} \quad (3-15)$$

where a_1 and a_2 are lattice parameters of the film at t_1 and t_2 temperatures, respectively.

3.4.2 Results

The lattice mismatches are shown in Table 3-1 as $\Delta a(\perp)/a$ values at temperatures of 25 and 200 °C for Cd compositions of 0.0, 0.17, 0.49, and 1.0. As expected the lattice mismatch decreases in the perpendicular direction to the substrate face along the <004> direction for the Zn-rich composition upon increasing temperature.

Table 3-1. Lattice mismatch values for various compositions and temperatures.

Temperature (°C)	$\Delta a(\perp)/a_{\text{GaAs}}$ (ppm)			
	$x = 0$ (ZnS)	$x = 0.17$	$x = 0.49$	$x = 1.0$ (CdS)
25	44,893	30,035	6104	139,500
200	43,531	28,090	5060	140,667

The TECs of the samples at various compositions as a function of temperature are shown in Figure 3-15. The graph does not show a linear relationship between the composition and the TEC. In the Cd-rich region, the TEC is nearly constant for Cd compositions $\geq x = 0.4$ and in the Zn-rich region, there is a sharp increase in the measured TEC.

For comparison purposes, the TECs of ZnS, CdS and GaAs are shown in Table 3-2 in a temperature range of 25 to 800 °C [102]. The results are in agreement with the TEC values of this study for the constituent binary compounds, ZnS and CdS.

Table 3-2. TECs of ZnS, CdS, and GaAs.

Material	TEC (cubic)	TEC (wurtzite: $\parallel c$)	TEC (wurtzite: $\perp c$)
ZnS	$6.5 \text{ to } 6.8 \times 10^{-6}$	4.5×10^{-6}	$5.9 \text{ to } 6.5 \times 10^{-6}$
CdS	6×10^{-6}	2.5×10^{-6}	5×10^{-6}
GaAs	6.72×10^{-6}	NA	NA

Figures 3-16 and 3-17 show the change in lattice constants as a function of temperature for films with a Cd composition of $x = 0.58$ and 0.55 , respectively. From this data, it is clear that the GaAs substrate expands more upon increasing temperature than the ZnCdS epilayer. As a result, an epilayer grown at lattice matched composition at growth temperature will be under compressive strain upon cooling to room temperature. As the film composition is shifted to Cd-rich compositions relative to the lattice matched composition of $x = 0.58$, the epilayer will remain under compressive strain since increased Cd content compositionally lowers the lattice constant., although the biggest cause of stress will be due to lattice mismatches and not different thermal expansion coefficients. For composition rich in Zn, the epilayer will still remain under compressive strain until the

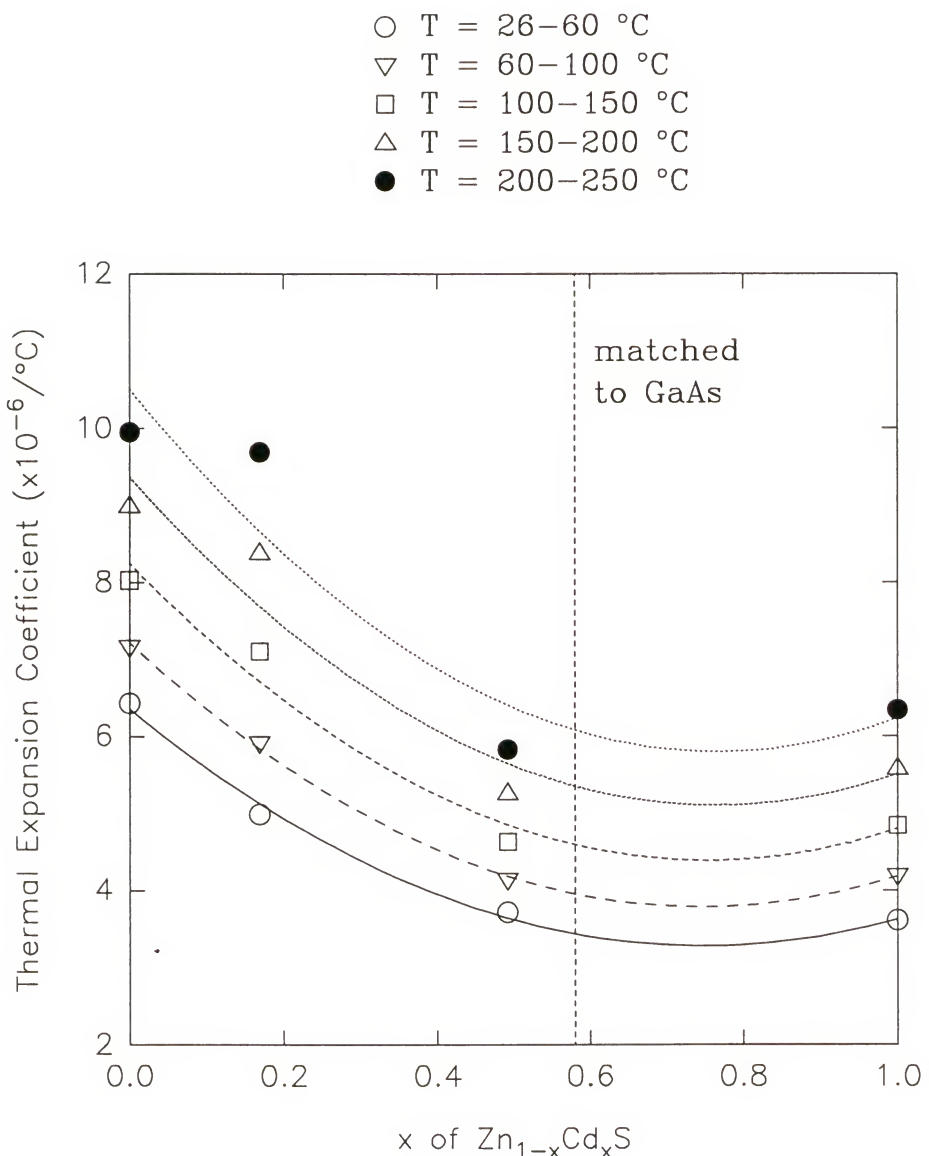


Figure 3-15. TECs at various composition and temperature.

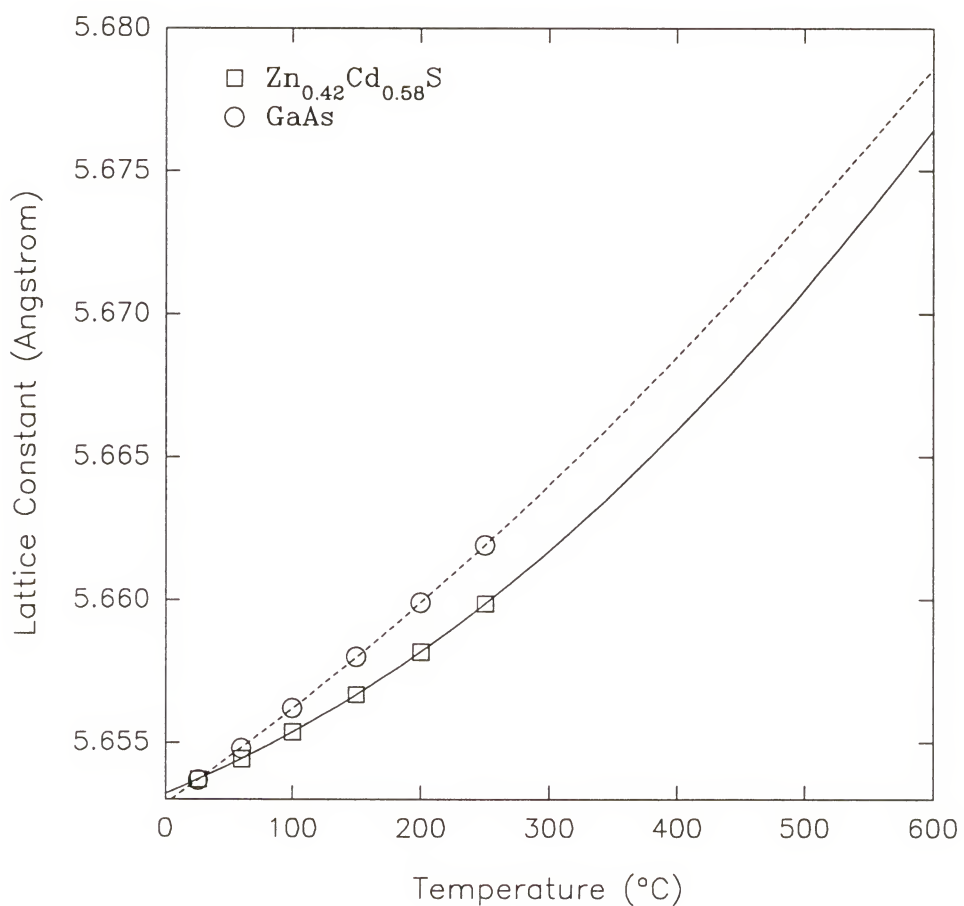


Figure 3-16. Variations of lattice constants with temperature for $\text{Zn}_{1-x}\text{Cd}_x\text{S}$ ($x = 0.58$) and GaAs.

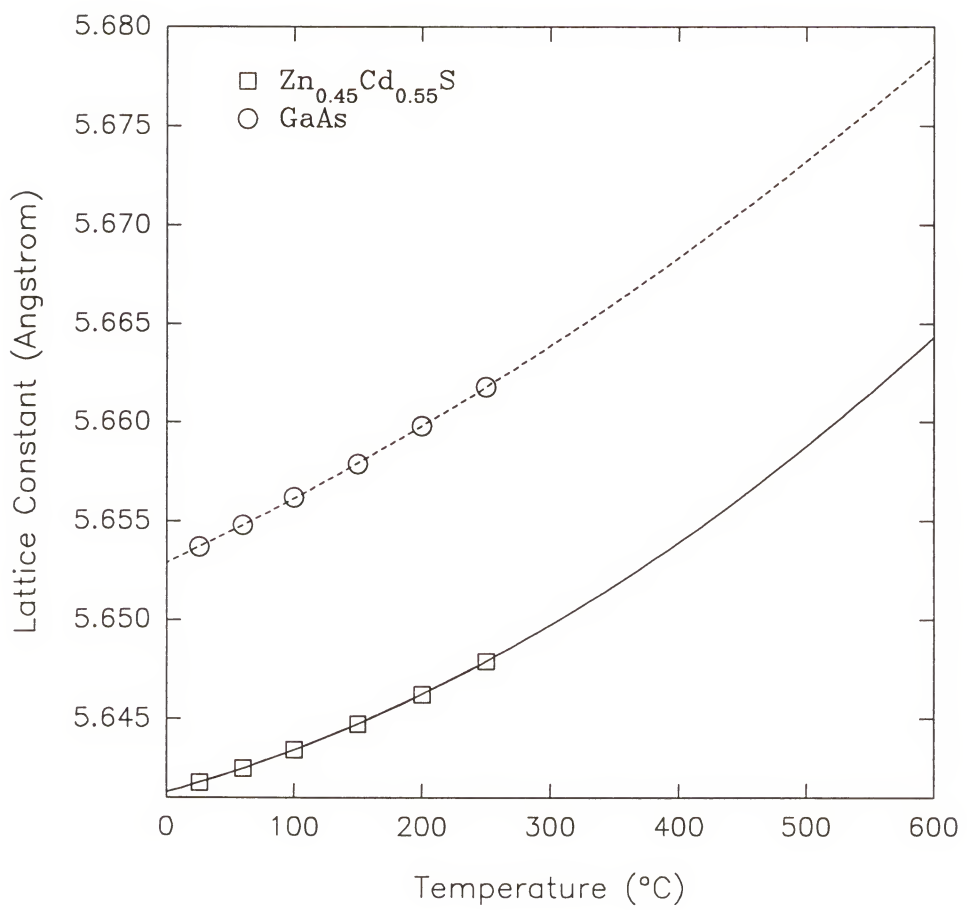


Figure 3-17. Variations of lattice constant with temperature for $\text{Zn}_{1-x}\text{Cd}_x\text{S}$ ($x = 0.55$) and GaAs.

composition reaches around 0.3 and then the epilayer will be under tensile strain since the TEC for the epilayer is now larger than that of the GaAs substrate.

When the data in Figure 3-16 is extrapolated in temperature, it suggests that the epilayer is lattice mismatched at a growth temperature of 550 °C by 0.04% at the Cd composition of $x = 0.78$. The data in Figure 3-18 suggests that when the sample is lattice matched at a growth temperature of 550 °C, it is lattice mismatched at room temperature by 0.035%. The temperature dependent lattice constant data in Figure 3-18 are fitted to a second order polynomial where the abscissa and ordinate are the lattice constants and temperature, respectively. The lattice constants are calculated based on extrapolated TECs at growth temperature from Figure 3-15. Iterations were performed until the lattice constants matched the GaAs substrate.

At lattice matched conditions at room temperature, the epilayer film can be inferred from these calculations that it is indeed under compressive strain which should minimize defect formation. Even at lower growth temperatures, the epilayer is always under compressive strain. The difference in TECs is not significant enough to be a major contributor to strain and thus defect formation.

3.5 Doping

A major challenge to the realization of optoelectronic devices in many II-VI material systems is the doping of the materials both p and n-type. Most II-VI systems are easily doped one type (usually n-type) but not the other, presumably due to compensation by native defects. Several approaches have been taken by researchers to develop effective

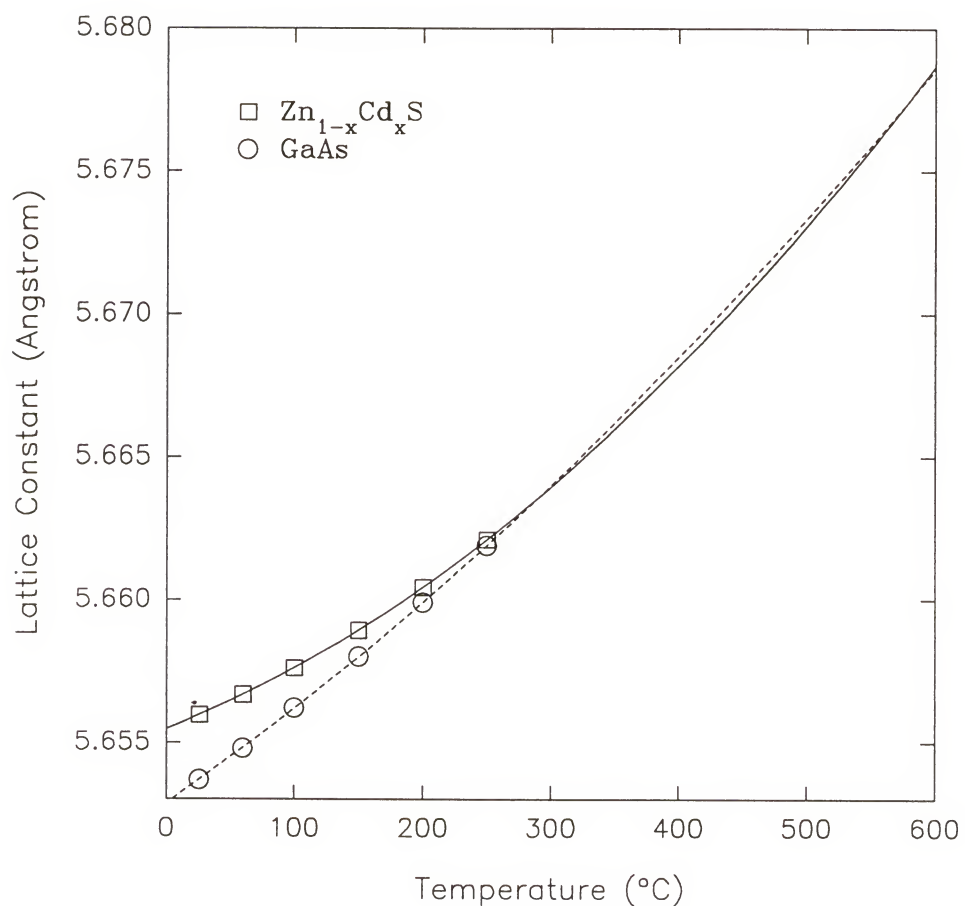


Figure 3-18. Variation of the lattice constants with temperature of GaAs and $Zn_{1-x}Cd_xS$, lattice matched to GaAs at $T_G = 550$ °C.

dopant strategies, but these workers have had limited success [103]. Thermodynamic analyses have been performed to predict dopant behavior from bulk thermodynamic properties. These analyses include a description of the point defect structure [104]. In particular, these calculations suggest that the concentration of native defects is much higher than in the III-V compound semiconductors. If is often the case that one ionized defect will dominate and yield the material intrinsically n or p-type. If the concentration of this dominant defect is high relative to desired dopant concentrations (10^{16} to 10^{19} cm⁻³), control of the doping level and type can not be achieved. Recipes for altering the native defect concentration include lowering the growth temperature to decrease their concentration and adjusting the gas phase phase stoichiometry to increase the concentration of compensating defects to comparable values. Low dopant solubilities at low temperatures, larger ionization energies for dopants in the wider bandgap II-VI materials, and defect complexes further complicate this issue. Of course, the atomic defect concentrations are not at equilibrium at room temperature and the kinetics of their formation and dissolution during cooling are important.

Photoluminescence studies were later performed to identify and quantify the defect species predicted from defect thermochemistry. They were not found, but instead, trace impurities were discovered in nominally undoped and pure materials. In reaction to this finding, attempts were made to grow II-VI materials of even higher purity as a partial solution to the problem of forming p-n junctions [105]. Currently, the inability to efficiently dope is attributed to imperfections of the crystal structure, more specifically

with unique properties of stacking faults/twin planes [106-107] and lattice relaxation around dopants [108].

Theoretical calculations offered by Harrison and Tersoff [109] and McCaldin et al. [110] predict that most of the II-VI materials can be n-type doped but not easily p-type doped: ZnS, ZnSe, CdS, and CdSe. The opposite is true for ZnTe; and CdTe can apparently be doped both n and p-type. A variety of feasible impurities for both n and p-type doping in II-VI compounds are listed in Table 3-3.

Table 3-3. Potential Donor and Acceptor Impurities in II-VI Compounds.

Group	Impurity	Substitution For	Type
IIIA	B, Al, Ga, In, Tl	Zn, Cd	D
VIIA	F, Cl, Br, I	S, Se, Te	D
IA	Li, Na	Zn, Cd	A
IB	Cu, Ag, Au	Zn, Cd	A
VA	N, P, As, Sb, Bi	S, Se, Te	A

NOTE: D is the donor and A is acceptor.

For n-type doping, Al, Ga, and In seem to be the most successful and for p-type doping, N, P, and Li have been used with limited success. Ideally, carrier concentrations of at least 10^{18} cm^{-3} should be producible for most device applications. Carrier concentrations on the order of 10^{17} cm^{-3} have been cited in literature for ZnSe, but some of these results can not be duplicated. A summary of n and p-type doping results for MOVPE grown material is listed in Tables 3-4 and 3-5.

In comparing the difficulty of achieving either n-type or p-type characteristics, the former is easier. Nevertheless, even with n-type doping, a problem exists of carbon contamination from the organometallic dopants used today. The main problem with n-

type doping is that the concentration of dopants in the gas phase is insufficient due to the low vapor pressure of common precursors or low extent of decomposition at the low growth temperature. This is true of TMAI with further complications of unwanted carbon contamination. Whether the solubility of aluminum in ZnCdS has been reached is still unknown since accurate thermodynamic data do not exist.

Table 3-4. Summary of n-type doping of MOVPE grown II-VI compounds.

Carrier Concentration (cm ⁻³)	Mobility (cm ² /V·s)	Resistivity (W·cm)	Source	Host Material	T _g (°C)	Reference
5.0×10 ¹⁷	400-460	3.7×10 ⁻³	EI	ZnSe	300	111
6.5×10 ¹⁷	400	0.05	TEAl	ZnSe	350	112
NR	NR	1.0	TMAI	ZnS	300	113
NR	NR	0.2	HCl	ZnS	300	113
10 ¹⁹	NR	10 ⁻¹ - 10 ⁻²	EI	ZnCdS: x of Cd = NR	300	37, 40
4.0×10 ¹⁸	110	NR	TEIn	ZnCdS: x of Cd = 0.8	NR	39

NOTE: NR is not reported, EI (ethyl iodide) is C₂H₅I, TEAl (triethyl aluminum) is (C₂H₅)₃Al, TMAI (trimethyl aluminum) is (CH₃)₃Al, and HCl is hydrogen chloride.

Table 3-5. Summary of p-type doping of MOVPE grown II-VI compounds.

Carrier Concentration (cm ⁻³)	Mobility (cm ² /V·s)	Resistivity (W·cm)	Source	Host Material	T _g (°C)	Reference
9.0×10 ¹⁷	39	0.2	Li ₃ N	ZnSe	450	114
1.0×10 ¹⁷	NR	NR	TBL	ZnSe	500	115
4.0×10 ¹⁶	0.24	6.4	TBL	ZnSe	550	116
7.2×10 ¹⁵	39.5	21.9	NH ₃	ZnSSe	500	117
.2×10 ¹⁵	20 - 50	10 ² -10 ³	NH ₃	ZnSe	350-500	118

NOTE: NR is not reported, Li₃N is lithium nitride, TBL (tert-butyl lithium) is (C₄H₉)₃Al, and NH₃ is ammonia.

It has been suggested that the difficulty of p-type doping is associated with self-compensation. For ZnSe, p-type doping is a serious problem and this may also be true for the pseudobinary ZnCdS. The detailed self-compensation mechanism is still unclear, however a few possibilities have been proposed. One reason may be that the intentional dopants may be amphoteric with a compensation ratio very close to unity. An examination of the group V amphoteric dopants in GaAs indicates that the compensation ratio changes in definite direction with the atomic number of the dopant element (size effect). Another possibility is that shallow dopants might occupy not only the electrically active substitutional sites but also the interstitial sites, thus limiting the free carrier concentration. Another proposal is that the dopants form neutral complexes with native defects. Chadi and Chang [108] have proposed that self-compensation of the acceptor impurities, As and P in ZnSe, is due to large lattice relaxations that activates the formation of positively charged defect centers.

In order to counteract the effects of self-compensation, a novel designer dopant manufactured at Florida State University by Professor Will Reese of the Chemistry Department was used: bis-trimethyl silial amido zinc (TMSAZ) as shown in Figure 3-19. In this new compound, zinc is pre-attached to two nitrogen atoms, each of which is attached to two silial groups. Theoretically, the nitrogen-silicon bonds should break first leaving a zinc with two nitrogen atoms bonded to it. If the correct bond cleavage occurs, then the nitrogen atom will be correctly placed on the sulfur site to produce p-type behavior, thus minimizing the extent of self-compensation. There is no report in the literature of p-type doping ZnCdS.

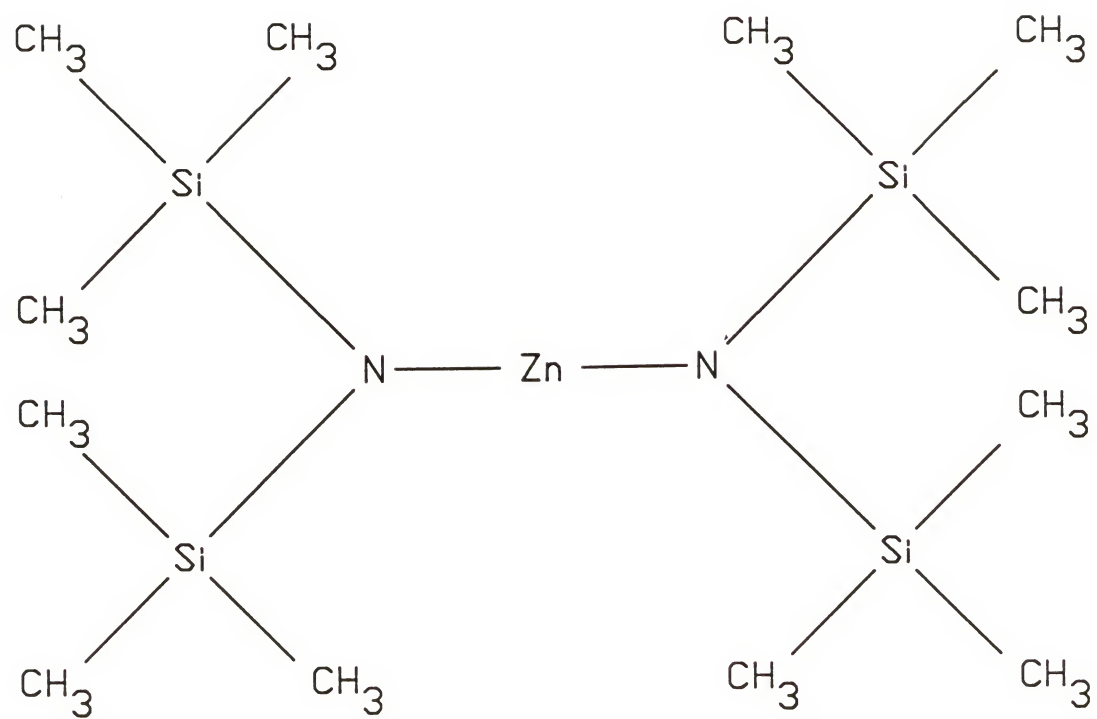


Figure 3-19. Schematic diagram of bis-trimethyl silial amido zinc (TMSAZ).

3.5.1 Experiment

The carrier concentration and mobility are measured by Hall experiments using the Van-der Pauw technique. Ohmic contacts were made from In dots pressed onto the material and then annealed in forming gas (8% H₂ and 92% N₂) for 30 minutes at 230 °C. For reference, undoped ZnCdS samples were analyzed for their background carrier concentrations. Unfortunately, the resistivity of these films exceeded the limits of detection for the Hall measurement system and carrier concentrations could not be measured. An inference can be made that the undoped ZnCdS has net carrier concentrations less than or equal to 10¹² cm⁻³.

3.5.2 Dopant p-type

Measurable carrier concentrations with TMSAZ could not be detected with Hall measurements. Again with poor ZnCdS crystallinity, these results are expected. A detrimental side effect is contamination caused by low purity of TMSAZ.

The PL spectra of ZnCdS doped with TMSAZ shown in Figure 3-20, exhibits luminescence peaks at approximately 1.9, 2.3, 2.5, and 3.0 eV. In comparison with a PL for nominally undoped ZnCdS in Figure 3-21, the substantially broad peak at 2.4 eV is apparent as well as the 3.0 eV peak for the epilayer. The near bandgap edge emission at 3.0 eV is most likely caused by free-to bound transitions from the conduction band to the relatively shallow acceptor levels or from shallow donors to the valence band. These transitions are characterized by a line width proportional to the kinetic energy of the free carriers in the conduction or valence band which is determined by the thermal energy.

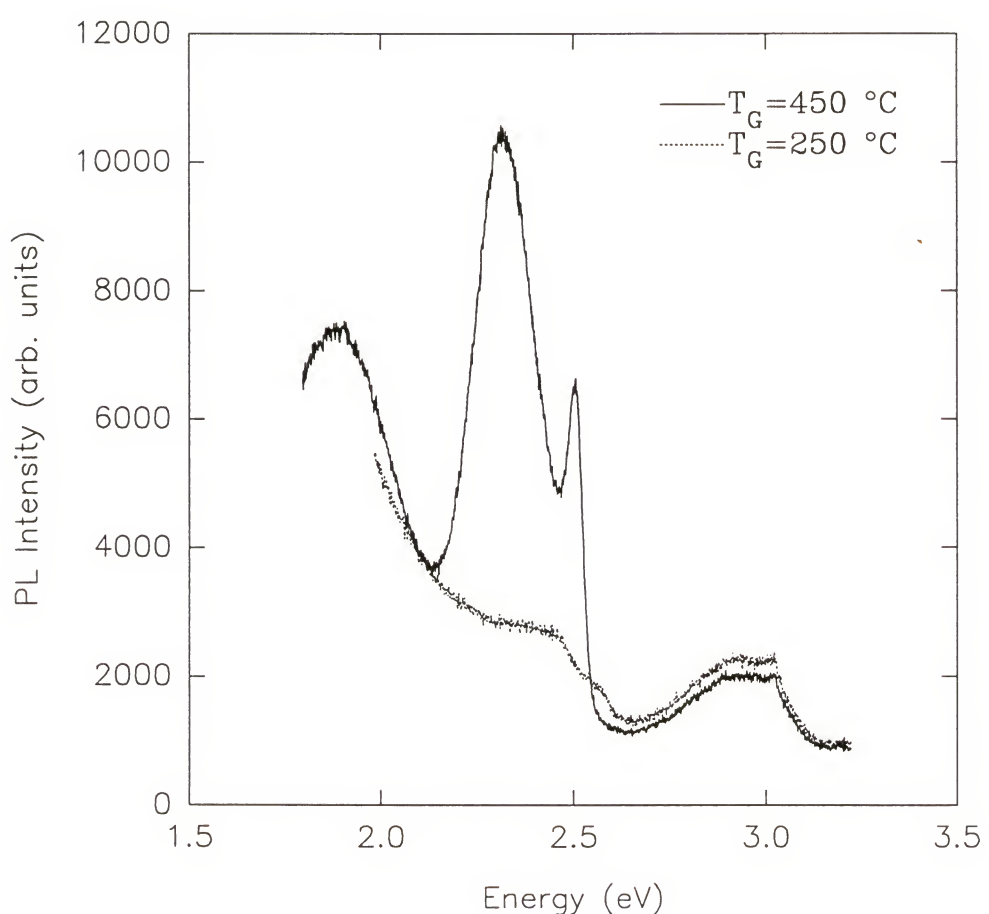


Figure 3-20. PL spectrum of ZnCdS doped with TMSAZ.

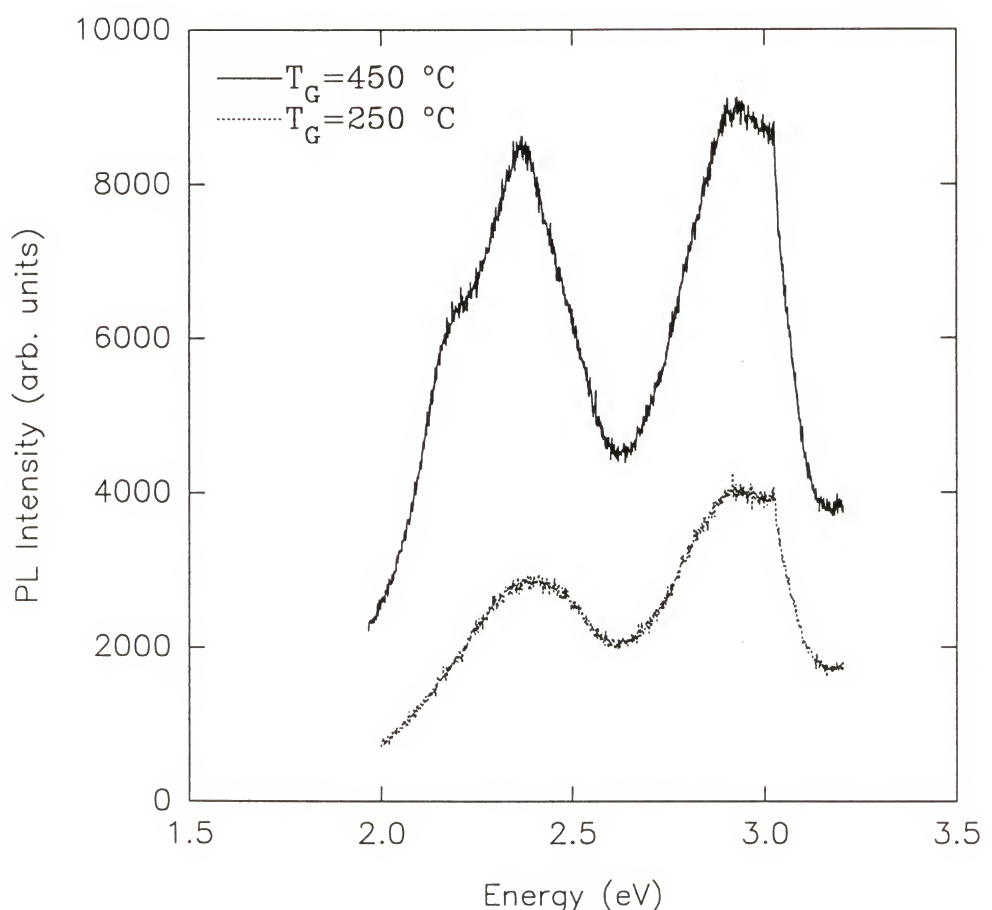


Figure 3-21. PL spectrum of nominally undoped ZnCdS.

Most likely the edge emission is not caused by donor-acceptor pair (D-A) transitions due to lack of sharp lines corresponding to various separations for each D-A pair.

The lower energy peaks are attributed to deep level emissions caused by carbon contamination as seen in nominally undoped epilayers. The intensity of these peaks increase with increase temperature due to more complete pyrolysis and further carbon incorporation. Clearly, at 450 °C, the ratio of the respective peaks is the largest. If the growth temperature were set at even higher temperatures, the amount of carbon contamination would not be expected to be much different since 450 °C is the critical point when most of pyrolysis has already occurred.

3.5.3 Dopants n-type

Figures 3-22 and 3-23 show the measured free carrier concentration as a function of the dopant flow rate of TEAl and TEGa, respectively for ZnCdS grown on both the (100) 2° and (111)A GaAs substrates. With TEAl as the dopant, the maximum carrier concentration for the (100) 2° substrate is $1.7 \times 10^{15} \text{ cm}^{-3}$ at a flow rate of 0.4 $\mu\text{mole/min}$ and for the (111)A substrate, it is $3.0 \times 10^{15} \text{ cm}^{-3}$ at a flow rate of 1.3 $\mu\text{mole/min}$. For TEGa, the maximum carrier concentration for the (100) 2° substrate is $3.0 \times 10^{14} \text{ cm}^{-3}$ at a flow rate of 0.6 $\mu\text{mole/min}$ and for the (111)A substrate, it is $4.0 \times 10^{15} \text{ cm}^{-3}$ at a flow rate of 0.6 $\mu\text{mole/min}$. The carrier concentrations are about three to four orders of magnitude lower than listed in Table 3.2 for ZnCdS. These low carrier concentrations are possibly caused by the poor crystallinity of the ZnCdS epilayers due to the high concentration of stacking faults/microtwins. This conclusion is supported by secondary ion mass

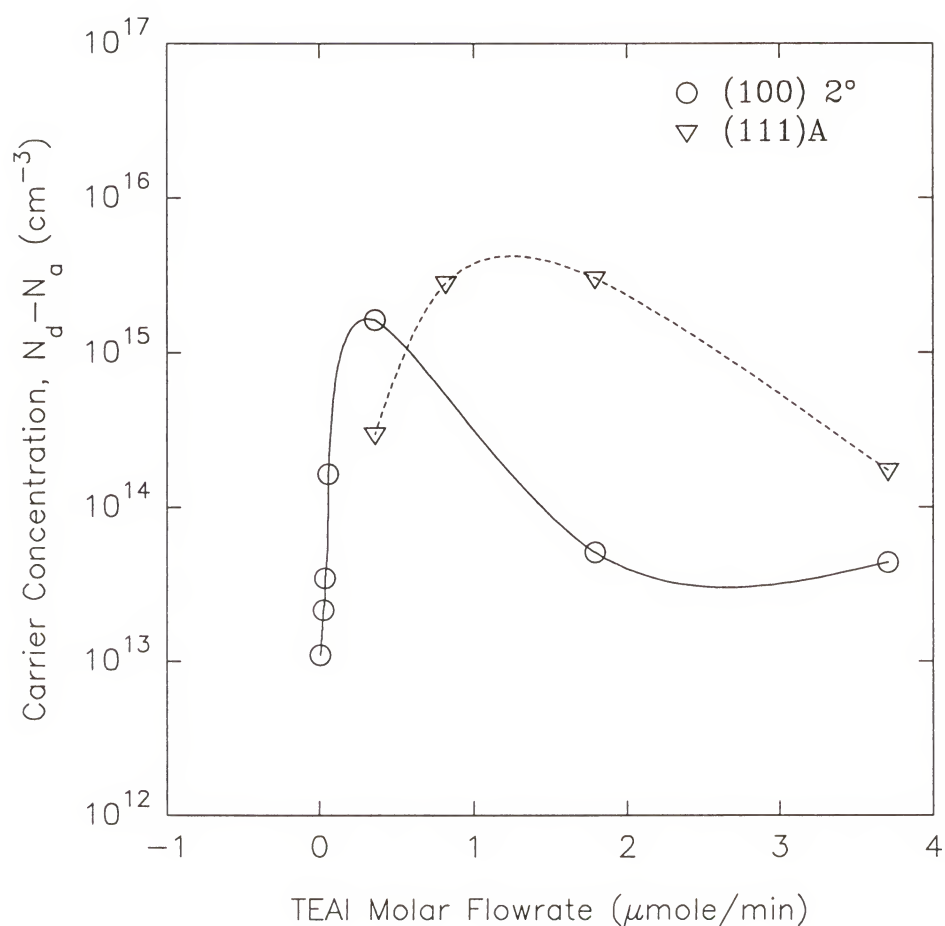


Figure 3-22. Dependence of net carrier concentration on TEAl flow rate.

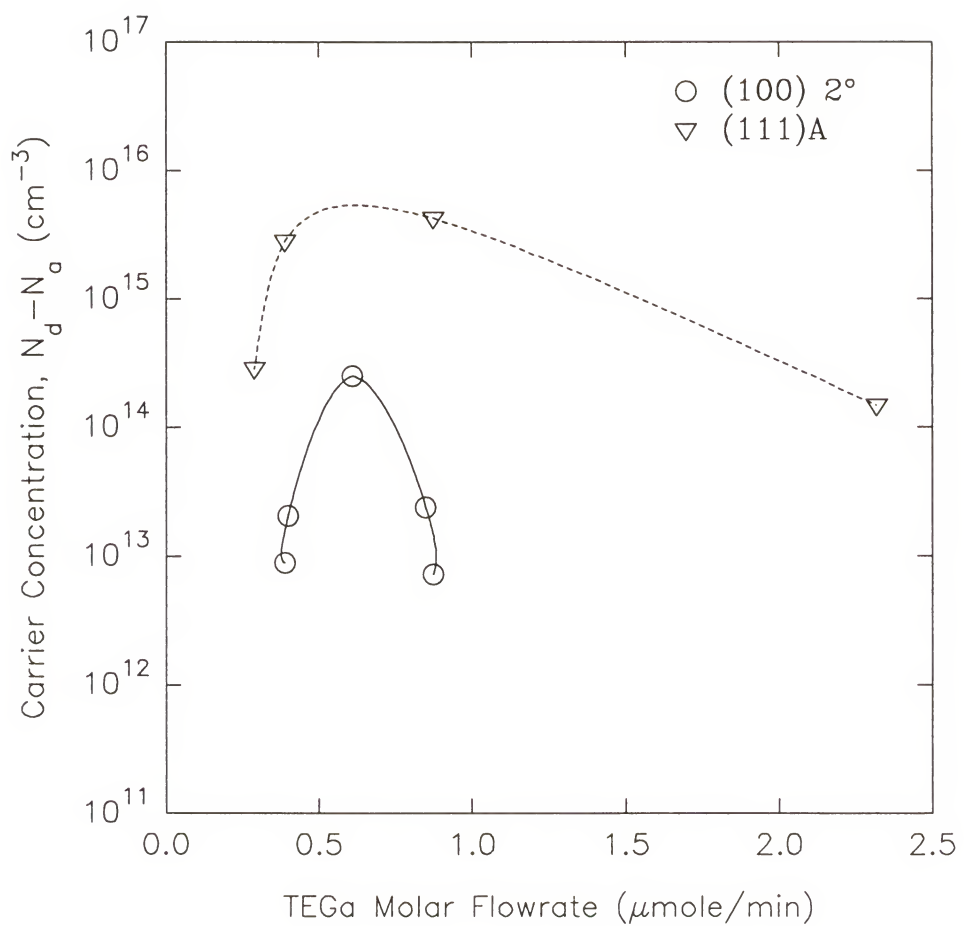


Figure 3-23. Dependence of net carrier concentration on TEGa flow rate.

spectroscopy (SIMS) data shown in Figure 3-24. The extent of Al and Ga incorporation are more than the measured free carrier concentration suggesting a large percentage of the dopant is electrically inactive.

At relatively low dopant (both Ga and Al) flow rates, the net carrier concentrations increase with increased dopant flow rate until a maximum point is reached and then the carrier concentration begins to decrease with further increase in the dopant flow rate. With over-doping, self-compensation begins to take effect.

In addition to low carrier concentrations, the doped ZnCdS films also exhibit low electron mobilities. With Al doping the electron Hall mobility for (100) 2° and (111)A substrates are 31 and 17 $\text{cm}^2/\text{V}\cdot\text{s}$, respectively. With Ga doping the electron Hall mobility for (100) 2° and (111)A substrates are 37 and 14 $\text{cm}^2/\text{V}\cdot\text{s}$, respectively. These measured mobilities are extremely low compared to values reported elsewhere; other authors cite the electron mobilities for ZnS and CdS to be 165 and 300 $\text{cm}^2/\text{V}\cdot\text{s}$ for ZnS and CdS, respectively [6]. These low mobilities are attributed to lattice and space charge scattering caused by the poor crystallinity of the epilayers.

One researcher has cited that nominally undoped ZnCdS exhibits n-type behavior and at 250 °C growth temperature, the carrier concentration is measured at around 10^{16} cm^{-3} ; and for layers grown at 400 °C, it is measured at 10^{18} cm^{-3} [36]. Figure 3-24 shows a SIMS analysis of a ZnCdS layer grown at 450 °C and this clearly indicates a buildup of Ga at the interface and some diffusion of the Ga from the substrate into the grown layers. This is a possible cause of the n-type behavior of the nominally undoped ZnCdS. Evidence of this Ga diffusion is also discussed elsewhere [119]. The carrier concentration

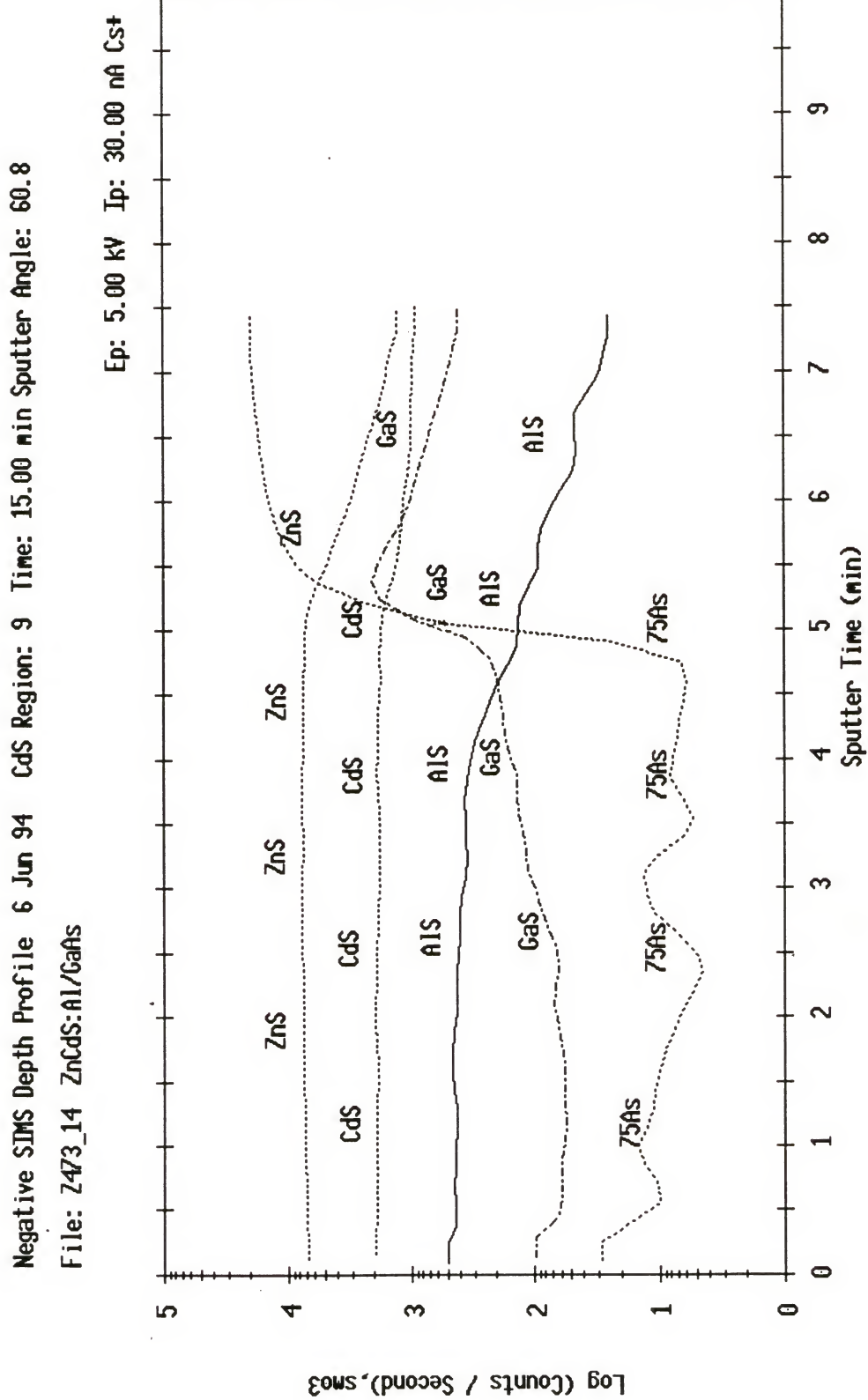


Figure 3-24. SIMS analysis of ZnCdS grown at 450 °C.

increases with increasing growth temperature. This suggests auto-doping due to possible contamination by diffusion of gallium from the substrate even up through a 2.0 μm epilayer [120]. Evidence of Ga diffusion for other heteroepitaxial II-VI systems has been reported elsewhere [119].

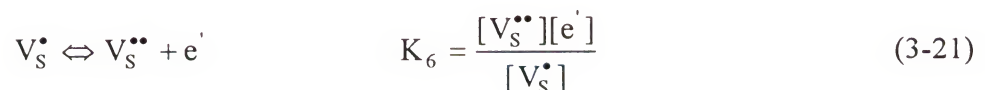
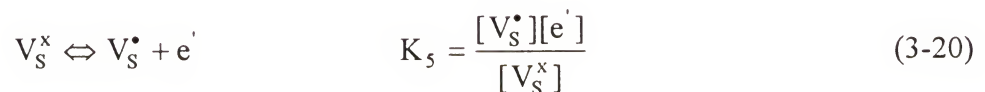
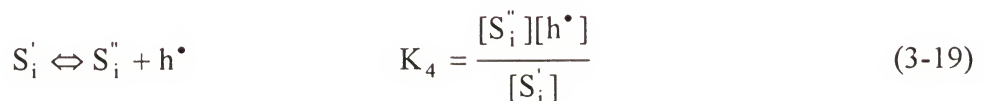
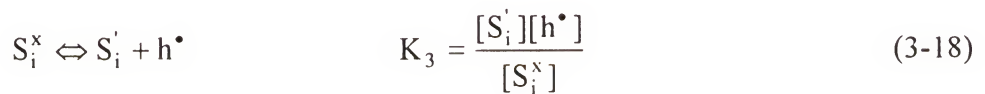
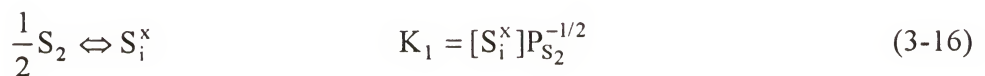
3.5.4 Point Defect Equilibrium Analysis

One possible explanation for the observed n-type behavior is that the native point defect structure dominates the free carrier concentration. In this discussion of the point defect structure, the Kröger-Vink notation will be used [121]. With this convention, the defect type is designated by a major symbol and the lattice site it occupies by a subscript. For example, an interstitial position is indicated by a subscript ‘‘i’’. The effective charge that a defect has in relation to the lattice site it occupies is designated with a superscript. The superscript symbols ‘‘x,’’ ‘‘dot,’’ and ‘‘prime’’ signify a net neutral, a net positive and a net negative charge, respectively. A set of species is then postulated based on experimental data and physical/chemical properties such as atomic sizes, binding energies, diffusivities, and conductivities. In the usual approach, these point defect species in the solid are allowed to come to equilibrium with an external phase of known state properties. This equilibrium is often expressed in the form of an independent set of reactions that can be solved for the defect concentrations as a function of the external equilibrium phase state.

It is postulated that the equilibrium between the growing solid and controlled vapor phases controls the electrical and optical properties of the film. In determining the

different types of defects for ZnCdS, a realistic scenario is one in which sulfide vacancies dominate at low sulfur partial pressures and sulfide interstitials dominate at high sulfur partial pressures (Frenkel disorder on the sulfur sublattice). In this model, the dominant defect structure resides on the sulfur sublattice where ZnCdS can be considered as simply MS where M is the sum of Zn and Cd. In other words, sulfur vacancies and sulfur interstitials are assumed to be the dominant point defects.

The expressions for defect generation and ionization for the defect equilibria for MS with Frenkel defects as the major defects present in the crystal can be described by the following independent set of chemical reactions:



The brackets do not indicate concentrations but site fractions of occupation. The last relationship requires that electroneutrality be satisfied.

$$[e^{\cdot}] + [S_i^{\cdot}] + 2[S_i^{\cdot\cdot}] = [h^{\bullet}] + [V_s^{\bullet}] + 2[V_s^{\bullet\bullet}] \quad (3-23)$$

There are a total of ten unknown variables: eight concentrations, sulfur partial pressure and temperature. If the equilibrium constants are known for various temperatures, the eight equations can be solved explicitly as a function of the external phase state (sulfur partial pressure and temperature). Unfortunately, these constants are not well known. Nevertheless qualitative conclusions can be drawn under special conditions.

3.5.4.1 Low sulfur partial pressure

At low P_{S_2} , reaction (3-16) indicates that $[S_i^x]$ will be low and so will $[S_i^{\cdot}]$ and $[S_i^{\cdot\cdot}]$ according to reactions (3-18) and (3-19) following Le Chetelier's Principle. According to reactions, (3-17), (3-20), and (3-21), respectively, $[V_s^x]$, $[V_s^{\bullet}]$, $[V_s^{\bullet\bullet}]$, and $[e^{\cdot}]$ will get large. The increase in the number of electrons will then drive reactions (3-20) to (3-22) to the left, thereby decreasing $[e^{\cdot}]$, $[V_s^{\bullet\bullet}]$, and $[h^{\bullet}]$. Since $[e^{\cdot}]$ is large once established by the low P_{S_2} , a small change in $[e^{\cdot}]$ will greatly affect the changes in reactions (3-18) and (3-19) and produce large changes in $[h^{\bullet}]$, $[S_i^{\cdot}]$ and $[S_i^{\cdot\cdot}]$. Therefore, Equation 3-23 can be approximated by:

$$[e^{\cdot}] \approx [V_s^{\bullet}] + 2[V_s^{\bullet\bullet}] \quad (3-24)$$

at low P_{S_2} . This expression can then be inserted into Equations 3-20 and 3-21 and an expression for $[V_S^x]$ can be derived. As a simplification to the derivation, other assumptions can be made.

If an assumption is made that $[V_S^\bullet] \gg 2[V_S^{\bullet\bullet}]$, in other words the dominant defect is $[V_S^\bullet]$ which means that $[e^\cdot] \approx [V_S^\bullet]$. Inserting this into Equation 3-20 and combining with Equations 3-16 and 3-17, gives

$$[e^\cdot] \approx [V_S^\bullet] = \left(\frac{K_5 K_2}{K_1} \right)^{1/2} P_{S_2}^{-1/4} \quad (3-25)$$

Even without the thermodynamic knowledge for reactions (3-16) to (3-18), the relationship of the electron concentration with the partial pressure of S_2 to the $-1/4$ power is a significant result. This shows that if the singly charged sulfur vacancies and the resulting electrons are the predominant defects in MX, then these concentrations can be controlled by P_{S_2} and the type of carriers can be dictated as well as the conductivity since

$$\sigma = nq\mu = [e^\cdot]q\mu \quad (3-26)$$

In addition the $[V_S^\bullet]$ can be determined by measuring the conductivity at different P_{S_2} .

If we assume that $[V_S^{\bullet\bullet}] \gg [V_S^\bullet]/2$, then Equation 3-24 becomes $[e^\cdot] = 2[V_S^{\bullet\bullet}]$. Proceeding in the same fashion as before with Equations 3-16, 3-17, 3-20, and 3-21, we get

$$[V_S^{\bullet\bullet}] = \left[\frac{K_6 K_5 K_2}{4K_1} \right]^{1/3} P_{S_2}^{-1/6} \quad (3-27)$$

$$[e'] = \left[\frac{K_6 K_5 K_2}{2 K_1} \right]^{1/3} P_{S_2}^{-1/6} \quad (3-28)$$

Again the electron concentration and conductivity can be determined and controlled by the partial pressure of sulfur according to $P_{S_2}^{-1/6}$. At low S_2 partial pressures, the ZnCdS epilayers should be n-type whether the power law dependence on P_{S_2} is $-1/6$ or $-1/4$. However, the VI/II ratio is typically high and so growth occurs at relatively high partial pressures.

3.5.4.2 High sulfur partial pressure

The limit of high partial pressure of sulfur is next considered to determine the effect of P_{S_2} on the defect concentrations. Under these conditions Equation 3-16 indicates that $[S_i^x]$ will be large and therefore so will $[S_i^{' }]$, $[S_i^{''}]$, and $[h^{\bullet}]$ according to Equations 3-18 and 3-19. Thus according to Equations 3-17, 3-20, 3-21, and 3-22, the defect concentration, $[V_S^x]$, $[V_S^{\bullet}]$, $[V_S^{\bullet\bullet}]$, and $[e']$ will be low at high P_{S_2} . The electroneutrality Equation 3-23 can be approximated or reduced to

$$[h^{\bullet}] = [S_i^{' }] + 2[S_i^{''}] \quad (3-29)$$

Again assumptions are made to simplify the algebra under the condition of high P_{S_2} . When singly charged S interstitials are the predominant defects, reaction (3-18) will dominate over reaction (3-19), where $[h^{\bullet}] = [S_i^{' }]$, and so it can be shown that

$$[h^{\bullet}] = [S_i^{' }] = (K_3 K_1)^{1/2} P_{S_2}^{1/4} \quad (3-30)$$

When doubly charged sulfur interstitials are the primary defects, $[h^{\bullet}] = 2[S_i^{''}]$. Thus,

$$[h^\bullet] = \left(\frac{K_4 K_3 K_1}{2} \right)^{1/3} P_{S_2}^{1/6} \quad (3-31)$$

$$[S_i^{\prime \prime}] = \left(\frac{K_4 K_3 K_1}{4} \right)^{1/3} P_{S_2}^{1/6} \quad (3-32)$$

Since ZnCdS is grown at high VI/II ratios (assumed relatively high S₂ partial pressures), the epilayer should behave with p-type behavior according to the defect analysis assuming no other cause. These predictions suggest that n-type behavior can be achieved only at relatively low sulfur partial pressures although ZnCdS growth occurs at assumed relatively high sulfur partial pressures. As a result, the defect analysis indicates that point defects caused by nonstoichiometry may not be the main cause for n-type behavior in nominally undoped ZnCdS.

3.6 Summary

The optical, physical, and electrical properties of Zn_{1-x}Cd_xS that are important to potential optoelectronic devices have been measured. The bandgap energy for the entire composition spectrum has been determined by reflectance measurements. The relationship between bandgap energy and composition is not linear but quadratic:

$$E_g(x) = E_g(ZnS) - 2.00x + 0.76x^2 \quad (3-33)$$

where E_g is the bandgap energy for varying Cd fraction (x) and E_g(ZnS) is assumed to be 3.6 eV. This bowing is typical of many II-VI materials. PL measurement of the band edge are consistent with these results. The complex refractive index was determined for x = 0.58 and x = 0.55 through ellipsometry. The measured values do not lie in between the

complex refractive indices of the constituent binary compounds, ZnS and CdS. The reason for this discrepancy is that bulk crystals were used as samples in the literature citations instead of thin films. In addition, the poor thickness uniformity made accurate measurements difficult. Absorption coefficients and complex dielectric constants are also calculated for completeness.

Thermal expansion coefficients were calculated from lattice constant measurements using HRXRD at various temperatures. Again the relationship between the TEC and Cd composition was nonlinear. With Cd rich epilayers, the TEC is nearly constant until the composition nears $x = 0.4$ and then near the Zn rich region, the TEC increases sharply.

The carrier concentrations were determined by Hall measurements using the Van der Pauw technique. The in-situ n-type dopant studies were performed with TEGa and TEAl. Unfortunately, neither provided high electron concentrations: 3.0×10^{15} and $4.0 \times 10^{15} \text{ cm}^{-3}$ for TEAl and TEGa, respectively. The background carrier concentration was measured on the order of $\sim 10^{13} \text{ cm}^{-3}$. A novel precursor, bis-trimethyl silial amido zinc, was used as a p-type dopant. The samples showed a high resistance beyond the detection limit of the apparatus. Some authors have cited ZnCdS with n-type behavior even though it is unintentionally undoped. Defect equilibrium analysis suggests that point defects caused by nonstoichiometry is not the source of this n-type behavior at high VI/II ratios. The most likely cause is Ga diffusion from the substrate into the epilayer during growth.

CHAPTER 4

MODEL OF SOLID VAPOR DISTRIBUTION

A method for calculating multicomponent phase diagrams for II-VI systems is necessary for understanding more thoroughly the relationship between the contacting fluid phase and the growing processes such as MOVPE and bulk crystal growth. Experimentally determining phase diagrams, including liquidus curves and tie lines, is an enormous undertaking which requires considerable time and the data often contains uncertainties due to long equilibration times in the solid solution. Thus, methods for predicting multicomponent phase diagrams from binary data are preferable.

One common method for predicting phase diagrams is based on the minimization of the Gibbs free energy which was originally developed by Eriksson [122]. Zinc chalcogenides [123], cadmium chalcogenides [124] and mixed solutions of HgCdTe [125] have all been analyzed using this approach and an associated solution model for the liquid phase. The calculation of phase diagrams, however, may not always be possible since solid solution data are not available. Thus predictive models are needed to estimate solution behavior. Once a description of the Gibbs energy of the phases is available, the variation of growth rate and the equilibrium partial pressures of the various species with process parameters can be estimated. Examples for III-V [126-129] and II-VI [130] systems can be found in the literature.

Several workers [131-139] have cited successful calculation of phase diagrams for III-V systems based upon the regular or quasichemical equilibrium approach of Guggenheim. The regular solution approach has been mostly used for extrapolation and interpolation of experimental data in ternary systems [140-143] and interpretation of III-V binary phase diagrams [144-148]. This approach has also been successfully applied to other systems such as CdBiPb, CdSnPb, and AlBiPb [149].

A full description of the $Zn_{1-x}Cd_xS$ phase diagram requires the following information: an expression (model) for the liquid $Zn_{1-y}Cd_yS$ solution and the $Zn_{1-x}Cd_xS$ pseudobinary solid solution; the Gibbs energy of pure components Zn, Cd, and S and the compounds ZnS and CdS; and assuming ideal solution behavior, the Gibbs energy of the vapor species Zn, Cd, and S. For applications to MOVPE, the phase field of interest is the solid-vapor two phase field. Thus, knowledge of the liquid phase properties is not needed. A lack of data, however, exists for describing the solid solution behavior and first principles or semi-empirical models must be used. Stringfellow developed a semi-empirical model, the delta lattice parameter (DLP) model, to calculate the interaction parameter, Ω , of regular solutions based solely on the lattice parameters of the binary compounds [150]. With a single adjustable parameter, this model has successfully predicted accurate values of Ω for most III-V systems. Fedders and Muller [151] later developed a model similar to the DLP to estimate Ω from the strain energy caused by lattice mismatch or bond distortion of the alloy.

For the first time, Ω is calculated using the DLP model derived specifically for II-VI systems and used to determine the solid-vapor distribution (SVD) of ZnCdS. Kisker and

Zawadzki [152] have estimated the SVD for several MOVPE grown II-VI systems such as ZnSeS and HgCdTe by applying the DLP model developed for III-V systems to II-VI systems.

4.1 Model Development and Results

For pseudobinary semiconductor systems, the lattice model is considered a solid solution of A atoms and B atoms on the same sublattice with each atom surrounded by Z nearest neighbors [131]. The energy of solution or interaction parameter is often considered a linear function of the bond numbers between nearest neighbor atoms and is given by the following expression,

$$\Omega_{ab} = Z \left[E_{ab} - \frac{(E_{aa} + E_{bb})}{2} \right] \quad (4-1)$$

The E_{ij} term reflects the interaction energy of an i-j nearest neighbor atom. In theory, this can be expressed explicitly in terms of partition functions from statistical mechanics. But the large number of atom-atom bonding and interactions make it impractical for an explicit expression of these partition functions and thus, necessitates approximate expressions.

One such approximation is put forth by Hildebrand [153]. In his model, the distribution of A and B atoms is considered random. As a result, the model is defined as a regular solution in which the enthalpy of mixing is non-zero, but the excess entropy of mixing is zero. This situation is internally inconsistent since it assumes a random configuration of atoms yet certain configurations are more energetically favored than others. A more consistent approximation is the quasi-chemical equilibrium formulation

proposed by Guggenheim [154]. In this approach, the distribution of A and B atoms is weighed exponentially by their bond energy and is expressed by the following equation:

$$\bar{X} = (N_A - \bar{X})(N_B - \bar{X}) \exp\left(\frac{-2\Omega}{ZkT}\right) \quad (4-2)$$

where N_A and N_B are number of A and B atoms, respectively, on a lattice of N sites with a coordination number Z . \bar{X} is the equilibrium or average number of interchanges between A and B. Ω is the interaction parameter and k is the Boltzman constant. As Ω/kT approaches zero (high temperature), the distribution of A and B atoms become random. In general, a mixture of atoms is considered a regular solution if it satisfies all the conditions of an ideal mixture with the exception that some configurations are more energetically favorable than others.

Nevertheless, as a crude treatment of the regular solution theory, the assumption is made that the atoms are randomly distributed and the enthalpy of mixing in a binary solution behaves as

$$\Delta H^M = x(1-x)\Omega \quad (4-3)$$

where x is the molar fraction. The problem lies in determining Ω . With no experimental data available, first principle or semi-empirical expressions must be used. The Phillips-Van Vechten dielectric model [155-156] suggests that the bonding energy which is related to ΔH^M , can be expressed in terms of the bandgap energy and some have even suggested that the relationship is linear for semiconductors [157-159]. The linear relationship between the bandgap energy and the binding energy has been established for both the III-V [160] and II-VI [161] systems. Phillips and Van Vechten suggest that the average

bandgap energy, E_g , should be used as opposed to just the average covalent bandgap energy, E_h , or the average ionic bandgap energy, C . In quantum mechanical terms, E_h and C reflect the results due to symmetric and antisymmetric potentials, respectively. Based on the parallel results of a simple two-level bonding-antibonding model and later used in Penn's model [162] of energy bands for sphalerite-structured semiconductors, the average bandgap energy is expressed as

$$E_g = E_h + iC. \quad (4-4)$$

For the III-V and IV semiconductors, the average bandgap energy has been empirically found to vary approximately as $a_o^{-2.5}$ [150]. In a parallel manner, the bandgap energy was calculated to vary approximately as $a_o^{-5.0}$ for II-VI semiconductors, which is quite different from the more covalent III-V and IV semiconductors. Figure 4-1 shows a plot of bandgap energy versus lattice constant showing the best fit with a -5.0 power law dependency on the lattice constant. The values for the bandgap energy are listed in Table 4-1. The best fit was determined through nonlinear regression based upon the Marquardt-Levenberg algorithm and the relationship is described as

$$E_g = k a_o^{-5.0} \quad (4-5)$$

where k is a proportionality constant, E_g (eV) is the bandgap energy and a_o (\AA) is the lattice constant. When determining the correlation between the bandgap energy and the lattice constant, the mercury chalcogenides were intentionally not used in the data base. The reason for this is that they are essentially semi-metals rather than semiconductors [163-170]. The anomalous inconsistency of the observed lattice constants with the

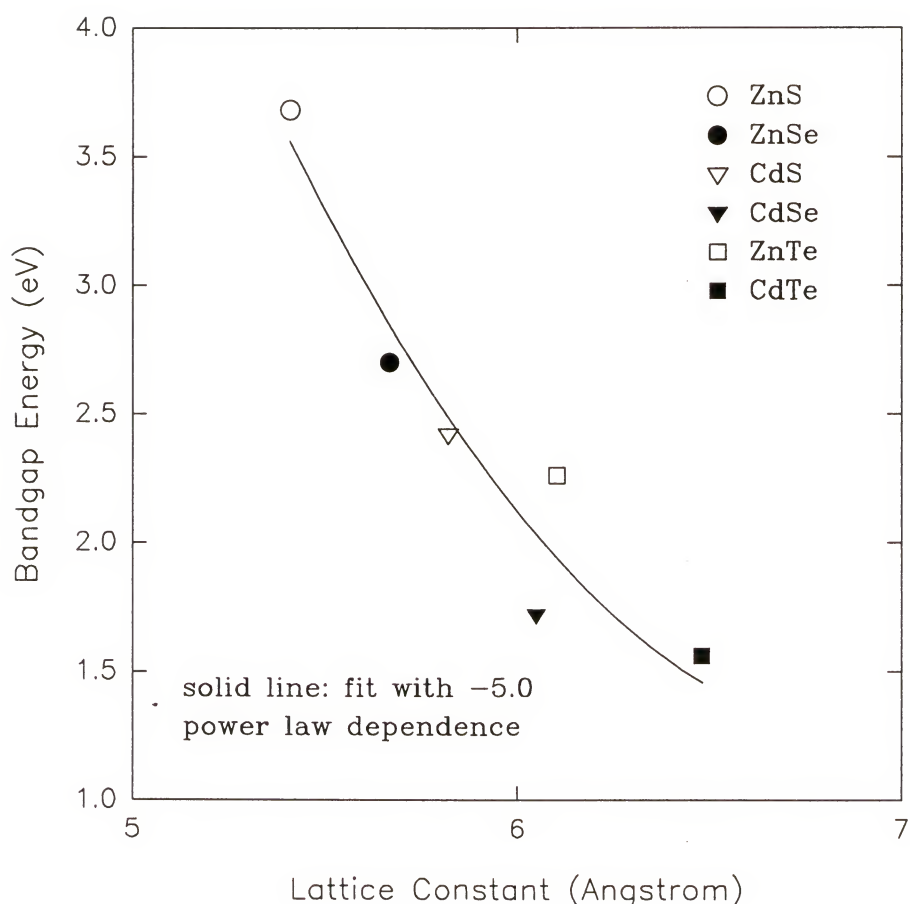


Figure 4-1. Fit between bandgap energy and -5.0 power law dependency on the lattice constant for selected cubic II-VI compounds.

calculated radii values [171] suggest that mercury chalcogenides should not be included although they are by strict definition members of the II-VI family.

Table 4-1. Bandgap energy and lattice constants for cubic II-VI semiconductors.

Compound	Lattice Constant ^a (Å)	Bandgap Energy ^b (eV)
ZnS	5.4093	3.68
ZnSe	5.6687	2.7
ZnTe	6.1037	2.26
CdS	5.820	2.42 ^c
CdSe	6.05	1.72 ^d
CdTe	6.481	1.56
HgS	5.851	-0.1 ^e
HgSe	6.084	-0.1 ^f
HgTe	6.460	0.1 ^f

^aAll lattice constants are from reference 172.

^bThe bandgap energy data are from reference 173 unless stated otherwise.

^cReferences 174-175

^dReference 176

^eReference 177

^fReferences 178-179

In combination with Equation 4-5, the enthalpy of atomization (ΔH^{at}), which is a measure of the binding energy, can be written as a power law dependence on the lattice constant

$$\Delta H^{at} = K a_o^{-5.0} \quad (4-6)$$

where K is a proportionality constant. Figure 4-2 displays the linear relationship between ΔH^{at} and $a_o^{-5.0}$ with an average constant of proportionality to be 1.87×10^8 cal/mole Å^{-5.0}.

For the II-VI materials, the calculated values of ΔH^{at} are listed in reference [161] and the lattice constants used in the calculations are listed in Table 4-1. Once again, because of

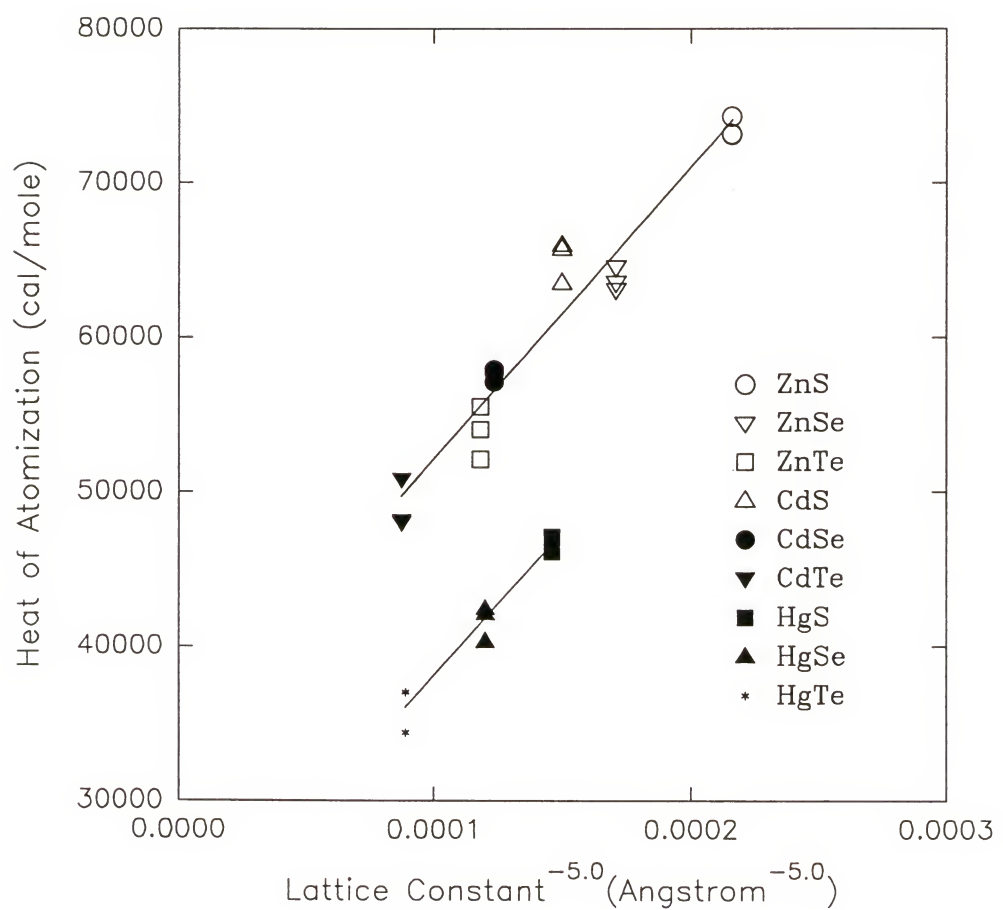


Figure 4-2. Linear relationship between ΔH^{at} and $a_o^{-5.0}$.

the semi-metallic nature of the mercury chalcogenides in comparison to the other II-VI compounds, the plot separates into two groups. The K value derived from the group containing the Cd and Zn chalcogenides is 1.86×10^8 cal/mole $\text{\AA}^{-5.0}$ and that for the group containing the Hg chalcogenides is 1.88×10^8 cal/mole $\text{\AA}^{-5.0}$. The similarity of both values instills confidence for these results. This method of obtaining the constant of proportionality has also been found to be valid in the III-V system.

For the III-V systems, the value of K was obtained by fitting Equation 4-8 with a least squares method to Ω values obtained by the reduction of available thermochemical and phase diagram data [150]. The best value is 1.15×10^7 cal/mole $\text{\AA}^{-2.5}$. The values obtained from $\Delta H^{\text{at}}/a_0^{-2.5}$ for III-V and IV compounds ranged from 1.14×10^7 to 1.48×10^7 with an average value of 1.26×10^7 . This is very close to the fitted value mentioned previously. This provides some confidence that the K value obtained using similar techniques from $\Delta H^{\text{at}}/a_0^{-5.0}$ for the II-VI materials will also be adequately accurate. Now the composition dependence of ΔH^M can be calculated from the following expression,

$$\Delta H^M = (1-x)\Delta H_A^{\text{at}} + x\Delta H_B^{\text{at}} - \Delta H_{\text{alloy}}^{\text{at}} \quad (4-7)$$

Upon substitution of Equations 4-3 and 4-6 into Equation 4-7, a relationship for the interaction parameter is determined as a function of the lattice constants, by setting the interaction parameter equal to the enthalpy of mixing at $x = 0.5$ and using Vegard's Law to estimate the lattice constant of the alloy at the equimolar composition:

$$\Omega = 4K \left\{ \frac{\left(a_A^{-5.0} + a_B^{-5.0} \right)}{2} - \left[\frac{\left(a_A + a_B \right)}{2} \right]^{-5.0} \right\} \quad (4-8)$$

The calculated values of Ω are listed in Table 4-2 as well as Ω values based on the -2.5 power law dependency on the lattice constant derived for III-V systems strictly for reference and comparative purposes.

Table 4-2. Ω values for II-VI systems.

II-VI (ABC)	$\Omega [a_o^{-5}]$ (cal/mole $\text{\AA}^{-5.0}$)	$\Omega [a_o^{-2.5}]$ (cal/mole $\text{\AA}^{-2.5}$)
ZnCdS	2709.2	3613.9
ZnCdSe	1730.1	2569.4
ZnCdTe	1027.7	1824.7
ZnHgS	3076.6	4130.2
ZnHgSe	2013.0	3009.8
ZnHgTe	926.8	1639.2
CdHgS	11.7	17.3
CdHgSe	10.7	17.4
CdHgTe	2.6	5.0
ZnSSe	1184.1	1529.9
CdSSe	573.6	881.2
HgSSe	566.6	882.4
ZnSTe	6574.2	9277.9
CdSTe	3734.5	6231.2
HgSTe	3145.6	5265.3
ZnSeTe	2184.0	3278.1
CdSeTe	1383.6	2428.8
HgSeTe	1044.0	1838.8

With Ω values for alloys in the II-VI system, the chemical potential of the solid solution can be calculated from regular solution theory. The solution model can then be used to predict the equilibrium solid-vapor distribution of MOVPE grown ZnCdS. According to Figure 2-14, the growth process is mass transfer limited in the temperature range 300 to 450 $^{\circ}\text{C}$. A mass transfer limited process implies that the growth reactions at the surface are rapid and therefore, the gas near the surface should be in equilibrium with

the pseudobinary solid solution. Since MOVPE growth is prepared in an excess of H₂S and the results show a linear dependence on the group II molar flow rate, growth is limited by the mass transfer of the Zn and Cd species. The view then is that the near surface vapor phase composition is in equilibrium with the solid and related to the bulk (inlet) composition by mass transfer. If mass transfer is by diffusion through a boundary layer and the molecular diffusivity of the reaction Zn and Cd species are identical, then the inlet Cd mole fraction should be identical to the mean surface mole fraction, and the bulk value can be used to calculate the equilibrium solid composition.

To formulate this mode, first define the Cd molar fraction in the gas phase as

$$y = \frac{P_{\text{DMCd}}^{\circ}}{(P_{\text{DMCd}}^{\circ} + P_{\text{DEZn}}^{\circ})} \quad (4-9)$$

where P[°]_i is the inlet partial pressure of the input metalorganic precursors (DMCd or DEZn). The formation of Zn_{1-x}Cd_xS can be conveniently represented by the following reactions.



According to mass spectrometric and Knudsen-cell vaporization studies of II-VI compounds [132], both CdS and ZnS predominantly vaporize as atomic group II species and S₂. The binary (CdS and ZnS) gaseous products are too low in concentration to be detected. Since the near surface gas phase is in equilibrium with the solid solution, the

concentration of other gaseous species (e.g., S, S₈, ZnS (g), and CdS (g)) can always be calculated.

Assuming an ideal gas solution, the equilibrium constant, K_{eq}, for these two reactions are defined by the following relationships:

$$K_{\text{CdS}} = \frac{a_{\text{CdS}}}{P_{\text{Cd}} P_{\text{S}_2}^{1/2}} \quad (4-12)$$

$$K_{\text{ZnS}} = \frac{a_{\text{ZnS}}}{P_{\text{Zn}} P_{\text{S}_2}^{1/2}} \quad (4-13)$$

where a_i is the activity of component i and P_i is the partial pressure near the growth surface.

The component activities in the solid solution can be represented by the regular solution model as

$$a_{\text{CdS}} = x \exp \left[\frac{\Omega(1-x)^2}{RT} \right] \quad (4-14)$$

$$a_{\text{ZnS}} = (1-x) \exp \left[\frac{\Omega x^2}{RT} \right] \quad (4-15)$$

where Ω is the interaction parameter between ZnS and CdS, x is the Cd composition, R is the gas constant, and T is the absolute temperature. Although the ratio of Cd to Zn is not known at the reacting surface, it is assumed that the ratio is the same as that in the bulk gas phase. As a result,

$$\frac{y}{1-y} = \frac{P_{\text{Cd}}^{\circ}}{P_{\text{Zn}}^{\circ}} \approx \frac{P_{\text{Cd}}}{P_{\text{Zn}}} \quad (4-16)$$

Upon substitution of Equations 4-12 to 4-15 into Equation 4-16, the following relationship for the solid-vapor distribution of $Zn_{1-x}Cd_xS$ is derived:

$$\frac{y}{1-y} = \left(\frac{K_{ZnS}}{K_{CdS}} \right) \left(\frac{x}{1-x} \right) \exp \left[\frac{\Omega(1-2x)}{RT} \right] \quad (4-17)$$

Figure 4-3 shows the results of the predictive model with experimental data. One plot shows the fit with $\Omega = 2709 \text{ cal/mole } \text{\AA}^{-5.0}$ and K_{ZnS}/K_{CdS} set to 0.823. The ratio of the equilibrium constants is used as the single fitting parameter. For an ideal solution, with $\Omega = 0$ and assuming the ratio of K_s is unity, a 45° line is plotted as reference. The fit of the model with experimental data is not expected to be very accurate because in deriving a value for Ω , the assumption that Vegard's Law holds true for the entire compositional range is incorrect. Figure 2-15 in Chapter 2 shows that the lattice constant only follows Vegard's law for two different composition ranges: (1) $x = 0.0$ to $x = 0.67$ and (2) $x = 0.67$ to $x = 1.0$. In the former region, the endpoints are the lattice constants for cubic structures of ZnS and CdS and for the latter region, the endpoints are the "a" lattice constant of the hexagonal structure of ZnS and the "c" lattice constant of the hexagonal structure of CdS. As a result, a different Ω value should be used in the model for the two respective composition regions.

In region 1 for the composition of 0.0 to 0.67, the respective bandgap energies, lattice constants, and heats of atomization calculated assuming Vegard's Law are used to calculate the functional form in the relationship of bandgap energy to the lattice constant, $E_g = ka_o^x$. Upon determination of the exponent, x , the constant K can be calculated for the

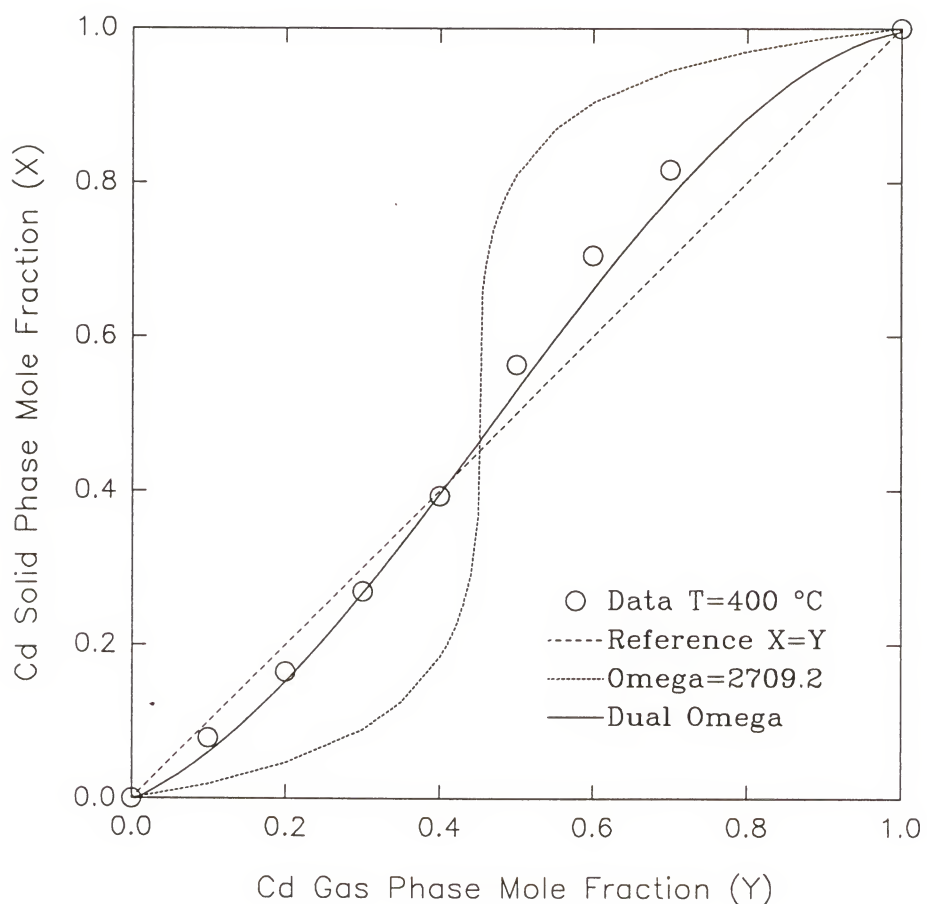


Figure 4-3. Fit of SVE model with ZnCdS data.

relationship $H^{at} = K a_o^x$. This was repeated for region 2 whose composition range is 0.67 to 1.0. The values used for these calculations are listed in Table 4-3.

Table 4-3. Parameters for two compositional regions of ZnCdS.

Composition x	Cubic Lattice Constant (\AA)	E_g (eV)	ΔH^{at} (cal/mole)
0.0	5.4093	3.6	306
0.67	5.6925	2.6012	285.23
1.0	6.74	2.38	275

The value of the bandgap energy for $x = 0.67$ is calculated from Equation 3-1 in Chapter 3; the heat of atomization is interpolated with the values of the binary constituent compounds; and the lattice constant is interpolated from Figure 2-15 in Chapter 2. Figure 4-4 shows the best fit of the bandgap energy with linear dependency on the lattice constant for the specific composition ranges of $x = 0$ to $x = 0.67$ and $x = 0.67$ to $x = 1.0$. Figures 4-5 and 4-6 describe the relationship between the heat of atomization and the lattice constant with the power dependence for the best fit for composition ranges of $x = 0$ to $x = 0.67$ and $x = 0.67$ to $x = 1.0$, respectively. The constant of proportionality are the slopes. The results for the functional exponent, the constant coefficient and Ω is listed in Table 4-4 below.

Table 4-4. Values of Fitting Parameters.

Region	x of $E_g = k a_o^x$	K of $H = K a_o^x$	Ω (cal/mole)
1 ($x = 0$ to 0.67)	-6.5	1.02×10^9	947.2
2 ($x = 0.67$ to 1)	-0.5	7.21×10^4	309.6

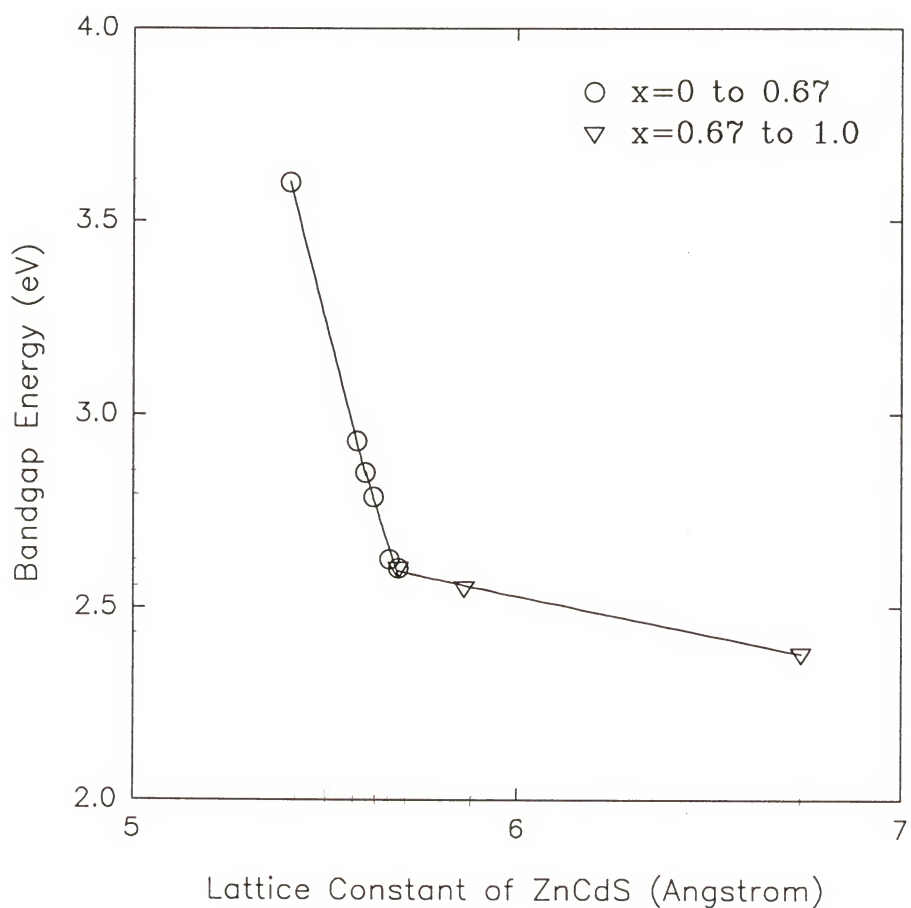


Figure 4-4. Best fit between bandgap energy and power law dependence for lattice constant of two composition ranges of $x = 0$ to $x = 0.67$ and $x = 0.67$ to $x = 1.0$.

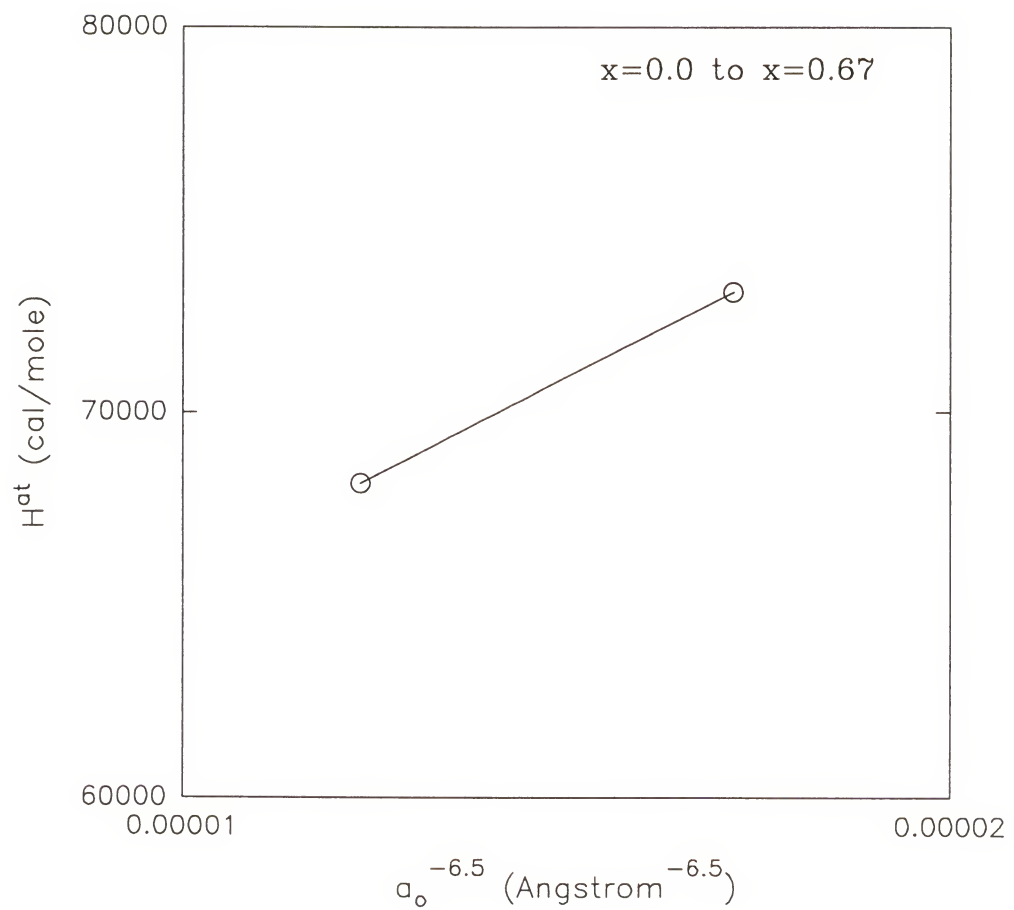


Figure 4-5. Linear relationship between ΔH^{at} and $a_o^{-6.5}$ for $x = 0$ to $x = 0.67$.

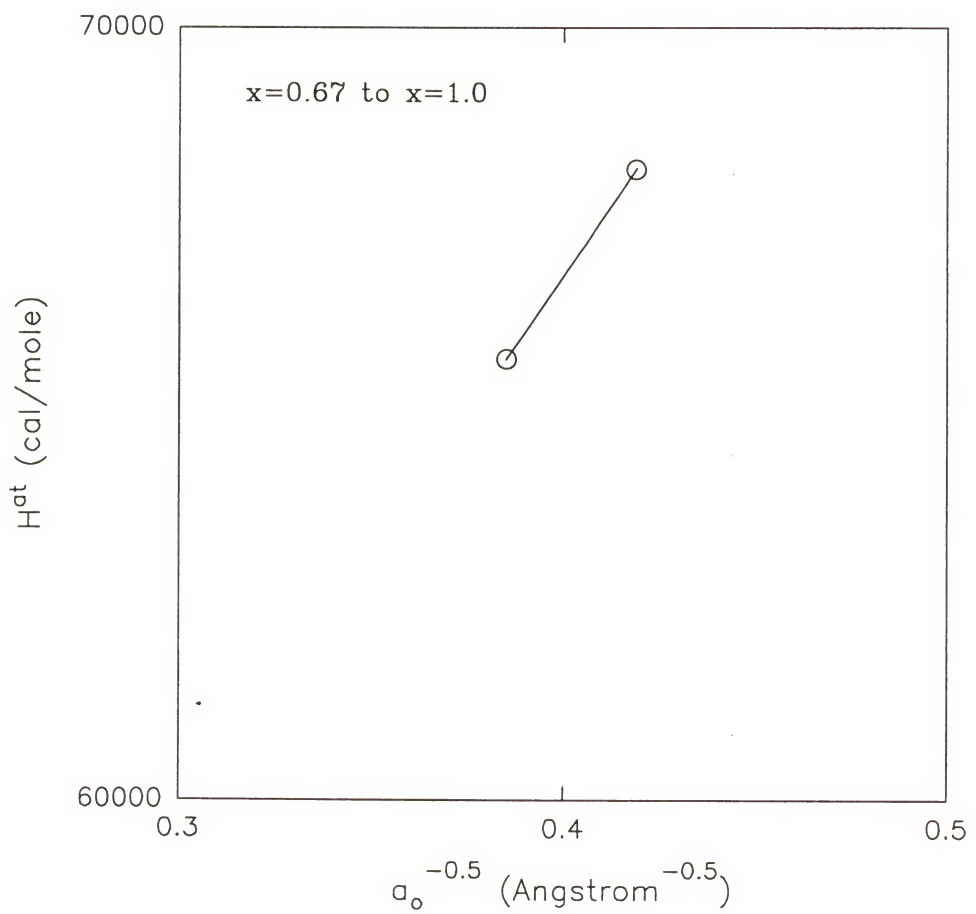


Figure 4-6. Linear relationship between ΔH^{at} and $a_o^{-0.5}$ for $x = 0.67$ to $x = 1.0$

From Figure 4-3, the model fits fairly well with the experimental data upon setting K_{Zn}/K_{Cd} to be 0.8854 for the best fit. There are no literature data on the equilibrium constants for the reactions of the growth process. It is quite remarkable that a model with essentially one fitting parameter can so accurately predict the solid-vapor distribution. To demonstrate the robustness of this model, Figure 4-7 shows the plot of the model fit with the data at temperatures of 27.59, 150, 250, and 350 °C. The model gives the correct trend of increasing Cd solid content with decreasing temperature. The data, however, are not a good test since the model predicts a distribution coefficient of unity at all temperatures at a Cd composition of $x = 0.5$. The room temperature data does not conform well with the model. This is not surprising since at room temperature, the solid composition is not expected to be in equilibrium with the gas phase composition. Referencing to Figure 2-14, the growth process is obviously kinetically limited below 300 °C. Since the film is Cd-rich relative to the vapor inlet, the Cd reactant apparently decomposes more rapidly than the Zn precursor.

This approach has also proved itself successful in describing solid-vapor equilibrium for many III-V systems [180], including the $GeAs_{1-x}Sb_x$ [181] and $InAs_{1-x}Sb_x$ systems [182]. To test the validity of this model further, it was applied to other II-VI systems. Figure 4-8 shows a plot of the solid composition of $ZnSe_xS_{1-x}$ grown by MOVPE as a function of the inlet gas composition. This system is more well behaved since both ZnS and ZnSe naturally occur in the same phase [183].

The Ω value used is 1184.1 as suggested in Table 4-4 and the best fit of 0.2 was used for the ratio of the equilibrium constants K_{ZnS}/K_{ZnSe} . The fit again is remarkably good

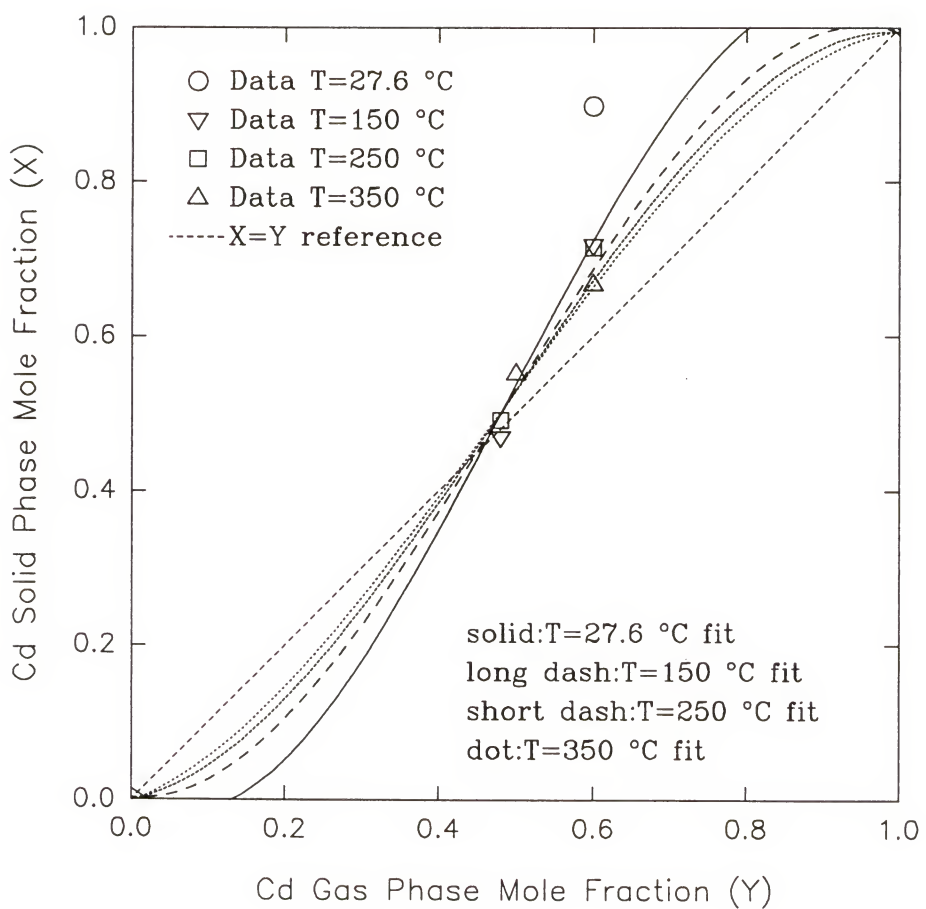


Figure 4-7. Comparison of SVE model with ZnCdS data at various temperatures. The fit for $T = 27.6 \text{ } ^\circ\text{C}$ is poor as the plot does not meet the endpoints, $(0,0)$ and $(1,1)$.

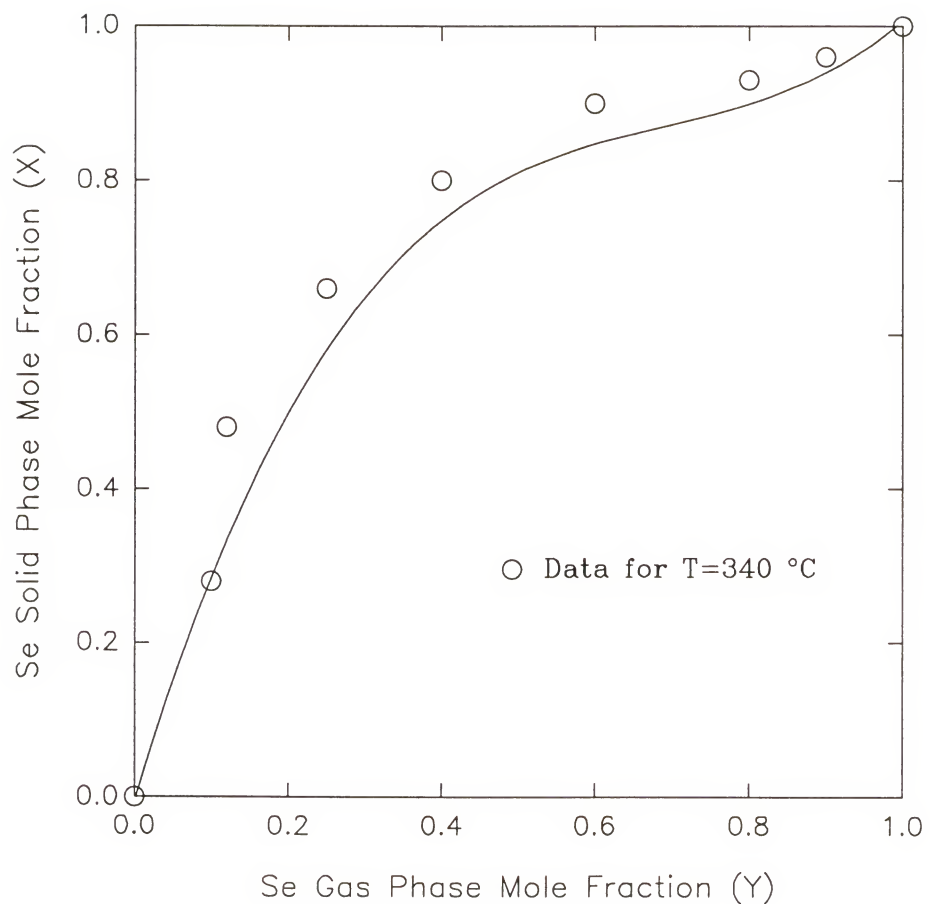


Figure 4-8. Fit of SVE model with ZnSSe.

considering that only one parameter was adjusted, although the validity of this model needs to be tested more with available data at other temperatures.

4.2 Summary

The solid vapor equilibrium of ZnCdS has been modeled using a regular solution model for the solid solution. Stringfellow's DLP model was invoked to calculate the interaction parameter between the constituent binary compounds. For the first time the interaction parameters were calculated based on material properties of II-VI compounds. The behavior of the II-VI systems was different than that of the III-V system in that the empirical exponent on the lattice constant in relation to the bandgap energy was -5.0 for the II-VI family and was -2.5 for the III-V systems. The interaction parameters were calculated with the assumption of a linear relationship between the lattice constant and the composition, and thus neglecting the bowing parameter. For ZnCdS, there are two distinct regions where approximate linearity holds. The interaction parameter is calculated for each respective region.

An expression that relates the solid phase composition with the gas phase composition was derived on the basis of equilibrium between the near surface gas phase and the film. The fit with experimental data is poor when the interaction parameter assuming Vegard's law is used but is quite accurate when the interaction parameter based upon the actual correlation between the lattice constant and composition is used. The fit is good with data points at 150, 250, and 350 °C. The fit is poor at 27.59 °C as expected

since equilibrium is not achieved at such a low growth temperature. This approach is shown to be valid for modeling solid vapor equilibrium of ZnSSe as well.

CHAPTER 5

WAVEGUIDE FABRICATION AND CHARACTERIZATION

Like any other solid state or gas laser, the semiconductor laser is characterized by monochromatic and coherent electromagnetic radiation when electrically charged. However, the semiconductor device is much smaller and easier to modulate at high frequencies. These unique qualities contribute to the successful application of the semiconductor laser in many scientific and commercial fields: optical-fiber communications, video recording, optical reading, high speed laser printing, eye surgery, high resolution gas spectroscopy, and pollution monitoring.

With a shorter wavelength relative to the current infrared technology, blue light will become more valuable for optical data storage and laser printing. The smaller spot size will increase the storage capability for a given area by a factor of four and enhance the resolution of laser printing [184-185]. Furthermore, blue light is the missing primary color for applications in flat panel displays and high definition televisions.

The main issue with fabrication of LEDs and lasers is the choice of the appropriate semiconductor materials for the laser design. The active layer must be a direct bandgap material for high probability of radiative recombination with band to band transitions between electrons and holes. The cladding layers must at least have higher bandgap energies and smaller refractive indices than the active layer for good carrier and optical confinement characteristics, respectively. The bandgap energy of the cladding layer must

be energetically bounded by the bandgap energy of the cladding layer in a normal configuration to confine both holes and electrons within the active layer. It must also be possible to dope the cladding layers n and p-type for carrier injection luminescence.

In the past, many II-VI compound semiconductors have demonstrated blue/green emission through photopumping experiments. ZnTe, ZnSSe, ZnSe, ZnMnSe, CdS, and CdSSe are the most recent materials [183, 186-189]. However, all these experiments were performed at temperatures below 200 K and room temperature current injection blue light emitting LEDs have been demonstrated with SiC [190] and ZnSe [191-193]. Appropriate confinement layers have to be grown to further develop them into laser diodes.

Lasers operate under the principle of stimulated emission. This requires the electron density of the excited state to be significantly greater than that of the ground state and this condition is often termed population inversion. For carrier injection luminescence, the cladding layers need to be adequately n and p-type doped to achieve population inversion during forward bias. Efficient radiative recombination of electrons and holes can only occur with sufficient carrier confinement to prevent stray diffusion of carriers away from the active layer in a DH structure. Electron affinities along with the bandgap energies of the active and cladding layers are used to calculate the extent of carrier confinement. To maintain stimulated emission and prevent domination by spontaneous emission, an optical resonant cavity is used, usually the Fabry-Perot cavity to increase the photon field. The flat reflective mirrors formed by cleaving are parallel to each other and perpendicular to the growth surface. In addition, optical confinement is necessary to minimize attenuation

of emitted electromagnetic radiation through the lossy cladding layers. Light loss will be reduced if the refractive index of the active layer is greater than that of the cladding layer. Otherwise, the light will transmit through the active/cladding layer interface instead of reflecting back internally within the active layer.

As a first step in fabrication of DH lasers, a waveguide of similar structure is photopumped to determine lasing capability and optical confinement. A symmetric three-layer slab waveguide structure has been investigated. ZnCdS/ZnSe/ZnCdS has been grown by the MOVPE technique and theoretical calculations have been performed to evaluate carrier concentration requirements, optical confinement, and carrier confinement.

5.1 Sample Preparation

The ZnCdS/ZnSe/ZnCdS waveguide structure was grown by the low pressure MOVPE technique on GaAs. In both cases the ZnCdS cladding layers are grown at 550 °C with a reactor pressure of 70 Torr. The solid phase composition ($x = 0.58$ Cd fraction) is lattice matched to the GaAs substrate. The overall Zn and Cd mole fractions are 0.39×10^{-4} and 1.68×10^{-4} , respectively. The VI/II ratio is 175. For ZnSe growth, the Zn mole fraction is 0.8×10^{-4} and the VI/II ratio is 100. The substrate orientations are (100) 0° and 2° toward the <110> direction; and (111)A and (111)B GaAs substrates supplied by Sumitomo Electric Company.

The ZnCdS cladding layers and the ZnSe active layer are 1.0 and 0.5 μm thick, respectively. The cleaning and pre-growth procedures are similar to those mentioned in Chapter 2. The samples were thinned on the substrate side and cleaved into 200 μm wide

resonators for photopumping. For the (100) substrates, the cleavage planes were perpendicular to the growth surface and so easily formed into resonators. For the (111) orientation, however, test cleaves were made to determine the angle it forms relative to one sawed edge. The wafers were then scribed and cleaved to form rectangular shaped resonators with the reflective edges parallel to each other. The solid phase composition and film thickness is determined by EPMA and cross sectional SEM, respectively.

5.2 Experiment and Results

A resonator is mounted on a holder to freely expose the pumping region. The photopumping light source is a 446 nm helium cadmium continuous wave laser. The intensity of the incident laser light source is modulated by a filter and a photodiode is used to measure the laser power. The light emission from the resonators is collected through an objective lens and directed into a grating monochromator for spectral analysis.

Optical gain is the main criterium for evaluating materials as potential lasers. The optical gain manifests itself through spectral narrowing in PL measurements [194]. In addition, excitation wavelength, power and temperature needed to achieve optical gain may also be revealed. PL measurements of an optical resonator should produce both spectral narrowing and a sharp spectral line. Figure 5-1 depicts the room temperature PL measurement of the ZnCdS/ZnSe/ZnCdS waveguide with laser power ranging from 400 to 250 mW at wavelengths between 450 and 475 nm. Unfortunately, spectral narrowing nor a sharp spectral line was observed. Although evidence of optical gain is not apparent, the

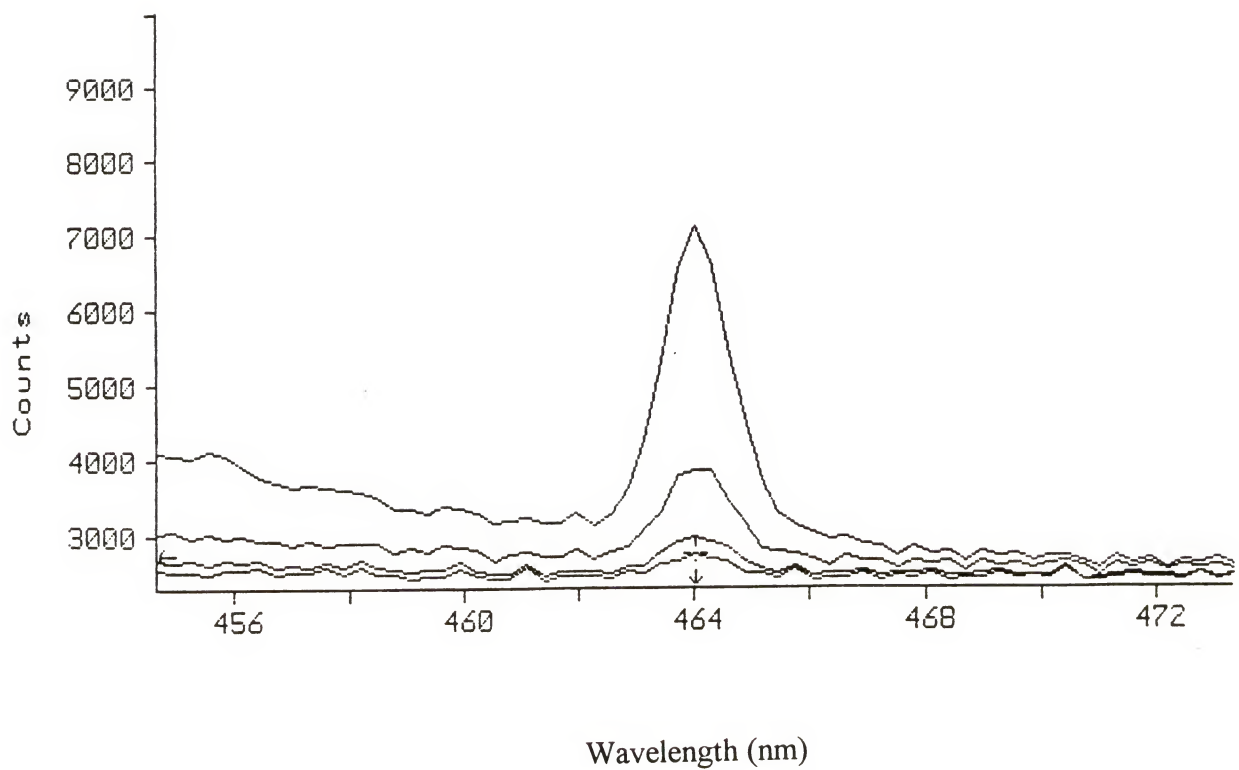


Figure 5-1. Room temperature PL measurement of ZnCdS/ZnSe/ZnCdS DH structure.

PL measurements indicate a maximum peak at 464 nm and the onset of excitation between 300 and 350 mW. The peak intensity of 464 nm suggests that ZnCdS is the source of optical excitation instead of ZnSe which is excited at slightly longer wavelengths.

The major factor for this anomalous behavior is the poor crystalline quality of the ZnSe active layer as indicated by the high FWHM of HRXRD peaks in Figure 5-2. This is presumably caused by a high defect density. The difference in lattice constants between ZnSe and ZnCdS lattice matched to GaAs can produce misfit dislocations that act as nonradiative recombination centers and hinder emission of light.

5.3 Theoretical Calculations

5.3.1 Optical Confinement

Unlike doped homostructures which may not have the necessary refractive index difference, heterostructures typically have an abrupt refractive index step of at least 10^{-2} . The double heterostructure laser provides a well defined dielectric waveguide and was the first injection laser to give continuous wave (cw) room temperature operation [195]. The DH laser is easier to quantitatively analyze than the homojunction structures because of its significant change in the refractive index that minimizes the effects of parameters that influence homostructures. A DH laser configuration with ZnSe as the active layer and n and p-type ZnCdS as confining layers is shown in Figure 5-3 (a). Similar structures with GaAs as the active layer and n and p-type AlGaAs as confining layers have been analyzed by several authors [196-197]. It is not necessary to analyze such a complicated structure

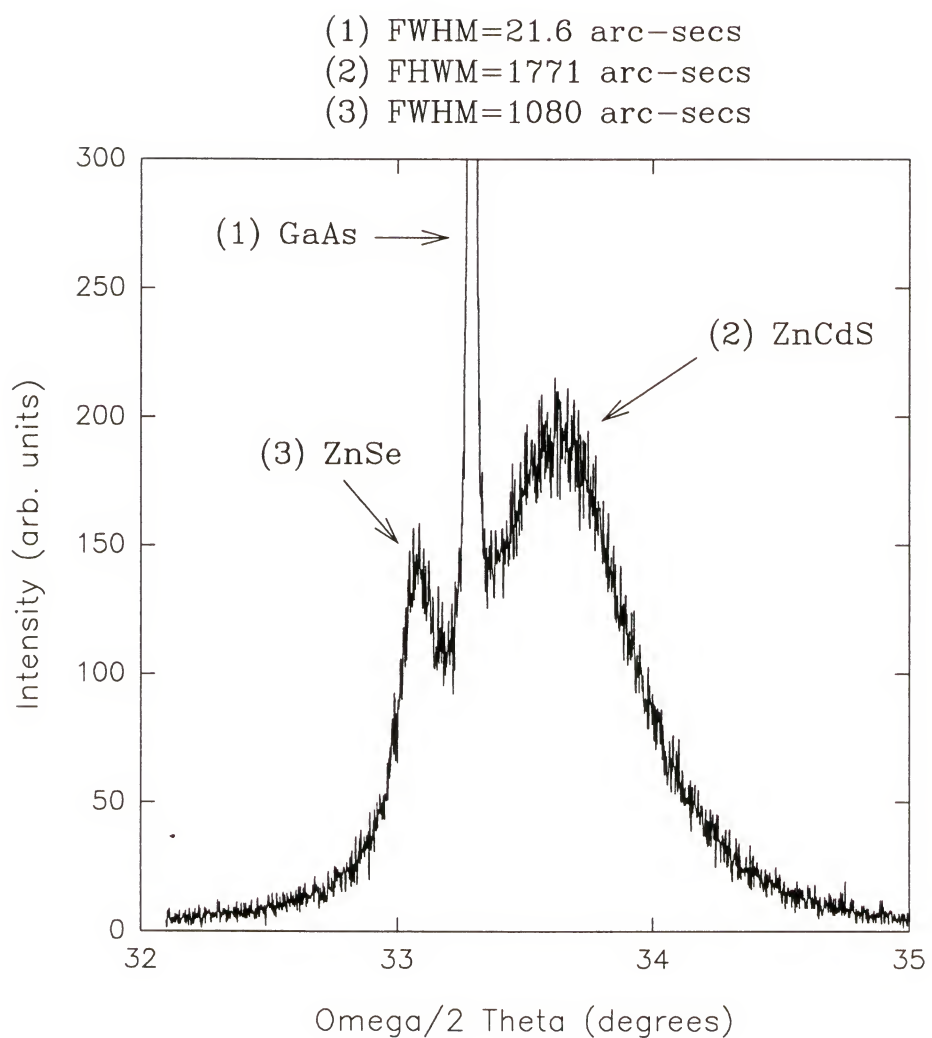
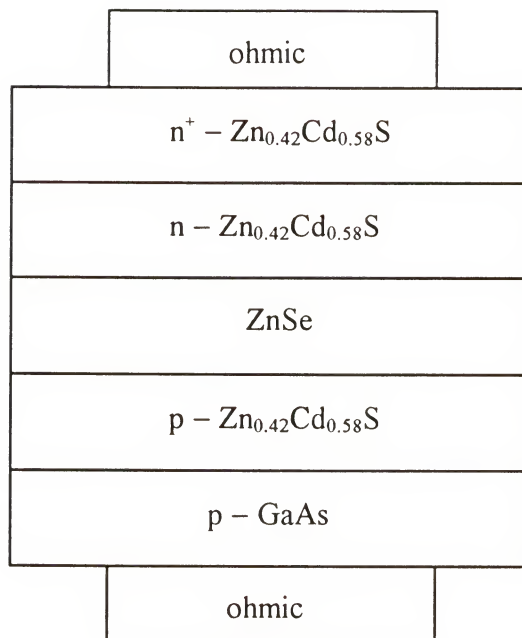
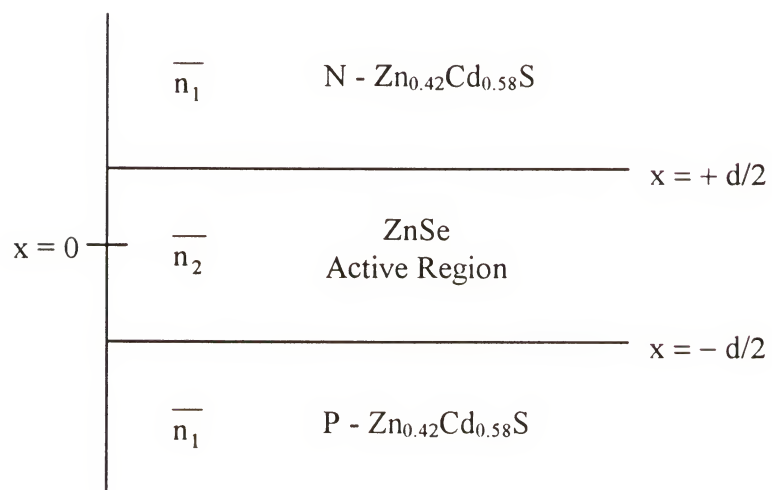


Figure 5-2. HRXRD peak of ZnCdS/ZnSe/ZnCdS DH structure.



(a)



(b)

Figure 5-3. Schematic of $\text{ZnCdS}/\text{ZnSe}/\text{ZnCdS}$ DH structure: (a) complete and (b) symmetric three layer slab waveguide.

and a simpler three-layer slab waveguide shown in Figure 5-3(b) provides the essential features of wave propagation in a laser structure.

The description of optical field distributions perpendicular to the junction plane of a heterostructure laser is derived from Maxwell's equations, more specifically the three-dimensional wave equation. The double heterostructure (DH) laser in its simplest form can be treated as a symmetrical three layer slab dielectric waveguide to describe wave propagation in a laser. The center layer is called the active layer and is where the light is generated. The two outer layers are called the cladding or confining layers since they prevent the loss of light once it is generated in the active layer. Differential equations describing the propagation of the electric field polarized transverse to the direction of propagation, the transverse electric (TE) field, is derived. Similar equations are derived for the magnetic field polarized transverse to the direction of the propagation, the transverse magnetic (TM) field. These fields are dependent on two spatial variables and time. The solution of these wave equations can be obtained through a separation of variables. The solutions indicate that for waveguiding in a three-layer slab, the refractive index of the active layer must be larger than that of the confining layers. Boundary conditions for the electric and magnetic fields applied at the interface results in the eigenvalue equation that permits only discrete, quantum values of the propagation constant. The resulting electric and magnetic field configurations for these discrete values of the propagation constants are more commonly called modes. The details of the calculations are described elsewhere [198].

Both the TE mode with the electric field polarized transverse to the direction of propagation and the TM mode with the magnetic field polarized transverse to the direction of propagation are studied. In order to solve the electric and magnetic field equations, boundary conditions are defined so that the tangential components of the electric and magnetic field are continuous at the dielectric interface. The analysis is simplified by considering even and odd solutions separately. The even and odd solutions for the TE and TM modes are shown below.

Even TE modes:

$$E_y = A_e \cos(\kappa x) \exp[j(\omega t - \beta z)] \quad \{AR\} \quad (5-1)$$

$$H_z = \left(\frac{-j\kappa}{\omega\mu_0} \right) A_e \sin(\kappa x) \exp[j(\omega t - \beta z)] \quad \{AR\} \quad (5-2)$$

$$E_y = A_e \cos\left(\frac{\kappa d}{2}\right) \exp\left[-\gamma\left(|x| - \frac{d}{2}\right) \exp[j(\omega t - \beta z)]\right] \quad \{CR\} \quad (5-3)$$

$$H_z = \left(\frac{-x}{|x|} \right) \left(\frac{j\gamma}{\omega\mu_0} \right) A_e \cos\left(\frac{\kappa d}{2}\right) \exp\left[-\gamma\left(|x| - \frac{d}{2}\right)\right] \exp[j(\omega t - \beta z)] \quad \{CR\} \quad (5-4)$$

Odd TE modes:

$$E_y = A_o \sin(\kappa x) \exp[j(\omega t - \beta z)] \quad \{AR\} \quad (5-5)$$

$$H_z = \left(\frac{j\kappa}{\omega\mu_0} \right) A_o \cos(\kappa x) \exp[j(\omega t - \beta z)] \quad \{AR\} \quad (5-6)$$

$$E_y = \left(\frac{x}{|x|} \right) A_o \sin\left(\frac{\kappa d}{2}\right) \exp\left[-\gamma\left(|x| - \frac{d}{2}\right)\right] \exp[j(\omega t - \beta z)] \quad \{CR\} \quad (5-7)$$

$$H_z = \left(\frac{-j\gamma}{\omega\mu_0} \right) A_o \sin\left(\frac{\kappa d}{2} \right) \exp\left[-\gamma\left(|x| - \frac{d}{2} \right) \right] \exp[j(\omega t - \beta z)] \quad \{CR\} \quad (5-8)$$

Even TM modes:

$$E_z = \left(\frac{j\kappa}{\bar{n}_2^2 \omega \epsilon_0} \right) B_e \sin(\kappa x) \exp[j(\omega t - \beta z)] \quad \{AR\} \quad (5-9)$$

$$H_y = B_e \cos(\kappa x) \exp[j(\omega t - \beta z)] \quad \{AR\} \quad (5-10)$$

$$E_z = \left(\frac{x}{|x|} \right) \left(\frac{j\gamma}{\bar{n}_1^2 \omega \epsilon_0} \right) B_e \cos\left(\frac{\kappa d}{2} \right) \exp\left[-\gamma\left(|x| - \frac{d}{2} \right) \right] \exp[j(\omega t - \beta z)] \quad \{CR\} \quad (5-11)$$

$$H_y = B_e \cos\left(\frac{\kappa d}{2} \right) \exp\left[-\gamma\left(|x| - \frac{d}{2} \right) \right] \exp[j(\omega t - \beta z)] \quad \{CR\} \quad (5-12)$$

Odd TM modes:

$$E_z = \left(\frac{-j\kappa}{\bar{n}_2^2 \omega \epsilon_0} \right) B_o \cos(\kappa x) \exp[j(\omega t - \beta z)] \quad \{AR\} \quad (5-13)$$

$$H_y = B_o \sin(\kappa x) \exp[j(\omega t - \beta z)] \quad \{AR\} \quad (5-14)$$

$$E_z = \left(\frac{j\gamma}{\bar{n}_1^2 \omega \epsilon_0} \right) B_o \sin\left(\frac{\kappa d}{2} \right) \exp\left[-\gamma\left(|x| - \frac{d}{2} \right) \right] \exp[j(\omega t - \beta z)] \quad \{CR\} \quad (5-15)$$

$$H_y = \left(\frac{x}{|x|} \right) B_o \sin\left(\frac{\kappa d}{2} \right) \exp\left[-\gamma\left(|x| - \frac{d}{2} \right) \right] \exp[j(\omega t - \beta z)] \quad \{CR\} \quad (5-16)$$

where $\kappa^2 = \bar{n}_T^2 \kappa_o^2 - \beta^2$, $\gamma^2 = \beta^2 - \bar{n}_1^2 k_o^2$, $\bar{n}_1 \equiv$ cladding layer, $\bar{n}_2 \equiv$ active layer, AR is the active region, and CR is the confining region.

These field components in the confining region that have exponential attenuation without phase shift in the transverse plane are called evanescent waves. The eigenvalue

equations are listed below for symmetric (even) and antisymmetric (odd) TM and TE waves.

$$\text{TE Even: } X \tan X = Y \quad (5-17)$$

$$\text{TE Odd: } -X \cot X = Y \quad (5-18)$$

$$\text{TM Even: } \left(\frac{n_1}{n_2} \right)^2 X \tan X = Y \quad (5-19)$$

$$\text{TM Odd: } -\left(\frac{n_1}{n_2} \right)^2 X \cot X = Y \quad (5-20)$$

$$X^2 + Y^2 = \left(n_2^2 - n_1^2 \right) \left(\frac{k_o d}{2} \right)^2 = R^2 \quad (5-21)$$

$$X > \frac{\kappa d}{2} \quad \text{where } \kappa^2 = \beta^2 - n_1^2 k_o^2 \quad (5-22)$$

$$Y = \frac{\gamma d}{2} \quad \text{where } \gamma^2 = n_2^2 k_o^2 - \beta^2 \quad (5-23)$$

$$k_o = \frac{2\pi}{\lambda} \quad (5-24)$$

where λ = wavelength of light, β is defined as the phase constant, d is the active layer thickness and; n_1 and n_2 are the refractive indices of the confining and active layers, respectively. The graphical solution to these eigenvalue equations is shown in Figure 5-4 through 5-7 for the even and odd modes. The intersection of the plots are the solutions and by solving the solutions in graphical form, the modes and cutoff are better visualized. For given modes, there is a cutoff for the thickness of the active layer. For $d = 0.2 \mu\text{m}$ active layer thickness, the solution crosses at the $m = 0$ or fundamental mode. No matter how small the thickness, it will never get cut-off for a symmetrical structure. The values

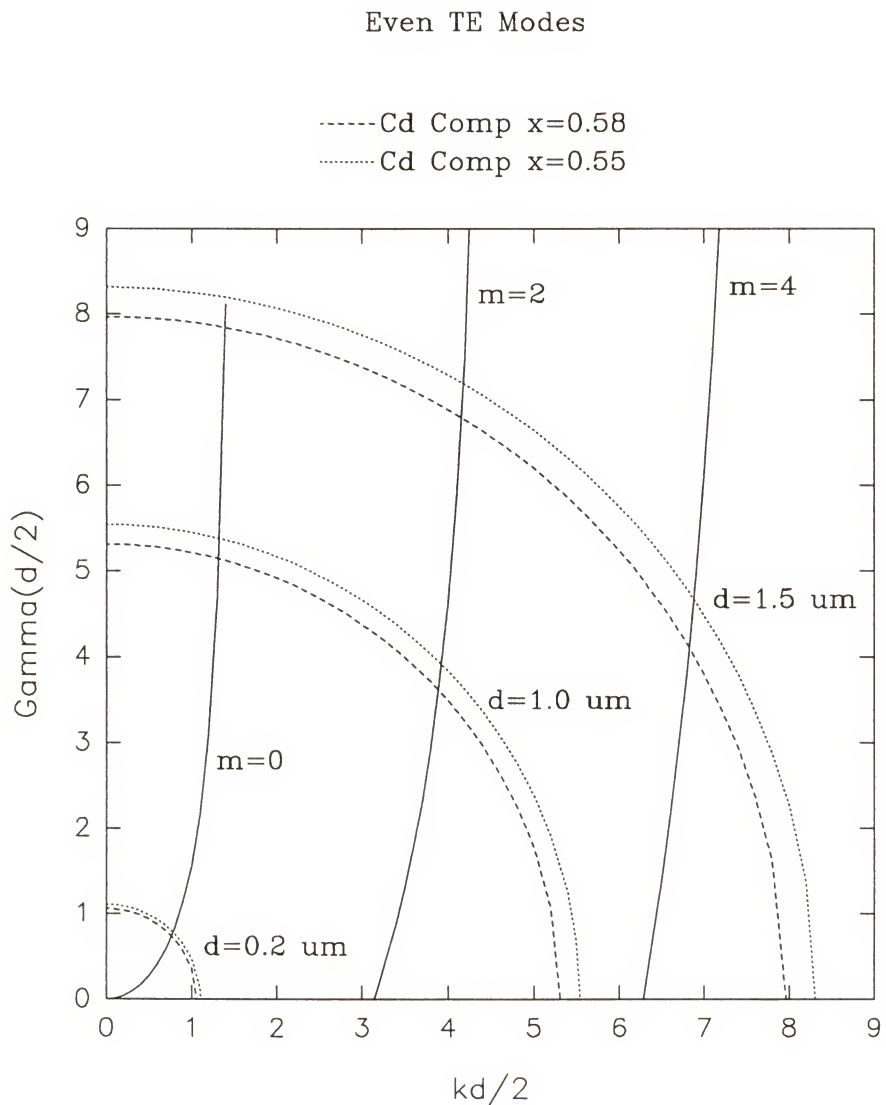


Figure 5-4. Eigenvalue solution for the even TE modes.

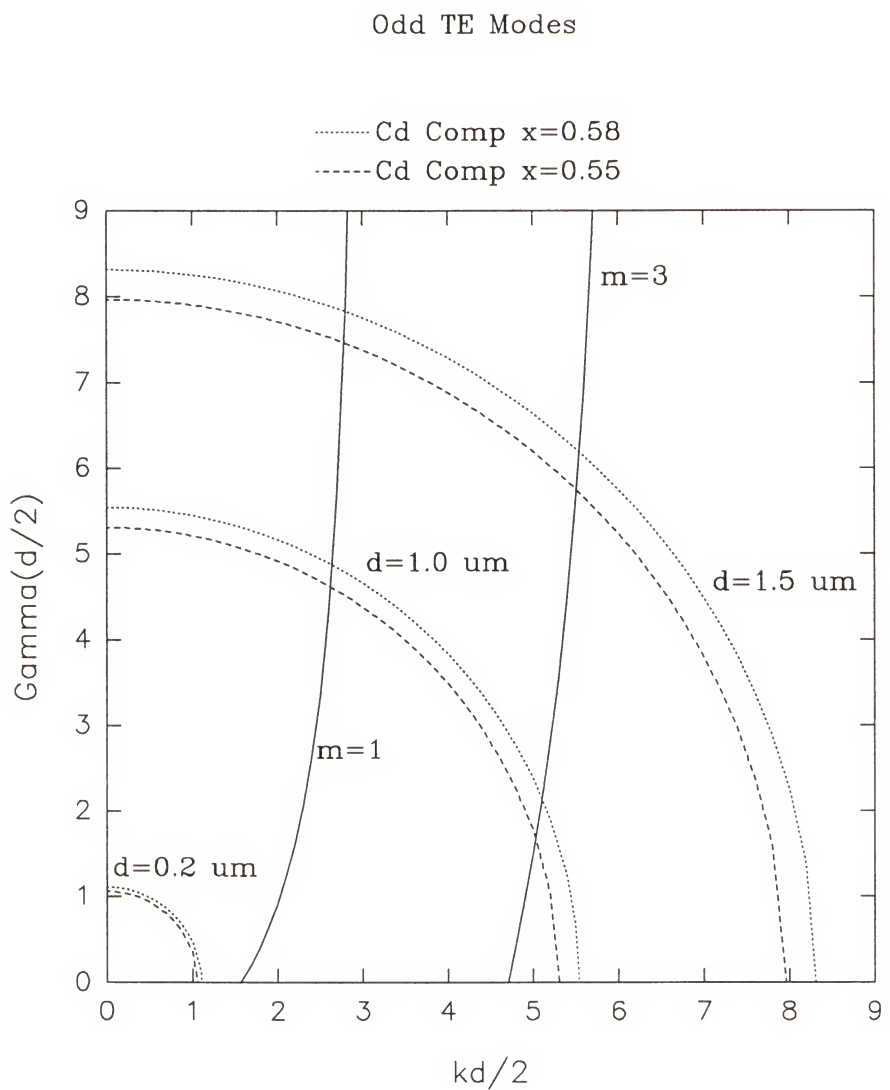


Figure 5-5. Eigenvalue solution for the odd TE modes.

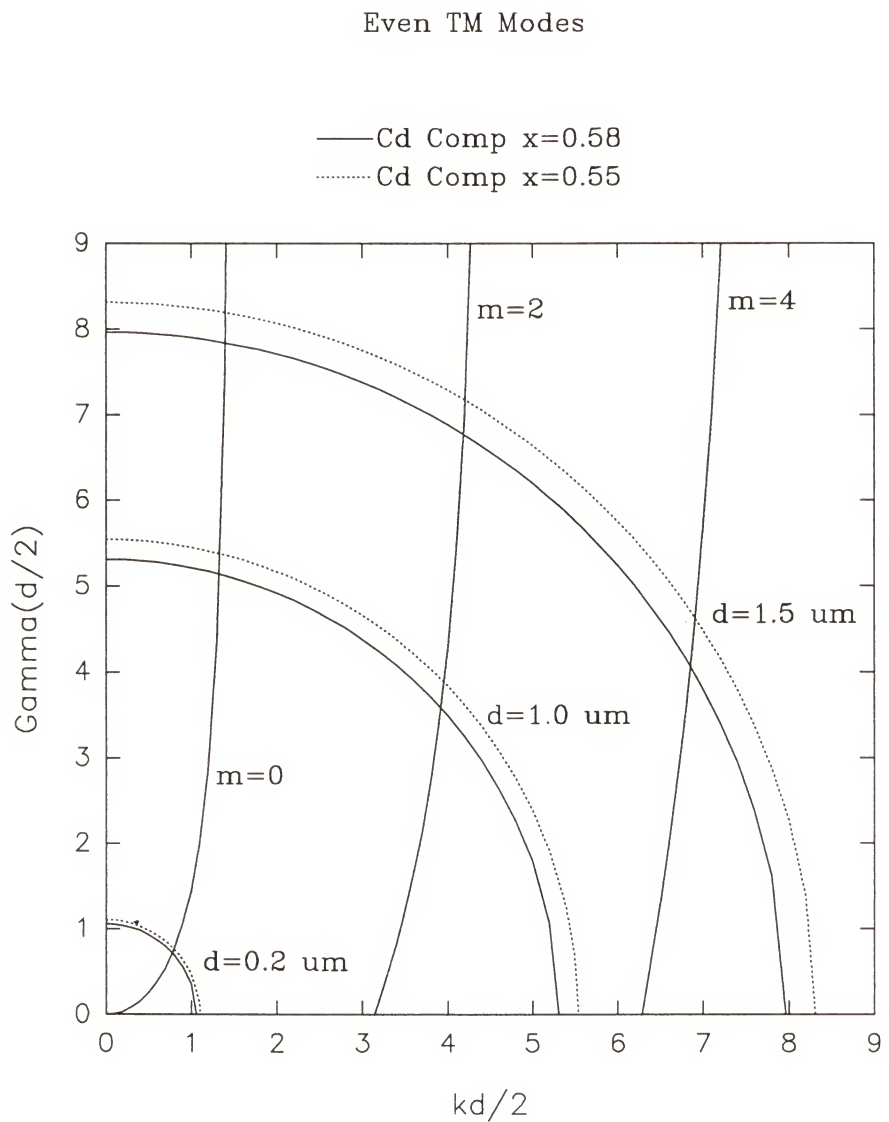


Figure 5-6. Eigenvalue solution for the even TM modes.

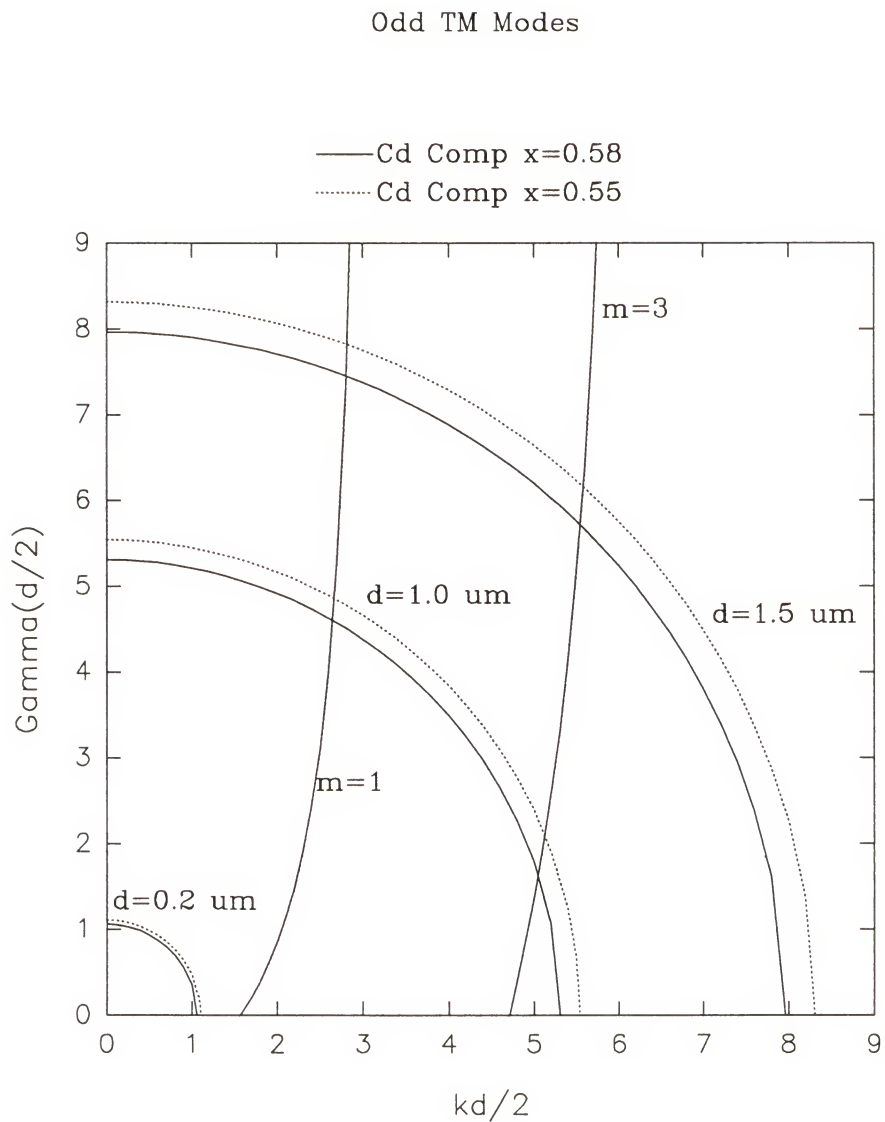


Figure 5-7. Eigenvalue solution for the odd TM modes.

of γ and κ obtained in this way permit calculation of the field distributions. The refractive indices for ZnCdS at $x = 0.58$, $x = 0.55$ and ZnSe are 2.7939, 2.7842, and 2.90, respectively at 460 nm, the wavelength of blue light. The refractive indices for ZnCdS are collected from Figures 3-9 and 3-10 in Chapter 3 and those of ZnSe from reference [199].

The term $\gamma d/2$ represents the exponential decay rate of the fields away from the active layer, a larger value means that the field is more tightly confined to the active layer. In comparison with TM waves, TE modes always experience greater confinement and can thus be considered the dominant mode. The value of $\gamma d/2$ is smaller for the TM mode as compared to the TE mode, which indicates further extension of the fields into the confining layers for the TM case. Such regions are lossy for heterostructure lasers and as a result fields tend to oscillate in the TE orientation.

The behavior of guided waves in heterostructure lasers can easily be seen by considering some representative examples. Numerical results are listed in Table 5-1. They were solved by the Newton-Raphson method.

Expressions for the symmetric and antisymmetric electric fields are used to determine E_y at $z = 0$ for $t = 0$ as shown in Figure 5-8. At the center of the waveguide the even modes always have the maximum and the odd modes are zero. Some of the E_y have considerable magnitude outside the active layer of the three-layer slab dielectric waveguide. That portion of the field is unavailable for interaction with the injected carrier density and does not contribute to stimulated emission in DH lasers. Since the stimulated emission and gain coefficient are related to the photon flux, it is important to consider the field distribution to determine the fraction of the optical mode within the laser active layer.

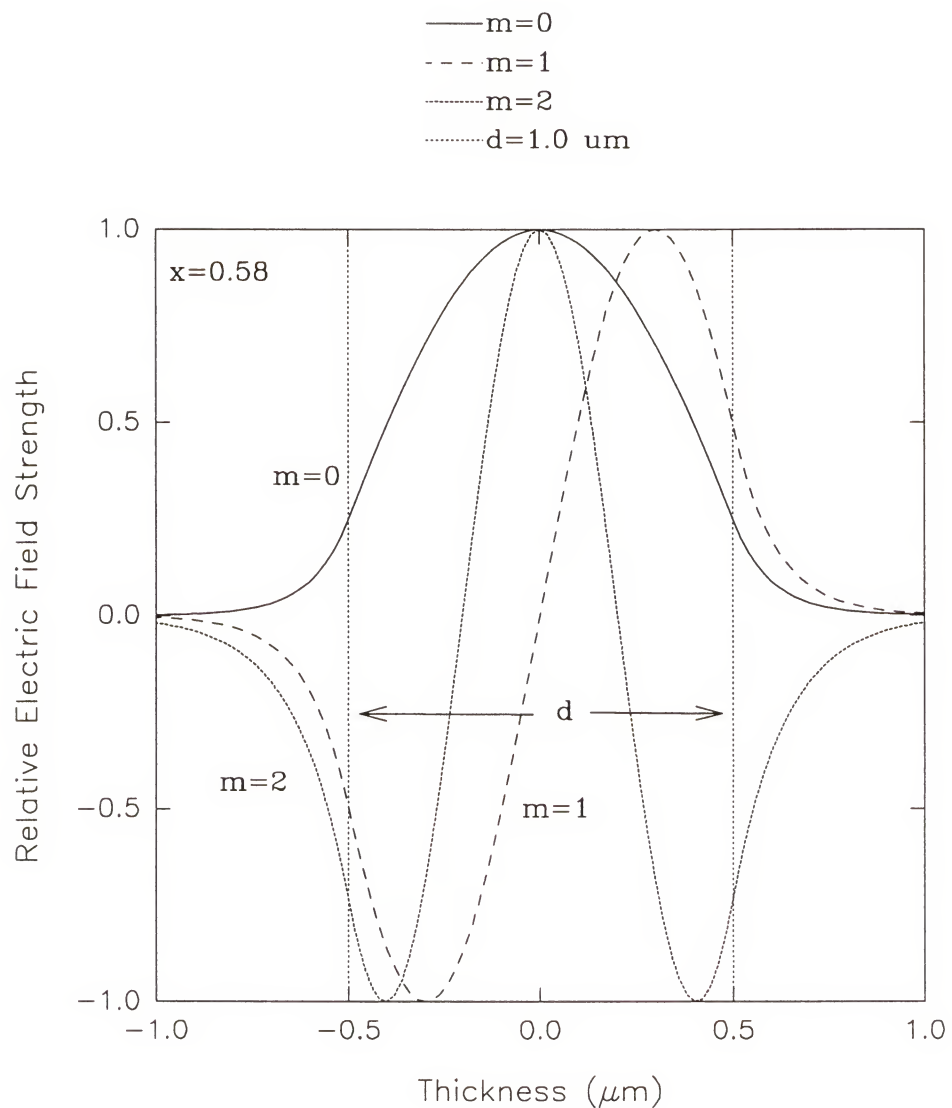


Figure 5-8. TE electric field strength for symmetric and antisymmetric modes.

The optical flux is given by the Poynting vector \mathbf{S} which shows that $\mathbf{E} \times \mathbf{H}$ is proportional to the $|E_y|^2$. Therefore, the optical intensity $|S| = I$ which is proportional to $|E_y|^2$ is a more useful quantity to consider for lasers than E_y . The extent of light confinement within the active layer may be represented by the confinement factor Γ which is defined as the ratio of the light intensity within the active layer to the sum of the light intensity both within and outside the active layer. A general expression for Γ is given as

$$\Gamma = \frac{\int_0^d E_y^2 dx}{\int_{-\infty}^{\infty} E_y^2 dx} \quad (5-25)$$

But since E_y^2 is a symmetric function, only half of the function needs to be considered so it is rewritten as

$$\Gamma = \frac{\int_0^{d/2} E_y^2 dx}{\int_0^{\infty} E_y^2 dx} \quad (5-26)$$

With Equation 5-1 and 5-3, Γ for the symmetric three-layer slab dielectric waveguide is given by the following expression:

$$\Gamma = \frac{\int_0^{d/2} \cos^2(\kappa x) dx}{\int_0^{d/2} \cos^2(\kappa x) dx + \int_0^{\infty} \cos^2\left(\frac{\kappa d}{2}\right) dx \exp\left[-2\gamma\left(x - \frac{d}{2}\right)\right] dx} \quad (5-27)$$

which gives

$$\Gamma = 1 + \frac{\cos^2\left(\frac{\kappa d}{2}\right)}{\gamma \left[\left(\frac{d}{2}\right) + \left(\frac{1}{\kappa}\right) \sin\left(\frac{\kappa d}{2}\right) \cos\left(\frac{\kappa d}{2}\right) \right]} \quad (5-28)$$

for the even TE modes. Similar equations for odd TE modes; and even and odd TM modes can be derived.

Table 5-1 Solutions to eigenvalue equations for symmetric three-layer slab waveguide: $n_2 = 2.9$ and $\lambda_o = 0.46 \mu\text{m}$.

d (μm)	m	β For $m = 0$	β/k_o	$\kappa d/2$	$\gamma d/2$
0.1	0	39.372	2.882	0.473	0.242
0.2	0	39.455	2.889	0.766	0.735
0.3	0	39.506	2.892	0.940	1.286
0.4	0	39.537	2.895	1.052	1.844
0.5	0	39.557	2.896	1.131	2.401
1.0	0	39.593	2.898	1.320	5.142
For $m=1$					
0.4	1	39.353	2.881	1.963	0.811
0.5	1	39.408	2.885	2.179	1.516
0.6	1	39.451	2.888	2.324	2.178
1.0	1	39.538	2.895	2.624	4.614
For $m = 2$					
1.0	2	39.450	2.888	3.890	3.612
1.5	2	39.529	2.894	4.162	6.788

Figure 5-9 illustrates that with richer Cd composition, the confinement factor becomes slightly reduced. For composition of $x = 0.58$ and 0.55 , the difference is small and insignificant. But this graph is just an illustration of the trends seen in confinement factors with composition variation. The variation of the optical intensity with active layer thickness is shown in Figure 5-10. As the active layer becomes smaller, the light spreads further into the confining layers and less of the total intensity is within the active layer. For the case of larger d where higher order modes are permitted, Figure 5-11 shows that

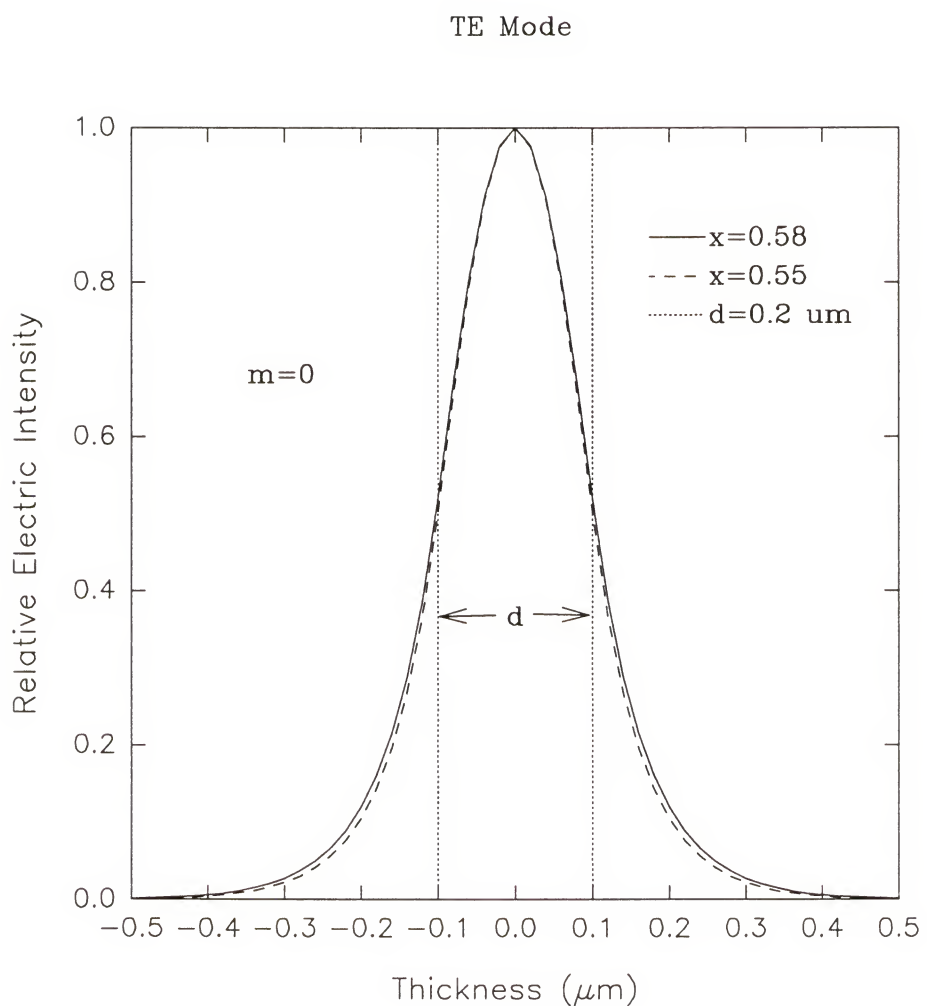


Figure 5-9. Dependence of TE electric intensity on ZnCdS composition.

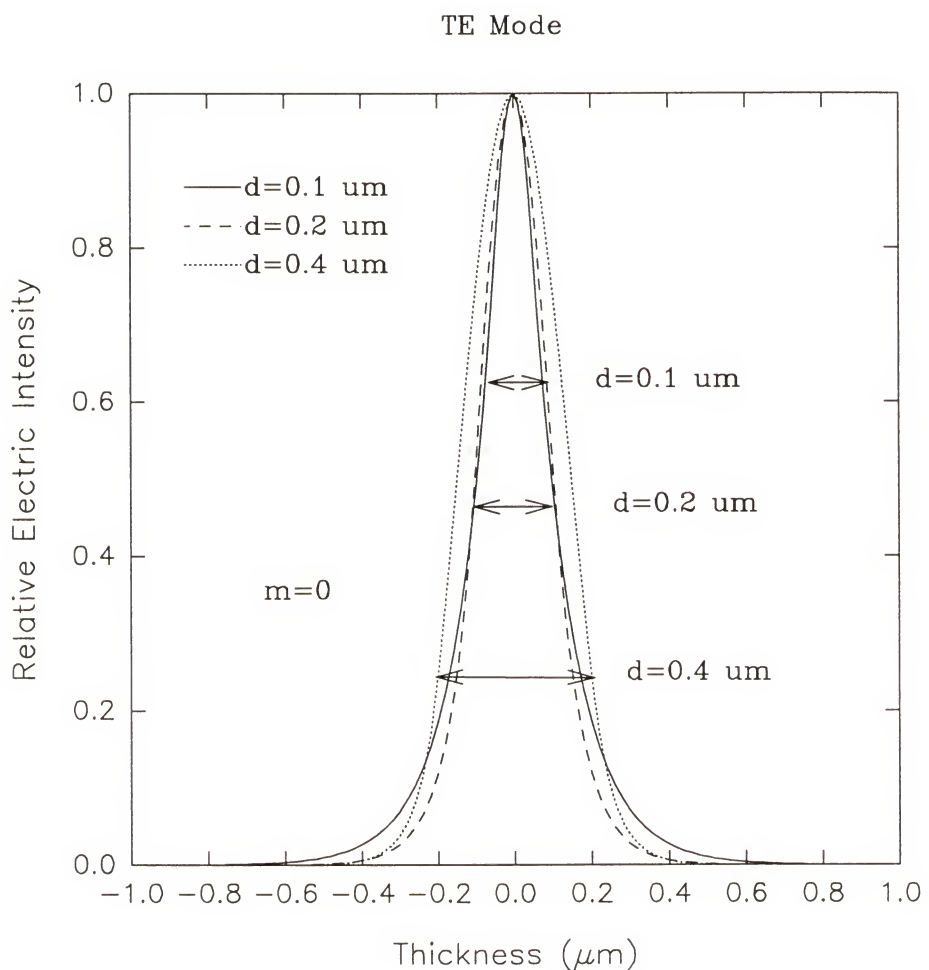


Figure 5-10. Variation of TE electric intensity with active layer thickness.

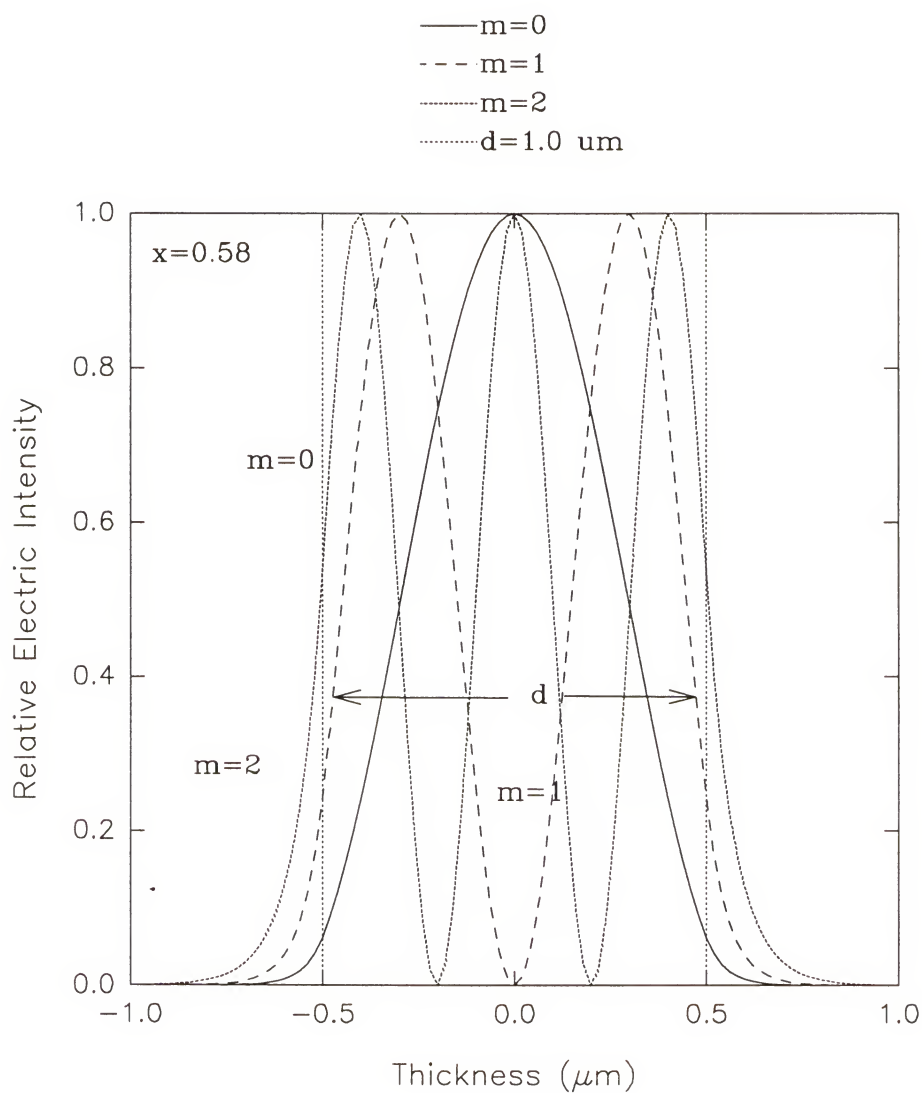


Figure 5-11. Variation of TE electric intensity with mode order.

as the mode order increases, more of the light intensity is outside the active layer. Therefore the lower the mode order, the higher the confinement factor.

Figure 5-12 shows calculation of the electron and carrier concentrations for intrinsic ZnSe in each band as a function of the quasi-Fermi levels based on the following equations.

$$n = \frac{1}{2\pi^2} \left[\frac{2m_e^*}{(h/2\pi)^2} \right]^{3/2} \left[\exp - \left(\frac{E_c - F_n}{kT} \right) \right]_0^{\infty} \frac{x^{1/2} dx}{e^x + 1/b} \quad (5-29)$$

$$p = \frac{1}{2\pi^2} \left[\frac{2m_h^*}{(h/2\pi)^2} \right]^{3/2} \left[\exp - \left(\frac{F_p - E_c}{kT} \right) \right]_0^{\infty} \frac{x^{1/2} dx}{e^x + 1/a} \quad (5-30)$$

where T is the absolute temperature, n is the electron concentration, p is the hole concentration, x is u/kT , a is $\exp\{[F_p - E_v]/kT\}$, and b is $\exp\{[E_c - F_n]/kT\}$. The results are shown in Table 5-2.

Typically, the Fermi levels are within the gap, so the factors (a or b) are $\gg 1$, and so can be ignored in the denominator and a closed form can be derived. Semiconductor laser systems are not in equilibrium and in addition, at least one of the quasi-Fermi levels must be within a band for population inversion to occur. As a result, (a or b) may be less than one and can not be ignored. The integrals are solved numerically using Simpson's rule. The necessary condition for amplification in a semiconductor is that a pumping mechanism creates an inversion such that $F_n - F_p > h\nu > E_g$, where $h\nu$ is the energy provided by some pumping scheme such as optical pumping with another laser or flash lamp, e-beam excitation, or by carrier injection. The critical carrier density can be calculated that corresponds to the bandgap energy of the active layer requiring the $E_c - F_n/kT$ to be the

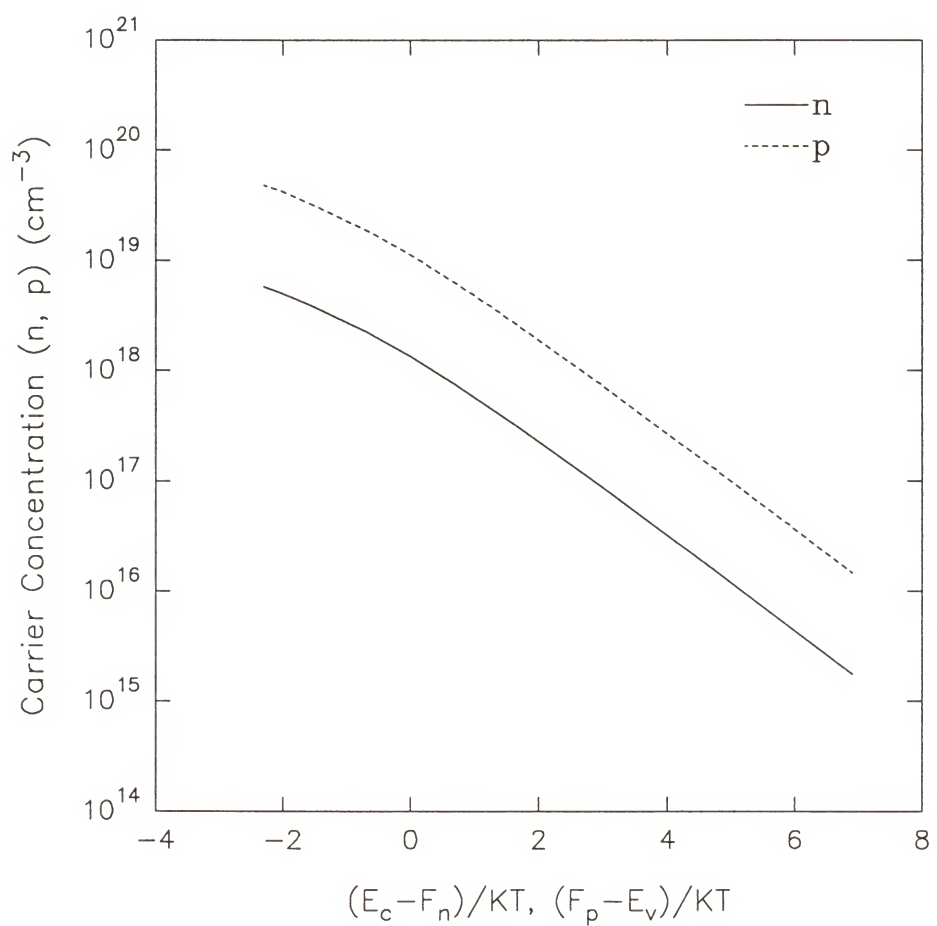


Figure 5-12. Carrier concentration as a function of quasi-Fermi levels.

same magnitude but opposite in sign with $F_p - E_v/kT$. From Table 5-2, the critical density is $n = p = 3.48 \times 10^{18} \text{ cm}^{-3}$. The carrier concentrations from Figures 3-22 and 3-23 in Chapter 3 show that the maximum carrier concentration is only approximately $5 \times 10^{15} \text{ cm}^{-3}$, about three orders of magnitude too low to obtain amplification.

Table 5-2 Carrier concentrations as a function of the quasi-Fermi levels.

(a,b)	$(E_c - F_n)/KT$ $(F_p - E_v)/KT$	n	p
		(cm^{-3})	(cm^{-3})
1000	6.91	1.76×10^{15}	1.46×10^{16}
100	4.61	1.75×10^{16}	1.46×10^{17}
50	3.91	3.50×10^{16}	2.93×10^{17}
20	3.0	8.65×10^{16}	7.24×10^{17}
10	2.3	1.71×10^{17}	1.42×10^{18}
7.75	2.05	2.18×10^{17}	1.82×10^{18}
5	1.61	3.30×10^{17}	2.76×10^{18}
3.9157	1.365	4.17×10^{17}	3.48×10^{18}
2	0.69	7.56×10^{17}	6.33×10^{18}
1	0	1.35×10^{18}	1.13×10^{19}
0.5	-0.69	2.26×10^{18}	1.88×10^{19}
0.2554	-1.365	3.48×10^{18}	2.91×10^{19}
0.2	-1.61	4.03×10^{18}	3.36×10^{19}
0.129	-2.05	5.1×10^{18}	4.29×10^{19}
0.1	-2.3	5.78×10^{18}	4.84×10^{19}

As an approximation to the threshold current density needed to obtain gain and oscillation with the proper feedback, some simple calculations will be performed largely based on data for GaAs since data does not exist for ZnSe. The excess electrons or holes created by this pumping scheme recombine according to the following kinetics:

$$\frac{dn}{dt} = -\beta np + G \quad (3-31)$$

where β is the recombination rate and is equal to $2 \times 10^{-10} \text{ cm}^{-3}/\text{sec}$ for GaAs and G is the generation (or pumping) rate. To maintain a steady state electron-hole pair density of $3.48 \times 10^{18} \text{ cm}^{-3} = n = p$, the generation rate of

$$G = \beta np = (2 \times 10^{-10})(3.48 \times 10^{18})^2 = 2.42 \times 10^{27} \text{ e-h pairs/cm}^3 \cdot \text{sec} \quad (3-32)$$

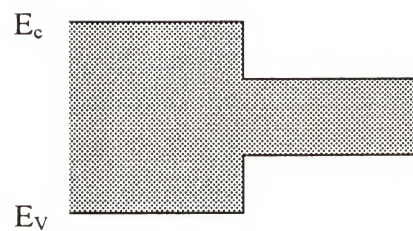
If these carriers are supplied by current injection and if they recombine in an active layer thickness of $1.0 \mu\text{m}$, the current density required is

$$J = ed \left(\frac{dn}{dt} \right) = (1.6 \times 10^{-19} \text{ cm}^{-3}) (1 \times 10^{-4} \text{ cm}) (2.42 \times 10^{27} \text{ A}) = 38.72 \text{ kA/cm}^2 \quad (3-33)$$

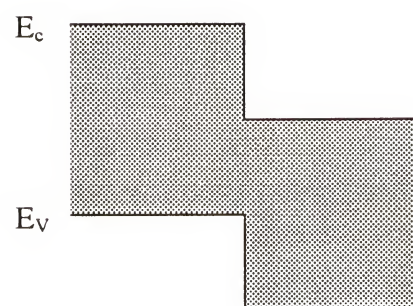
If the current is larger than this value, one can expect gain and oscillation with the correct feedback. This value is about a factor of 7.5 times larger than that for GaAs which is around 5.17 kA/cm^2 [200]. The main reason for this is the effective mass of the electrons and holes for the ZnSe is much larger than those of GaAs. The m_e is $0.067 m_o$ and m_h is $0.55 m_o$ for GaAs where m_o is the resting electron mass. The m_e is $0.17 m_o$ and m_h is $0.71 m_o$ for ZnSe [201].

5.3.2 Carrier Confinement

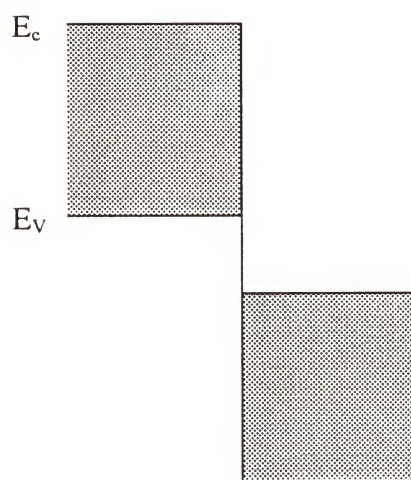
The conduction and valence band edge offsets need to be calculated to determine if the double heterojunctions will provide good carrier confinement. Figure 5-13 illustrates several possibilities for the relative alignments for the conduction and valence bands for heterostructures: normal, staggered, and broken gap. The normal alignment is desirable for double heterostructure devices. Since the smaller bandgap energy of the active layer will be positioned in between the valence and conduction bands of the larger bandgap



(a)



(b)



(c)

Figure 5-13. Configurations of band edge offset for heterojunctions: (a) normal, (b) staggered, and (c) broken gap.

cladding layer. With this alignment, the barriers reduce the diffusion of holes and electrons away from the active region. In the staggered alignment, the holes are well confined, but there is no barrier to reduce the electrons from diffusing into the cladding layer. In the broken gap alignment, there is no confinement of either carrier. The potential barrier in the normal alignment prevents diffusion of electrons to the p-type region and prevents the diffusion of holes into the n-type region since electrostatic forces will cause opposite charges to attract. These bandgap configuration are normally estimated from electron affinity values.

The electron affinities for ZnS, CdS and ZnSe are 3.90, 4.79, and 4.09 eV respectively [202]. The electron affinity of $Zn_{0.42}Cd_{0.58}S$ is approximated by linear interpolation of the values for the constituent binary compounds. According to an analysis with the difference in electron affinities equaling ΔE_c , the alignment type is predicted to be staggered with the conduction band of ZnSe (active layer) 0.33 eV above the conduction band of ZnCdS (cladding layer) and the valence band of ZnSe 0.79 eV above the valence band of ZnCdS.

These results are further confirmed by calculations based on photothreshold values. Predicting the extent of these band edge discontinuities has always been a problem. The linear combination of atomic orbitals (LCAO) provides a framework to describe electronic structure and energy levels in terms of atomic term values which are measured from the vacuum level. The term value is defined as the negative of the energy required to remove the electron from the atom and place it at rest an infinite distance away. In light of this definition, photothreshold is defined as the energy required to remove an electron from the

highest occupied state to infinity. The energy of the valence-band maximum can be written as

$$E_v = \frac{(\varepsilon_p^c + \varepsilon_p^a)}{2} - \sqrt{v_2^2 + v_3^2} \quad (3-34)$$

where ε_p^c is the energy of the p orbital for the cation, ε_p^a is the energy of the p orbital for the anion, v_2 is the covalent energy and v_3 is the polar energy. The covalent and polar energy can be further defined as

$$V_2 = \frac{2.16\hbar^2}{md^2} \quad (3-35)$$

$$V_3 = \frac{\varepsilon_1 + \varepsilon_2}{2} \quad (3-36)$$

where \hbar is Planck's constant, m is the electron mass and d is the internuclear distance (i.e., the bond length).

Unfortunately, the absolute values are not meaningful, but the relative values are. There are several reasons for the inaccuracy of the values. The main contributing factor to the overlap interaction of orbitals is kinetic energy that will increase the electronic energy and thereby reduce the photothreshold. The reconstruction of the surface due to dangling bonds can introduce dipole layers at the surface which will normally increase the photothreshold. This is true because it has been found that negatively charged atoms tend to move out from the surface and positively charged atoms tend to move inward. The expression for the photothresholds does not take into account any of this and expectedly

do not match with the experimental results. However, empirical results show that the true values are only off by an additive constant which gives the relationship:

$$\Phi = |E_v| - 3.8 \text{ eV} \quad (3-37)$$

where E_v is the valence band edge. The valence band edges for some II-VI materials are reproduced in Table 5-3 [203].

Table 5-3. Valence band edge for II-IV materials.

Material	$-E_v$ (eV)
ZnSe	10.58
CdTe	9.32
ZnS	11.4
MgTe	9.33
CdS (hex)	11.12
ZnTe	9.5
CdSe	10.35

The main trends seem to indicate that photothreshold increases with increasing polarity and with decreasing metallicity. The main influence on the photothreshold is given by the p-state energy of the nonmetallic atom and then to a lesser extent by the p-state energy of the metallic atom.

The valence band discontinuities or band offsets can be determined by simply subtracting the corresponding valence band edge values in the Table 5-3. The conduction band discontinuity or band offset can be determined by taking into account the correction for the bandgap on each side of the heterojunction. For alloys the values can be interpolated between the two binary constituents.

In general as a first approximation, the bandgap energies can also be interpolated, but this is not true for changes in alloys for direct to indirect bandgap energies and those that change crystal structure. Interpolation will not be correct for the net gap to be determined. This method has proven successful for Ge/Si, Ge/GaAs, GaAs/Ga_{0.8}A_{10.2}As and InP/CdS systems. This method has also correctly predicted that for the InAs/GaSb system that the valence-band maximum on the GaSb side lies above the conduction-band minimum on the InAs side [203]. The predicted results have shown to match with experimental data very well. A self consistency test has shown that this technique should work reasonably well for heterojunctions with reasonably lattice matched conditions and this is usually the case.

As an example of the calculations, we shall use ZnCdS as the cladding layer and ZnSe as the active layer. As mentioned before, the composition at lattice-matched conditions to GaAs is Zn_{0.42}Cd_{0.58}S. At this composition the bandgap energy is 2.71 eV. Assuming a linear relationship for the valence band edge in Table 5-3, the corresponding $-E_v$ is 11.24 eV. The $-E_v$ for ZnSe is 10.58 eV. The difference is 0.66 eV and is comparable to the value of 0.79 eV estimated from the electron affinities. This indicates that the valence band edge of the ZnSe active layer is 0.66 eV above the valence band edge of the cladding layer ZnCdS. The difference in bandgap energies of the cladding and active layers $2.71 - 2.58 \text{ eV} - \Delta E_v = -0.53 \text{ eV}$. This means that the maximum conduction band of the active layer is higher in energy relative to the maximum conduction band of the cladding layer. This suggests that for ZnSe/ZnCdS system, the alignment of the

conduction and valence bands is staggered and would not be suitable for electron carrier confinement.

Let E_g^c and E_g^a be the bandgap energies of the cladding and active layer. Let ΔE_v be the valence band edge offset which is equal to $E_v^a - E_v^c$ with the convention that the electron energy increases as y' increases. If the ΔE_v is a positive number, the minimum valence band edge of the active layer is lower in energy, higher in the electron energy y axis than the minimum valence band edge of the cladding layer. Conversely, if ΔE_v is a negative number, the minimum valence band edge of the active region is higher in energy, lower on the electron energy scale relative to the minimum valence band edge of the cladding layer. The conduction band offset is calculated by the following equation:

$$\Delta E_c = \Delta E_g^a - \Delta E_g^c + \Delta E_v$$

If ΔE_c is negative, the maximum conduction band edge of the active layer is lower in energy and thereby lower in the y -axis than the maximum conduction band edge of the cladding layer. Conversely, if ΔE_c is a positive number, then the maximum conduction band edge of the active layer is higher in energy and higher in the y -axis by magnitude of that amount relative to the maximum conduction band edge of the cladding layer. Table 5-4 summarizes the band edge calculations for two systems using the data.

5.3.3 Physical Aspects of Laser Fabrication

Since the cleavage planes are perpendicular to each other for (100) GaAs substrates, it is much easier to form waveguides than it is for (111) substrates. Simple charge balance

Table 5-4. Calculated band edge offsets.

Active Layer	Cladding Layer	ΔE_v (eV)	ΔE_c (eV)	Alignment Type ¹
ZnSe	Zn _{0.42} Cd _{0.58} dS	0.66	0.53	s
ZnSe	ZnS _{0.05} Se _{0.95} ^a	0.043	-0.13	n

¹ s = staggered and n = normal

^a lattice matched conditions to GaAs [204]

reasons provide reasonable explanations for (110) natural cleavage planes of polar zinc blende structures that includes ZnCdS at lattice matched conditions to GaAs. The surface energy as a first approximation is proportional to the number of bonds that are cut. For polar semiconductors, the two types of dangling hybrid bonds must be considered where the surface electronic structure plays a role. Those associated with nonmetallic atoms will have lower energy compared to the metallic ones. Cleaving a polar structure on a (111) plane leaves one entire surface of metallic atoms and the opposite surface of nonmetallic atoms. Placing the electrons on the dangling bond of lower energy will leave a huge surface charge on each of the two surfaces. The resulting charge separation requires too much energy; hence such a plane is not favorable. Similar considerations for the (100) planes show that it too is not favorable if done on a planar cut. In contrast, a (110) surface is half metallic and half nonmetallic and the electrostatic energy gain by this arrangement surpasses the extra energy required to break the bonds. Thus the (110) surface is the natural cleavage plane for polar semiconductors. The (001) oriented substrate is used for growth of laser materials because the natural cleavage plane (110) forms right angles to it and cleaves into parallel reflective faces to form a Fabry-Perot

resonant cavity. If the material is grown on (111) substrates, the sides will be 60° from each other and will make it difficult to form such amplifying resonant cavities.

5.4 Summary

A symmetric three layer waveguide with ZnSe as the active layer and $Zn_{0.42}Cd_{0.58}S$ as the cladding layers has been fabricated and photopumped. The results do not show any spectral narrowing nor sharp spectral line indicative of lasing and waveguiding. The main problem is that the cladding layers were luminescing rather than the ZnSe active layer which is caused by poor crystallinity or wrong wavelength.

The optical confinement for a ZnCdS/ZnSe/ZnCdS DH waveguide was determined based upon measured refractive indices. The optical field distributions are derived from Maxwell's equations. Graphical solutions to the TE and TM eigenvalue equations reveal the modes and cutoff. Furthermore the optical confinement factor is derived from the electric field components of the TE modes. The confinement factor is reduced with higher Cd composition, higher mode order, and thinner active layer.

The carrier confinement for a ZnCdS/ZnSe/ZnCdS DH laser structure was estimated from values of electron affinities and supported by photothreshold values. The calculations show that the configuration for this system is staggered with possibility of hole confinement but not of electron. For comparison, the ZnSSe/ZnSe/ZnSSe system shows a normal configuration and has the possibility of both electron and hole confinement.

CHAPTER 6 CONCLUSIONS AND FUTURE WORK

Although ZnCdS grown by low pressure MOVPE has potential in applications of blue-light emitting optoelectronic devices, further developmental work is necessary to improve the crystallinity and to control both the p and n-type intentional doping.

The lowest FWHMs of HRXRD peaks are 2000 and 500 arc-seconds for epilayers grown on (100) and (111) family of orientations, respectively. The poor crystallinity is believed to be a result of a high density of stacking faults as suggested by surface energy considerations of each respective growth plane. Growth temperature, VI/II ratio, substrate orientation, buffer layer, growth rate, and etchants were studied to determine their effects on crystallinity by either the Taguchi method or the standard method of varying one parameter while keeping others fixed. Table 2-9 in Chapter 2 lists the conditions for ZnCdS growth with the best crystalline quality and thickness uniformity.

High growth temperature consistently produces the best quality ZnCdS epilayers due to promotion of 2-D growth and suppression of 3-D growth. This has been explained through the nucleation and growth mechanism. Initially, the VI/II ratio seemed unimportant, but is shown to be convoluted with the growth temperature. High quality films are grown with specific growth temperatures and supersaturation. As expected, lower growth rate produces better quality films due to increased residence time. The long duration allows more time for the reactants to find the correct lattice sites. Only the

ammonia hydroxide etchant was shown to provide good quality epilayers irrespective of the substrate orientation. ZnSe buffer layers are grown prior to growth of ZnCdS to improve the epilayer crystallinity, but this procedure did not result in an improvement. The FWHM of HRXRD peaks is much larger than without the ZnSe buffer layer whether grown on (100) or (111) planes. Use of a GaAs buffer layer may be more beneficial.

The high reactivity between the metalorganics (DEZn and DMCd) and H₂S is a strong possibility for poor crystallinity. Low growth pressure and introduction of reactants through separate inlet lines are some of the precautionary measures taken to minimize parasitic gas phase reactions. Nevertheless, a different chemical reaction needs to be adopted to decrease the reactivity.

The use of heterocyclic sulfur compounds have been shown to produce no significant premature reactions. Thiophene (C₄H₄S) and tetrahydrothiophene (C₄H₈S) have been used to grow ZnS by MOVPE [205]. Although the growth temperatures are comparable to those reported for the hydride reactions, the added advantage of minimal premature reaction is encouraging. The heterocyclic compounds generally are used to grow ZnS at temperatures between 450 to 550 °C while for the hydrides, the temperature is set at 550 °C. The absence of premature reactions indicate a lower reactivity of these heterocyclic compounds with the metal-alkyls as compared to that of the hydrides. The high reactivity of the hydride with the MOs is explained by the mechanistic pathway of the reaction.

The H₂S acts as a Lewis base and the metal-alkyls (DMCd and DEZn) act as Lewis acids and react willingly even at room temperature. This involves the combination of an

electron donating base with an electron accepting acid and the subsequent elimination of a methyl group plus an active hydrogen. One way in which room temperature reactivity may be reduced is to limit the electron donating properties of the group VI atom which normally has two lone pairs of electrons available for reaction. In the case of aromatic compounds such as thiophene and tetrahydrothiophene, one of the lone pairs of electrons must be delocalized into the ring system to make the aromatic sextet of electrons. This in turn could result in the lone pair of electrons being more tightly bound and therefore the heterocyclic compounds become much weaker electron donors than the hydride sources. As a result, the aromatics are less likely to react with the metal-alkyls than the hydrides at low temperatures.

Another possibility is the use of carbon disulfide (CS_2) as the new source for sulfur [206]. This in conjunction with DEZn have been used to grow ZnS and should be promising for growing alloys as well. This new sulfur compound has several advantages. It is less expensive than the sulfur alkyls such as the heterocyclic compounds. It is also easier to handle since it is a volatile liquid as compared to the gaseous H_2S . But most importantly, this is also shown to have no premature reactions when combined with DEZn or DMZn.

The reactor design also needs improvement to obtain films with high quality and good thickness uniformity. The necessary requirements for good reactor cell design are the following:

1. Temperature gradients across the susceptor should be avoided.
2. Laminar flows free of convection should exist.

3. All profiles should be fully developed.
4. The top wall should preferably be water-cooled in order to establish a well-defined temperature gradient.
5. Minimize dead volumes to avoid vortex formation.
6. Long heated susceptor which spans the length of the reactor.

Although most of these items have been adopted in the reactor design, a water cooled jacket around the growth zone should help minimize deposition on the reactor walls and maintain laminar flow.

The optical, physical and electrical properties have also been measured. The bandgap energy for the entire compositional spectrum of ZnCdS has been determined by reflectance measurement and confirmed by PL measurement. The relationship between bandgap energy and solid phase composition fits a quadratic expression. This bowing is typical of other II-VI systems. The bandgap energy at lattice matched conditions is 2.71 eV which is well within the blue and purple region of the visible spectrum.

The TECs have also been calculated from measured lattice constants at various temperatures. The lattice constants have been measured perpendicular to the growth surface only along the <004> direction by HRXRD. The results show that the ZnCdS epilayer grown on GaAs will always be under compressive strain even when grown at low temperatures. Thermal mismatch is not of sufficient magnitude to produce a high density of strain induced dislocations.

The carrier concentrations with n and p-type doping have been determined by Hall measurements with the Van der Pauw technique. TEAl and TEGa are used for in situ n-

type dopant studies. The results showed inadequate electron concentrations of about 10^{15} cm^{-3} which is approximately three orders of magnitude lower than required for injection carrier luminescence. A novel p-type dopant, bis-trimethyl silial amido zinc, showed high resistivity with no measurable hole concentrations. PL measurements show that more deep level optically active defects were introduced. These are most likely due to carbon contamination.

Without adequate carrier concentrations, injection devices are impossible. Although p-type behavior is difficult to achieve in II-VI compounds due to self compensation, n-type behavior should not be difficult to achieve. One major cause of poor carrier concentrations is the poor crystallinity of the epilayer. With distorted lattices and high point defect concentrations, the dopants will not be able to sit in the correct lattice site. Chlorine has found good success in n-type doping ZnSe and this should be investigated for ZnCdS [207].

Ohmic contacts on ZnCdS need to be further investigated. The low carrier concentrations determined by Hall measurements may be inaccurate due to high resistivity of the contact. Although this may be a huge undertaking, this is necessary for accurate assessment of doping studies.

A model based on regular solution theory has been developed to predict the solid vapor equilibrium (SVE) of ZnCdS at various temperatures. The model fits the experimental data fairly well. For the first time, the interaction parameter between the binary constituent compounds have been calculated using Stringfellow's DLP model based

specifically on material properties of II-VI compounds. As a testament to the applicability of the SVE model, it is used to predict the solid vapor equilibrium for ZnSSe with success.

A symmetric three layer slab waveguide (ZnCdS/ZnSe/ZnCdS) is fabricated and photopumped to assess the lasing capabilities of the active layer and the confining abilities of the cladding layer. Spectral narrowing and a sharp spectral line were not visible; an indication of a poor lasing medium and poor optical confinement. The peak position of the spectrum indicates that the ZnCdS is luminescing instead of the active layer. This suggests poor crystallinity of ZnSe grown on ZnCdS. A thin ZnCdS film grown on GaAs is also photopumped and again spectral narrowing is not seen due to poor crystallinity.

Calculations were made to determine the optical field distribution and optical confinement of the ZnCdS/ZnSe/ZnCdS waveguide. Eigenvalue equations for transverse electric and transverse magnetic waves derived from Maxwell's equations are graphically solved. Results show that the TE is the dominant mode. Increasing Cd composition in ZnCdS cladding, decreasing the active layer thickness, and higher mode order all decrease optical confinement. Calculations also show that the minimal hole and electron carrier concentrations are roughly 10^{18} cm⁻³ to obtain population inversion and maintain stimulated emission.

The possibility of carrier confinement is studied through calculations based on electron affinities. For a $Zn_{0.42}Cd_{0.58}S/ZnSe/Zn_{0.42}Cd_{0.58}S$ DH structure, the bandgap alignment is a staggered configuration. This suggests that hole confinement is possible but not electron confinement. Calculations based on photothreshold values also confirm this.

For comparison, $\text{ZnS}_{0.05}\text{Se}_{0.95}/\text{ZnSe}/\text{ZnS}_{0.05}\text{Se}_{0.95}$ aligns in a normal configuration with possibility of both electron and hole configuration.

Although ZnCdS has potential for applications in blue light emitting optoelectronics, other alternatives need to be investigated such as ZnMgCdS and ZnSSe .

REFERENCES

- [1] S. M. Sze, *VLSI Technology*, McGraw-Hill Book Company, New York, 1988.
- [2] G. Moore, *Electron Aust.* 42, 14 (1980).
- [3] R. N. Noyce, *The Microelectronics Revolution* (edited by T. Forester), MIT Press, Cambridge, 1981.
- [4] S. Fujita, unpublished work at Chiba University, Japan.
- [5] H. C. Casey, Jr. and M. B. Panish, *Heterostructure Lasers*, Academic Press, New York, 1987.
- [6] Dieter K. Schroder, *Semiconductor Material and Device Characterization*, John Wiley and Sons, Inc., New York, 1990.
- [7] B. Ray, *II-VI Compounds*, Pergamon Press, Oxford, 1969.
- [8] M. A. Haase, H. Cheng, J. M. DePuydt, and J. E. Potts, *J. Appl. Phys.* 67, 448 (1990).
- [9] K. Akimoto, T. Miyajima, and Y. Mori, *Jpn. J. Appl. Phys.* 28, L531 (1989).
- [10] W. A. Bryant, *J. Mat. Science* 12, 1285 (1977).
- [11] H. Hartmann, *J. Cryst. Growth* 31, 323 (1975).
- [12] S. Fujita, H. Mimoto, and T. Noguchi, *J. Cryst. Growth* 45, 281 (1978).
- [13] E. Veuhoff, W. Pletschen, P. Balk, and H. Luth, *J. Cryst. Growth* 55, 30 (1981).
- [14] F. J. Morris and H. Fukui, *J. Vac. Sci. Technol.* 11, 506 (1974).
- [15] M. B. Panish and S. Sumski, *J. Appl. Phys.* 55, 3571 (1984).
- [16] S. Yoshida, S. Misawa, and A. Itoh, *Appl. Phys. Lett.* 26, 461 (1975).

- [17] K. Yoneda, Y. Hishida, T. Toda, H. Ishii, and T. Niina, *Appl. Phys. Lett.* 45, 1300 (1984).
- [18] D. A. Cusano, in *Physics and Chemistry of II-VI Compounds*, (edited by M. Aven and J. S. Prener), North Holland Publishing Co., Amsterdam, 1967.
- [19] F. J. Studer, D. A. Cusano, and A. H. Young, *J. Opt. Soc. Am* 41, 559 (1951).
- [20] H. Ando, A. Taike, M. Konagai, and K. Takahashi, *J. Appl. Phys.* 62, 1251 (1987).
- [21] A. Yoshikawa, H. Oniyama, S. Yamaga, and H. Kasai, *J. Cryst. Growth* 95, 572 (1989).
- [22] R. R. Chamberlin and J. S. Skarman, *J. Electrochemical Soc.* 113, 86 (1966).
- [23] R. R. Chamberlin and J. S. Skarman, *Solid State Electronics* 9, 819 (1966).
- [24] W. M. Yim and E. J. Stofko, *J. Electrochem. Soc.* 119, 381 (1972).
- [25] S. G. Parker, J. E. Pinnell, and L. N. Swink, *J. Phys. Chem. Solids* 32, 139 (1971).
- [26] H. M. Manasevit, *J. Cryst. Growth* 22, 125 (1974).
- [27] J. B. Mullin, S. J. C. Irvine, and J. Tunnicliffe, *J. Cryst. Growth* 68, 214 (1984).
- [28] B. Cockayne and P. J. Wright, *J. Cryst. Growth* 68, 223 (1984).
- [29] T. Yao, Y. Makita, and S. Maekawa, *Appl. Phys. Lett.* 35, 97 (1979).
- [30] T. Yao, M. Ogura, S. Matsuoka, and T. Morishita, *Jpn. J. Appl. Phys.* 22, L144 (1983).
- [31] R. Park, H. Mar, and N. Salansky, *Appl. Phys. Lett.* 46, 386 (1984).
- [32] A. Yoshikawa, K. Tanaka, S. Yamaga, and H. Kasai, *Jpn. J. Appl. Phys.* 23, L424 (1984).
- [33] S. Fujita, Y. Matsuda, and A. Sasaki, *Jpn. J. Appl. Phys.* 23, L360 (1984).
- [34] A. Yoshikawa, S. Yamaga, K. Tanaka, and H. Kasai, *J. Cryst. Growth* 72, 13 (1985).

- [35] W. Stutius, *Appl. Phys. Lett.* 33, 656 (1978).
- [36] P. J. Wright, B. Cockayne, and A. J. Williams, *J. Cryst. Growth* 72, 23 (1985).
- [37] S. Yamaga, A. Yoshikawa, and H. Kasai, *J. Cryst. Growth* 99, 432 (1990).
- [38] S. Fujita, S. Hayashi, M. Funato, and S. Fujita, *J. Cryst. Growth* 99, 437 (1990).
- [39] K. Nishimura, K. Sakai, Y. Nagao, and T. Ezaki, *J. Cryst. Growth* 117, 119 (1992).
- [40] S. Yamaga and A. Yoshikawa, *J. Cryst. Growth* 117, 353 (1992).
- [41] M. K. B. Saidin, G. J. Russel, A. W. Brinkman, and J. Woods, *J. Cryst. Growth* 101, 844 (1990).
- [42] S. Fujita, M. Funato, S. Hayashi, and S. Fujita, *Jpn. J. Appl. Phys.* 28, L898 (1989).
- [43] T. L. Chu, S. S. Chu, J. Britt, C. Ferekides, and C. Q. Wu, *J. Appl. Phys.* 70, 2688 (1991).
- [44] A. Dhar, S. Chaudhuri, and A. K. Pal, *J. Mat. Sci.* 26, 4416 (1991).
- [45] G. K. Padam, G. L. Malhotra, and S. U. M. Rao, *J. Appl. Phys.* 63, 770 (1987).
- [46] Y. Yamada, Y. Masumoto, J. T. Mullins, and T. Taguchi, *Appl. Phys. Lett.* 61, 2190 (1992).
- [47] A. Yoshikawa, A. Shirai, S. Yamaga, and H. Kasai, *Jpn. J. Appl. Phys.* 25, 673 (1986).
- [48] S. Yamaga, A. Yoshikawa, and H. Kasai, *Jpn. J. Appl. Phys.* 26, 1002 (1987).
- [49] L. J. Giling, *J. Electrochem. Soc.* 129, 634 (1982).
- [50] P. W. Bohn and R. C. Manz, *J. Electrochem. Soc.* 132, 1981 (1985).
- [51] Gerald B. Stringfellow, *Organometallic Vapor-Phase Epitaxy: Theory and Practice*, Academic Press, Inc., Boston, 1989.
- [52] I. B. Bhat, N. R. Taskar, and S. K. Ghandi, *J. Electrochem. Soc.* 134, 195 (1987).

- [53] B. A. Joyce, J. H. Neave, and B. E. Watts, *J. Mater. Science* 15, 1 (1969).
- [54] C. C. Hsu, J. S. Yuan, R. M. Cohen, and G. B. Stringfellow, *J. Appl. Phys.* 59, 395 (1986).
- [55] M. Kondow, H. Kakibayashi, S. Minagawa, Y. Inoue, T. Nishino, and Y. Hamakawa, *Appl. Phys. Lett.* 53, 307 (1988).
- [56] S. G. Bailey, G. A. Landis, and D. M. Wilt, *J. Electrochem. Soc.* 136, 3444 (1989).
- [57] L. J. Giling, in *Crystal Growth of Electronic Materials* (edited by E. Kaldis), Elsevier Science Publishers, B. V., Amsterdam, 1985.
- [58] Ban V. S. and S. L. Gilbert, *J. Cryst. Growth* 31, 284 (1975).
- [59] R. Takahashi, Y. Koga, and K. Sugawara, *J. Electrochem. Soc.* 119, 1406 (1972).
- [60] S. Berkman, V. S. Ban, and N. Goldsmith, *Heterojunction Semiconductors for Electronic Devices* (edited by G. W. Cullen and C. C. Wang), Springer, New York, 1977.
- [61] V. S. Ban, *J. Electrochem. Soc.* 125, 317 (1978).
- [62] R. Byron Bird, Warren E. Stewart, and Edwin N. Lightfoot, *Transport Phenomena*, John Wiley and Sons, Inc., New York, 1960.
- [63] T. Koyama, T. Yodo, H. Oka, K. Yamashita, and T. Yamasaki, *J. Cryst. Growth* 91, 639 (1988).
- [64] A. S. Grove, *Physics and Technology of Semiconductor Devices*, John Wiley and Sons, Inc., New York, 1967.
- [65] H.C. Theuerer, *J. Electrochem. Soc.* 108, 649 (1961).
- [66] M. Heuken, J. Söllner, W. Bettermann, K. Heime, B. Bollig, and E. Kubalek, *Mater. Sci. Eng. B* 9, 189 (1991).
- [67] R. Bruinsma and A. Zangwill, *J. Physique* 47, 2055 (1986).
- [68] W. A. Jesser, *Mater. Sci. and Eng.* 4, 279 (1969).

- [69] M. K. B. Saidin, G. J. Russell, A. W. Brinkman, and J. Woods, *J. Cryst. Growth* 101, 844 (1990).
- [70] S. Kaneko, H. Aoki, Y. Kawahara, and F. Imoto, *J. Electrochem. Soc.* 131, 1445 (1984).
- [71] W. R. Holman and F. J. Huegal, *J. Vac. Sci. Technol.* 11, 701 (1974).
- [72] D. B. Holt, *J. Phys. Chem. Solids* 27, 1053 (1966).
- [73] S. Kaneko, H. Aoki, Y. Kawahara, and F. Imito, *J. Electrochem. Soc.* 134, 1445 (1984).
- [74] B. Cockayne, P. J. Wright, M. S. Skolnick, A. D. Pitt, J. O. Williams, and T. L. Ng, *J. Cryst. Growth* 72, 17 (1985).
- [75] O. Ueda, S. Komiya, S. Yamakoshi, and T. Kotani, *Jpn. J. App. Phys.* 20, 1201 (1981).
- [76] B. Segall and D. T. F. Marple, in *Physics and Chemistry of II-VI Compounds*, (edited by M. Aven and J. S. Prener), North Holland Publishing Co., Amsterdam, 1967.
- [77] H. L. Hwok, *J. Phys. D* 16, 2367 (1983).
- [78] K. Kaneko, M. Ayabe, and N. Watanabe, *Inst. Phys. Conf. Ser.* 33a, 216 (1977).
- [79] T. F. Marple, *J. Appl. Phys.* 35, 1241 (1964).
- [80] W. L. Bond, *J. Appl. Phys.* 36, 1674 (1965).
- [81] R. M. A. Azzam and N. M. Bashara, *Ellipsometry and Polarized Light*, North Holland Press, Amsterdam, 1977.
- [82] P. G. Snyder, M. C. Rost, G. H. Bu-Abbud, J. A. Woolam, and S. A. Alterovitz, *J. Appl. Phys.* 60, 3293 (1986).
- [83] R. E. Collins, *Rev. Sci. Insts.* 61, 2029 (1990).
- [84] D. E. Aspnes, in *Handbook of Optical Constants of Solids* (edited by E. Palik), Academic Press, Orlando, 1985.
- [85] H.G. Tompkins, *A User's Guide to Ellipsometry*, Academic Press, Inc., Boston, 1993.

- [86] D. D. Sell, H. C. Casey Jr., and K. W. Wecht, *J. Appl. Phys.* 45, 2650 (1974).
- [87] F. Stern, *Phys. Rev.* 133, A1653 (1964).
- [88] J. Zoroofchi and J. K. Butler, *J. Appl. Phys.* 44, 3697 (1973).
- [89] W. D. Johnson, Jr., *Appl. Phys. Lett.* 24, 494 (1974).
- [90] J. M. Gaines, R. R. Drenten, K. W. Haberern, T. Marshall, P. Mensz, and J. Petruzzello, *Appl. Phys. Lett.* 62, 2462 (1993).
- [91] M. A. Haase, J. Qiu, J. M. DePuydt, and H. Cheng, *Appl. Phys. Lett.* 59, 1271 (1991).
- [92] H. Okuyama, T. Miyajima, Y. Morinaga, F. Hiei, M. Ozawa, and K. Akimoto, *Electron. Lett.* 28, 1978 (1992).
- [93] H. Jeon, J. Ding, W. Patterson, A. V. Nurmikko, W. Xie, D. C. Grillo, M. Kobayashi, and R. L. Gunshor, *Appl. Phys. Lett.* 59, 3629 (1991).
- [94] R. Bisaro, P. Merenda, and T. P. Pearsall, *Appl. Phys. Lett.* 34, 100 (1979).
- [95] M. Leszczynski, A. Kulik, and P. Ciepielewski, *Phys. Stat. Sol. (a)*, 119, 495 (1990).
- [96] B. W. James and B. Yates, *Cryogenics* 5, 68 (1965).
- [97] N. Waterhouse and B. Yates, *Cryogenics* 8, 267 (1968).
- [98] R. B. Roberts, *J. Phys. E: Sci. Instrum.* 8, 600 (1975).
- [99] S. J. Bennet, *J. Phys. E: Sci. Instrum.* 10, 525 (1977).
- [100] G. K. White, *Cryogenics* 1, 151 (1961).
- [101] W. L. Bond, *Acta Cryst.* 13, 814 (1960).
- [102] H. Hartmann, *J. Cryst. Growth* 31, 323 (1975).
- [103] J. O. McCaldin, *J. Vac. Sci. Technol. A* 8, 1188 (1990).
- [104] F. A. Kröger, *J. Phys. Chem. Solids* 26, 1717 (1965).

- [105] P. J. Dean, *J. Lumin.* 18/19, 755 (1979).
- [106] B. Fitzpatrick, G. Neumark, R. Bhargava, and J. Vermaak, *Physica B* 116, 487 (1983).
- [107] G. F. Neumark, *J. Appl. Phys.* 65, 4859 (1989).
- [108] D. J. Chadi and K. J. Chang, *Appl. Phys. Lett.* 55, 575 (1989).
- [109] W. A. Harrison and J. Tersoff, *J. Vac. Sci. Technol. B* 4, 1068 (1986).
- [110] J. O. McCaldin, T. C. McGill, and C. A. Mead, *Phys. Rev. Lett.* 36, 56 (1976).
- [111] A. Yoshikawa, H. Nomura, S. Yamaga, and H. Kasai, *J. Appl. Phys.* 65, 1223 (1989).
- [112] W. Stutius, *J. Appl. Phys.* 53, 284 (1982).
- [113] S. Yamaga, A. Yoshikawa, and H. Kasai, *J. Cryst. Growth* 86, 252 (1988).
- [114] T. Yasuda, I. Mitsuishi, and H. Kukimoto, *Appl. Phys. Lett.* 52, 57 (1987).
- [115] H. Mitsuhashi, A. Yahata, T. Uemoto, A. Kamata, M. Okajima, K. Hirahara, and T. Beppu, *J. Cryst. Growth* 101, 818 (1990).
- [116] A. Yahata, H. Mitsuhashi, K. Hirahara, and T. Beppu, *Jpn. J. Appl. Phys.* 29, L4 (1990).
- [117] I. Suemune, K. Yamada, H. Masato, T. Kanda, Y. Kan, and M. Yamanishi, *Jpn. J. Appl. Phys.* 27, L2195 (1988).
- [118] A. Ohki, N. Shibata, K. Ando, and A. Katsui, *J. Cryst. Growth* 93, 692 (1988).
- [119] B. Cockayne, P. J. Wright, G. W. Blackmore, J. O. Williams, and T. L. Ng, *J. Mat. Sci.* 19, 3726 (1984).
- [120] T. Yao, Y. Makita, and S. Maekawa, *Appl. Phys. Lett.* 35, 97 (1979).
- [121] F. A. Kröger and H. J. Vink, *Solid State Physics*, Vol. 3 (edited by F. Seitz and D. Turnbull), Academic Press, New York, 1956.
- [122] G. Eriksson, *Chem. Scripta* 8, 100 (1975).
- [123] R. C. Sharma and Y. A. Chang, *J. Cryst. Growth* 88, 193 (1988).

- [124] R. C. Sharma and Y. A. Chang, *J. Electrochem. Soc.* 136, 1536 (1989).
- [125] T. Tung, C. Su, P. Liao, and R. F. Brebrick, *J. Vac. Sci. Technol.* 21, 117 (1982).
- [126] A. Koukitu, T. Suzuki, and H. Seki, *J. Cryst. Growth* 74, 181 (1986).
- [127] A. Koukitu and H. Seki, *J. Cryst. Growth* 76, 233 (1986).
- [128] H. Seki and A. Koukitu, *J. Cryst. Growth* 74, 172 (1986).
- [129] M. Yoshida and H. Watanabe, *J. Electrochem. Soc.* 132, 1733 (1985).
- [130] I. Liaw, K. Chou, and M. Lin, *J. Cryst. Growth* 87, 529 (1988).
- [131] G. B. Stringfellow and P. E. Greene, *J. Phys. Chem. Solids* 30, 1779 (1969).
- [132] G. B. Stringfellow, *J. Cryst. Growth* 27, 21 (1974).
- [133] G. B. Stringfellow, *J. Phys. Chem. Solids* 33, 665 (1972).
- [134] G. B. Stringfellow and P. E. Greene, *J. Electrochem. Soc.* 117, 1075 (1970).
- [135] G. B. Stringfellow and P. E. Greene, *J. Electrochem. Soc.* 117, 1301 (1970).
- [136] G. A. Antypas and C. W. James, *J. Appl. Phys.* 41, 2169 (1970).
- [137] G. A. Antypas, *J. Electrochem. Soc.* 117, 700 (1970).
- [138] D. T. J. Hurdle and E. R. Pike, *J. Mater. Sci.* 1, 399 (1966).
- [139] M. Ilegems and G. L. Pearson, *Gallium Arsenide* (edited by C. I. Pearson), Institute of Physics and the Physical Society, London (1969).
- [140] Y. Furukawa and C. D. Thurmond, *J. Phys. Solids* 26, 1535 (1965).
- [141] M. B. Panish, *J. Phys. Chem. Solids* 27, 291 (1966).
- [142] M. B. Panish, *J. Electrochem. Soc. Solids* 113, 224 (1966).
- [143] M. B. Panish, *J. Electrochem. Soc. Solids* 114, 516 (1967).
- [144] C. Wagner, *Acta Metall.* 6, 309 (1958).

- [145] W. F. Schottky and M. B. Bever, *Acta. Metall.* 6, 320 (1958).
- [146] L. J. Vieland, *Acta. Metall.* 11, 137 (1963).
- [147] C. D. Thurmond, *J. Phys. Chem. Solids* 27, 785 (1965).
- [148] J. R. Arthur, *J. Phys. Chem. Solids* 28, 2257 (1967).
- [149] K. Hagemark, *J. Phys. Chem.* 72, 2316 (1968).
- [150] G. B. Stringfellow, *J. Phys. Chem. Solids* 34, 1749 (1973).
- [151] P. A. Fedders and M. W. Muller, *J. Phys. Chem. Solids* 45, 685 (1984).
- [152] D. W. Kisker and A. G. Zawadzki, *J. Cryst. Growth* 89, 378 (1988).
- [153] J. H. Hildebrand, *J. Am. Chem. Soc.* 51, 66 (1929).
- [154] E. A. Guggenheim, *Mixtures*, Oxford University Press, Oxford (1952).
- [155] J. C. Phillips, *Phys. Rev. Lett.* 20, 550 (1968).
- [156] J. C. Phillips and J. A. Van Vechten, *Phys. Rev. B* 2, 2147 (1970).
- [157] N. A. Guryanova, *The Chemistry of Diamond-like Semiconductors*, M.I.T. Press, Cambridge, 1965.
- [158] N. N. Sirota, *Semiconductors and Semimetals*, Vol. 4, Chapter 2, Academic Press, New York, 1968.
- [159] M. Grade and W. Hirschwald, *Ber. Bunsenges. Phys. Chem.* 86, 899 (1982).
- [160] K. Kulkarni, *Ground State Properties of Tetrahedral Intermetallic Compounds*, Indian Institute of Technology, Bombay, India, 1976.
- [161] D. R. Penn, *Phys. Rev.* 128, 2093 (1962).
- [162] C. R. Pidgeon and S. H. Groves, *II-VI Semiconducting Compounds*, International Conference (edited by D. G. Thomas), Benjamin, New York, 1967.
- [163] T. C. Harman, *II-VI Semiconducting Compounds*, International Conference, (edited by D. G. Thomas) Benjamin, New York, 1967.

- [164] L. Sosnowski and R. R. Galazka, II-VI Semiconducting Compounds, International Conference, (edited by D. G. Thomas) Benjamin, New York, 1967.
- [165] S. H. Groves, R. N. Brown, and C. R. Pidgeon, Phys. Rev. 161, 779 (1967).
- [166] L. Sniadower and R. Kowalczyk, Phys. Status Solidi 25, 233 (1968).
- [167] G. B. Wright, A. J. Strauss, and T. C. Harman, Phys. Rev. 125, 1534 (1962).
- [168] K. J. Siemsen and H. D. Riccius, Phys. Status Solidi 37, 445 (1970).
- [169] R. Zallen and M. Slade, Bull. Amer. Phys. Soc. 15, 290 (1970).
- [170] J. C. Phillips and J. A. Van Vechten, Phys. Rev. B 2, 2147 (1970).
- [171] W. L. Roth, Physics and Chemistry of II-VI Compounds, (edited by M. Aven and J. S. Prener), North-Holland Publishing Company, Amsterdam, 1967.
- [172] A. Freundlich, Journal De Physique 5, 50 (1989).
- [173] S. M. Sze, Physics of Semiconductor Devices, John Wiley and Sons, New York, 1981.
- [174] M. Balkaivski and R. D. Waldren, Phys. Rev. 112, 123 (1958).
- [175] R. G. Wheeler and J. D. Dimmock, Phys. Rev. 125, 1805 (1962).
- [176] J. C. Phillips and J. A. Van Vechten, Phys. Rev. B 2, 2147 (1970).
- [177] T. C. Harman, in II-VI Semiconducting Compounds, 1967 International Conference (edited by D. G. Thomas), Benjamin, New York, 1967.
- [178] S. H. Groves, R. N. Brown, and C. R. Pidgeon, Phys. Rev. 161, 779 (1967).
- [179] P. Goldfinger and M. Jeunehomme, Phys. Rev. 126, 2851 (1963).
- [180] G. B. Stringfellow, J. Cryst. Growth 62, 225 (1983).
- [181] Fukui and Horikoshi, Jpn. J. App. Phys. 19, L53 (1980).
- [182] W. Stutius, J. Electron. Mater. 10, 95 (1981).
- [183] R. L. Gunshor and L. A. Kolodziejski, IEEE LEOS Annual Conference, Paper SDL7.3, Boston, Mass., Nov. 4-9, 1990.

- [184] D. G. Feitelson, Optical Computing, MIT Press, Cambridge, Mass. 1988.
- [185] D. A. Cammack, R. J. Dalby, H. J. Corncilissen, and J. Khurgin, *J. Appl. Phys.* 62, 3071 (1987).
- [186] R. B. Blysmal and W. M. Becker, *Appl. Phys. Lett.* 47, 1039 (1985).
- [187] A. M. Glass and K. Tai, *Appl. Phys. Lett.* 53, 834 (1988).
- [188] W. D. Johnson, *J. Appl. Phys.* 42, 2731 (1971).
- [189] I. Sumune, K. Yamada, H. Masato, Y. Kan, and M. Yamanishi, *Appl. Phys. Lett.* 54, 981 (1989).
- [190] J. A. Constance, *Trans. IEEE* 15, 3 (1991).
- [191] R. M. Park, M. B. Troffer, C. M. Rouleau, J. M. DePuydt, and M. A. Haase, *Appl. Phys. Lett.* 57, 2127 (1990).
- [192] K. Akimoto, T. Miujima, and U. Mori, *Jpn. J. Appl. Phys.* 29, L529 (1990).
- [193] J. Ren, K. A. Bowers, V. Sneed, D. L. Dreifus, J. W. Cood Jr., J. F. Schetzina, and R. M. Kolbas, *Appl. Phys. Lett.* 57, 1901 (1990).
- [194] K. L. Shaklee, R. E. Nahory, and R. F. Leheny, *J. Luminescence* 7, 284 (1973).
- [195] I. Hayashi, M. B. Panish, P. W. Foy, and S. Sumski, *Appl. Phys. Lett.* 17, 109 (1970).
- [196] J. K. Butler, H. Kressel, and I. Ladany, *IEEE J. Quantum Electron.* QE-11, 402 (1975).
- [197] W. Streifer, R. D. Burnham, and R. D. Scifres, *IEEE J. Quantum Electron.* QE-12, 177 (1976).
- [198] D. Marcuse, Light Transmission Optics, Van Nostrand Reinhold, New York, 1972.
- [199] E. D. Palik, Handbook of Optical Constants, Academic Press, New York, 1985.
- [200] J. T. Verdeyen, Laser Electronics, 2nd ed, Prentice Hall, Englewood Cliffs, New Jersey, 1989.

- [201] M. Aven and J. S. Prener, Physics and Chemistry of II-VI Compounds, North-Holland Publishing Company, Amsterdam, 1976.
- [202] Y. S. Park and B. K. Shin, Recent Advances in Injection Luminescence in II-VI Compounds, Academic Press, New York, 1977.
- [203] W. A. Harrison, Electronic Structure and the Properties of Solids, W. H. Freeman and Company, San Francisco, 1980.
- [204] W. Stutius, *J. Electron. Mat.* 10, 95 (1980).
- [205] P. J. Wright, R. J. M. Griffiths, and B. Cockayne, *J. Cryst. Growth* 66, 26 (1984).
- [206] S. Takata, T. Minami, T. Miyata, and H. Nanto, *J. Cryst. Growth* 86, 257 (1988).
- [207] K. Ohkawa, T. Mitsuyu, and O. Yamazaki, *J. Appl. Phys.* 62, 3216 (1987).

BIOGRAPHICAL SKETCH

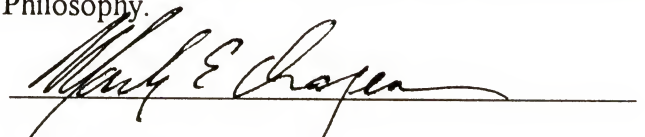
The author, Joe Sung Cho, was born on July 5, 1965, in Seoul, South Korea. He and his family immigrated to the United States in 1971 to Los Angeles, California. He graduated from Harvard School For Boys in 1983. Subsequently, he attended the University of California, Berkeley, and graduated in 1988 with a B.S. in Chemical Engineering. Thereafter, he worked at Intel Corporation in Santa Clara, California for about a year and a half. He then attended the University of Florida in Gainesville to begin his Ph.D. program.

I certify that I have read this study and that in my opinion it conforms to acceptable standards of scholarly presentation and is fully adequate, in scope and quality, as a dissertation for the degree of Doctor of Philosophy.



Timothy J. Anderson, Chairman
Professor of Chemical Engineering

I certify that I have read this study and that in my opinion it conforms to acceptable standards of scholarly presentation and is fully adequate, in scope and quality, as a dissertation for the degree of Doctor of Philosophy.



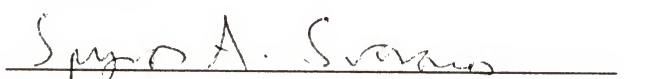
Mark Orazem
Professor of Chemical Engineering

I certify that I have read this study and that in my opinion it conforms to acceptable standards of scholarly presentation and is fully adequate, in scope and quality, as a dissertation for the degree of Doctor of Philosophy.



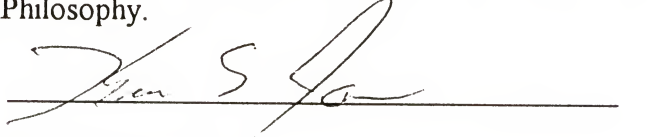
Chang-Won Park
Associate Professor of Chemical Engineering

I certify that I have read this study and that in my opinion it conforms to acceptable standards of scholarly presentation and is fully adequate, in scope and quality, as a dissertation for the degree of Doctor of Philosophy.



Spyros Svoronos
Professor of Chemical Engineering

I certify that I have read this study and that in my opinion it conforms to acceptable standards of scholarly presentation and is fully adequate, in scope and quality, as a dissertation for the degree of Doctor of Philosophy.



Kevin S. Jones
Associate Professor of Materials Science and
Engineering

This dissertation was submitted to the Graduate Faculty of the College of Engineering and to the Graduate School and was accepted as partial fulfillment of the requirements for the degree of Doctor of Philosophy.

August 1995



Winfred M. Phillips
Dean, College of Engineering

Karen A. Holbrook
Dean, Graduate School